NESTOR

A Neutrino Astroparticle Physics Laboratory for the Mediterranean

March 23, 2013

The NESTOR Collaboration:

E. Anassontzis, P. Assimakopoulos, M. Barone, G. Fanourakis, C. Goudis, G. Grammatikakis, P. Hantzios, S. Katsanevas, C. Kourkoumelis, C. Markou, J. Mc Nutt, T. Mikolajski, L. Moraitis, A. Nicolaidis, P. Pramantiotis, L. K. Resvanis*, I. Siotis, S. A. Sotiriou, G. Voulgaris

University of Athens, National Observatory of Athens, NRCPS "Demokritos", University of Crete, University of Ioannina, University of Patras, University of Thessaloniki

L. Sulak

Boston University

A. E. Ball, B. Langeset†

CERN

H. Bradner

University of California, San Diego and Scripps Institution of Oceanography

A. M. Cartacci, A. Odian, M. P. De Pascale, F. Grianti, B. Monteleoni, V. A. Naumov

INFN and University of Florence

L. Trasatti, V. Valente

INFN Frascati

J. G. Learned, V. J. Stenger

University of Hawaii

U. Keusen, P. Koske, J. Rathlev, G. Voigt

University of Kiel

G. De Marchis, L. Piccari

Fondazione Bordoni, Rome

M. Bonori, S. Bottai, A. Capone, F. Massa, E. Valente

INFN Rome and University "La Sapienza"

I. F. Barinov, A. V. Butkevich, L. G. Dedenko,A. O. Deineko, V. A. Gaidash, S. K. Karaevsky, A. A. Mironovich, A. A. Permyakov, N. M. Surin, A. V. Trenikhin, L. M. Zakharov, I. M. Zheleznykh, V. A. Zhukov

Institute for Nuclear Research, Russian Academy of Sciences

T. A. Demidova, A. P. Eremeev, V. T. Paka, M. N. Platonov, V. K. Rucol, N. A. Sheremet

Institute of Oceanology, Russian Academy of Sciences

V. I. Albul, V. V. Ledenev, A. A. Paramonov

Experimental Design Bureau of Oceanological Equipment, Russian Academy of Sciences

N. de Botton, P.-H. Carton, M. Cribier, F. Feinstein, Ph. Goret, J.-C. Languillat, S. Loucatos, L. Moscoso, J.-P. Passérieux, J. Poinsignon, Ph. Rebourgeard, F. Rondeaux, Y. Sacquin, J.-P. Schuller, A. Tabary, D. Vignaud, D. Vilanova

CEA, DSM, DAPNIA/SPP, CE-Saclay

U. Camerini, R. March

University of Wisconsin

*Spokesperson.

†Contribution on Long Base Line Project.

Contents

List of Tables

List of Figures

Preface

NESTOR is a project aiming to build a deep sea telescope eventually reaching the sensitive size of one cubic kilometer. The project will expand to reach this size in well defined steps using a modular design.

The physics aims of the project are:

- The birth of high energy neutrino astronomy via the study of high energy neutrino astrophysics, the quest for cosmic accelerators (galactic and extragalactic) and supernovae detection.
- Particle physics via the search for dark matter particles, neutrino oscillations (atmospheric and long baseline), ultra high energy neutrino interactions, monopole searches and possibly proton decay.
- The unexpected.

The evolution of NESTOR is expected to go through the following stages:

- Construction and operation of the prototype NESTOR tower with a sensitive area of 20,000 square meters.
- Construction of other towers increasing the sensitive area to over 100,000 square meters.
- Expanding the telescope to go well over 1,000,000 square meters of sensitive area.

Part I

Scientific Justification

Chapter 1

Astroparticle Physics with Neutrino Telescopes

1.1 Introduction

The cosmic ray spectrum (fig. 1.1) shows clearly that there exist cosmic rays with energies of at least up to 3×10^{20} eV. These highest energy particles must be extragalactic because they are too energetic to be trapped in our galaxy by the galactic magnetic field. So neutrinos and gamma rays at high energies must exist because they are the ultimate decay products of interacting cosmic rays in the cosmos.

Figure 1.1: High energy cosmic ray flux.

Astronomy means pointing back to the source, i.e. the origin of production. From the charged cosmic rays only those of the highest energies (probably protons) are not bent significantly by the galactic magnetic field. Therefore only a very low flux of cosmic protons are useful in pointing back to their origin. Neutrons are not very useful either, because only those with energies greater than 10^{18} eV live long enough to cross our galaxy. Unfortunately this flux is very low also. So, they can not be helpful if their origin is outside our galaxy. Moreover protons (or heavier nuclei) with energies above 4×10^{19} eV interact significantly with the primordial 2.7 K microwave background. Their energy is rapidly degraded and eventually these particles generated at the highest energies get buried in the background of lower energies. So, charged hadrons cannot provide us informations for distances further away than 20–30 Mpc.

EGRET observations of gamma rays with energies up to the tens of GeVs and the recent observation of Mk421 by the WHIPPLE, Mount Hopkins atmospheric Čerenkov telescope, around 1 TeV have stimulated calculations on the interaction of very high energy gamma rays with the ambient intergalactic photons [1, 2]. The calculations can be interpreted to show that the mean free path of gamma rays with energies above some hundreds of GeV is around 100 Mpc due to scattering with the intergalactic ambient infrared and ultraviolet starlight. This conclusion combined with the well known calculations that show that gamma ray attenuation due to scattering with the 2.7 K background is very serious for gamma rays with energies of hundreds of TeVs, fig. 1.2, leaves the neutrinos as the only promising particles for TeV or Higher Energy Astronomy.

Figure 1.2: Redshift at which the absorption by infra-red background radiation and cosmic microwave background radiation would reduce the gamma ray flux by e-fold versus gamma ray energy (from ref. [3]).

The neutrinos not only go through interstellar space without suffering any attenuation

but they also escape their progenitor's acceleration and target sites without suffering any absorption. Therefore the only way to measure the emission/production spectrum at the source is to measure the spectrum of the neutrinos arriving on earth.

The inescapable conclusion is that neutrinos allow us to explore "further" and "deeper" in the cosmos than with any other particle known to date. The question is "what is the neutrino flux intensity?" or conversely, how big a detector do we need in order to start the field of Neutrino Astronomy?* The only reasonable way to answer this question is to use the experience gained over the last 30 years or so by the construction and operation of the first and second generation neutrino telescopes and scale up by a few orders of magnitude in well defined steps. Each step should have the potential to contribute significantly to astrophysics or particle physics. Relic neutrinos from the Big Bang fill the Universe but no one has yet proposed a practical way to detect them. Low energy neutrinos of keV to $\sim$ 1 MeV are emitted continuously from the interior of stars like our sun. At this moment there are at least half a dozen solar neutrino telescopes in operation, but there is no proposal to detect neutrinos produced in the interior of other stars. Slightly higher energy neutrinos ($\sim$15–20 MeV) are produced during the explosions of supernovae and one can argue successfully that the birth of neutrino astronomy happened with the detection of supernova 1987A by KAMIOKANDE and IMB. But no one has yet proposed a practical way to detect supernovae neutrinos further away than the immediate neighbourhood of our galaxy.

Neutrinos in the higher energies are produced from decays of particles produced from cosmic rays interacting and the subsequent cascades in the earth's atmosphere. These so called "atmospheric neutrinos" have an energy spectrum shown in fig. 1.3 (see chapter 3 for details). The shape of this spectrum is caused by the competing processes of meson production and decay in a target medium (the atmosphere) of continuously changing density.

Neutrinos with energies in the range of one to a few hundred GeV for example may also come from the annihilation of WIMPs in the sun or the central core of the earth (see chapter 6).

Neutrinos from point sources are decay products of particles produced in hadronic interactions in potential cosmic accelerators such as neutron stars, black holes and young supernova remnants. Our own galaxy is full of such candidates. Further the cosmos has Active Galactic Nuclei (AGN) and they are very promising sources of ultra high energy neutrinos. Detection of neutrinos from point sources would unambiguously establish the existence of high energy hadronic interactions e.g.

$$\begin{array}{lcccccc} p + \text{target} & \rightarrow & \pi^0, & & \pi^{\pm} & + & \cdots \\ & & \downarrow & & \downarrow & & \\ & & \gamma\gamma & & \mu^{\pm}\nu_{\mu} & & \\ & & & & \downarrow & & \\ & & & & e^{\pm}\nu_{\mu}\nu_{e} & & \end{array}$$

*The reader is referred to the truly pioneering work done by the DUMAND group which is published in the the various DUMAND Workshop Proceedings and the DUMAND Proposals. A review of the subject was given by Learned in the 13th European Cosmic Ray Symposium [5] (see also ref. [6]). In what follows we have used these documents extensively.

Figure 1.3: Integral spectra of atmospheric neutrinos below 50 GeV.

The observation on earth of gammas from π^0 decay can only be a rare event, because the target must be thick enough in order to produce π^0's and at the same time thin enough ($\sim$ 5–100 g/cm^2) so as not to absorb the π^0 decay gammas and then these gammas should not interact with interstellar matter or the ambient starlight ultraviolet and infrared photons or the primordial 2.7 K microwave photons during their very long trip to the earth. On the other hand high energy photons (up to a few TeV) can be produced not only in hadronic processes via π^0 decay but also by purely electromagnetic processes e.g. inverse Compton scattering or synchrotron radiation of energetic electrons and then they must escape the general environment of the target before they get absorbed.

1.2 Physics Scope

The physics aim of neutrino telescopes covers one or more of the following topics (in order of descending neutrino energy):

1. Neutrino Astronomy (galactic and extragalactic) and the search for cosmic accelerators [4, 7].

2. High Energy Physics (a few examples follow):

3. Search for dark matter particles. Their annihilation or decay will eventually give neutrinos e.g. neutralinos trapped in the sun or the earth (see chapter 6).

4. Ultra high energy neutrinos have energies beyond 10^7 GeV. No terrestrial accelerator can produce these energies. If the neutrino telescope is large enough the limitation of low flux can be, in part, overcome and this might be the only way for high energy physics to reach these energies. In any case we can start right away, the experimental problems of neutrino telescopes are well understood. Multiple W/Z production [8, 9]. Search for possible substructure of the elementary particles i.e. compositeness of quarks and leptons [10, 11] (see chapter 8).

5. Neutrino oscillations using neutrinos produced in the atmosphere. The large range of the available oscillation length (15 km to 13,000 km) gives an extremely good sensitivity of $\Delta m^2 \sim 10^{-4}$ eV^2 (see refs. [12, 13, 14, 15] and chapter 5).

6. Long baseline neutrino oscillations using one of the high energy physics accelerators (see refs. [14, 16, 17] and chapter 7).

7. Proton decay (in the sense that the ultimate background to proton decay experiment is atmospheric neutrino interactions and therefore a low threshold neutrino telescope can also be a proton decay detector).

8. Supernovae detection.

9. Magnetic monopoles.

10. The unexpected. A new observational window will open up with these neutrino telescopes. No one has ever viewed sites in the universe shielded by more than a few hundreds grams of matter. One should keep in mind that every time a new brand of astronomy opened up, a new class of phenomena was discovered.

The experimental requirements for the study of the above physics topics look incompatible at first glance e.g. low vs high energy threshold, good angular accuracy vs coarse, high fractional coverage with sensitive photocathode area vs maximizing the detector's sensitive area, etc. After a couple of decades of operating small prototypes and R & D the high energy physics community seems to have the right tools to build a detector to study all the above. The approach must be stepwise and modular. The detector of today's measurements is the prototype for tomorrow's experiments. The signal of today's measurement probably would be the background of tomorrow's experiments.

1.3 Production of Astrophysical High Energy Neutrinos

There exist some excellent review articles on the subject and the reader is referred to Berezinsky [4], Gaisser [18] and Thorne [19]. The point one should stress here, is that according to Stenger's calculations [7] the optimal condition for high energy neutrino production in a cosmic beam dump (e.g., in a X-ray binary system) is a column density ≥ 100 g/cm^2, target density $\leq 10^{-8}$ g/cm^3 and a primary proton spectral index $\gamma \leq 2$. Then, a beam of neutrinos above 1 TeV would be produced at a rate of 10% of the

protons that strike the source. Under these conditions the neutrino flux emitted is at least 3 times bigger than the corresponding gamma ray flux produced by the same hadronic interactions. The photon interaction cross section is many orders of magnitude larger than the neutrino cross section, therefore high energy gamma rays can be destroyed much easier than neutrinos either near the source of their production by interacting with the matter or during their vast flight distance to earth by interacting with the 2.7 K background or the infrared and ultraviolet starlight as well as with interstellar gas and dust. The inescapable conclusion is that we should expect more and more copious very high energy neutrino sources than gamma ray sources.

Another class of sources which has become rather popular in the last few years is neutrinos produced in the vicinity of Active Galactic Nuclei (AGN). In this mechanism, neutrinos originate from the decay of mesons which in turn are the decay products of photoproduced Δ resonances:

$$\begin{array}{ccccccc} p\gamma & \rightarrow & \Delta^+ & \rightarrow & \pi^+ n & \text{or} & \pi^0 p \\ & & & & \downarrow & & \downarrow \\ & & & & \mu^+ \nu_\mu & & \gamma\gamma \\ & & & & \downarrow & & \\ & & & & e^+ \nu_e \overline{\nu}_\mu & & \end{array}$$

Recent calculations show that although signals from individual AGNs will not be detectable with the neutrino detectors presently under construction, the sum of all AGNs [20] should be detectable.

Finally, we should mention that high energy neutrinos may also originate from heavy (hundreds of GeV) dark matter particles (or antiparticles) e.g., WIMPs which are trapped in the sun or the earth and which eventually annihilate with their antiparticles producing neutrinos amongst other particles.

1.4 Choosing the Neutrino Energy

In order to detect neutrinos from the previously mentioned sources it is advantageous to focus on high energy neutrino detection. The reason is simple. The mere word astronomy implies that one ought to be able to point back to the source with high angular accuracy. In neutrino detection we cannot achieve the angular accuracy of traditional astronomy. Neutrinos are detected by observing mainly the muon which is produced from the charged current neutrino interactions with matter, in the vicinity of the detector.

In high energy neutrino astronomy usually, one is NOT required to detect the vertex of the neutrino interaction, in this way one maximizes the available detection volume. The physics of the interaction is such that the angle between the detected muon and the parent neutrino direction [21] for 63% of the charged current events is $< 1.5^\circ/\sqrt{E\,(\mathrm{TeV})}$. So, if a source is observed with a dozen events or so, one can greatly improve the directional determination by determining the centroid of the distribution and reach accuracies of a fraction of a degree. The pointing improves also with increasing energy because the muon goes further forward. Another parameter which improves with energy is the range of the muon ($\propto E_\mu$ until 1 TeV and then $\propto \log E_\mu$) and thus the effective detection volume of

the detector is increased proportionately. A fall in statistics resulting from the decreasing neutrino spectrum is partly compensated for by the increase of the cross section ($\propto E_\nu$ until about 10 TeV and then $\propto \log E_\nu$).

Further, the signal to noise ratio increases with energy for the following reason. The inherent background comes from atmospheric neutrinos, which are the result of cosmic ray interactions in the atmosphere. The spectral index γ_ν of the flux of atmospheric neutrinos [23] follows that of the cosmic ray spectrum and is ~ 2.7 up to 100 GeV or so, but then at higher energies it becomes ~ 3.7, while neutrinos produced extraterrestrially follow the hard core ($\gamma \sim 2.0 - 2.2$) cosmic ray spectrum. So, for neutrino energies larger than 100 GeV the signal to noise improves with energy.

For all the above reasons it is advantageous to optimize the telescope for detection of high energy neutrinos. One should keep in mind though, that the current design of neutrino telescopes with phototubes directed towards the earth (in order to minimize background from downcoming cosmic rays that reach the detector) can be disadvantageous for the detecting very high energy neutrinos (e.g., from AGNs) because the earth is no longer transparent to them (e.g., the mean free path for a 500 TeV neutrinos is about one diameter of the earth). Therefore the upward coming neutrinos of energy larger than a few hundred TeV will be severely attenuated.

1.5 Backgrounds in Neutrino Telescopes

The first large-scale neutrino telescopes were designed for proton decay experiments e.g., KAMIOKANDE and IMB. The neutrino interactions in or around the big proton-decay experiments were considered to be a source of background, but, in the quest for neutrino astronomy, part of yesterday's background can be today's signal. However, on the earth's surface the background due to the downcoming cosmic ray muon is overwhelming, the signal (for calculational purposes now we consider the atmospheric neutrinos as the signal) to noise (called up to down ratio) is of the order of 10^{-12}. Therefore, for shielding purposes, neutrino telescopes are located in deep mines inside mountains or in deep water. For instance, 4000 mwe of shield reduces the up to down ratio to about 10^{-4}. So, it is essentially impossible in the energy regime below 10 TeV to do neutrino astronomy by looking for downcoming muons, because neutrino induced muons are indistinguishable from downcoming cosmic ray muons. This is the reason that for those muons which originate outside the detector (and therefore no vertex determination is possible) only muons coming up from the lower hemisphere are useful.

Then the only remaining background is due to the omnipresent atmospheric neutrinos because the earth is transparent to them. In general, well shielded detectors can look up at about 20° *above* the horizon, while shallow detectors (1000 mwe) can look up only *below* the horizon. The kinematics of neutrino production and the multiple scattering is such that the best overall angular resolution is $\sim 1°$. So in order to find point sources of neutrinos one would at best divide the sky into 1° square pixels and plot the detected muon direction in a declination versus right ascension plot. A source would manifest itself as standing above the background caused by the atmospheric neutrino interactions, which constitute a flat background (with a slight zenith dependence visible over tens of degrees).

Quoting ref. [7], we present in table 1.1 the backgrounds in a 1° pixel of DUMAND.

Source	Background (y^{-1}pixel^{-1})
^{40}K and other random noise	0.40 ± 0.08
Single cosmic ray muons	0.63 ± 0.36
Multiple cosmic ray muons	0.15 ± 0.07
Atmospheric neutrinos	0.13 ± 0.01
Total	1.31 ± 0.38

Table 1.1: Backgrounds in DUMAND.

Note that even in deep water experiments like DUMAND and NESTOR the largest background is due to cosmic rays. In a shallow water experiment at 1 km depth this background should be greater by a factor of 500 than that at 4.8 km. That means that the same detector is about one order of magnitude less sensitive in shallow depth than at greater depth (4–5 km). On the other hand as noted in table 1.1, ocean detectors suffer (at the single photoelectron level) from backgrounds caused by radioactive ^{40}K and bioluminescence. One can deal with these backgrounds with coincidence techniques and pulse height analysis cuts. AMANDA in the polar ice is free of these backgrounds, albeit at a depth of 1000 meters.

These details of deployment depth and composition of the surrounding medium introduce subtle biases so one cannot scale simply by detector area in comparing different detectors. Lastly, depending on the emission energy spectrum of the source, one can improve the signal to noise by demanding higher energy neutrinos (although Čerenkov detectors are very crude energy measuring devices).

1.6 IMB – KAMIOKANDE – MACRO Results

There exists a two year old review of high energy neutrino astronomy [22]. So we will mainly focus on the progress in the field during the last two years.

Following the procedure outlined above, IMB and KAMIOKANDE have plotted their data [24], fig. 1.4 with granularity which is commensurate with their angular resolution. Clearly there is no event clustering of statistical significance.

KAMIOKANDE quotes limits from point sources which range from 2×10^{-14} cm^{-2}s^{-1} for Vel X-1 to 8.5×10^{-14} for Her X-1. In the XXII International Cosmic Ray Conference (Calgary, 1993) the MACRO collaboration [25] reported on 230 days of data taking and calculated limits at the 95% C.L. of steady muon emission of 5.8×10^{-13} cm^{-2}s^{-1} for Cyg X-3 and Her X-1. For the Crab they find 6.0×10^{-13} cm^{-2}s^{-1}. They improved these upper limits by a factor of 2 by taking advantage of the temporal characteristics of these sources which are known from photon astronomy.

Table 1.2 lists the large underground detectors operating in the 80's and 90's. It is obvious that the field needs larger detectors.

Detector	Location	Area (m^2)	Technique	Primary Purpose
IMB*	Ohio, USA	400	Water Čerenkov	Proton decay
KAMIOKANDE	Japan	120	Water Čerenkov	Proton decay
Fréjus*	France	100	Flash tubes + Fe	Proton decay
SOUDAN 2	Minnesota, USA	100	Drift tubes + Fe	Proton decay
MACRO	Gran Sasso, Italy	800	Liquid scintillator + streamer tubes	monopoles
LVD	Gran Sasso, Italy	500	liquid scintillator + streamer tubes	supernovae ν

*It has been terminated.

Table 1.2: Large underground detectors operating in the 80's and 90's.

1.7 How Big a Detector?

Let us change line of approach now. Consider the recently reported gamma ray observations [26] and use the detected gamma ray flux to calculate the required detector sensitive area.

In the TeV range of energies the WHIPPLE air Čerenkov γ-ray experiment has detected the following fluxes:

Crab Nebula: 2.5×10^{-11} gammas/(cm^2 s)
Markarian 421: 7.5×10^{-12} gammas/(cm^2 s)

Most likely the gamma ray flux from the Crab is electromagnetic in origin but no one doubts the hadronic origin (i.e. π^0 decay products) of the gamma rays from Markarian 421, which is a well known AGN. Therefore one can safely assume the pessimistic case of equal rate of production of gamma and neutrinos at the site of Markarian 421 and keep in mind that it is much easier to absorb gamma rays than neutrinos in their 100 Mpc journey from Markarian 421 to earth. One should mention here that Markarian 421 is the closest blazar on the GRO catalogue of AGNs that emit GeV gamma rays.

It has been calculated in ref. [7] that a deep underwater detector with a sensitive area of 20,000 m^2 (e.g. DUMAND II or the first phase of NESTOR) will be able to detect, in one year's observation, a source with a neutrino flux greater than 1.2×10^{-10} $cm^{-2}s^{-1}$ at energy greater than 1 TeV.

Comparing this with the gamma ray flux from Markarian we draw the conclusion that we need a detector that should quickly reach a sensitive area of 200,000 m^2 and then go beyond to 1,000,000 m^2 in order to harvest the physics. Conventional particle detectors e.g., scintillators, drift tubes, resistive plate chambers etc. cost about 10,000 to 20,000 Swiss francs per square meter. This means that a 10^5 m^2 detector will cost $\sim$ 2000 million Swiss francs which is twice the CERN budget for one year. The implication is that the cost must be reduced by a factor of $\simeq$ 100. This is the reason why the water Čerenkov technique is chosen.

1.8 Large Volume Water Čerenkov Detectors

The index of refraction of sea water at 500 atm. is about 1.35, which corresponds to a Čerenkov angle of 42°. In other words, relativistic particles will "illuminate" the sea water within a 42° cone, emitting about 250 Čerenkov photons/cm (between 0.3 and 0.5 μm) a range where most photomultipliers have a reasonable sensitivity. Then, depending on the water transmissivity (ranging from 20 m in clear lakes and bubble free clear ice to 50–60 m in clean deep ocean waters), one can instrument large areas of water fairly cheaply, at a cost of about 100 Swiss francs per square meter, which is the target. The long range of muons in water helps tremendously, a 1 TeV muon has a range of about 2.5 km in water! The high energy physics community has accumulated considerable experience with the water Čerenkov technique mainly from the three big proton decay experiments IMB, HPW and KAMIOKANDE and the various test-deployments down to 4,000 m as done with the DUMAND I and the NESTOR tests, Lake Baikal experiment at 1,000 m and AMANDA in the ice. The deep underwater large Čerenkov neutrino experiments will also deploy hydrophones in the hope of determining very high energy neutrino interactions acoustically, the threshold of this technique is in the PeV range. The acoustic pulse is produced by the thermal expansion of the water when heat is deposited by the interaction. The energy transfer is very inefficient, about 10^{-9} [22], but the advantage is that the attenuation length, in the frequency range of 10–20 kHz, is of the order of a few kilometers. So, one could instrument literally, many cubic kilometers at low cost. DUMAND II is deploying hydrophones, while in the acoustic version of NESTOR, called SADCO [27], preliminary tests show that the usual 14° C ambient temperature of the bottom of the Mediterranean is more advantageous for acoustic detection (lower threshold) than the 4° C ocean bottom temperature. In any case it is far too early to make any comments on the acoustic detection technique. In order to demonstrate some of the advantages of the water Čerenkov technique we show in fig. 1.5 the reconstruction efficiency as a function of the distance from the central axis of the NESTOR detector for vertical muons of energy 1 TeV, 10 TeV and 100 TeV. One should note that a reconstruction efficiency of 80 % is achieved with vertical muons that cross 50 to 100 m outside the detector.

Even if a 10^5 m^2 detector finds neutrino sources, the physics of this field will not be harvested until square kilometer detectors come into operation. For this reason the quest for neutrino astronomy has three benchmarks.

- The reliable operation over a few years of a detector of 10,000 to 20,000 m^2 (i.e. a detector ten to twenty times bigger than the largest neutrino telescope in operation today).
- The quick growth of this detector to cover a sensitive area of 100,000 m^2.
- The subsequent expansion of the detector in order to instrument 1 km^2 in a timely and affordable fashion.

In order to give the reader a feeling for the expected event rate of a generic deep water 20,000 m^2 neutrino telescope, we present table 1.3, from ref. [22].

Source	$E_\mu >$ 100 GeV	$E_\mu >$ 10 TeV	$E_{\rm cas} >$ 1 TeV	$E_{\rm cas} >$ 100 TeV	Model
Sum of AGNs	154	66	276	264	SDSS
	109	23	113	52	Protheroe
	366	75	379	172	Biermann
	897	148	680	125	Sikora
Atmosphere	2950	22.8	3435	5	Volkova

Table 1.3: The number of muon and cascade events per year expected in DUMAND II from AGNs according to various models presented at the Hawaii Workshop in March'92 [20] and for atmospheric neutrinos.

1.9 Description of Current Projects

The sky coverage by each of the four neutrino telescopes under construction listed in table 1.4 is shown in fig. 1.6. Note that DUMAND and NESTOR are 177° apart in longitude, so their combination will monitor the cosmos continuously.

Detector	Location	Date – E.Y.O.*	Area (m^2)	Depth (mwe)	Technique	Threshold (GeV)
Baikal NT-200	Siberia	1996	3000	1100	WČ	10
DUMAND II	Hawaii	1996	1000**	4760	WČ	20
NESTOR***	Greece	1997	20,000	3700	WČ	Few
AMANDA	Antarctic	**?**	8000	**?****	WČ in ice	Few

*Expected Year of Operation.

**The quoted area corresponds to the DUMAND II triad of strings. The full DUMAND will have 20,000 m^2.

***Stage I, one tower only.

****Presumably, $\approx$ 2000.

Table 1.4: High energy neutrino telescopes currently under construction.

1.9.1 AMANDA

The AMANDA project [28] aims at building a neutrino telescope in the ice of the South Pole at a depth of 1000 m. Although the transparency of the ice had not been measured in situ, it was expected to be around 20 m. In this experiment, 1.2 km long holes were to be drilled in the ice, the phototubes to be placed in and some hours later they would be frozen in. The cost and the limited supply of fuel in the South Pole is such that only 8 inch diameter holes can be drilled. As a result of this, the AMANDA phototubes will only have about 1/4 the photocathode area of the 15 inch diameter phototubes used by Baikal, DUMAND and NESTOR. On the other hand AMANDA has the advantage that the Antarctic sea is fairly free of radioactive background.

The original plans of the full AMANDA array (fig. 1.7) consisted of 9 strings placed in a cylindrical configuration, on the surface of a 30 m radius cylinder, with a tenth string on the axis of the cylinder. The 10 strings are identical, they are 200 m long each, with one phototube every 12 meters, the total number of phototubes is 200. The array was to be located at a depth of 1000 m. The effective area and depth of the AMANDA array are similar to that of the Baikal telescope.

During the winter (Australian summer) of 1993–94 the collaboration deployed four strings to a depth of 1000 m, the deployment of a fifth string at the end of January '94 was not completed due to the breakdown of the drill and the approaching bad weather [29]. They have studied [30, 31] the ice transmissivity using their laser calibration system. Contrary to claims [32] the ice does not seem to be bubble free, at least not at depths of 1000 m. Unfortunately the scattering length is extremely short [33]: it varies from about 0.1 m at a depth 800 m to about 0.2 m at a depth 1000 m, independent of wavelength (within the interval 410 nm to 610 nm), fig. 1.8. This means that after traversing a few meters the direction of the Čerenkov light is totally randomized and therefore one cannot reconstruct the direction of the muon. However by doing an elaborate study of the calibration data they fit the absorption length of 59 meters. In a shallow detector this is a mixed blessing because it shows that the effective area is much larger than what was originally anticipated. Given the shallow depth of 800–1000 m the downcoming high flux of cosmic ray muons cannot be rejected because the very short scattering length does not permit any reconstruction of direction. Since the four deployed strings are frozen in (i.e. cannot be retrieved) the collaboration plans to use them together with their future array. Since one is concerned that the short scattering length might be caused not only by air bubbles alone but by dust, volcanic ashes or fluorescence, a program of measuring the optical properties of ice below 1000 m seems prudent. The collaboration did not do any drilling in the South-Pole during the 94-95 Australian summer [30]. For the recent status report, see ref. [34].

1.9.2 Lake Baikal

The lake Baikal experiment [35] will be composed of 192 large (15 inch) phototubes (fig. 1.9). The deployment is made in the spring when the lake is frozen, so a solid platform is available. In the spring of '93 part of the detector was deployed, consisting of 36 phototubes, the darkened phototubes in fig. 1.9.

Table 1.5 summarizes the characteristics of the full detector and of the one which was deployed in '93 (NT-36). The water transmission length is $\sim$ 20 m and it varies with the seasons. Further, there seems to be an optical background in the water similar in magnitude to the ^{40}K in the ocean.

The data is transferred to shore via cable. The detector deployed in '93 operated for almost one year, 30 of the 36 phototube channels were operating by August '93 and by the spring of '94, only 18 [36]. Most of them had some intermittent problems, possibly connected with the substandard manufacture of a switch. All the photomultipliers themselves performed well and there were no problems with water leaks. The laser calibration system worked well. In the spring of '94 (April) again 36 photomultipliers were deployed in a different configuration than in '93. At the end of August '94, 30 channels were working satisfactorily [37]. Clearly they must improve the reliability of the electronics. The group is studying and understanding the detector performance. They made tremendous progress with their reconstruction algorithms and their up-down rejection. They have demonstrated that their single muon agrees well with their Monte Carlo and find evidence for muon bundles. They also understand well the zenith response of their detector to downcoming muons. They have not reported yet the reconstruction of any neutrino events. They have calculated preliminary limits on monopole fluxes (i.e. for a magnetic GUT monopole) which are below the Parker limit (10^{-15} cm^{-2} s^{-1} sr^{-1}) at velocities $\beta < 10^{-4}$ and/or catalysis cross section $\sigma_0 > 10^{-8}$ cm^2 [38].

The group deserves the whole-hearted congratulations of the international scientific community because they managed to deploy and operate the world's first underwater neutrino telescope under the very difficult conditions that prevail in Russia at the present. Another 36 phototubes have been deployed in the spring of '95. Current results from the Baikal experiment were presented in the XXIV International Cosmic Ray Conference (Rome, 1995). The most recent status can be found in refs. [39, 40].

1.9.3 DUMAND II

The DUMAND experiment [21, 41] is the progenitor of the new generation neutrino telescopes. They have been studying the problem for more than one dozen years now. They have offered a number of solutions and have developed and made available the technology required to operate and deploy neutrino telescopes in the water. The full DUMAND II array (fig. 1.10) will be deployed at a depth of 4800 m, near Hawaii, and it will consist of an octagon of nine strings (eight on the perimeter and one in the center). A total of 216 large (15 inch) phototubes will be deployed facing downwards. There will be 24 phototubes per string in 10 meter intervals. The radius of the octagon will be 52.5 m, matching the 45 m long light transmission length that they have measured in the blue part of the spectrum. The total enclosed instrumented mass is about 2.7 Mtons. The

	Full detector NT-200	NT-36
Location	51°50′ N, 104°20′ E	the same
Configuration	heptagonal prism with 7 sides and 1 central string	3 strings
Dimension	side length 18.7 m, height 70 m	
Depth	1.08 to 1.15 km	the same
Geometrical volume	88.5×10^3 m^3	3.04×10^3 m^3
Number of PMTs	192	36
Muon threshold energy	≈ 10 GeV	
Effective area	2300 m^2 for 1 TeV muons 4100 m^2 for 10 TeV muons	270 m^2 for 1 TeV muons 1000 m^2 for 10 TeV muons
Median mismatch angle	1.3° (1 TeV muons, isotropic flux)	3.9°
Number of downward muons	> 10 GeV: 3×10^8 y^{-1} > 100 TeV: 2×10^3 y^{-1}	4.5×10^7 y^{-1}
Number of upward muons from atmospheric neutrinos	> 20 GeV: 490 y^{-1} > 1 TeV: 30 y^{-1}	60 y^{-1}
Aperture for upward muons	180° to 110°	
Needed rejection factor to identify atmospheric neutrinos	10^6	

Table 1.5: Some characteristics of the Lake Baikal arrays.

sensitive area for a muon of one TeV energy will be 20,000 m^2 with an angular resolution of better than one degree (standard deviation). Table 1.6 summarizes the characteristics of the array.

The DUMAND II threshold for upcoming atmospheric neutrinos will be larger than 10 GeV so they should be able to study atmospheric neutrino oscillations because they will collect about 3000 atmospheric upcoming neutrino events per year in the full nine string array.

The DUMAND collaboration deployed successfully in December '93 a 36 km long electro-optical cable from the detector to the shore, together with a junction box (the plug in box for distribution of electrical power and receipt of data via optical fibers). One string of 22 photomultipliers was also attached to the junction box as well as the environmental and control instruments. Data were taken for a while and in fact one double muon event was reconstructed (cosmic ray). Due to a faulty connector, water entered inside the housing which controls the string electronics and the power supplies shorted out. The string was recovered in January '94 and was repaired. The other two strings are now ready. The collaboration is ready now to deploy a triad of strings. In order to do this they must use a bathyscaphe which will hook the three string to the junction box (and therefore to the cable) which is awaiting on the ocean floor. This operation is scheduled for 1996.

Location	19.725° N, 156.326° W
Array dimensions	105 m diameter × 230 m high
String spacing	40 m side, 52.5 m to center
Number of strings in array	8 in octagon, 1 in center
Sensor spacing along strings	10 m
Number of optical sensors/string	24
Total number of optical sensors	$9 \times 24 = 216$
Height of first sensor above bottom	100 m
Depth of bottom	4750 m
Sensor pressure envelope	17" (43.2 cm) O.D., glass sphere
Optical sensor	15" photomultiplier
Volume of array, contained	1.8×10^6 m^3
Target area for through-going muons	23,000 m^2 horizontal, 7850 m^2 vertical up-going, 2500 m^2 down-going
Effective target volume for 2 TeV muons	1.0×10^8 m^3
Effective target volume for 1 TeV cascades	7.0×10^5 m^3
Muon energy threshold	$20 \div 50$ GeV
Track reconstruction accuracy	$0.5° \div 1.0°$
Cascade detection threshold	≈ 1 TeV
Downgoing muon rate	3/minute
Atmospheric neutrino rate for throughgoing muons	3500/yr
Atmospheric neutrino rate for contained events above 1 TeV	50/yr
Point source sensitivity	$(4 \div 7) \times 10^{-10}$ cm^{-2} s^{-1} above 1 TeV
Contained event sensitivity	10^{-8} cm^{-2} s^{-1} above 1 TeV

Table 1.6: Summary of the physical characteristics of the full DUMAND II array.

1.9.4 NESTOR

The NESTOR is located, near the S-W of Greece, a 8 km by 9 km horizontal plateau at a depth of 3800 m [14]. The depth is constant to within ±50 m over the entire plateau. The plateau is at a mere distance of 7.5 miles from the shore, compared to 25 miles for DUMAND. Extensive studies of the water transmissivity have been made employing I) spectrophotometric analysis of a very large number of samples, II) deployment of photometers in situ (i.e. down to 4000 m) and III) large acceptance photometric measurements in situ. These measurements show that the water transmission length in the blue part of the spectrum is about 55 m [42, 43]). The underwater currents have been measured over five years and they have been found to be minimal [44] i.e. a few centimeters per sec or less. Last, the sedimentology analysis is completed [45]. The NESTOR design differs from that of DUMAND and AMANDA in that it deploys half the phototubes looking upwards, like Baikal, thus having a 4π sensitivity and at the same time shielded by 3500 mwe. A total of 168 15 inch phototubes are employed, like in DUMAND, but they are clustered closer so that a lower threshold can be reached. We have been making tests in situ, since 1991,

of a half scale model of our basic detector element. This is a horizontal rigid hexagon of 16 m radius made out of titanium. At each one of the corners and at the center there is a pair of two 15 inch phototubes (one looking up and the other one down). By stacking 12 of these hexagons in the vertical, with a distance between hexagons of 20 m, we create a tower (fig. 1.11, left).

Fig. 1.11 (right) shows that the effective area of a single NESTOR tower is equivalent to the full DUMAND II. The whole tower will be deployed in a single operation, currently planned for the spring of '97, its sensitive area for TeV muons will be $\sim$ 20,000 m^2.

The collaboration hopes to quickly find additional funds to build other towers in order to deploy them in a hexagonal fashion around the first tower and at a distance of 100–150 meters from it (fig. 1.12, left).

This array would have a sensitive area larger than 10^5 m; it would provide an overall angular resolution better than 1° (fig. 1.12, right), it would have an enclosed mass of > 20 Megatons and a total cost of about 20 million dollars. Within each one of the 7 towers the energy threshold is a few GeV, i.e. a low threshold active target of 1.5 Megaton mass.

In fig. 1.13 one can see the flat response of the effective area as a function of the cosine of the zenith angle for 1° and 5° accuracy in reconstructing the muon direction.

With one NESTOR tower we claim to be able to do almost the same astrophysics of the full DUMAND II plus two experiments unique to NESTOR: one is atmospheric neutrino oscillations by doing a full zenith fit of the atmospheric neutrinos in an internally normalizable way, independent of cosmic ray flux calculations. The other is a long baseline neutrino oscillations experiment from CERN in conjunction, perhaps, with another experiment at Gran Sasso which on a two dimensional projection falls on a straight line drawn between CERN and NESTOR. A description of the general ideas behind these two experiments follows (see chapters 5 and 7 for details).

Atmospheric Neutrino Oscillations

Results by the KAMIOKANDE, IMB and SOUDAN 2 collaborations [46, 47, 48, 49] suggest that as much as 40 % of the atmospheric ν_μ events in the energy range from 0.2–1.5 GeV have oscillated to some other type of neutrino. Other, less sensitive but better shielded experiments did not record any effect [50, 51, 52]. NESTOR will be able to test this by studying atmospheric neutrino oscillations at a higher energy regime (above 5 GeV). For the study of oscillations one should require to see the event vertex within the detector: the so called contained events. The higher energy regime diminishes the sensitivity of the study on geomagnetic effects, the uncertainties of the Oxygen cross section, and other nuclear effects. The NESTOR design is such that (for contained events) the top floors can be used to "veto" downcoming cosmic rays, therefore one can be sensitive to neutrinos arriving from all zenith angles. This way, the available oscillation length L varies continuously from 10 km to 13,000 km giving NESTOR an unprecedented sensitivity in Δm^2 spanning four orders of magnitude. We will study the oscillations as a disappearance experiment, that is, by measuring the ratio of muons coming from different zenith angles. As long as the method is based on the measurement of angular distribution, it is independent on the knowledge of the absolute normalization of the atmospheric neutrino flux. Thus the experiment will be internally normalizable i.e. comparing the

expected number of neutrinos coming from all directions to anyone chosen as the "control" direction. This way, the angular distribution of muon neutrinos should be roughly flat. If there is a variation with the zenith angle, it would be caused uniquely by neutrino oscillations i.e. muon neutrino oscillations to another species.

The downcoming cosmic ray muons are usually a major obstacle to the detection of contained neutrino events in shallow water detectors, but in this case they present a difficult but manageable background. Fig. 1.14 shows the flux of downcoming muons per year compared to the number of contained atmospheric neutrino events as a function of the zenith angle. The ratio of signal to background from 0 to 60 degrees is of the order of 10^{-4}. Studies have shown that one can reject the downcoming cosmic ray muons at this level, by using veto or vertex reconstruction techniques.

Finally, fig. 1.15 shows the sensitivity of one year running of this experiment for one year's data (contained events i.e. reconstructed vertex within the detector). The analysis is made under the assumption of ν_μ disappearance. The systematic errors due to the separation between ν_μ and ν_e interactions are not included, but they are estimated to be less than 10%, therefore comparable to the statistical errors. Note that NESTOR's sensitivity includes the "KAMIOKANDE solution" (neutrinos detected by KAMIOKA with energy below 1 GeV [46] and those above [47]).

Long Baseline Oscillations with CERN

A complementary study to the atmospheric neutrino oscillation can be conducted with a long baseline experiment with a CERN beam. As part of the work on the LHC, injection transfer lines are being designed to bring the fast extracted beams from the SPS to the new collider. The primary proton beam for a neutrino production target to feed Gran Sasso with only minor modifications can be derived from TI48 which links SPS/LSS4 to LHC/P8.

Seen from CERN, Gran Sasso and NESTOR have approximately the same azimuth Calculations by Mayoud (CERN) are listed in table 7.1 (see chapter 7). One sees that a neutrino beam pointing to NESTOR would have to be diverted by only 1 degree to the west in azimuth (easily accommodated), and 5 degrees downwards in declination, with respect to the one pointing to Gran Sasso.

For the latest long base line beam design for NESTOR [53], with a horn and a reflector, for a 450 GeV beam, the lateral beam spread at the NESTOR is flat to $\pm$ 2.0 km around the target point, so targeting should not be a problem. We calculate that for 10^{19} protons on target a 200 kt detector. For example, one NESTOR tower should detect about 15,000 contained events. Such an experiment will require more photomultipliers per tower and more than one tower appropriately configured to enhance e/μ separation.

The separation of μ from e and hadrons in the detector is under study. Preliminary MC results indicate that it will be possible to distinguish between "muonless" (NC) and "muonfull" (CC) events, by using the time distribution of the events (Čerenkov light from muons comes earlier than the one from the hadronic or electromagnetic showers) and the longitudinal shower development of the event (the muons distribute their Čerenkov light evenly while electrons emit their light according to the development of the electromagnetic shower). The systematic effect due to this statistical separation is estimated to be of the

order of 10 %. The CERN neutrino beam produced by the 450 GeV SPS beam with horn and reflector, targeting NESTOR, will produce the sensitivity shown on fig. 1.16, for one year's running (10^{19} protons on target). It will cover the area of small mixing angles, due to better statistics, provided that we will be able to control the systematics.

1.10 An Affordable 1 km^2 Detector

Assuming operational success of the 7 tower hexagon of hexagonal NESTOR towers the next step is obvious: employ another six towers in a hexagonal fashion 150 meters around the first hexagon and fill in the gaps between them in the perimeter with six strings (fig. 1.17).

Each string has 24 phototubes (15 inches each) clustered in pairs and spaced with the same spacing between floors of the towers. This addition of six towers and six strings will cost less than 25 million dollars, and the array will have a sensitive area of 430,000 m^2. For the following step it is sufficient to use strings only with 24 phototubes each. Employing 18 strings $\sim$ 150 meters outside the last perimeter will only cost 5 million dollars and the total sensitive area will be 850,000 m^2 for a total cost of 45 million dollars. The enclosed mass will be about 300 Megatons, of which 4 or 5 will be contained within each tower with local energy threshold of a few GeV.

Figure 1.4: Upward muon data.

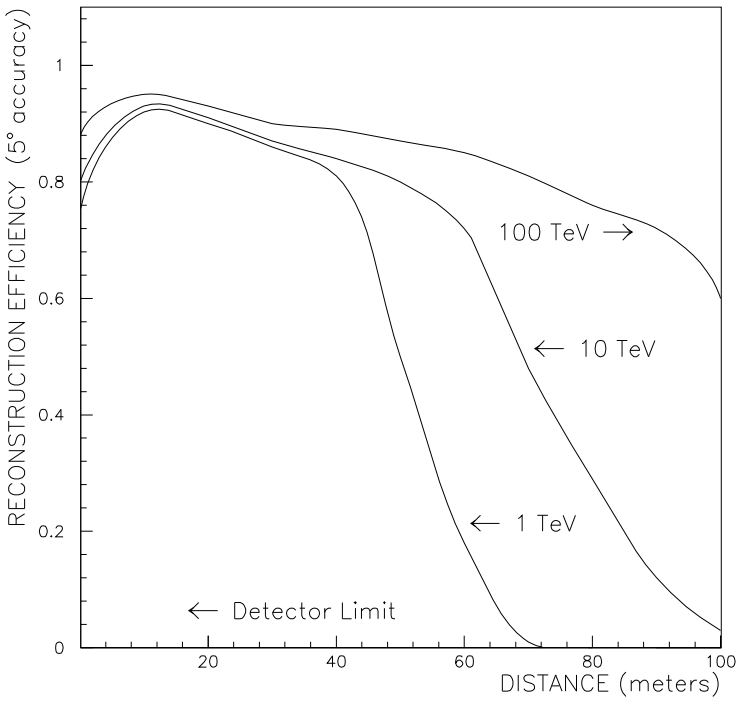

Figure 1.5: Reconstruction efficiency with 5° angular accuracy for one NESTOR tower for different muon energies.

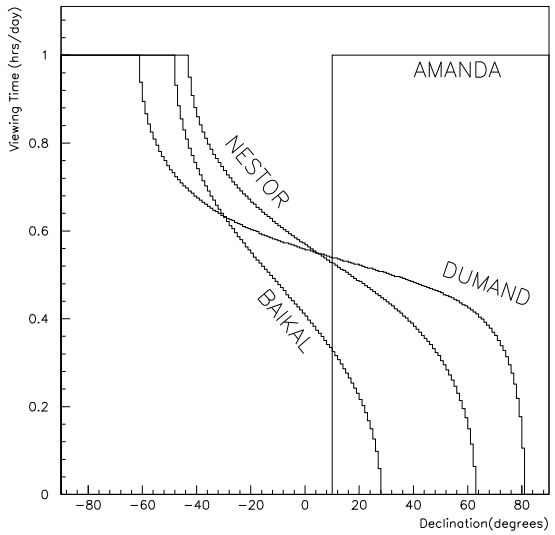

Figure 1.6: Sky coverage of neutrino telescopes.

Figure 1.7: The AMANDA array (as planned originally).

Figure 1.8: Inverse scattering length.

Figure 1.9: The Lake Baikal array.

Figure 1.10: The DUMAND II array.

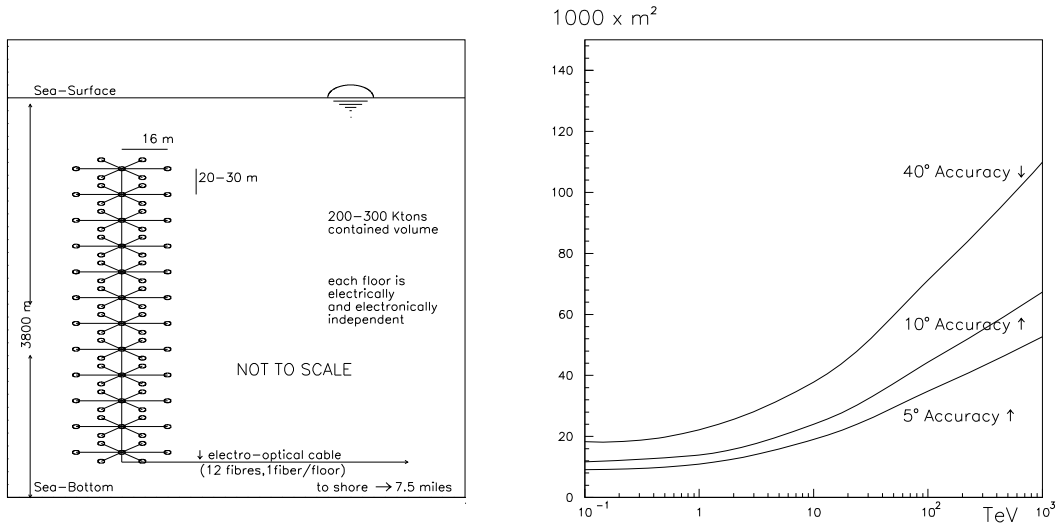

Figure 1.11: A NESTOR tower (left) and its effective area for muon direction reconstruction accuracies of 5°, 10° and 40° versus the muon energy (right).

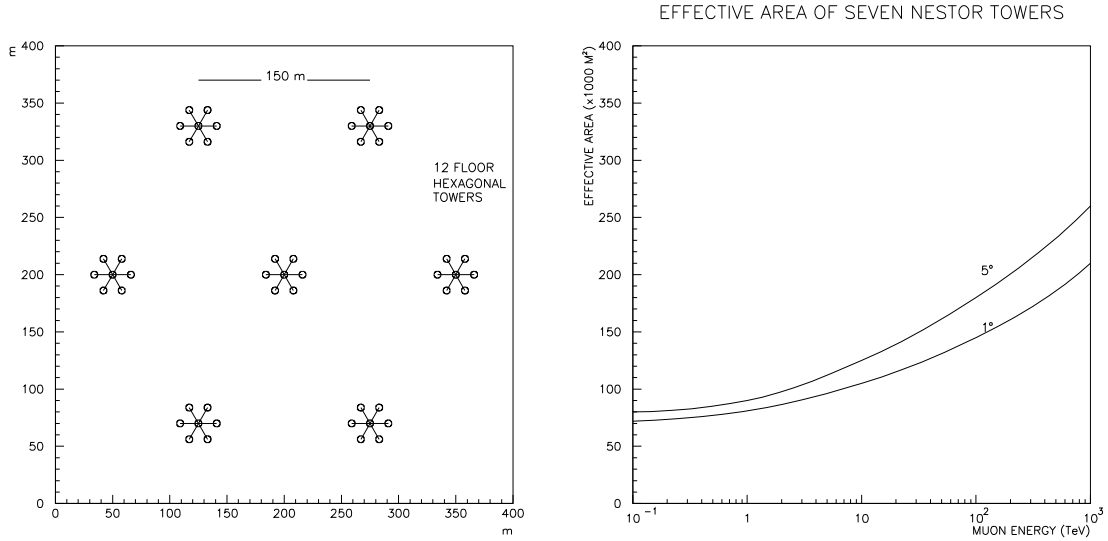

Figure 1.12: The full NESTOR array (left) and its effective area for muon direction reconstruction accuracy of 1° and 5° versus the muon energy (right).

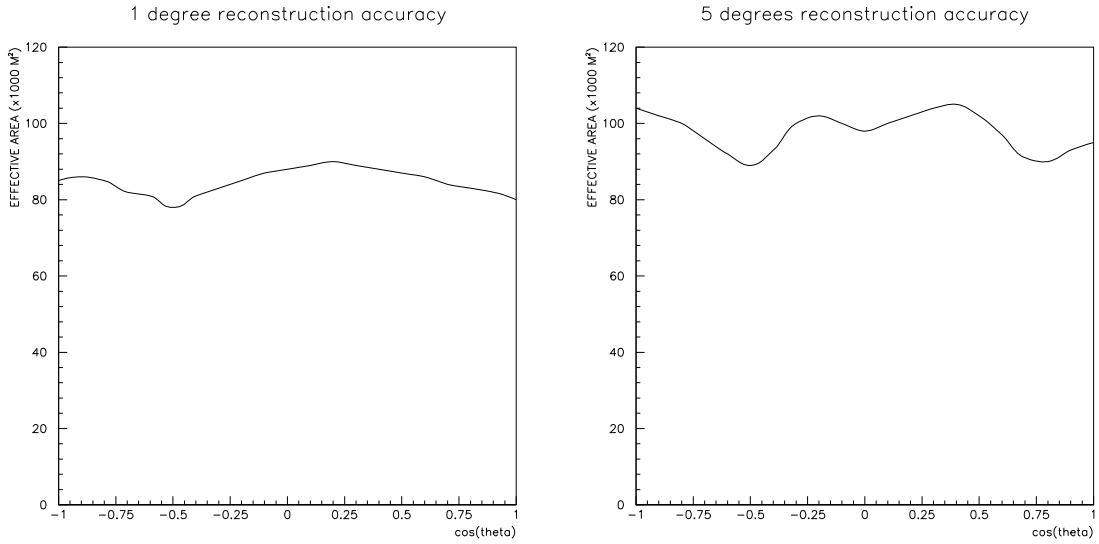

Figure 1.13: The effective area as a function of the cosine of the zenith angle for 1° and 5° accuracy in reconstructing the muon direction ($\cos\vartheta > 0$ means downward-going muons).

Figure 1.14: Downcoming muon flux.

Figure 1.15: Atmospheric oscillations limits.

Figure 1.16: Long-base line oscillations limits.

Figure 1.17: 1 km^2 NESTOR.

Chapter 2

Celestial Point Sources for NESTOR

2.1 Introduction

The extension of observational astronomy to very high energies gave birth to a new branch of astronomy, namely the very high energy and ultra high energy astronomy and astrophysics. Most of the progress in this field has been made in the γ-ray observations (see for reviews refs. [54, 55]). The observations of VHE and UHE γ-rays from celestial sources point to the direction of highly energetic primary particles accelerated to these high energies. In isolated pulsars, it is very well established that electrons are responsible for the observed high energy γ-ray emission. On the other hand, protons can be accelerated more efficiently easily to these high energies since they do not loose energy as easily as electrons via the inverse Compton effect and synchrotron radiation. Objects that can accelerate protons to very high energies are expected, in addition to photons, to yield neutrinos as well through hadronic interactions (see, for example, ref. [4]). Direct proof for the existence of protons accelerated to extreme energies are the cosmic rays that bombard the earth. Cosmic rays, through their interactions with the earth atmosphere, create a strong background that does not allow to easily distinguish neutrino point sources above the horizon, even in the TeV energy range. The major projects under construction are designed to look for sources below the horizon, since the earth is transparent to neutrinos, in order to avoid the severe atmospheric background.

NESTOR, at a latitude of $36°37.5'$ N and a longitude of $21°33'$ E, can see most of the sky except for its northernmost part. In fig. 2.1 we show a map of the sky with the galaxy and various candidate sources, as well as a reference to NESTOR horizon. Objects that are always above the horizon cannot be easily resolved by NESTOR due to the cosmic ray induced background. Objects that are always below the horizon can be observed for 24 hours a day. Objects in between rise and set and can be observed for part of the day. The great depth of NESTOR ($\sim$ 3800 m) permits to extend the view limit to $10°$ above the horizon (or more depending on the energy of the muons, e.g., even $20°$) thanks to the intervening water mass which suppresses the cosmic ray background. Adopting a view limit of $10°$ above the horizon (in the TeV region) we can calculate the viewing time for various objects as a function of declination. This is shown in fig. 2.2 where we compare the four major projects under construction. Note that since NESTOR and DUMAND are essentially back to back (i.e. $177°$ in longitude), their combination will monitor the

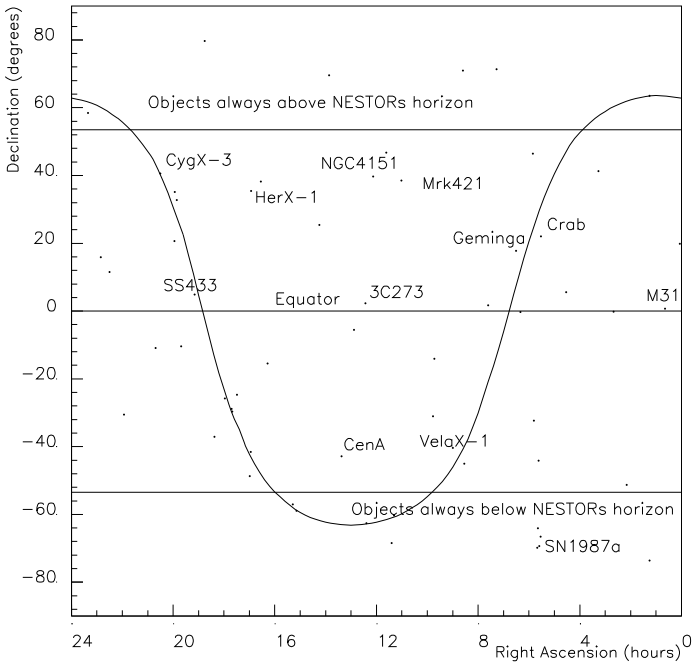

Figure 2.1: Map of candidate high energy sources and the boundaries of NESTOR horizon system. A deep sea water neutrino detector like NESTOR should be able to extend its view limit at least 10° (if not 20°) above the horizon.

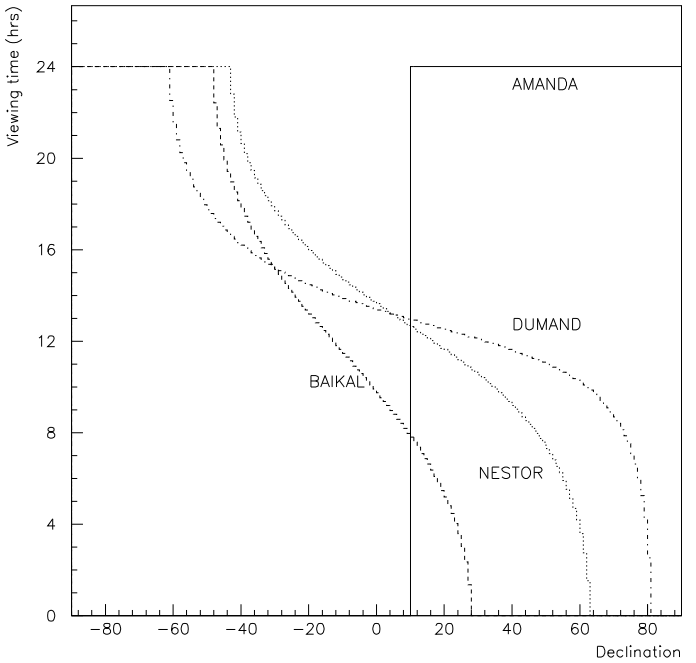

Figure 2.2: Viewing time of the four major high energy neutrino detectors as a function of declination.Viewing limits: 10° below the horizon for AMANDA/Baikal and 10° above the horizon for DUMAND/NESTOR.

whole sky 24 hours a day, thanks to their complementary positions.

2.2 The γ-ray Data

In order to calculate neutrino event rates for various objects we have to know the emitted high energy spectrum in each case. Actually, this is NESTOR will attempt to do (among other) things once it is operating. Therefore, we need an indirect estimate of the neutrino spectra for the various candidate sources. For this purpose, we use the corresponding high energy γ-ray spectra. The usual, reasonable assumption made in this case is that the VHE γ-rays are produced through pion decays in hadronic interactions (predominantly $p\gamma$ in AGN and pp in X-ray binaries). Neutral pions produce only photons, but charged pions produce neutrinos as well. The final yields in neutrinos are comparable to those in γ-rays [7, 56, 57, 58].

In the past decades there have been reported VHE and UHE detections of various objects, although many of these detections are marginal. Most prominent among these objects are the Crab pulsar/nebula, the X-ray binaries Her X-1 and Cyg X-3, and the BL Lac object Mrk 421 (table 2.1).

Object	Declination	Type	Distance	Viewing time
Crab PSR	+22.0	PSR-SNR	2 kpc	11.3 hrs/day
Mrk 421	+38.5	BL Lac (AGN)	100–200 Mpc	9.7 hrs/day
Cyg X-3	+40.8	LMXRB-PSR	11 kpc	9.2 hrs/day
Her X-1	+35.6	LMXRB-PSR	5 kpc	10.0 hrs/day

Table 2.1: VHE gamma-ray sources and their characteristics.

Individual observations or upper limits and compilations for each source can be found in refs. [54, 55, 59, 60, 61, 62, 63, 64] and in references therein. The reported observations come from satellites (energy regime: MeV–GeV) and ground based observatories through the atmospheric Čerenkov technique (energy regime: TeV) and the air shower technique ($E > 100$ TeV). Not all of the observations are equally significant, since in many cases the statistical significance is low (3–4σ). Moreover, in other cases no γ-rays have been detected from the sources, placing upper limits which are lower than the claimed fluxes. On the other hand, it is true that these sources are highly variable in the rest of the electromagnetic spectrum (from X-rays to radio wavelengths). AGNs show variability with time scales from years to minutes suggesting very compact sources. X-ray binaries exhibit bursts and episodic emission of sporadic nature with time scales from minutes to days (see the previous references for the γ-ray part of the spectrum).

Although many of the claimed VHE/UHE γ-ray detections have been questioned in the past on the basis of poor statistics, for certain objects there exists evidence that they are indeed high energy γ-ray emitters. Her X-1, for example, exhibits a 35 day periodicity in the X-rays (possibly due to the precession of the neutron star or the accretion disk) with nearly all emission concentrated in two peaks during each cycle. The reported episodes of TeV γ-ray emission are all confined with the "on" phases of this periodicity [64], despite

the low statistical significance of each observation individually. From all the sources, the best established in VHE γ-rays is the Crab, which in some cases shows episodes of high statistical significance ($> 10\sigma$). However this object is not expected to be a VHE neutrino emitter (see discussion in section 2.4).

The adopted integrated VHE/UHE γ-ray spectra of the objects of table 2.1 are based on the fluxes reported in the previous references. We used the reported fluxes, time averaged over the total observing time, in each case. We further reduced the fluxes in every energy channel by averaging over the whole observing time, including the times of reported non-detections.

From the integrated spectra of the objects, we obtained the corresponding differential spectra which were used as input for the calculation of neutrino event rates (next section), assuming that the sources emit equal amounts of photons and neutrinos. Note that so far we have not considered any attenuation of photons on source or along their journey towards the earth (section 2.4).

2.3 Calculation of ν Event Rates

The calculation of neutrino event rates for the various sources includes the following steps:

- We take the neutrino spectrum (equal to the gamma-ray spectrum) for the point sources. We also take the predicted spectrum of the diffuse AGN background from various models (Sikora AGN [58], Stecker AGN [65], Protheroe AGN [66], and Biermann AGN [67]).

- We calculate atmospheric neutrino fluxes using the data by Butkevich et al. [68] (see table A.3 in Appendix)*.

- We then follow the procedure outlined by Katsanevas [16] for calculating the high energy interactions. The attenuation of neutrinos through the earth, the muon range, the effective area of NESTOR, and the neutrino/antineutrino cross sections (using DFLM [69] and Lipari's parametrization [70]) are shown in fig. 2.3 as a function of energy.

- Finally, for the point sources we reduce the event rates using the viewing time (table 2.2) as fraction of a day.

2.4 Results and Discussion

The calculations were performed for both one and seven NESTOR towers (stages I and II) and the results are given in table 2.2.

*No account has been taken in our calculation of prompt neutrino contribution (see chapter 3) because it is inessential below 10 TeV.

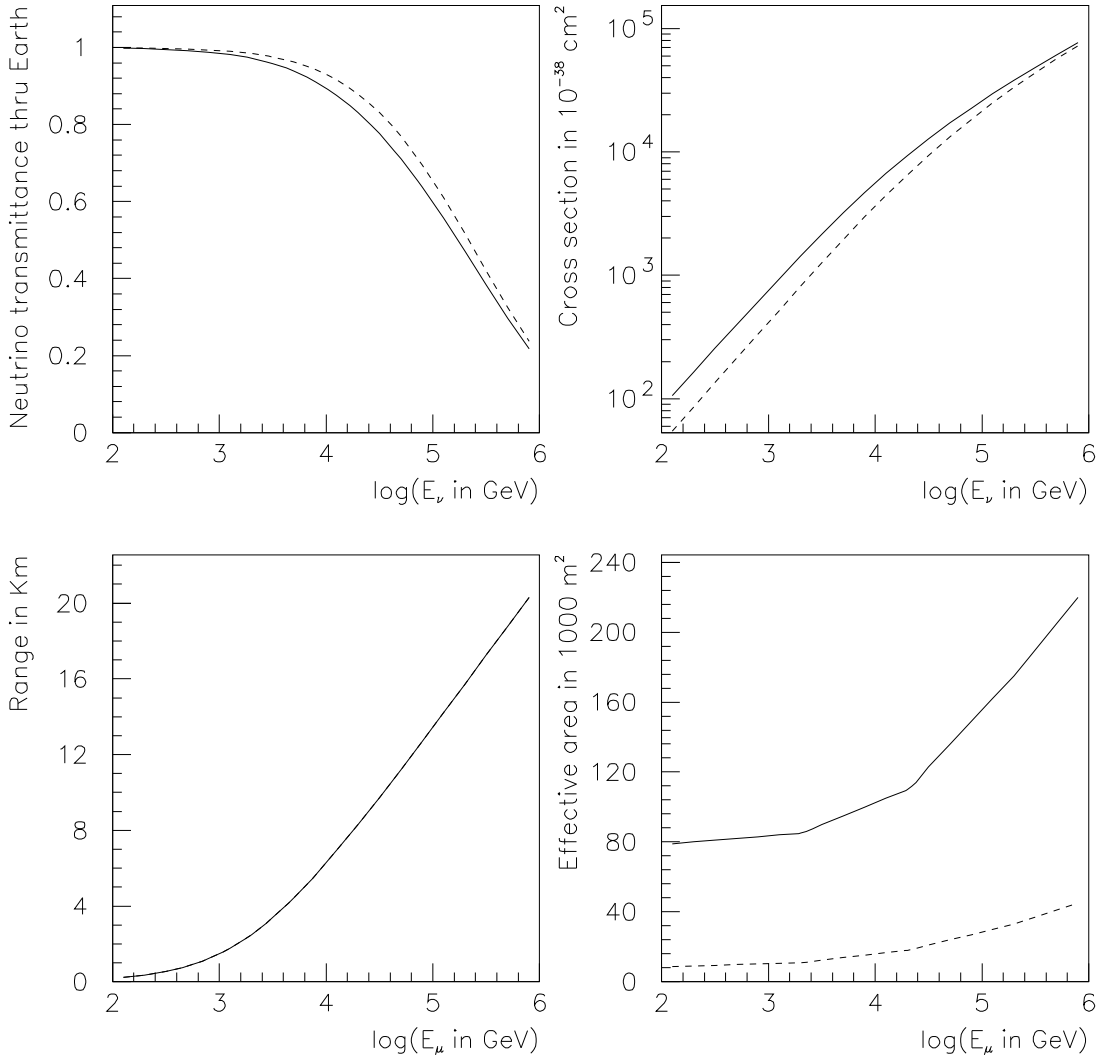

Figure 2.3: The parameters used for calculating the high energy interactions as a function of energy. In the upper two diagrams, solid curves refer to neutrinos and dashed curves to antineutrinos. In the lower right diagram the solid curve refers to seven NESTOR towers (1° resolution) and the dashed curve to a single NESTOR tower (5° resolution). For the diffuse sources (40° resolution) the effective areas are about two times higher.

Object	Stage I (1 tower) (> 1 TeV) – (> 10 TeV)	Stage II (7 towers) (> 1 TeV) – (> 10 TeV)
Her X-1	1.2 – 1.0	5.0 – 4.0
" (active)	110 – 95	400 – 330
Cyg X-3	0.8 – 0.6	2.5 – 2.1
XRB bursts	1.1 – 0.8	4.0 – 3.0
Mrk 421	0.4 – 0.3	1.3 – 1.1
" (active)	2.0 – 1.7	7.0 – 6.0
3C273	3.0 – 2.5	8.0 – 6.5
3C279 (active)	16 – 12	53 – 42
Atmospheric	2.0 – 0.14	0.6 – 0.04

Table 2.2: Expected number of events per year for the point sources (lower limits). For the XRB bursts the numbers are events/burst. The resolution for a single tower is 5° while for the 7 towers it is 1°.

In fig. 2.4 we show the lower limits to the expected event rates of the point sources as a function of muon energy (seven NESTOR towers with an angular resolution of 1°).

From this diagram we can see that the optimum muon energy range at which we can look for point sources begins at the TeVs. Below 100 GeV the atmospheric background dominates and does not allow the detection of point sources. In the following paragraphs, we discuss the results for each class of objects individually.

2.4.1 The Crab Pulsar/Nebula

This is an isolated pulsar embedded in an expanding shell of gas, the remnant of a supernova that went off $\sim$ 1000 years ago. The X-ray and low energy γ-ray spectra are consistent with synchrotron emission and inverse Compton scattering from relativistic electrons/positrons in the envelope of the supernova remnant. Relativistic protons cannot be present in the Crab nebula because if the object had the average galactic ratio of relativistic proton to electron energy ($\sim$ 100), then the outward pressure would accelerate the gaseous shell much faster than observed [71]. Moreover, if the relativistic electrons were secondaries to protons, then UHE γ-ray emission from neutral pion decays would have been a few orders of magnitude higher than observed [54]. So, we do not expect neutrinos from this object.

2.4.2 Mrk 421

This is a BL Lac object (active galaxy). Neutrinos are expected from such objects, predominantly from $p\gamma$ interactions due to the intense radiation field. The expected event rates for Mrk 421 are lower limits due to the fact that while neutrinos escape freely once generated, γ-rays suffer attenuation in the source. In table 2.2, We give rates for both the quiescent state and the active state of this object (the latest observations by the WHIPPLE observatory revealed a burst of activity ten times brighter [72]).

The VHE/UHE γ-ray opacity $\mu_{\gamma\gamma}$ of the sources under consideration is caused by their intense radiation field: $\gamma\gamma \rightarrow e^+e^-$. The electron/positron pairs, through synchrotron radiation and inverse Compton scattering, emit γ-rays of lower energy and eventually X-rays. Thus, a good deal of the initial high energy γ-rays are transformed to lower energy γ-rays and X-rays. Within the MeV energy range, the optical depth τ to pair production (the emerging radiation decreases by $e^{-\tau}$) for a spherically symmetric source of radius R is roughly [73]:

$$\tau = \mu_{\gamma\gamma} R \approx \frac{L_\gamma}{10^{29}\ \mathrm{erg\,sec^{-1}}},$$

where L_γ is the luminosity of the source in the MeV range. For TeV γ-rays, the energy threshold of target photons for pair production starts in the UV–X-ray region, where the AGN are much brighter than in the MeV range and thus the optical depth is even higher. For the parameters of Mrk 421, the optical depth to pair creation can be anywhere between 0.1 and 100. If, for example, $\tau = 1$ then the neutrino flux will be 3 times higher than that of the γ-rays which we used for our calculations, and with $\tau = 5$ this factor grows to 150.

At this point we must emphasize the fact that Mrk 421 is the closest active galaxy to the earth (of the EGRET observation) at a redshift z = 0.031, and the only one observed at VHE γ-rays by the WHIPPLE group [62]. On the other hand, there are many active galaxies observed in the MeV–GeV energy range by EGRET [63] brighter than Mrk 421 and with similar spectral indices (for example, 3C279 at its active state is $\sim$ 40 times brighter than Mrk 421), but which have not been observed at higher energies. This has been attributed to attenuation of VHE γ-rays from these objects through $\gamma\gamma$ interactions with the extragalactic starlight and infrared photons [1]. At the redshift of Mrk 421 this happens to photons with energy $E_\gamma >$ a few TeV, but the rest of the EGRET active galaxies are much more distant, most of them at a redshift z $\sim$ 1. At this redshift, photons with energy greater than 100–200 GeV are attenuated significantly and this may be the reason that these active galaxies have not been detected at VHE γ-rays despite the fact that they are brighter than Mrk 421. While this is true for photons, neutrinos do not suffer this attenuation and therefore NESTOR can expect to see more active galaxies brighter than Mrk 421, especially when they are in their most active state.

As an example, we give in table 2.2 the expected rates for the quiescent state of 3C273 based on model calculations (see ref. [74]) and the active state of 3C279 (extrapolated from the EGRET energy range since it has the same spectral index as Mrk 421).

2.4.3 Her X-1 and Cyg X-3

These are binary pulsars. Unlike the AGNs their radiation field is not as intense (orders of magnitude lower). The dominant channel for neutrino production here is through *pp* interactions of protons accelerated by the pulsar with target material anywhere in the system (beam-dump process [7]). As mentioned in section 2.2, these systems are bursting/variable sources from radio to γ-rays.

For Her X-1 we give the expected event rates for both the quiescent and active state. VHE/UHE γ-ray bursts have been reported lasting from minutes to days (episodes of

enhanced and/or pulsed emission). The brightest γ-ray bursts stand 2–3 orders of magnitude higher than the time averaged flux spectrum. For such bright bursts lasting for 5 hours. For instance, NESTOR at stage II will observe a few neutrinos per burst. Again here all the calculated numbers are lower limits because of the opacity in the γ-rays due to matter column density in the sources.

The optimum conditions for the beam-dump process to produce VHE/UHE γ-rays and neutrinos are [7]: density $\rho < 10^{-7} - 10^{-8}$ g/cm^3 and column density a few $< x < 200 - 300$ g/cm^2. At higher densities pions may interact before decay. Above $x \sim 50$ g/cm^2 γ-rays suffer attenuation. In the X-ray binaries we can have minimal or total absorption of the high energy γ-rays, depending on the geometry of the systems the location of the target material, and the inclination ($\imath$) [75]. Possible targets for the beam-dump process in the X-ray binaries are: a) the atmosphere of the secondary star, b) the accretion disk, and c) the accretion column formed by the poles of the neutron stars' magnetic field. All these are valid for Her X-1 which is an almost edge-on binary system ($\imath \sim 87^\circ \pm 3^\circ$). Cyg X-3 is a lower inclination system ($\imath > 70^\circ$) and only (a) and (c) can serve as targets here.

2.4.4 The Diffuse AGN Background

Apart from the point sources, another candidate celestial source of neutrinos is the diffuse AGN background. This background is the combined emission from all AGNs which are distributed more or less uniformly all over the sky. We examine here four models of this background [58, 65, 66, 67] and the results are given in table 2.3.

In fig. 2.5 we show the event rates as a function of muon energy for a single NESTOR tower. All models beat the atmospheric background above $E_\mu \sim 10$ TeV.

Model	Stage I (1 tower) (> 1 TeV) – (> 10 TeV)	Stage II (7 towers) (> 1 TeV) – (> 10 TeV)
Protheroe	13500 – 10800	40000 – 32000
Sikora	760 – 690	2000 – 1970
Biermann	280 – 220	750 – 640
Stecker	120 – 120	380 – 380
Atmospheric	1500 – 120	4000 – 420

Table 2.3: Expected number of events per year for the diffuse AGN background.

2.5 Conclusions

From the discussion in the previous section it is clear that the diffuse AGN background is the most promising candidate celestial neutrino source for NESTOR. Our calculations for the diffuse AGN background give appreciable event rates in the TeVs (hundreds to thousands events/yr) even for one tower ($\sim$ 20,000 m^2). On the other hand, the calculations for the point sources for seven towers ($\sim$ 100,000 m^2) give lower limits to the expected event rates in the range: 1–400 events/yr. The corresponding event rates drop by a factor of 3 for one tower. Among the point sources, individual AGN at their active state are the best candidates (many tens of events per year). The bright bursts of X-ray binaries are a good possibility too, since in this case we expect to see a minimum of ~ 4 events in the course of a few hours. A very prolonged active state of the X-ray binaries would yield a much higher yearly event rate but it is not very likely that these objects can stay in the high state for periods as long as a year. The above numbers came from the γ-ray fluxes and we did not take into account any attenuation of the photons in the sources.

As we saw in the previous section, the neutrino fluxes can be higher by one or even two orders of magnitude under favorable conditions and in this case a single NESTOR tower would be able to detect a few point sources. Despite this possibility, it looks that NESTOR is necessary to move to 7 towers in order to detect point sources in the sky. In the ultra high energies the other detectors (e.g. DUMAND and AMANDA) will suffer from the UHE neutrino absorption inside the earth because they have their PMTs looking downward only. NESTOR having 4π optical modules is not seriously affected from this absorption.

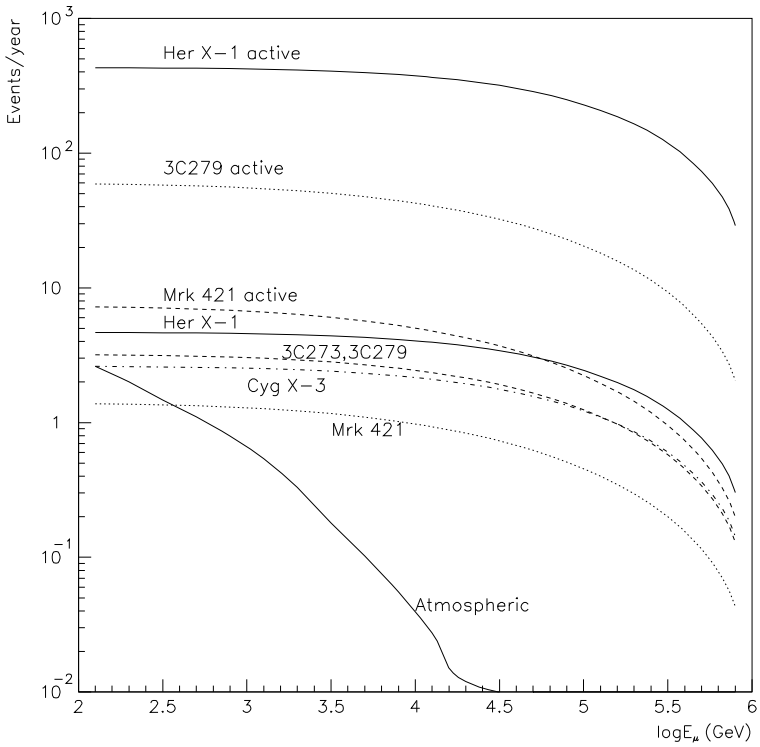

Figure 2.4: Lower limits to the expected event rates of the point sources. The calculations refer to 7 NESTOR towers and no attenuation of photons has been taken into account.

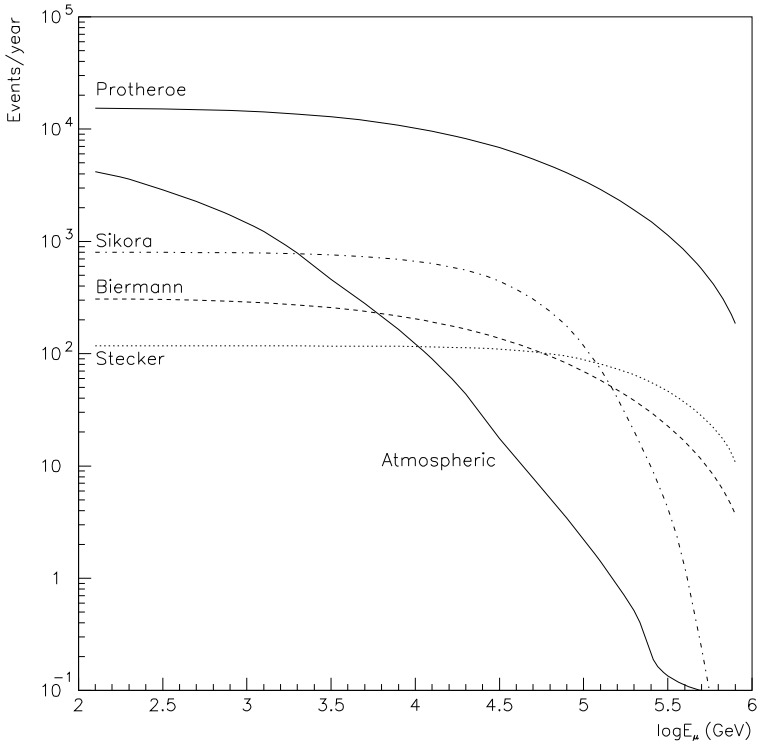

Figure 2.5: Expected event rates for the diffuse AGN background. The calculations have been done for a single NESTOR tower.

Chapter 3

Atmospheric Neutrino Flux

3.1 Introduction

Atmospheric neutrinos (AN) represent an unavoidable background for most of the astrophysical experiments with NESTOR discussed in this proposal, such as the detection of extraterrestrial neutrinos generated in AGNs and in other astrophysical sources (see chapter 2), neutrinos produced in the annihilation of neutralinos captured in the earth and the sun (see chapter 6), and the direct detection of relativistic cosmic WIMPs [76].

At the same time, the AN flux is a natural instrument for studying neutrino oscillations (see chapter 5) and neutrino interactions with matter at energies beyond the reach of accelerator experiments. Measurements of the cross sections for $\nu_l N$ and $\overline{\nu}_l N$ charged-current interactions at $\sqrt{s} \sim m_W$ ($E_\nu \sim 3.4$ TeV) provide an important test for the standard model [77]. With modern accelerators the interactions of neutrinos are studied at energies up to several hundreds of GeV (besides the single very high energy HERA data point recently extracted from the $ep \to \nu X$ cross section), whereas deep underwater experiments with ANs will enable to enlarge the region of neutrino energies, up to a few tens of TeV. Future "KM3" telescopes will be able to study the production of the standard vector $q\overline{q}$ resonances (ρ, D_s^* and possibly $\overline{t}b$) and the resonant W^- production ($E_\nu^{\rm res} = m_W^2/(2m_e) \simeq 6.3$ PeV) in $\overline{\nu}_e e^-$ annihilation [78] as well as hypothetical nonstandard interactions of neutrinos like interactions induced by off-diagonal neutral currents or the charged-current processes with production of supersymmetric particles or with an exchange of light leptoquarks [79] and so forth*.

In both cases – to correct for the neutrino background and to use the AN flux as the subject of investigations with NESTOR – there is a need to employ accurate and detailed calculations of the energy spectra and angular distributions of AN over a wide range of energies (from ~ 3 GeV up to the multi-PeV region) as well as calculations of the passage of neutrinos through the earth with consideration of their absorption and regeneration.

*Considerable attention has been recently focussed on a possible nonperturbative behaviour in the electroweak sector of the standard model, at energies above a threshold $\sqrt{\hat{s}_0} \gg m_W$, responsible for multiple production of gauge and Higgs bosons in νN interactions with a sizeable cross section (see chapter 8). But the AN flux of the appropriate energies (above ~ 10 PeV) is too small; hopefully, AGN neutrinos will give the possibility of studying this phenomenon with NESTOR.

3.2 (π, K) Neutrinos

The physics of neutrino production in the atmosphere is well understood [80, 81, 82, 83, 84]. Muon and electron (anti)neutrinos[†] come from the decays of unstable particles generated in the collisions of primary and secondary particles with air nuclei. However, the process of AN generation is rather complicated because the primaries and secondaries (both stable and unstable) can interact in the atmosphere repeatedly with absorption, regeneration and dissipation of energy through ionization; muons change their polarization due to energy loss; meteorological and geomagnetic effects are also essential in general case.

Low-energy AN's ($E_\nu < 10-15$ GeV) are produced mainly in the two-particle leptonic decays of charged pions and kaons and also in the muon decay which is the only source of ν_e and $\overline{\nu}_e$ in this energy range (table 3.1); muon polarization is an essential factor affecting the flavour ratio

$$R = \frac{\nu_e + \overline{\nu}_e}{\nu_\mu + \overline{\nu}_\mu}$$

as well as the neutrino to antineutrino ratio.

Particle	Exclusive decay mode	Branching ratio
$\mu^\pm$	$e^\pm + \nu_e(\overline{\nu}_e) + \overline{\nu}_\mu(\nu_\mu)$	$\simeq 100\%^*$
$\pi^\pm$	$\mu^\pm + \nu_\mu(\overline{\nu}_\mu)$	$\simeq 100\%$
$K^\pm$	$\mu^\pm + \nu_\mu(\overline{\nu}_\mu)$	$(63.51 \pm 0.18)\%$
	$\pi^0 + e^\pm + \nu_e(\overline{\nu}_e)$	$(4.82 \pm 0.06)\%$
	$\pi^0 + \mu^\pm + \nu_\mu(\overline{\nu}_\mu)$	$(3.18 \pm 0.08)\%$
K_L^0	$\pi^\pm + e^\mp + \overline{\nu}_e(\nu_e)$	$(40.0 \pm 0.9)\%^{**}$
	$\pi^\pm + \mu^\mp + \overline{\nu}_\mu(\nu_\mu)$	$(27.0 \pm 0.4)\%$
*Including radiative mode $e^\pm + \nu_e(\overline{\nu}_e) + \overline{\nu}_\mu(\nu_\mu) + \gamma$.		
**Including radiative mode $\pi^\pm + e^\mp + \overline{\nu}_e(\nu_e) + \gamma$ with low-momentum γ quantum.		

Table 3.1: The main neutrino sources.

The problem of low-energy AN flux is being discussed intensively at present in the context of the anomalous flavour ratio observed in KAMIOKANDE (in the sub-GeV [46] and multi-GeV [47] energy ranges), IMB [48], and SOUDAN 2 [49] because the observed anomaly gives the long-expected hint for "new physics" (neutrino oscillations or proton decay!). Although two other (tracking) experiments, Fréjus [51, 52] and NUSEX [50], have reported no effect, they do leave (because of small statistics) some room for an interpretation of the KAMIOKANDE–IMB–SOUDAN 2 data in terms of maximal $\nu_\mu - \nu_\tau$ mixing [52] or in terms of threefold maximal mixing with the first and second generation neutrinos being nearly degenerate [86]. At the same time, the explanation of the KAMIOKANDE result with the proton decay hypothesis [87] is still remaines to be among the living, though it is highly improbable.

[†] ν_τ and $\overline{\nu}_\tau$ are practically absent in the AN flux at all energies of present interest.

With the hopes for new physics we must be on call to correct the KAMIOKANDE – IMB – SOUDAN 2 results subject to possible neutron background [88] (see also discussion in ref. [52]). According to Ryazhskaya [88], a significant high energetic neutron flux originating from interactions of cosmic-ray muons in the surrounding rock near a detector could be expected. Some of these neutrons traversed the veto counter designed for charged particles and the neutral pions produced by interactions of the neutrons inside the detector may lead to an excess of electron-like (showering) events. This background is expected to be negligible for the detectors Fréjus and NUSEX located at large depths, but it may be significant for KAMIOKANDE, IMB and SOUDAN 2 due to the shallow depths of these experiments. This point needs further consideration.

Calculations of the low-energy AN flux were reported in a number of papers [89, 90, 91, 92, 93, 94, 95] (see also refs. [98] for further information and refs. [81, 82, 83, 84, 85] for reviews of the present-day status of the problem). These calculations are complicated convolutions of the primary spectrum with the inclusive energy spectrum of secondaries: the lack of Feynman scaling in the hadron-nucleus interactions, non-power spectrum of primary cosmic rays (+ geomagnetic effects and solar modulation), ionization energy losses, and the nonisothermicity of the atmosphere complicate the analysis of the nuclear-cascade process at energies of primaries below a few tens of GeV. Besides, the simplest superposition model for nucleus-nucleus collisions – commonly accepted in cosmic ray physics at high energies – is inoperable here as a good approximation and other, more sophisticated approaches are necessary (see, for example, refs. [83, 94, 96]). Although the inputs and methods employed in the cited papers are significantly distinct, all calculations agree within a range of about 5% for the flavor ratio. Much larger differences exist among the results for the absolute flux and shape of the energy spectra. These are the central problems in the right interpretation of the R anomaly.

As an example, we show in fig. 3.1 the $\nu_\mu + \overline{\nu}_\mu$ and $\nu_e + \overline{\nu}_e$ energy spectra averaged over the zenith and azimuth angles for the Kamioka site, as calculated in refs. [89, 90, 92, 94]. As is seen from the figure, the calculation ref. [90] has a harder spectrum than the other calculations[‡]. The maximum difference between the calculations for the absolute flux ranges up to almost 100% at $E_\nu = 100$ MeV. In the new, improved calculation by the Bartol group [95], the AN spectra were significantly reduced in the sub-GeV energy range (especially for the location of KAMIOKANDE), due mainly to the improved treatment of the geomagnetic cutoffs [97]. Now, their spectra are in good agreement with the result of Honda et al. [94]. The maximum difference with the result of ref. [90] is about 55% for the Kamioka site but, as before, about 90% for the IMB site. A discussion of the main reasons for the disagreements among the calculations at low energies is given in ref. [85].

Luckily, the most important effects in the sub-GeV range (geomagnetic cutoff, solar modulation of the primary cosmic-ray spectrum, strong scaling violation in hadronic interactions) are of no concern for our purposes. All low-energy calculations are in close agreement above 2–3 GeV and the multi-GeV energy range of the AN spectrum has been studied in greater detail.

[‡]A remark is in order. Several bugs in the implementation of the code of Lee and Koh [92] (which is a 3-dimensional version of the model of hadronic interactions used by Bartol group [89]) have been discovered recently [85]. When these are removed, the results of ref. [92] are essentially the same as those of ref. [89] at $E_\nu > 200$ MeV.

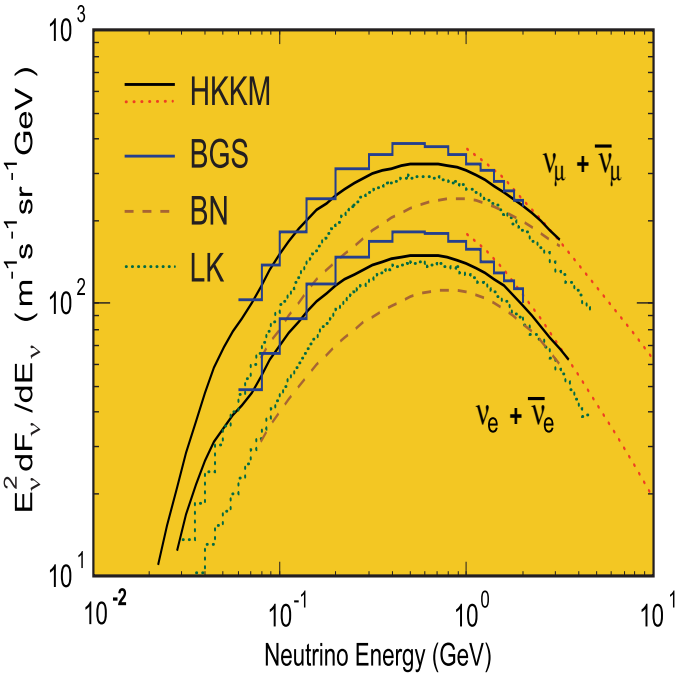

Figure 3.1: Predicted low-energy AN fluxes (multiplied by E_ν^2) for the Kamioka site at middle solar activity. The curves marked by HKKM, BGS, BN, and LK are from refs. [94], [89], [90], and [92], respectively. The dotted lines are the result of ref. [94] obtained without geomagnetic cutoff.

At higher energies (above 10–15 GeV), the semileptonic decays of charged and neutral kaons become important (table 3.1) and hence the differential cross sections for kaon production in NA, πA and KA interactions are required for the calculations. The high-energy AN flux consists mainly of ν_μ and $\overline{\nu}_\mu$. For example, at $E_\nu = 1$ TeV, $R \simeq 0.03$ at $\vartheta = 0°$ and $R \approx 0.08 - 0.09$ at $\vartheta = 90°$ (where ϑ is the zenith angle). Muon decays give an essential contribution to the electron neutrino flux up to $E_\nu \simeq 40$ GeV but at higher energies (up to ~ 10 TeV), the K_{e3} decays are the dominant channels for ν_e and $\overline{\nu}_e$ production and thus their inclusion is essential for the evaluation of the flavour ratio in the high-energy AN flux. Pion production due to kaon decays (table 3.2) gives a small but not completely negligible contribution to the AN flux and can affect the flavour ratio.

The most recent and detailed calculations of the (π, K) neutrino flux at high energies were performed in refs. [68, 99, 100, 101, 94, 102]. For earlier calculations see refs. [103, 104, 105, 96] and references therein. The comparison between five different predictions of the $\nu_\mu + \overline{\nu}_\mu$ and $\nu_e + \overline{\nu}_e$ energy spectra for near horizontal and near vertical directions in the energy range $1 - 10^4$ GeV is shown in fig. 3.2.

For reference, we give in Appendix a detailed compilation of the results from refs. [104] (tables A.1 and A.2), [68] (table A.3) and [100] (table A.4) for the (π, K) AN spectra at 6 zenith angles ($\cos\vartheta = 1.0,\ 0.6,\ 0.4,\ 0.3,\ 0.2,\ 0.1,\ 0$) over a wide range of neutrino energies. It should be pointed out that the data on the part of the spectra below ≈ 10 GeV presented in these tables are adequate only for rough estimates, because many of the

Particle	Exclusive decay mode	Branching ratio
K_S^0	$\pi^+ + \pi^-$	$(68.61 \pm 0.28)\%$
K_L^0	$\pi^+ + \pi^- + \pi^0$	$(12.38 \pm 0.21)\%$
$K^\pm$	$\pi^\pm + \pi^0$	$(21.16 \pm 0.14)\%$
	$\pi^\pm + \pi^\pm + \pi^\mp$	$(5.59 \pm 0.05)\%$
	$\pi^\pm + \pi^0 + \pi^0$	$(1.73 \pm 0.04)\%$

Table 3.2: The main pionic decays of kaons.

physical effects essential in this range were ignored in refs. [68, 100, 104] (strong scaling violation, ionization energy loss of charged particles, and so on). What's more, below 2–3 GeV the AN spectra depend on geographical coordinates (due to the geomagnetic effects) and time (due to solar modulation of the primary spectrum). Thus the results of the aforementioned, more precise calculations [83, 94, 97, 95] must be consulted for a closer examination of this part of the AN flux.

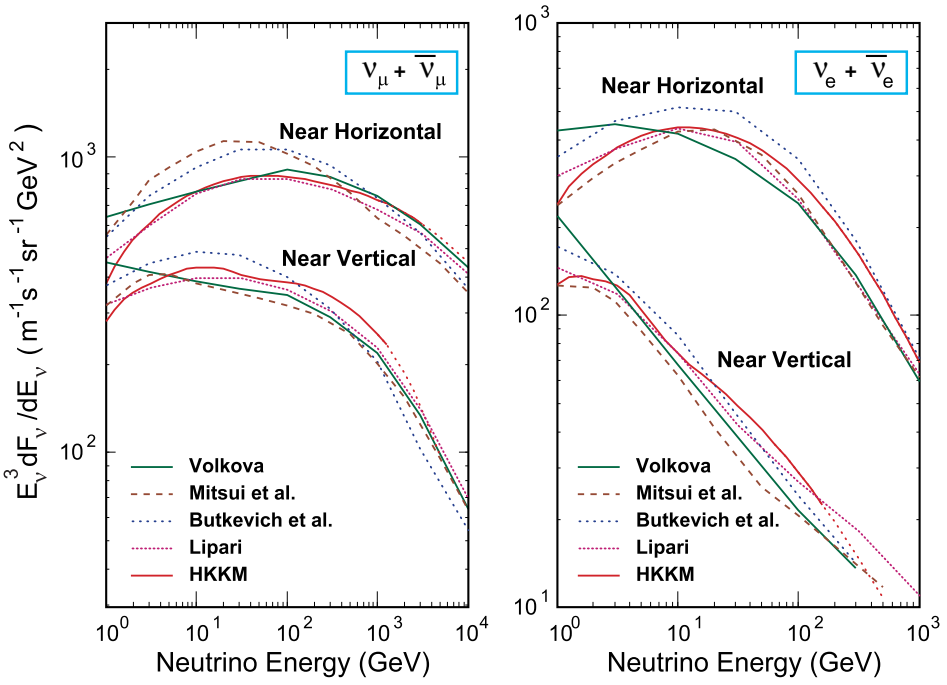

Figure 3.2: Predicted AN fluxes (multiplied by E_ν^3) at $E_\nu > 1$ GeV for near horizontal and near vertical directions. The curves marked by HKKM, V, MMK, BDZ, and L are from refs. [94] ($\cos\vartheta = 0 - 0.1$ and $0.9 - 1.0$), [104] ($\cos\vartheta = 0.05$ and 1), [105] ($\vartheta = 87°$ and $0°$) [68] ($\cos\vartheta = 0$ and 1), and [100] ($\cos\vartheta = 0.05$ and 1), respectively. The dotted curves have the same sense as in fig. 3.1.

3.3 Prompt Neutrinos

The dominant contribution to the AN flux at very high energies[§] is due to semileptonic decays of charmed hadrons (mainly $D^{\pm}$, D^0, $\overline{D}^0$ and Λ_c^+). The AN from this source are called prompt neutrinos. There are numerous exclusive decay modes of charmed particles with a lepton pair and one or more hadrons in the final state [106]; the inclusive semileptonic decays of D and Λ_c^+ are shown in table 3.3. The calculation of the prompt neutrino flux (and even the energy range in which the prompt neutrinos should dominate) is very model dependent [107, 108, 109]. As yet, this flux cannot be unambiguously predicted for lack of a generally accepted model for charm production at high energies.

Particle	Icllusive decay mode	Branching ratio
$D^{\pm}$	$e^{\pm} + \nu_e(\overline{\nu}_e)$ + anything	$(17.2 \pm 1.9)\%$
	$\mu^{\pm} + \nu_\mu(\overline{\nu}_\mu)$ + anything	–
D^0	$e^+ + \nu_e$+anything	$(7.7 \pm 1.2)\%$
	$\mu^+ + \nu_\mu$+anything	$(10.0 \pm 2.6)\%$
$D_s^{\pm}$	$e^{\pm} + \nu_e(\overline{\nu}_e)$ + anything	$< 20\%$
	$\mu^{\pm} + \nu_\mu(\overline{\nu}_\mu)$+anything	–
Λ_c^+	$e^+ + \nu_e$ + anything	$(4.5 \pm 1.7)\%$
	$\mu^+ + \nu_\mu$+anything	–

Table 3.3: Semileptonic decays of charmed hadrons (inclusive modes).

The salient and model-independent features of the prompt neutrino flux are that it is practically isotropic within a wide energy range (namely, at 10 TeV $< E_\nu < 3 \times 10^3$ TeV, the maximum anisotropy is about 3–4%) and the neutrino to antineutrino ratio and the flavour ratio are both about 1. These features provide a way to discriminate the prompt neutrino contribution through the analysis of the angular distribution[¶] and the relationship between "muonless" and "muonfull" neutrino events in NESTOR.

Within the region of isotropy, the differential energy spectrum of prompt neutrinos $(\nu_\mu + \overline{\nu}_\mu)$ is described by the following simple expression:

$$\frac{dF_\nu^{\rm pr}}{dE_\nu} = F_\nu^0 \left(\frac{E_\nu^0}{E_\nu}\right)^{\gamma_\nu+1} \left[1 + \left(\frac{E_\nu^0}{E_\nu}\right)^{\gamma_\nu}\right]^{-a_\nu} ,$$

with the model-dependent constant parameters F_ν^0, E_ν^0, γ_ν, and a_ν. As an illustration let us consider briefly the predictions derived from the two phenomenological models for charm production – recombination quark-parton model (RQPM) and quark-gluon string model (QGSM). According to the calculation of ref. [108],

[§]For muon neutrinos, at $E_\nu > 10 - 100$ TeV for vertical and at $E_\nu > 100 - 1000$ TeV for horizontal neutrino flux; for electron neutrinos at energies which are an order of magnitude less (see below).

[¶]Moreover, the anisotropy of the flux of prompt muons (that is the muons originated from charm decay) at the same energies is also very small ($< 20\%$). This can be a help in deciding the problem.

Model:	RQPM		QGSM	
E_ν (TeV)	$\vartheta = 0°$	$\vartheta = 90°$	$\vartheta = 0°$	$\vartheta = 90°$
10^3	5.07×10^{-21}	5.24×10^{-21}	1.15×10^{-21}	1.18×10^{-21}
3×10^3	2.04×10^{-22}	2.25×10^{-22}	4.53×10^{-23}	4.88×10^{-23}
10^4	4.85×10^{-24}	6.43×10^{-24}	1.08×10^{-24}	1.35×10^{-24}
3×10^4	1.22×10^{-25}	2.27×10^{-25}	2.86×10^{-26}	4.67×10^{-26}
10^5	1.58×10^{-27}	4.94×10^{-27}	4.01×10^{-28}	1.03×10^{-27}
3×10^5	2.40×10^{-29}	1.18×10^{-28}	6.42×10^{-30}	2.61×10^{-29}
10^6	2.14×10^{-31}	1.48×10^{-30}	5.77×10^{-32}	3.55×10^{-31}

Table 3.4: Differential energy spectra of prompt $\nu_\mu + \overline{\nu}_\mu$ (in units $\mathrm{cm}^{-2}\,\mathrm{s}^{-1}\,\mathrm{sr}^{-1}\,\mathrm{GeV}^{-1}$) at super-high energies for vertical and horizontal directions as calculated in ref. [108] with two models of charm production.

$$F_\nu^0 = 4.65 \times 10^{-18}\ \mathrm{cm}^{-2}\,\mathrm{s}^{-1}\,\mathrm{sr}^{-1}\,\mathrm{GeV}^{-1},$$
$$E_\nu^0 = 10^5\,\mathrm{GeV},\ \ \gamma_\nu = 1.96,\ \ a_\nu = 0.157$$

for RQPM and

$$F_\nu^0 = 1.19 \times 10^{-18}\ \mathrm{cm}^{-2}\,\mathrm{s}^{-1}\,\mathrm{sr}^{-1}\,\mathrm{GeV}^{-1},$$
$$E_\nu^0 = 10^5\,\mathrm{GeV},\ \ \gamma_\nu = 2.01,\ \ a_\nu = 0.165$$

for QGSM. Using these values of parameters, it can be found that vertical intensities of the (π, K) muon neutrinos and prompt muon neutrinos become equal at $E_\nu \approx 32$ TeV (RQPM) or $E_\nu \approx 170$ TeV (QGSM). The corresponding energies for horizontal intensities are about 340 TeV (RQPM) and about 1700 TeV (QGSM). A very low prompt neutrino flux was predicted recently in ref. [109] using a pQCD based model for charm production.

At super-high energies, the prompt neutrino flux becomes anisotropic as evident from table 3.4. Thus at $E_\nu = 10^5$ TeV, the ratio of horizontal and vertical intensities of ν_μ's is about 3.1 and 2.6 for RQPM and QGSM, respectively. However, the absolute value of the flux is very small here so, it is hoped that uncertainties in the prediction for the AN angular distribution will not be a serious handicap to study extraterrestrial super-high-energy neutrinos with NESTOR.

3.4 The Major Sources of Differences Among the Calculations

The comparison of the energy spectra of $\nu_\mu + \overline{\nu}_\mu$ and $\nu_e + \overline{\nu}_e$ calculated in the quoted papers with different models for primary spectrum, inclusive cross sections, etc., shows (fig. 3.2) that the discrepancy between the results for the muon neutrinos in the energy range 3–500 GeV is of the order of 30–35% for near vertical directions and $\sim$ 35–40% for near horizontal direction, while at higher energies (to a few TeV) it is less than 25% for all directions. In the case of electron neutrinos the discrepancy is about 45–50%

(vertical) and 40–45% (horizontal) at 3–100 GeV (with the only exception: the $\nu_e + \overline{\nu}_e$ flux calculated in ref. [99] differs enormously from all other predictions at $E_\nu < 100$ GeV and it is in apparent contradiction with the recent Fréjus data [52]) and decreases to 20–30% at $E_\nu \approx 1$ TeV. This discrepancy is acceptable for some astrophysical experiments with NESTOR within the next few years, but is inadequate to analyze the present-day underground and future underwater experiments on neutrino oscillations by a change in the total neutrino flux [80, 82]. The possible changes in the angular distribution (due to oscillations) are vastly less model-dependent (chapter 5). The difference in the predictions for the multi-TeV energy range, which is most important for the calculation of the AN background for astrophysical experiments (chapter 2), is much bigger and drastically increases with energy ranging up to an order of magnitude in the region where the prompt neutrinos dominate (see ref. [108] for a detailed comparison of different charm-production models). As is seen from the tables A.2, A.3 and A.4, the ratios $\nu_\mu/\overline{\nu}_\mu$ and (to a smaller degree) $\nu_e/\overline{\nu}_e$ for the (π, K) neutrinos are also model-dependent at $E_\nu = 10 - 10^3$ TeV[‖]. For the most part this is due to our lack of understanding of the composition of primaries and mechanism of kaon production at high energies.

Increasing the accuracy in the calculation of the measurable characteristics of the AN flux will become increasingly urgent. Major input data required for calculating the AN flux are the spectrum and chemical composition of primary cosmic rays, total inelastic and differential inclusive cross sections of hadron-nucleus and nucleus-nucleus interactions over a wide kinematic range (primarily in the range of fragmentation of the projectile). The above-mentioned discrepancies in different calculations of the AN flux are due mainly to the incompleteness in the current knowledge of these input parameters. This holds, to a greater or lesser extent, for low, intermediate, high, and super-high energies. The main uncertainty in the AN flux calculation within the sub-TeV range is related to the absence of good data and theoretical models for K meson production in the fragmentation range, the so called, in cosmic ray physics, K/π problem. Within the range of prompt neutrino dominance, the principal problem is of course the charm production problem. An additional significant source of uncertainty has to do with the differential widths of inclusive semileptonic decays of charmed hadrons.

3.5 Atmospheric Muons

The only tool for verification of the calculated AN flux is the flux of muons generated in the stratosphere in the same processes as neutrinos. The recent balloon-born measurements of the muon spectra and charge ratio at high altitudes in the atmosphere using Matter Antimatter Spectrometer Systems (MASS and MASS 2) [110] give us this possibility for low energies (below $\approx$ 40 GeV). Preliminary results from Isotope Matter Antimatter eXperiment (IMAX) [111] and High Energy Antimatter Telescope (HEAT) [112] for the μ^- flux and muon charge ratio (as a function of atmospheric depth) are in agreement with the MASS data in the sub-GeV energy range. It is hoped that further experiments

[‖]Curiously, the situation is opposite for the sub-GeV energy range: here, a serious disagreement (up to about 20%) prevails in the $\nu_e/\overline{\nu}_e$ ratio predicted by different models (see refs. [83, 94]). This is one of the obstacles to an unambiguous interpretation of the R anomaly observed with underground detectors.

with MASS, IMAX and HEAT will provide to make the precision normalization of the low-energy AN spectra at different geomagnetic cutoffs. However, a large body of direct spectrometer measurements of the sea-level muon spectrum at high energies (see e.g. refs. [113, 114] for a compilation of data) are in rather poor agreement to one another, even though each of the experiments by itself has typically quite good statistical accuracy. Thus the current sea-level data are not very useful for this purpose. The situation could be improved considerably in future, if the proposal [115] to use the L3 detector at LEP for the accurate measurement of the cosmic-ray muon spectrum between 20 GeV and 20 TeV would be carried out.

At the same time, a quite representative array of data on the cosmic-ray muon depth-intensity relation (DIR) in rock (underground experiments ERPM, KGF, Baksan, Fréjus, NUSEX, SOUDAN 2, MACRO, LVD) and, to a lesser extent, in water (in particular, from Baikal, DUMAND and NESTOR prototypes) has been accumulated to date. The data available through 1993 are compiled in ref. [114], and the recent results are presented in papers of the MACRO, LVD and Baikal Collaborations [116, 117, 39, 118]. As is shown in ref. [114], the currently available data of underground measurements are more self-consistent, relative to the ground-level data, for depths up to 5–6 km of w.e. (corresponding roughly to 3–4 TeV of muon and neutrino energy at sea level) and hence they may be of utility to check the nuclear-cascade models at energies of primaries up to about 50–100 TeV. Unfortunately, the data at depths more than 5–6 km of w.e. are much less reliable. Preliminary analysis suggests that, through a correlation between the measured and calculated muon DIR, one can obtain an accuracy in the AN flux normalization better than 10%, at energies below a few TeV. Not bad. A careful calculation of the muon flux from the upper atmosphere to deep underground/underwater is therefore directly related to the AN problem.

The main contribution to the total systematic error in the underground measurements of the muon DIR comes from uncertainty and variability in the rock density and composition above the detector. This problems can be overcome by subsequent measurements underwater, where the matter overburden is well known and highly homogeneous. However, there is another problem common to underground and underwater measurements of DIR. It is the problem of muon bundles. Misidentification of a muon bundle and a single muon is an apparent source of systematics. On the other hand, the current theoretical predictions for the fraction of muon bundles vs depths are very model-dependent. It is beyond the scope of this chapter to review this many-sided problem more fully. Here we can do no more than call attention to its importance for the solution to the AN problem. In order to improve our knowledge at higher energies it is necessary to carry out measurements of the intensity of single muons and muon groups and also, if at all possible, of the muon energy spectra at large depths in the ocean using slant directions. Needless to say these measurements are of direct interest to traditional cosmic ray physics, and not just to neutrino astrophysics.

Chapter 4

Atmospheric Neutrino Oscillations with NESTOR

4.1 Introduction

One of the physics questions to which NESTOR (with one tower) can provide an answer in a relatively short time after turning on, is that of neutrino oscillations. The possible existence of neutrino oscillations was proposed many years ago by Pontecorvo and is still very topical since their existence may provide answers to open questions such as the dark matter, the atmospheric ν_e/ν_μ low energy anomaly which is observed by the IMB, KAMIOKANDE and SOUDAN 2 underground experiments (see references in chapter 1). Assuming two flavor mixing (ν_a, ν_b), the oscillation probability is given by

$$P_{a\to b}(\Delta m^2, \sin^2 2\theta) = \sin^2 2\theta \sin^2(1.27\Delta m^2 L/E_\nu), \tag{4.1}$$

where $\Delta m^2 = m_a^2 - m_b^2$ is the difference of the squares of the mass eigenvalues in eV^2, θ is the two flavor mixing angle, L is the neutrino propagation length in km and E_ν is the neutrino energy in GeV. NESTOR can cover regions in the $(\sin^2 2\theta, \Delta m^2)$ plane which are not accessible to conventional experiments at accelerators or reactors. Moreover, NESTOR has a low energy threshold and can detect neutrinos of a few GeV (around 2 GeV and higher), which makes it unique among the other underwater experiments. Given the rapidly decreasing atmospheric neutrino spectrum (see chapter 3) and the low energy threshold, NESTOR will accumulate sufficient statistics in a relatively short running time.

Eq. (5.1) clearly shows that for a given value of $\sin^2 2\theta$ the lower bound of Δm^2 is proportional to E_ν/L. The search for neutrino oscillations using atmospheric neutrinos benefits from variations of neutrino paths through the earth in the range of 15 km to 13,000 km. Thus, due to the low energy threshold, NESTOR will be sensitive to an extremely wide range of Δm^2.

Due to limited statistics, most underground experiments can only detect neutrino oscillations by a change in the total neutrino flux, whereas in our case the possible existence of neutrino oscillation can be detected as changes both in the total neutrino flux as well as in the angular distribution, in the latter case independent of absolute normalization.

4.2 Contained Events

In this section, our study is limited to a sample of contained events. By this we define events which have their vertex within the sensitive area of the detector (a cylinder with a radius of 16 m and a length of 220 m). The fluxes of the atmospheric neutrinos used for the present study (as inputs to the Monte Carlo) are those of Butkevich et al. [68] and are shown on figs. 1.3 in chapter 1 and 3.2 in chapter 3 (see also table A.3 in Appendix). In our energy range we have mostly ν_μ's and $\bar{\nu}_\mu$'s and a small fraction of ν_e's because at these energies cosmic ray muons seldom decay in flight. In order to understand the systematics, we have checked that the total number of contained events resulting using different AN flux calculations [68, 104, 105] (see chapter 3) do not differ by more than $\pm 10\%$ and that the angular distributions given by different models do not differ by more than $\pm 6\%$ within the considered energy range.

The integrated number of contained events expected in one NESTOR tower – before any efficiency correction, for a year's running, above the E_ν threshold – is shown in fig. 5.1 as a function of the neutrino energy thresholds.

Figure 4.1: Integrated number of events expected in one NESTOR tower per year from atmospheric ν_μ and ν_e interactions (not corrected for efficiency) above the E_ν threshold.

Now one has to correct for efficiencies – detection and reconstruction efficiency combined – for detecting an interacting neutrino within our sensitive volume as a function of the neutrino energy. These efficiencies were calculated very carefully. A detailed simulation was used based on the GEANT–Čerenkov generation routines which simulate the Čerenkov light from the various particles which are above the Čerenkov threshold and track the light up to our phototubes. The generated light was then used as an input to the NESTOR algorithm [119] to reconstruct the primary tracks which emitted the light. This was the first time that the new Čerenkov light addition to the GEANT code was used and a lot of debugging had to be done. As a further check we compared the standard NESTOR simulation [119], which is a modified version of the DUMAND code, with the GEANT one, and we found out that the former was not reliable for energies less than 10 GeV. So the efficiencies used for the present study are the ones obtained using the GEANT light generation.

The oscillation study was performed as a disappearance experiment by studying the zenith angle dependence of the flux. To be more precise, we look for differences between the number of downcoming ν_μ, which have the smaller oscillation lengths (~ 15 km), and the number of neutrinos coming from the sides or upcoming. The upcoming ν_μ travel the greatest distance before interacting in the detector (~ 13000 km, the diameter of the earth). The variation of the path length with zenith angle (ϑ) is shown in fig. 5.2.

Figure 4.2: The path length (in km) of neutrinos as a function of zenith angle.

Due to symmetry in the zenith distribution around the horizontal and vertical directions in the absence of $\nu_\mu \to \nu_e$ oscillations the number of up coming should be equal to the downcoming. Any deviation from this equality will give indications of the ν_μ oscillations, which will be further enhanced by the so called matter effects for the $\nu_\mu \to \nu_e$ oscillations [120]; we are exploring a unique region in L and E_ν where these effects may further enhance the oscillation signal. They are due to the interaction of ν_e with the electrons in matter and are expected to be important only for path lengths of the order of the earth's diameter.

To perform this investigation we divide the range of zenith angles in six bins equally spaced in $\cos\vartheta$ (i.e. in $d\Omega$) as shown in fig. 5.3.

Figure 4.3: Visualization of the six zenith bins used for this study.

The number of ν_μ in each bin has to be compared to the Monte Carlo calculation which includes the theoretical prediction [68] and takes into account the reconstruction efficiency obtained using events with a generated vertex within our sensitive volume. Fig. 5.4 shows the reconstruction efficiencies, for 20° reconstruction accuracy, as a function of the neutrino energy, calculated as described previously, for: (a) the angular bin close to vertical $0° - 48°$, (b) the intermediate angular bin $49° - 71°$, and (c) the angular bin close to horizontal $72° - 90°$.

The total number of ν_μ events expected per year over threshold is 576. We now form the ratio, R, of the number of μ events in the i-th bin to the number of events in the first (close to the vertical) bin. The efficiency is not flat with respect to the zenith, as shown in fig. 5.4. Fig. 5.5 shows the values of the ratio R for the five angular bins (the R for the first bin is equal to 1, by definition, so it is not shown). The crosses represent the value of R in the absence of oscillations and the dotted line shows the ratios expected in the presence of oscillations corresponding to the best fit for the KAMIOKANDE multi-TeV data in terms of $\nu_\mu \to \nu_e$ oscillations ($\sin^2 2\theta = 1.0$ and $\Delta m^2 = 1.8 \times 10^{-2}$ eV^2) [47]. It will be no sensible change in our analysis with the use of the "second KAMIOKANDE solution" ($\sin^2 2\theta = 1.0$, $\Delta m^2 = 1.6 \times 10^{-2}$ eV^2) related to $\nu_\mu \to \nu_\tau$ oscillations.

Figure 4.4: Reconstruction efficiencies as a function of the neutrino energy for the first three angular bins (efficiencies are equal for the symmetrical bins below the horizontal).

The number of cosmic ray muons expected in a year's running for the three relevant angular bins is shown in fig. 5.6, together with the number of expected muons from atmospheric neutrino interactions. One clearly sees from this figure that we need a rejection power of about 10^{-5} in order to distinguish – in at least the first angular bins – the events due to neutrinos generated in the atmosphere from badly reconstructed events induced by cosmic rays. Note that in absence of oscillations the expected numbers will be equal for the symmetrical bins below the horizontal.

In order to study this rejection power, we have generated about 1,000,000 events from single atmospheric muons using the muon energy spectrum at 3000 m calculated in Ref. [121] and the $\cos^{4.8}\vartheta$ angular dependence as we measured it in the 1992 Vityaz cruise [14]. Four events passed our minimal cuts and reconstructed as contained events. This gives us a rejection factor of 4×10^{-6}. In the first angular bin the number of expected downcoming muons to be recorded in our detector from cosmic rays is about 2.6×10^7 per year. If we multiply this number by the above rejection factor we end up with 100 contained events from misreconstructed cosmic rays. The precision of this number is poor and we have to increase the number of the simulated events to reach a precision of 3%. The number of 100 background events has to be compared with about 160 contained events from atmospheric neutrinos. At this stage, we can marginally discriminate, in the first bin, the neutrinos from cosmic rays. There is still work in progress trying to impose further cuts (especially using the Čerenkov light produced by the hadrons of the

interaction in order to get a better vertex determination) and improve our reconstruction algorithm in order to improve the rejection power.

Figure 4.5: The value of R (as explained in the text) vs $\cos\vartheta$. The dotted line is the expected ratio in presence of oscillations corresponding to the best fit of the "KAMIOKA solution" ($\sin^2 2\theta = 1.0$ and $\Delta m^2 = 1.8 \times 10^{-2}$ eV^2).

Taking into account all the above factors we can now proceed and form the allowed/excluded contours in the $(\sin^2 2\theta, \Delta m^2)$ plane for a year's running. These are shown in fig. 1.15 (chapter 1) together with the upper straight line which reproduces the CHORUS/NOMAD sensitivity and with the KAMIOKANDE allowed region. Calculating the error bars of fig. 5.5 and the limits of fig. 1.15 we have taken into account, together with the statistical error for a year's running, a systematic error of 6%. The latter reflects the uncertainty in the e/μ identification power of our apparatus.

In order to investigate our systematics due to different model predictions, we have repeated the same analysis using the AN spectra from Refs. [104, 105]. No significant difference has been observed.

Fig. 1.15 shows clearly that after one year's running we can reach limits for the oscillations down to $\Delta m^2 > 3 \times 10^{-4}$ eV^2 and $\sin^2 2\theta > 0.15$ with a detector which is flux calculation independent and self-normalizable.

Figure 4.6: The expected number of contained atmospheric neutrino events per year (dotted line) in one NESTOR tower, as a function of the angular bin. For comparison, the number of throughgoing cosmic ray muons expected in a year's running is shown (solid line).

4.3 Upward muons

An alternative approach to the item of atmospheric neutrino oscillations can be provided by the measurement of the muon flux produced by atmospheric neutrino interactions in the matter surrounding the detector.

The main disadvantages of this approach compared to the one of contained events are the relative high mean energy of interacting neutrinos which produce the flux of detectable muons and the impossibility to distinguish between neutrino induced muons and atmospheric downward muons.

To avoid the latter effect we will restrict our attention to zenith angles greater than 85° (see fig. 1.14 in chapter 1 for a comparison between downcoming muons and contained events which are a factor ≈10 less than the not contained events considered here). The reduction of the viewing angle will not allow to test the up-down symmetry for atmospheric neutrinos but a normalization of the absolute flux is still possible using the horizontal flux.

The differential fluxes of neutrino induced muons have been calculated following the method given in Ref. [80] where we have considered the two AN fluxes of Butkevich et al. [68] and of Volkova [104], the muon energy loss by Lohmann, et al. [122], the three sets of structure functions by Owens [123], Martin, Roberts and Stirling (MRS (A)) [124], and Glück, Reya and Vogt (GRV) [125] in which the evolution of the structure functions has been considered at next-to-leading order. The production point of each muon has been generated outside the cylinder considered for the contained events. Both water and

rock have been considered for the muon generation and propagation to the detector (the sea-bottom has been considered flat, which is a good approximation).

The fluxes have been combined with the detector efficiencies calculated as a function of the zenith angle and of the muon energy. The reconstructed events in one year of data taking as a function of the considered angular bin are plotted in fig. 4.7. The full line is relative to the flux of Butkevich et al., GRV structure functions and no oscillations, the dotted line refers to the same parametrization but with the vacuum oscillations $\nu_\mu \to \nu_\tau$ indicated by the KAMIOKANDE multi-GeV analysis [47] ($\sin^2 2\theta = 1.0$ and $\Delta m^2 = 1.6 \times 10^{-2}$ eV^2).

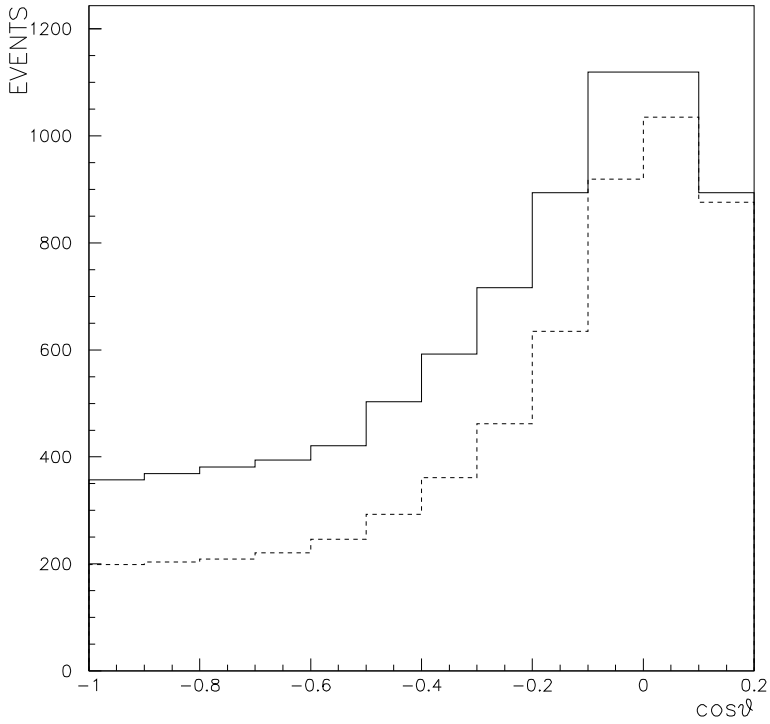

Figure 4.7: Reconstructed AN induced muons in one year's running. The full line refers to no oscillation, the dotted line to the "second KAMIOKANDE solution" for $\nu_\mu \to \nu_\tau$ oscillations.

In order to reduce the systematics due to theoretical predictions we have normalized the absolute flux to the horizontal flux and the results for the ratio

$$\frac{N_{\rm up}}{N_{\rm horiz}} = \frac{EVENTS\ (-1.0 \leq \cos\vartheta \leq -0.8)}{EVENTS\ (-0.1 \leq \cos\vartheta \leq\ 0.1)}$$

are shown in table 4.1. Looking at the table, we can argue that the KAMIOKANDE indications for $\nu_\mu \to \nu_\tau$ oscillations will be easily verified.

The predictions of the various models for the ratio $N_{\rm up}/N_{\rm horiz}$ do not differ by more than 5%, which is of the same order of the statistical error in one year's running. The effect

$\sin^2 2\theta$	Δm^2 (eV^2)	AN Flux	Structure functions	$N_{\rm up}/N_{\rm horiz}$
0	0	Volkova	MRS	0.314
1	0.016	Volkova	MRS	0.202
0	0	Volkova	Owens	0.317
1	0.016	Volkova	Owens	0.204
0	0	Volkova	GRV	0.321
1	0.016	Volkova	GRV	0.208
0	0	Butkevich et al.	MRS	0.318
1	0.016	Butkevich et al.	MRS	0.201
0	0	Butkevich et al.	Owens	0.321
1	0.016	Butkevich et al.	Owens	0.203
0	0	Butkevich et al.	GRV	0.325
1	0.016	Butkevich et al.	GRV	0.207

Table 4.1: Ratio of Events for Upward and Horizontal Muons.

due to the background of badly reconstructed atmospheric muons (taking into account also the ^{40}K background) can give a considerable contribution to the errors. This effect is under investigation. Taking into account the fact that also the systematic effects due to theoretical approximations are not well understood, we have considered in calculating the sensitivity to neutrino oscillations different errors for the ratio $N_{\rm up}/N_{\rm horiz}$: from an optimistic 10% to a pessimistic 20%. Results for the sensitivity in one year's running are summarized in table 4.2.

Error	$\sin^2 2\theta_{\rm min}$ $[\Delta m^2 = 4\times10^{-3}]$	$\Delta m^2_{\rm max}$ (eV^2) $[\sin^2 2\theta = 1]$	$\Delta m^2_{\rm min}$ (eV^2) $[\sin^2 2\theta = 1]$
10%	0.44	2.3×10^{-1}	3.5×10^{-4}
15%	0.66	1.1×10^{-1}	1.1×10^{-3}
20%	0.87	4.0×10^{-2}	2.5×10^{-3}

Table 4.2: Sensitivity to $\nu_\mu \to \nu_\tau$ oscillations in one year's running for different error estimates (at 90% C.L.).

Chapter 5

Atmospheric Neutrino Oscillations with NESTOR

5.1 Introduction

One of the physics questions to which NESTOR (with one tower) can provide an answer in a relatively short time after turning on, is that of neutrino oscillations. The possible existence of neutrino oscillations was proposed many years ago by Pontecorvo and is still very topical since their existence may provide answers to open questions such as the dark matter, the atmospheric ν_e/ν_μ low energy anomaly which is observed by the IMB, KAMIOKANDE and SOUDAN 2 underground experiments (see references in chapter 1). Assuming two flavor mixing (ν_a, ν_b), the oscillation probability is given by

$$P_{a\to b}(\Delta m^2, \sin^2 2\theta) = \sin^2 2\theta \sin^2(1.27\Delta m^2 L/E_\nu), \tag{5.1}$$

where $\Delta m^2 = m_a^2 - m_b^2$ is the difference of the squares of the mass eigenvalues in eV^2, θ is the two flavor mixing angle, L is the neutrino propagation length in km and E_ν is the neutrino energy in GeV. NESTOR can cover regions in the $(\sin^2 2\theta, \Delta m^2)$ plane which are not accessible to conventional experiments at accelerators or reactors. Moreover, NESTOR has a low energy threshold and can detect neutrinos of a few GeV (around 2 GeV and higher), which makes it unique among the other underwater experiments. Given the rapidly decreasing atmospheric neutrino spectrum (see chapter 3) and the low energy threshold, NESTOR will accumulate sufficient statistics in a relatively short running time.

Eq. (5.1) clearly shows that for a given value of $\sin^2 2\theta$ the lower bound of Δm^2 is proportional to E_ν/L. The search for neutrino oscillations using atmospheric neutrinos benefits from variations of neutrino paths through the earth in the range of 15 km to 13,000 km. Thus, due to the low energy threshold, NESTOR will be sensitive to an extremely wide range of Δm^2.

Due to limited statistics, most underground experiments can only detect neutrino oscillations by a change in the total neutrino flux, whereas in our case the possible existence of neutrino oscillation can be detected as changes both in the total neutrino flux as well as in the angular distribution, in the latter case independent of absolute normalization.

5.2 Contained Events

In this section, our study is limited to a sample of contained events. By this we define events which have their vertex within the sensitive area of the detector (a cylinder with a radius of 16 m and a length of 220 m). The fluxes of the atmospheric neutrinos used for the present study (as inputs to the Monte Carlo) are those of Butkevich et al. [68] and are shown on figs. 1.3 in chapter 1 and 3.2 in chapter 3 (see also table A.3 in Appendix). In our energy range we have mostly ν_μ's and $\bar{\nu}_\mu$'s and a small fraction of ν_e's because at these energies cosmic ray muons seldom decay in flight. In order to understand the systematics, we have checked that the total number of contained events resulting using different AN flux calculations [68, 104, 105] (see chapter 3) do not differ by more than $\pm 10\%$ and that the angular distributions given by different models do not differ by more than $\pm 6\%$ within the considered energy range.

The integrated number of contained events expected in one NESTOR tower – before any efficiency correction, for a year's running, above the E_ν threshold – is shown in fig. 5.1 as a function of the neutrino energy thresholds.

Figure 5.1: Integrated number of events expected in one NESTOR tower per year from atmospheric ν_μ and ν_e interactions (not corrected for efficiency) above the E_ν threshold.

Now one has to correct for efficiencies – detection and reconstruction efficiency combined – for detecting an interacting neutrino within our sensitive volume as a function of the neutrino energy. These efficiencies were calculated very carefully. A detailed simulation was used based on the GEANT–Čerenkov generation routines which simulate the Čerenkov light from the various particles which are above the Čerenkov threshold and track the light up to our phototubes. The generated light was then used as an input to the NESTOR algorithm [119] to reconstruct the primary tracks which emitted the light. This was the first time that the new Čerenkov light addition to the GEANT code was used and a lot of debugging had to be done. As a further check we compared the standard NESTOR simulation [119], which is a modified version of the DUMAND code, with the GEANT one, and we found out that the former was not reliable for energies less than 10 GeV. So the efficiencies used for the present study are the ones obtained using the GEANT light generation.

The oscillation study was performed as a disappearance experiment by studying the zenith angle dependence of the flux. To be more precise, we look for differences between the number of downcoming ν_μ, which have the smaller oscillation lengths ($\sim$ 15 km), and the number of neutrinos coming from the sides or upcoming. The upcoming ν_μ travel the greatest distance before interacting in the detector ($\sim$ 13000 km, the diameter of the earth). The variation of the path length with zenith angle (ϑ) is shown in fig. 5.2.

Figure 5.2: The path length (in km) of neutrinos as a function of zenith angle.

Due to symmetry in the zenith distribution around the horizontal and vertical directions in the absence of $\nu_\mu \to \nu_e$ oscillations the number of up coming should be equal to the downcoming. Any deviation from this equality will give indications of the ν_μ oscillations, which will be further enhanced by the so called matter effects for the $\nu_\mu \to \nu_e$ oscillations [120]; we are exploring a unique region in L and E_ν where these effects may further enhance the oscillation signal. They are due to the interaction of ν_e with the electrons in matter and are expected to be important only for path lengths of the order of the earth's diameter.

To perform this investigation we divide the range of zenith angles in six bins equally spaced in $\cos\vartheta$ (i.e. in $d\Omega$) as shown in fig. 5.3.

Figure 5.3: Visualization of the six zenith bins used for this study.

The number of ν_μ in each bin has to be compared to the Monte Carlo calculation which includes the theoretical prediction [68] and takes into account the reconstruction efficiency obtained using events with a generated vertex within our sensitive volume. Fig. 5.4 shows the reconstruction efficiencies, for 20° reconstruction accuracy, as a function of the neutrino energy, calculated as described previously, for: (a) the angular bin close to vertical $0° - 48°$, (b) the intermediate angular bin $49° - 71°$, and (c) the angular bin close to horizontal $72° - 90°$.

The total number of ν_μ events expected per year over threshold is 576. We now form the ratio, R, of the number of μ events in the i-th bin to the number of events in the first (close to the vertical) bin. The efficiency is not flat with respect to the zenith, as shown in fig. 5.4. Fig. 5.5 shows the values of the ratio R for the five angular bins (the R for the first bin is equal to 1, by definition, so it is not shown). The crosses represent the value of R in the absence of oscillations and the dotted line shows the ratios expected in the presence of oscillations corresponding to the best fit for the KAMIOKANDE multi-TeV data in terms of $\nu_\mu \to \nu_e$ oscillations ($\sin^2 2\theta = 1.0$ and $\Delta m^2 = 1.8 \times 10^{-2}$ eV^2) [47]. It will be no sensible change in our analysis with the use of the "second KAMIOKANDE solution" ($\sin^2 2\theta = 1.0$, $\Delta m^2 = 1.6 \times 10^{-2}$ eV^2) related to $\nu_\mu \to \nu_\tau$ oscillations.

Figure 5.4: Reconstruction efficiencies as a function of the neutrino energy for the first three angular bins (efficiencies are equal for the symmetrical bins below the horizontal).

The number of cosmic ray muons expected in a year's running for the three relevant angular bins is shown in fig. 5.6, together with the number of expected muons from atmospheric neutrino interactions. One clearly sees from this figure that we need a rejection power of about 10^{-5} in order to distinguish – in at least the first angular bins – the events due to neutrinos generated in the atmosphere from badly reconstructed events induced by cosmic rays. Note that in absence of oscillations the expected numbers will be equal for the symmetrical bins below the horizontal.

In order to study this rejection power, we have generated about 1,000,000 events from single atmospheric muons using the muon energy spectrum at 3000 m calculated in Ref. [121] and the $\cos^{4.8}\vartheta$ angular dependence as we measured it in the 1992 Vityaz cruise [14]. Four events passed our minimal cuts and reconstructed as contained events. This gives us a rejection factor of 4×10^{-6}. In the first angular bin the number of expected downcoming muons to be recorded in our detector from cosmic rays is about 2.6×10^7 per year. If we multiply this number by the above rejection factor we end up with 100 contained events from misreconstructed cosmic rays. The precision of this number is poor and we have to increase the number of the simulated events to reach a precision of 3%. The number of 100 background events has to be compared with about 160 contained events from atmospheric neutrinos. At this stage, we can marginally discriminate, in the first bin, the neutrinos from cosmic rays. There is still work in progress trying to impose further cuts (especially using the Čerenkov light produced by the hadrons of the

interaction in order to get a better vertex determination) and improve our reconstruction algorithm in order to improve the rejection power.

Figure 5.5: The value of R (as explained in the text) vs $\cos\vartheta$. The dotted line is the expected ratio in presence of oscillations corresponding to the best fit of the "KAMIOKA solution" ($\sin^2 2\theta = 1.0$ and $\Delta m^2 = 1.8 \times 10^{-2}$ eV^2).

Taking into account all the above factors we can now proceed and form the allowed/excluded contours in the $(\sin^2 2\theta, \Delta m^2)$ plane for a year's running. These are shown in fig. 1.15 (chapter 1) together with the upper straight line which reproduces the CHORUS/NOMAD sensitivity and with the KAMIOKANDE allowed region. Calculating the error bars of fig. 5.5 and the limits of fig. 1.15 we have taken into account, together with the statistical error for a year's running, a systematic error of 6%. The latter reflects the uncertainty in the e/μ identification power of our apparatus.

In order to investigate our systematics due to different model predictions, we have repeated the same analysis using the AN spectra from Refs. [104, 105]. No significant difference has been observed.

Fig. 1.15 shows clearly that after one year's running we can reach limits for the oscillations down to $\Delta m^2 > 3 \times 10^{-4}$ eV^2 and $\sin^2 2\theta > 0.15$ with a detector which is flux calculation independent and self-normalizable.

Figure 5.6: The expected number of contained atmospheric neutrino events per year (dotted line) in one NESTOR tower, as a function of the angular bin. For comparison, the number of throughgoing cosmic ray muons expected in a year's running is shown (solid line).

Chapter 6

Indirect Detection of Non Baryonic Dark Matter

6.1 Introduction

The comparison between the estimates of the mass density in the universe inferred from the spatial distribution of luminous objects, with the assumption that the ratio of mass to the luminosity is uniform, and by analyzing gravitational effects produced by objects at different scales of distances yields to the conclusion that the major part of matter of the universe is dark [126].

Going to larger and larger scales, more and more mass is inferred. The contribution of galactic halos to the matter density in the universe is $\Omega \approx 0.1$. The density estimated by the study of rich clusters of galaxies is $\Omega \approx 0.1 - 0.3$. The velocity distribution of galaxies at very large scales indicates larger values of density $\Omega \approx 0.3 - 1$.

This latter value is compatible with the critical density $\Omega = 1$ predicted by inflationary theories. On the other hand, the visible star density contributes only at the level of $\Omega \approx 0.01$ which represent only 1–3% of the total density; the remainder is dark.

Dark matter may be nonbaryonic dark particles like axions, massive neutrinos, WIMPs and CHAMPs, or baryonic matter, like dust, gas or massive compact objects.

Primordial nucleosynthesis calculations [127] show that the baryonic component must stay in the range $\Omega = 0.01$ to 0.1. Thus, non baryonic dark matter in the Universe is required to explain larger values of Ω.

The comparison of the rotation velocity of objects in spiral galaxies with what is expected by assuming that the gravitational potential is generated only by the visible objects clearly shows that a large amount of invisible matter is present even at the scale of a galaxy.

With the assumption of a spherical halo in equilibrium in our Galaxy the rotation velocity (V) is given by the equation

$$m\frac{V^2}{R} = G\frac{mM(< R)}{R^2}, \tag{6.1}$$

where G is the gravitational constant, m is the mass of the rotating object and $M(< R)$ is the total mass inside a sphere of radius R. Assuming a constant velocity $V = 220$ km/s,

the equation (6.1) gives

$$M(< R) = \frac{RV^2}{G} \simeq 10^{11} M_\odot \left(\frac{R}{10\text{kpc}} \right).$$

The matter density is, therefore, proportional to R^{-2} while the visible matter shows an exponential behaviour.

Since the galactic halos contribution ($\Omega \approx 0.1$) to the matter density in the Universe is equal to the upper bound of the baryonic component and larger than the visible stars density ($\Omega \approx 0.01$), it is possible that both baryonic and non baryonic dark matter are present in the halo of the Milky Way. This is the reason why during the last few years an intense activity is developing in order to inspect both fields.

For the baryonic dark matter search, a direct method consists in trying to observe dark astrophysical objects. As an example one can mention the search of massive halo objects (MHO) like aborted stars (brown dwarfs for instance). Few tens of candidates have been observed but the data are too scarce. A systematic search of such objects must be undertaken to establish an unbiased spatial distribution.

An indirect method consists in detecting the influence of the presence of MHOs on the light curves of visible stars (microlensing). Up to now several candidates have been reported by three experiments [128, 129, 130] which are monitoring the luminosity of stars in the Large Magellanic Cloud (LMC) and in the galactic bulge.

The global sensitivity for objects in the bulge with a total of 1.6×10^6 monitored stars is lower than for objects in the LMC, where a total of 1.3×10^7 stars were monitored. Nevertheless, 14 events have been reported for stars in the bulge and only 5 for stars in the LMC. This could be an indication that these events are mainly due to object in the disk (disk dark matter or faint stars).

An estimate of the expected events has been done by the EROS collaboration [131]. The two events observed by this experiment is between 15% and 45% of the expected value if the dark halo were entirely composed of massive compact dark objects with masses above $0.02\, M_\odot$. Since no event has been observed with time scales corresponding to masses between $10^{-7} M_\odot$ and $0.02 M_\odot$, it is excluded at 90% of confidence level that the dark halo is entirely composed of MHOs with masses in this range. It is also excluded that such objects could account for as much as 20 to 40% of the halo, depending on the mass function hypotheses [132].

In the case of non baryonic dark matter, a direct method consists in detecting nuclear recoils produced by these particles in low-background low-threshold counters. An intense activity has been developed in the R & D for this approach. The results of these studies are encouraging but progress are needed in lowering the background counting rate and the energy threshold and in increasing the total detector mass running in stable conditions.

An indirect method consists in detecting neutrinos produced by their annihilation in the core of astrophysical objects. Neutrino telescopes which are sensitive to neutrinos with energies above 5–10 GeV are particularly well suited for this purpose.

6.2 The Neutralino

In the MSSM the supersymmetric partners of the neutral bosons are four neutralinos: the two partners of the neutral SU(2) and U(1) gauge bosons (gauginos), $\tilde{W}_3$ and $\tilde{B}$, and the two partners of the neutral Higgs particles (higgsinos), $\tilde{H}_1^0$ and $\tilde{H}_2^0$. Their 4×4 mass matrix $\mathcal{M}$ depends on the $\tilde{B}$ and $\tilde{W}_3$ masses, M_1 and M_2, on the parameter μ describing the mixing between the two Higgs superfields in the superpotential, and on the ratio of the two vacuum expectation values $\langle H_1^0 \rangle = v_1$ and $\langle H_2^0 \rangle = v_2$:

$$\mathcal{M} = \begin{pmatrix} M_1 & 0 & -M_Z \cos\beta \sin\theta_W & M_Z \sin\beta \sin\theta_W \\ 0 & M_2 & M_Z \cos\beta \cos\theta_W & -M_Z \sin\beta \cos\theta_W \\ -M_Z \cos\beta \sin\theta_W & M_Z \cos\beta \cos\theta_W & 0 & -\mu \\ M_Z \sin\beta \sin\theta_W & -M_Z \sin\beta \cos\theta_W & -\mu & 0 \end{pmatrix},$$

where the β parameter is given by $\tan\beta = v_2/v_1$, M_Z is the Z mass and θ_W is the Weinberg angle. With the assumption of the existence of a grand unification the $\tilde{B}$ mass results $M_1 = \frac{5}{3} M_2 \tan^2\theta_W$. The lightest neutralino is a linear combination of photino ($\tilde{\gamma}$), zino ($\tilde{Z}$) and higgsinos ($\tilde{H}_{1,2}^0$):

$$\chi = a_1\tilde{\gamma} + a_2\tilde{Z} + a_3\tilde{H}_1^0 + a_4\tilde{H}_2^0, \tag{6.2}$$

where the a_i depend only on M_2, μ and $\tan\beta$; $\tilde{\gamma}$ and $\tilde{Z}$ are linear combinations of gauginos $\tilde{B}$ and $\tilde{W}_3$:

$$\begin{aligned} \tilde{\gamma} &= \tilde{B}\cos\theta_W + \tilde{W}_3 \sin\theta_W, \\ \tilde{Z} &= -\tilde{B}\sin\theta_W + \tilde{W}_3 \cos\theta_W. \end{aligned}$$

Note that in the framework of this model the gaugino fractional weight $P = a_1^2 + a_2^2$ plays an important role.

In the MSSM there are three neutral Higgs bosons, but, due to relationships depending on radiative effects, they may be described by a single mass parameter m_h. Although many parameters are present in the theory ($\tan\beta$, M_2, μ, P, m_h, and the masses of the top-quark and of the superpartners of the quarks and leptons) they are not entirely unconstrained. For instance the $\tan\beta$ value is constrained to be $1 < \tan\beta < m_t/m_b \simeq 25$ and there is a one-to-one correspondence between (M_2, μ) and (P, m_χ) at fixed $\tan\beta$.

6.3 The Neutrino Induced Flux

Neutrino telescopes would be sensitive to neutrinos produced in the annihilation of neutralinos captured in the core of astrophysical objects like 'the sun and the earth.

The neutralinos move in the halo of the Galaxy with velocities of few hundreds of km/s and loose energy by elastic scattering on the nuclei forming the matter of the sun or of the earth when they cross them. The escape velocity is 11.2 km/s at the earth surface and 617.5 km/s at the sun surface. Since neutralinos have typical velocities of ≈ 300 km/s they are captured by the sun quite efficiently, while the probability that they are captured by the earth is smaller unless their mass closely matches the mass of an element abundant

in the earth. Due to the energy loss the neutralinos accumulate to the core and, then annihilate by pairs. The subsequent decay of particles produced in the various final states would generate a flux of high-energy neutrinos.

A description of the mechanism has been done by many authors [133, 134, 135]. The differential equation governing the time evolution of the number N of neutralinos in a macroscopic body is

$$\dot{N} = C - C_A N^2, \tag{6.3}$$

where C is the capture rate of the relic neutralinos given by [136, 137]

$$C = \frac{\varrho_\chi}{v_\chi} \sum_i \frac{\sigma_i}{m_\chi m_i} M_i \langle v_{\rm esc}^2 \rangle_i X_i, \tag{6.4}$$

where ϱ_χ is the neutralino local density, v_χ is the neutralino mean velocity, the sum runs on all the nuclei i of mass m_i, σ_i is the cross section of the neutralino elastic scattering on the nucleus i, M_i is the total mass of the element i in the macroscopic body, $\langle v_{\rm esc}^2 \rangle_i$ is the square escape velocity averaged over the distribution of the element i, and X_i is a factor which takes into account of kinematical properties occurring in the neutralino-nucleus interactions. The quantity C_A in (6.3) is [136, 138]

$$C_A = \langle \sigma v \rangle \left(\frac{m_\chi \varrho}{3 m_{\rm Pl}^2 T} \right)^{3/2},$$

where T and ϱ are the central temperature and the central density of the celestial body and $m_{\rm Pl}$ is the Plank mass.

The time evolution of N is obtained by solving the equation (6.3)

$$N(t) = C \tau_A \tanh\left(\frac{t}{\tau_A} \right)$$

with $\tau_A = (C C_A)^{-1/2}$. The annihilation rate of neutralinos $\Gamma_A = C_A N^2/2$ is thus

$$\Gamma_A = \frac{C}{2} \tanh^2\left(\frac{t}{\tau_A} \right). \tag{6.5}$$

This formula shows that the annihilation rate is an increasing function of time with an asymptotic value $C/2$ and a time scale τ_A, which depends on the neutralino mass. The equilibrium between annihilation and capture ($\Gamma_A \sim C/2$) is reached when $t > \tau_A$.

The value of C_A is higher by a factor $\simeq 3000$ for the earth than for the sun. On the contrary the capture rate C given in (6.4) is higher for the sun than for the earth by a factor of at least 10^9 [134]. This means that the value of τ_A for the sun is always lower than for the earth. Calculations performed by Bottino et al. [139] show that due to the age of the solar system ($t_\odot = 4.5 \times 10^9\,{\rm yr}$) the equilibrium between the capture and the annihilation is reached for the whole range of m_χ, whereas for the earth the equilibrium conditions depend on the values of the parameters and a substantial suppression in Γ_A occurs for values of m_χ above 100 GeV.

Moreover, while the sun may be considered as a point source, the earth has a finite angular extension. In this case one has to define a neutralino spatial density which depends on the position $\mathbf{r}$ referred to the earth center, which is given by [139]

$$n(r) \propto \exp[\beta m_\chi (r/R_\oplus)^2]$$

with $\beta = 1.87$ GeV^{-1} and $r = |\mathbf{r}|$. The neutralino spatial density has, thus, a gaussian behaviour as a function of the distance to the center of the earth. The dispersion of this distribution is $\sigma = R_\oplus/\sqrt{2\beta m_\chi}$. Therefore, the effective extension of the source is a decreasing function of the neutralino mass. The solid angle subtended by the source has an angular half-aperture is 10° for $m_\chi = 10$ GeV, 3° for $m_\chi = 100$ GeV and 1° for $m_\chi = 1$ TeV.

The differential flux of neutrinos produced by the annihilation of neutralinos is

$$\frac{d\phi_\nu}{dE_\nu} = \frac{\Gamma_A}{4\pi R^2} \sum_f B_f \left[\frac{dN}{dE}\right]_f .$$

where R is the distance of the source, the sum runs over all annihilation channels f, and B_f is the branching ratio for the annihilation into the final state f.

6.4 The Sensitivity of a Generic Detector

Neutrinos are detected either using contained events where the charged-current interaction νN produces a lepton in the detector or using upward-going muons produced by $\nu_\mu N$ charged-current interactions in the medium surrounding the detector. The cross section for a charged-current interaction is proportional to the neutrino energy and the range of a muon is proportional to the muon energy. The rate for contained events is, thus, proportional to the neutrino energy and the rate for neutrino-induced throughgoing muons is proportional to the square of the neutrino energy. Therefore at high energies the detection of neutrinos results to be more efficient by using throughgoing muons than by using contained events. This is the reason why we will concentrate to this method of detection.

Monte Carlo simulations are needed to calculate the sensitivity of a given detector to neutrinos produced in the annihilation of neutralinos in the earth or in the sun. The determination of neutrino spectra involves hadronization of the annihilation products, interaction of the particles in the resulting cascades with the medium in the macroscopic body, production of neutrinos by the decay of hadrons and interaction of neutrinos with the medium as they propagate from the production point to the surface of the earth or sun. The muon spectra at the detector is derived by taking into account the geometrical correction due to the solid angle subtended by the neutrino source, the muon production in the νN interaction in the medium surrounding the detector, and the energy losses and angular spread due to the interactions of the muon in the medium during its propagation from the production point to the detector entry.

Comparisons of the predicted muon flux with observations of detectors IMB [140] and KAMIOKANDE [135] have been performed [134, 135]. Only models where the neutralino is a mixed gaugino-Higgsino state and the mass of the lightest Higgs boson is near the current limits imposed by LEP [141] are inconsistent with the upper limits on the muon flux.

In order to quantify how the exploration of neutralinos may be improved with the next generation neutrino detectors the minimal exposure At (the product of the detector area by the exposure time) necessary to detect a neutralino signal has been calculated [139] as

a function of the neutralino mass for different values of the gaugino fractional weight P. In this calculation the Higgs mass m_h has been set to the value of 50 GeV, the sfermion masses have been set at the value $m_{\tilde{f}} = 1.2 m_\chi$ when $m_\chi > 45$ GeV and $m_{\tilde{f}} = 45$ GeV otherwise, only the stop quark mass is assigned a larger value of 1 TeV. The top mass is fixed at $m_t = 170$ GeV. For $\tan\beta$ the value $\tan\beta = 8$ has been used.

Fig. 6.1 shows the comparison of the expected flux of muons with energy above 10 GeV at the entry of a generic detector induced by the annihilation of neutralinos in the earth's core for different hypotheses of mass of the neutralino. In these distributions ϑ_z is the angle between the muon direction and the zenith direction (the nadir angle).

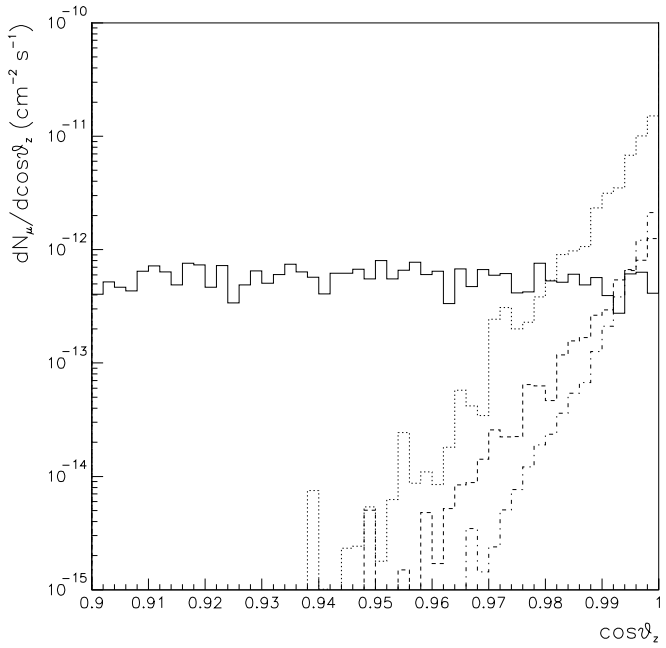

Figure 6.1: Muon angular distributions. The solid histogram is the angular distribution expected for the background of atmospheric neutrinos. The dashed, dotted and dash-dotted lines are respectively the expected distributions for muon induced by the interactions of neutrinos produced by the annihilations of neutralinos with $m_\chi = 40, 60$ and 120 GeV in the earth's core by assuming $P = 0.5$.

This figure clearly shows that the signal would be peaked around $\cos\vartheta_z = 1$, while the background of muons produced by the interactions of neutrinos generated in cosmic ray cascades in the atmosphere have a flat distribution. The muon flux is maximum for $m_\chi \simeq 60$ GeV because the presence of iron in the earth's core makes it particularly efficient in capturing neutralinos with a mass around this value.

Due to the neutralino spatial distribution, higher the mass more the angular distribution of muons is peaked. This means that the angular cut can be optimized depending on the neutralino mass.

Fig. 6.2 shows the differential spectra of neutrinos produced by the neutralino annihilations with different hypotheses for the neutralino mass.

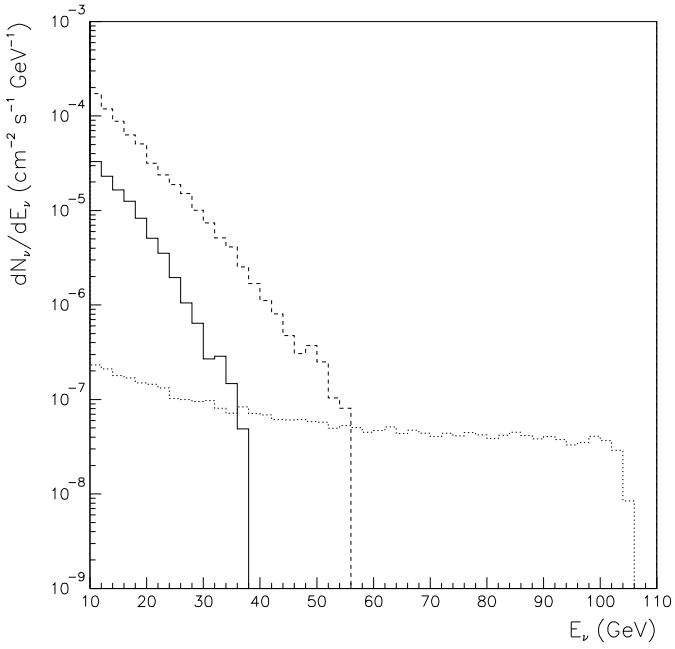

Figure 6.2: Differential energy spectra of neutrinos from neutralino annihilations in the earth. The solid, dashed and dotted lines are respectively for $m_\chi = 40, 60$ and 120 GeV ($P = 0.5$).

The muon flux at the detector depends on the neutrino energy spectrum, the differential $\nu_\mu N$ charged current cross section, and the energy losses and multiple scattering of muons in the medium surrounding the detector. Starting with the neutrino spectra depicted in fig. 6.2 the muon fluxes are calculated by taking into account of the mechanisms enumerated above.

Fig. 6.3 shows the differential energy spectra of muons in a cone with an half-aperture of 10° around the vertical direction produced by the neutrinos. These distributions are compared to the distribution due to the atmospheric neutrinos background in the same solid angle.

Due to large variations of the S/B ratio the detector sensitivity strongly depends on the neutralino mass hypothesis. The sensitivity may be defined as the minimal exposure $(At)_{\min}$ necessary to see a 4σ effect (with a signal of at least 4 events). This quantity has been estimated in ref. [139] for neutralino annihilations in the earth's core. The calculation has been performed by using an angular cut of 30° around the vertical direction. The variations of $(At)_{\min}$ as a function of the neutralino mass are shown in fig. 6.4a for three values of the gaugino fractional weight $P = 0.1, 0.5$ and 0.9. The neutralino local density ϱ_χ is assumed to be equal to the local value of the total dark matter density ϱ_l when the relic abundance $\Omega_\chi h^2$ is at the level of an $(\Omega h^2)_{\min}$ consistent with ϱ_l. When

$\Omega_\chi h^2 < (\Omega h^2)_{\rm min}$ the value of ϱ_χ has been rescaled by the factor $\Omega_\chi h^2/(\Omega h^2)_{\rm min}$. The very pronounced peaks in the plot of fig. 6.4a are due to the s–poles in the $\chi - \chi$ annihilation cross section which reduces the value of $\Omega_\chi h^2$.

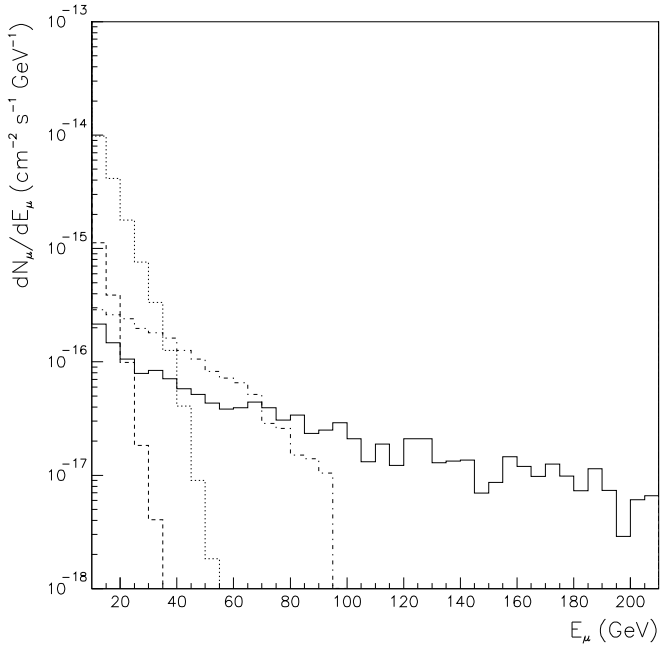

Figure 6.3: Differential spectra of muons propagating in a cone with an half-aperture of 10° around the vertical direction for the hypothesis of neutralino annihilations in the earth. The solid histogram is the differential spectrum expected for the background of atmospheric neutrinos. The dashed, dotted and dash-dotted lines are respectively the expected spectra of muons induced by the interactions of neutrinos produced by the annihilations of neutralinos with $m_\chi = 40, 60$ and 120 GeV in the earth's core ($P = 0.5$).

A very low value of $(At)_{\rm min}$ is necessary ($\simeq 50\,{\rm m}^2$ yr) for a neutralino mass value around the iron nucleus mass, but exposures above $10^4\,{\rm m}^2$ yr are necessary to detect masses above 100 GeV. However, due to the different features of the angular distributions for the signal (illustrated for instance in fig. 6.1), the necessary exposure may be optimized by choosing the angular window which maximize the S/B ratio depending of the neutralino mass hypothesis. This procedure yields to new values of the necessary exposure $(At)_{\rm opt}$ which is displayed in fig. 6.4b. This method would improve the minimal sensitivity required to observe the signal for high neutralino masses.

The minimal exposure necessary for neutralino annihilations in the sun has been also calculated. Fig. 6.5 shows the variations of ϵAt as a function of the neutralino mass where ϵ is the on-source duty factor.

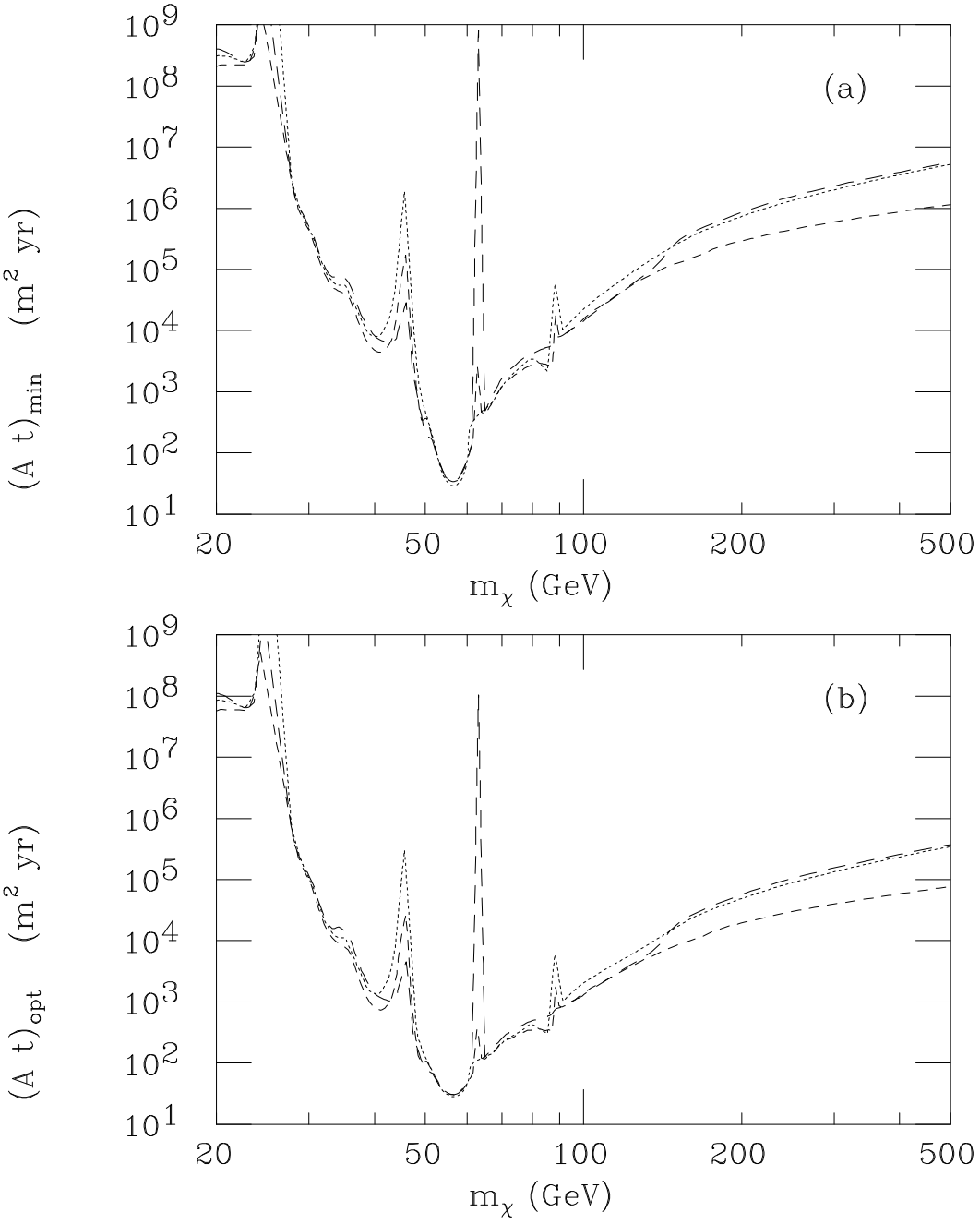

Figure 6.4: Exposure necessary to have a 4σ effect as a function of neutralino mass m_χ. The figure refers to a signal coming from the earth. The three representative neutralino compositions are $P = 0.1$ (dotted line), 0.5 (short-dashed line), 0.9 (long-dashed line). In figure (a) $At_{\rm min}$ is displayed keeping the half-aperture angle of the detector fixed at 30° from the center of the earth. Figure (b) displays the exposure $At_{\rm opt}$ obtained by optimizing the cut depending on the neutralino mass value.

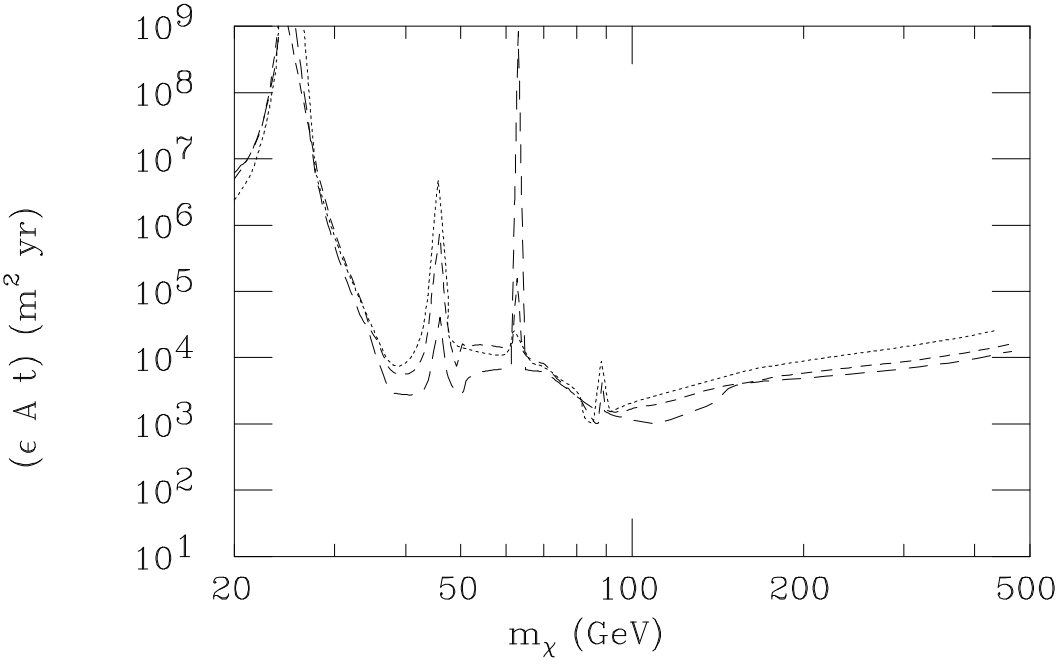

Figure 6.5: Effective exposure (ϵAt) necessary to have a 4σ effect as a function of neutralino mass m_χ. The on-source duty factor is represented by ϵ. The figure refers to a signal coming from the sun. The three representative neutralino compositions are $P =$ 0.1 (dotted line), 0.5 (short-dashed line), 0.9 (long-dashed line). The half-aperture of the detector is fixed at 5° from the sun.

With the exposures that can be reached with the detectors operating today ($\simeq 10^3\,\mathrm{m}^2$ yr) only neutralino annihilations in the earth can be explored in the mass range 50–100 GeV. The exploration about neutralinos using the flux from the sun requires at least $10^4\,\mathrm{m}^2$ yr. The next generation detectors would provide exposures larger than $10^5\,\mathrm{m}^2$ yr allowing the simultaneous exploration of neutralinos using both the neutrino fluxes from the earth's core and from the sun in the range 35 GeV $< m_\chi <$ 500 GeV.

The predictions given above depend sensitively on several free parameters. For instance the expected signals increase with the value of $\tan\beta$. The signal from the Sun may be enhanced or suppressed by an order of magnitude by varying this value in the range 2–20. Moreover, the earth signal is roughly proportional to m_h^{-4}. The choices made in ref. [139] for the Higgs and sfermion masses correspond to their present lower bounds. This has been done in order to quote what is the minimum exposure necessary to be sensitive to the earth and sun signals and to describe how the exploration of neutralinos may be improved by expanding the size of the experimental apparatus.

6.5 The Sensitivity of One NESTOR Tower

The effective exposures given in figs. 6.4 and 6.5 are the product of the sensitive area by the exposure time. If the sensitive area is known the exposure time necessary to detect a signal can be easily derived.

In the case of one NESTOR tower the calculation of the sensitive area $A_{\rm eff}$ has been performed by generating muons in any direction, at different energies and passing at different distances from the detector:

$$A_{\rm eff} = \int_S \eta dS.$$

where η is the efficiency to reconstruct the muon direction within an angular cut with respect to the generated direction; the integration is extended to a surface S perpendicular to the generated muon direction and very large when compared to the transmission length for the Čerenkov light. The sensitive area $A_{\rm eff}$ is a function of the direction and of the energy of the muon and depends on the angular cut value.

For each value of the neutralino mass the energy spectrum of the neutrinos produced in the annihilation has been obtained. This allowed us to calculate the mean value of $A_{\rm eff}$, averaged on the neutrino direction, with a cut of 5° on the angle between the generated and the reconstructed directions. This quantity is plotted in fig. 6.6 as a function of the neutralino mass.

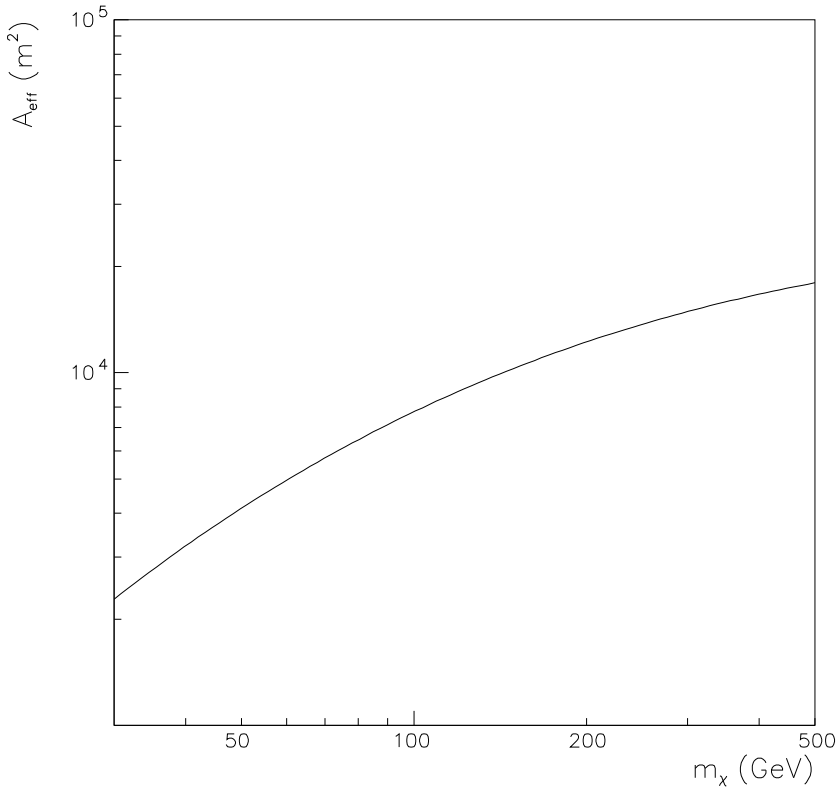

Figure 6.6: Mean sensitive area $A_{\rm eff}$ for one NESTOR tower, averaged on the neutrino direction, with a cut of 5° on the angle between the generated and the reconstructed directions, as function of the neutralino mass.

The exposure time necessary to detect a 4σ effect from the earth's core and from the sun with one NESTOR tower has been estimated by computing the ratio between the values of the exposures shown in figs. 6.4 and 6.5 by the values of $A_{\rm eff}$ shown in fig. 6.6.

The on-source duty factor has been taken equal to 0.5 for the calculation using the sun as a source of neutrinos. This yields to the minimal exposure times shown in fig. 6.7 as a function of the neutralino mass m_χ. This figure shows that in one year of running time one NESTOR tower could detect neutralinos with masses in the range 50–140 GeV from the earth's core and with masses in the range 80–200 GeV from the sun.

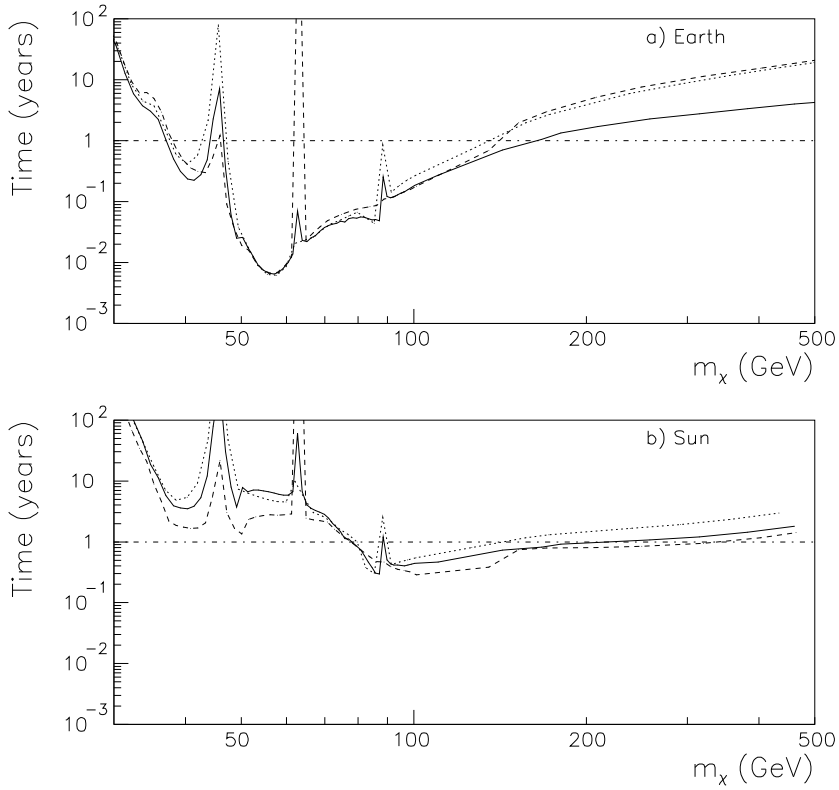

Figure 6.7: Minimal exposure time necessary to detect a 4σ effect with one NESTOR tower as described in the text. Figure (a) refers to a signal coming from the earth's core and figure (b) is for neutrinos from the sun. The three neutralino compositions are $P = 0.1$ (dotted line), 0.5 (solid line), 0.9 (dashed line).

These prediction depend strongly on the choice of the parameters of the model as discussed above. Nevertheless, fig. 6.7 shows how the limits of the detectable neutralino mass ranges are sensitive to the exposure time especially for the neutralino annihilations in the sun. With the choice of the parameters made in ref. [139], fig. 6.7 shows also that an exposure larger by a factor of 10, for instance, would allow to explore the whole interesting mass range.

Chapter 7

A Long-Base Line Neutrino Beam for Gran-Sasso/NESTOR

7.1 Introduction

The probability for two flavor neutrino oscillations is given by Eq. (5.1). As a rule of thumb the minimum statistical sensitivities for the mixing angle θ and for the difference of the mass squares Δm^2 are given approximatively by the following formulae [142]:

$$P_{\min} = \sin^2 2\theta_{\min} \sim \frac{\sqrt{N}}{N}, \tag{7.1}$$

$$\Delta m^2_{\min} \sim \sqrt{P_{\min}} \left(\frac{E_\nu}{1.27L} \right) \text{ eV}^2, \tag{7.2}$$

where N is the number of detected events, L is the neutrino propagation length (in km) and E_ν is the neutrino energy (in GeV).

Thus, in order to maximize sensitivity, it is necessary to have the longest possible base-line and lowest threshold energy whilst detecting sufficient neutrino events for statistical significance.

As noted above (see chapters 1, 3 and 5), results of KAMIOKANDE, IMB and SOUDAN 2 experiments suggest that perhaps as much as 40% of atmospheric ν_μ neutrinos in the energy range from 0.2 to 1.5 GeV have oscillated to some other type of neutrinos [46, 48, 49]. However, Fréjus and NUSEX experiments do not record any effect [51, 50, 52]. The recent "multi-GeV" studies by KAMIOKA [47], have confirmed their previous "sub-GeV" result [46], and have even shown a zenithal distribution of the ratio ν_e/ν_μ consistent with $\nu_\mu \to \nu_e$ or $\nu_\mu \to \nu_\tau$ oscillations.

Two accelerator experiments, CHORUS [143] and NOMAD [144], looking for ν_τ appearance at larger Δm^2 in the present CERN wide-band neutrino beam are currently taking data; first results are expected in 1995-96. Clearly one would like to continue with controlled beam experiments because they have the following advantages over the atmospheric data:

- Initial flavor composition is well known (typically $\nu_e/\nu_\mu \sim 0.01$).

- Control of the beam polarity. One can switch between ν and $\overline{\nu}$ to study matter enhanced oscillations (MSW effect [145]).
- Control of the energy. One can typically obtain beam energy dispersions σ_E of about 5 GeV.
- One may specify the direction cosines and time of arrival of the neutrino, improving efficiency and reducing backgrounds to almost zero.
- Higher statistics, giving sensitivity to lower mixing angles.
- Control of the beam energy which provides a way to differentiate between oscillations from ν_μ to either ν_e or ν_τ.

7.2 General Design Considerations

Proton accelerators produce essentially μ neutrino beams from the decay of pions and kaons, derived when an extracted beam strikes an external target; these "parent" particles are focused towards the detector and left to decay in an evacuated tunnel to produce muons and ν_μ. The muons and remaining hadrons are stopped by shielding at the end of the decay tunnel leaving only the neutrinos to continue to the detector. A smaller fraction of ν_e are also produced from kaon decays and from secondary decays of muons, giving an unwanted background in $\nu_\mu \rightarrow \nu_e$ searches.

The ratio of pions to kaons produced from protons interacting in the target is roughly 10:1; the decay length for pions is about 56 m/GeV and for kaons around 7.5 m/GeV. The average neutrino energy produced by pion decay is some 43% of the pion energy whereas for kaons the neutrino has, on average, some 95% of the parent kaon energy. Thus for a decay path of some 600 metres only 40% of the 23 GeV pions will have decayed to give neutrinos around 10 GeV whereas essentially all kaons of 23 GeV will have decayed, to give neutrinos of 22 GeV. This leads essentially to two superimposed ν_μ energy spectra, dominated by the pion generated contribution at lower energies with a smaller kaon contribution at higher energy.

In order to obtain acceptable neutrino event rates at a detector many hundreds of kilometres from the source it is essential to have an efficient target in which most of the incident protons interact but which, at the same time, gives minimal absorption and scattering to the hadrons produced. The focusing system must have a large acceptance for the parent pions and kaons in the required energy range and produce as near a parallel beam as possible; even so, the flux at the detector is largely dominated by the decay kinematics of neutrino production.

This study concentrates on co-axial magnetic lenses (so called horns and reflectors) since these give substantially higher acceptance at low energies than it can usually be achieved with quadrupole lenses; they also give the particle sign selection which in-line quadrupoles do not. However some simulations of quadrupole triplet focusing are made and a possible application is considered. Narrow energy band beams have not been studied since the reduction in flux due to the momentum selection seems unacceptable. Other

focusing systems such as plasma or lithium lenses may have some advantages over "conventional" horns but usually have limited acceptance and are not known to have the same level of reliability in operation. A prime consideration in the design of a neutrino beam is the very high levels of induced radioactivity around the target station and focusing system; to ensure reliability and minimize personnel exposure it is essential to avoid all organic compounds and materials giving rise to long half-life decay products or contamination.

Interest in a long baseline neutrino beam from CERN has been stimulated by three factors:

- as part of the LHC project at CERN, new transfer lines are required to bring fast extracted protons from the SPS to the LHC; the detailed layout is still under study but it has been shown [146] that it would be possible to derive a neutrino beam from the TI 87 line linking SPS-LSS4 to the LHC/LEP ring near point 8;
- during the period of LHC installation it may be possible to run the SPS machine in an essentially dedicated mode with substantially shorter duty cycles; later, during LHC operation, beam would be available outside the LHC filling periods;
- two substantial neutrino detector facilities exist or are under development which lie in the general direction of such a beam:
  - the Gran Sasso underground laboratory at 731 km,
  - the deep underwater neutrino laboratory NESTOR in the Mediterranean at 1676 km.

Table 7.1 [147] gives the absolute coordinates of CERN and these detector sites showing that the directions from CERN are within 1.68 degrees in azimuth and 5.24 degrees in declination. The possibility of providing neutrino beams to each of these facilities using common or shared beam equipment is clearly attractive; the additional cost of providing a double facility is principally in the civil engineering cost of an enlarged section of the transfer line and the two decay tunnels.

Place	λ	ϕ	A_z	δ	Distance
CERN	6.07320	46.2442	–	–	–
Gran Sasso	13.5744	42.4525	122.5020	3.283	731 km
NESTOR	21.3500	36.3500	124.1775	8.526	1676 km

Table 7.1: Absolute equatorial coordinates (λ, ϕ) and relative azimuth and declination with respect to CERN beam TI48 (A_z,δ) of Gran Sasso and NESTOR (the angles are in degrees).

It is also worth noting that possibilities of a long baseline beam and detector are under active study in the USA and a letter of intent by the MINOS Collaboration was submitted in January leading to a formal proposal in June 1995. The most probable layout seems to be a beam from the Fermilab Main Injector (120 GeV protons) to the SOUDAN site at 732 km distance [148].

We report here the results for a NESTOR detector having an area of 40×240 m^2 situated at 1676 km.

7.3 Beam Simulation and Design

The version 3.21 of GEANT [149] has been used to simulate the beam line; realistic values for material thicknesses, magnetic field strengths, etc. The only exception to this is in the comparison of production models where so called "perfect focusing" (P.F.) has been used.

The proton beam is assumed to have a normal intensity distribution with a RMS of 0.5 mm where it hints a beryllium target of 3 mm diameter; different proton energies and target configurations are examined. To reduce statistical fluctuations, half a million proton interactions in the target have been simulated. The products of the hadronic interactions are tracked through the optical system, focused and allowed to decay. Secondary interactions, absorption and multiple scattering in all materials are included. Each decay occurring within the decay tunnel generates 1000 neutrinos which are projected to the detector plane; fluxes and event rates in the detectors are weighted accordingly and there is no evidence that this introduces serious systematic errors*. The tables and plots for neutrino flux are renormalized to 10^{13} protons on target, and event rate per kiloton to 10^{19} protons on target, which roughly corresponds to a good years running at current duty cycles.

A major systematic uncertainty in estimating neutrino fluxes comes from the model of hadronic interactions used to obtain the production spectra. This is particularly true at energies which are low compared to the incident proton energy where the production is dominated by cascade processes. Three production models have been compared with P.F. with a fixed angular acceptance of ± 1.5 radian:

(i) a thermodynamic model using parameters from Atherton ($E_p > 200$ GeV) [150] and Barton ($E_p < 200$ GeV) [151],

(ii) GHEISHA [152], and

(iii) FLUKA [153].

Recent versions of FLUKA are thought to reproduce accurately the low energy part of the production spectrum and detailed comparisons have recently been made with existing experimental data [154]. It is the principal model used for LHC hadronic simulations.

The results of this comparison, for rates at Gran Sasso distances and P.F. are shown in table 7.2 and fig. 7.1. The hadronic secondaries are forced to be exactly parallel at the entry of a 3 meter radius decay tunnel starting 2 meters behind the target center. The target used for this comparison was a diluted target consisting of 6 beryllium rods 10 cm long and 1.5 mm radius separated by 5 cm gaps. The target geometry used is different from the subsequent configuration. So table 7.2 should be used only for a comparison between hadronization models.

The thermodynamic model with Atherton/Barton parameters gives consistently 50% less flux and number of events compared to FLUKA, and the spectrum is much harder. This is to be expected since it is known that fits to experimental data below 25% of the

*Runs with 100 neutrinos per hadron decay give the same results within statistics.

proton energy are poor with these parameters. The energy spectrum given by GHEISHA oscillates below 60 GeV and above 100 GeV and it is harder than FLUKA. This results in an overall higher flux and event rate by 25–30%. These effects can be seen in both the table 7.2 and fig. 7.1.

E_p (GeV)	Atherton/Barton	FLUKA	GHEISHA
	ν fluxes/10^{13} p/m^2		
80	1.9×10^4	2.7×10^4	2.4×10^4
160	5.1×10^4	7.5×10^4	7.9×10^4
400	1.6×10^5	2.4×10^5	2.8×10^5
	Events/10^{19} p/kt		
80	81	120	110
160	387	568	709
400	2270	3215	4260
	$\langle E_\nu^{-2} \rangle^{-1/2}$ (GeV)		
80	7.5	6.7	6.2
160	12.8	10.9	14.0
400	24.9	18.1	19.7

Table 7.2: Neutrino fluxes, event rates (assuming 100% detection efficiency) and neutrino mean energy with P.F. and fixed acceptance for three hadronic production models and a detector of cross sectional area 20×20 m^2 at Gran Sasso.

Because of limited experimental production data at energies below 25% of the incident proton energy, it is not possible to conclude that any one production model is better than any other. In the energy range of interest, there is some evidence that FLUKA is the best model and it has therefore been used for the remainder of this study in order to make comparisons between different optical systems and layouts; however the uncertainty in quoted fluxes and event rates must be considered to be of the order of 20–25%.

Simulations of the beam line take as origin the approximate center of production in an extended target (Z_0) and this is used as the focal point for the focusing system. The elements are:

- A diluted cylindrical beryllium target 80 cm to 120 cm long and 1.5 mm radius. See table 7.3 for the exact configurations.

Configuration	Z position (cm)	segments	length (cm)	radius (mm)	gap (cm)
80, 120, 160 GeV	-45	8	10	1.5	5
450 GeV	-45	12	10	1.5	5
P.F.	-40	1	120	1.5	–

Table 7.3: Target configurations.

- Different configurations of magnetic horns and reflectors. The horn is a co-axial lens with its inner conductor made of 8 conical pieces. We have used 3 different horns designed to focus tracks of 15, 20, and 40 GeV/c momentum. The reflector is also a co-axial lens, designed to allow the well focused parent particles from the

horn to pass undisturbed but to correct the focusing of under- and over-focused hadrons. The inner conductor consists of 4 conical sub-elements. We have used 4 different reflectors which, when combined with the appropriate horn, focus tracks of 20, 25, 40, and 70 GeV/c momentum. See table 7.4 for a list of their geometrical characteristics.

Configuration	Z position (cm)	inner radii (cm)	length (cm)
H15 (15 GeV)	+60	0.35–3.2	290
H20 (20 GeV)	+60	0.35–2.7	290
H40 (40 GeV)	+60	0.35–2.5	290
R20 (20 GeV)	+1050	5.5–11.0	600
R25 (25 GeV)	+1050	5.0–13.8	600
R40 (40 GeV)	+1050	5.2–11.0	600
R70 (70 GeV)	+1050	4.0– 8.6	600

Table 7.4: Horn (H) and reflector (R) configurations.

- Different quadruple triplets. Triplets of focusing-defocusing-focusing quadrupoles effectively approach a thin lens optical element. We have simulated 2 such configurations: one focusing 20 GeV and one 40 GeV tracks. These triplets are not charge selective, both negative and positive charged particles are focused. They have, in general, a smaller acceptance than the horn+reflector systems but give no absorption in the effective aperture. Better focusing is obtained by lowering the field of the central quadrupole. See table 7.5 for a list of their geometric characteristics.

Configuration	Z pos. (cm)	aperture (cm)	lengths (cm)	Tip Fields (T)	drift gap (cm)
Q20 (20 GeV)	49	30	180, 360, 180	1.5, 1.449, 1.5	49
Q40 (40 GeV)	53	20	207, 414, 207	1.5, 1.452, 1.5	495

Table 7.5: Quadrupole configurations.

- Finally the decay tunnel is assumed to be under vacuum, and to have a length of 1000 m and a radius of 2 m. In front of the decay tunnel there is a 2 mm thick titanium window.

Extremely useful debugging and optimization tools used extensively for the above designs were the graphics capabilities of GEANT++. Using ray tracing techniques, an example of which is seen in figures 7.2 and 7.3, the behaviour of the focusing elements could be studied, before launching the time-consuming long runs for flux and event rate estimations. Fig. 7.4 shows clearly the focusing and defocusing effect of the combination 20 GeV horn and 40 GeV reflector on positive and negative parents.

7.4 Fluxes, Event Rates and Backgrounds

7.4.1 Flux and Event Rates for Different Focusing Energies

The energy of the incident protons determines the overall envelope of the neutrino spectrum and has the greatest influence on the intensity of neutrinos produced at all energies. The function of the focusing system is to select a particular energy range from the overall production spectrum and deliver these to the detector as efficiently as possible.

The fluxes and event rates of muon neutrinos are given in table 7.6 for a number of incident proton energies and various focusing systems, together with the neutrino average energy and the fractional background of electron neutrinos, for the NESTOR detector*

E_p (GeV)	P.F.	H20	H20R40	H20R20	H15	H15R25
	ν fluxes ($10^3\nu/10^{13}p/\mathrm{m}^2$)					
80	6.7	1.1	1.7	1.7	1.1	1.7
120	11.0	2.1	3.1	2.8	1.8	2.9
160	17.0	2.8	4.6	4.0	2.5	4.2
450	58.0	9.2	15.0	12.0	7.5	13.9
	Events/$10^{19}p$/kt					
80	27(9)	4	8	7	4	7
120	61(22)	8(0.35)	15(0.35)	11(0.35)	7(0.4)	12(0.2)
160	116(40)	12(0.9)	23(0.75)	16(0.8)	11(0.8)	19(0.7)
450	657(300)	55(8)	93(8)	64(9)	44(5)	72(10)
	$\langle E_\nu^{-2}\rangle^{-1/2}$ (GeV)					
80	6.3	6.1	7.5	6.3	5.7	6.9
120	7.7	7.0	8.1	7.2	5.9	7.6
160	9.7	7.6	9.3	7.3	9.3	8.0
450	14.6	9.5	10.7	9.0	8.7	9.4
	ν_e/ν_μ (%)					
80	0.66	1.00	0.74	0.83	1.00	0.14
120	0.61	1.00	1.00	1.00	1.15	0.77
160	0.50	1.00	1.00	1.00	1.18	1.25
450	0.50	2.50	1.50	1.71	2.20	1.57

Table 7.6: Neutrino fluxes, event rates, neutrino mean energy and flavor ratio at NESTOR for 6 different beam geometries and 4 energies. The numbers in parentheses give the $\overline{\nu}_\mu$ rates.

The proton beam energies of 80 and 160 GeV has been previously considered in a number of scenarios where one might benefit from a higher repetition rate from the accelerator by running below the peak energy of 450 GeV; the energy of 120 GeV is also included for comparison with the Fermilab Main Injector beam to SOUDAN 2. It is clear that

*Assuming 100% detection efficiency.

operating at the highest energy is more efficient and cannot be compensated by doubling or even tripling the repetition rate.

For the different focusing systems, it would seem that the 20 GeV horn and 40 GeV reflector system (H20R40) gives a good compromise between the flux/event rate obtained and the average energy of the neutrino spectrum in order to have good sensitivity to oscillations with the expected detector efficiencies.

It is instructive to compare the spectrum with overall envelope obtained with P.F. Although, P.F. is not a realistic option as it focuses all energies parallel to the beam axis and takes no account of absorption, multiple scattering, etc., it gives an estimate of the maximum "available" neutrino flux. The focusing system delivers 22–29% of the "available" neutrino flux to the detector, which indicates that it is well matched to the production spectrum; however, when looking at event rates, the efficiency of the focusing system is around 20–25% at lower proton energies and drops to 13–14% at 450 GeV.

Fig. 7.5 shows clearly the effect where at 120 GeV proton energy, the focusing system selects a large fraction of the available spectrum which falls down above 30 GeV, whereas at 450 GeV proton energy the fraction collected is much smaller because the parent mesons are produced at much higher energy. It is quite possible to design a focusing system such as the H40R70 system (see fig. 7.6), which selects a higher energy bite of the spectrum and, while giving lower flux than the H20R40 system, provides a higher event rate with a higher mean energy.

The yields are shown in table 7.7. One obtains a 40–50% increase of the yield and a 30–40% increase in energy. In the same table we also report the reverse focusing polarity results. One observes, as expected a dramatic decrease in flux and event rate, and further one sees that ν_μ flux is still comparable to the $\overline{\nu}_\mu$ one. Finally, for comparison purposes we have included a High Energy (H.E.) focusing similar to the one in use for CHORUS/NOMAD. In comparison with the H20R40 option one obtains the 75% of the yield, with double average energy.

Geometry	ν fluxes	Events	$\langle E_\nu^{-2}\rangle^{-1/2}$ (GeV)	ν_e/ν_μ (%)
H20R40	15.0	93 (8)	10.7	1.50
H20R40 $\overline{\nu}$ focus	1.8	24 (38)	17.5	2.66
H40R70	16.0	134 (6)	14.6	1.20
CHORUS/NOMAD focus	4.6	71	20.6	–

Table 7.7: Neutrino fluxes, event rates, neutrino mean energy and flavor ratio at NESTOR for 4 different beam geometries, using a 450 GeV proton beam. The numbers in parentheses give the $\overline{\nu}_\mu$ rates. Units are the same as in table 7.6.

7.4.2 Radial Beam Dimensions

The radial distribution of the beam with the realistic focusing system (H20R40) in flux is shown in fig. 7.7 for 80, 120, 160, and 450 GeV proton beams and in event rate in fig. 7.8.

The widths of these distributions are of the order of 1.75–2 km at the Gran Sasso site and 3.5–4 km at the NESTOR site. It is interesting to note that there is a relatively large flat top. About 90% of the flux is contained within a 1–1.5 km, making less critical the task of beam pointing. One mrad targeting precision is well within the capabilities of present systems.

7.4.3 Optimum Length and Radius of the Decay Tunnel

Fig. 7.9 shows the integrated percentage of the ν_μ neutrinos that pass through the fiducial area of NESTOR, as a function of the radial distance R from the beam axis and the distance z along this axis of the neutrino generation point.

One sees that a decay tunnel of ~ 1.5 m radius contains the 95% of the events that finally fall within the detector acceptance. A decay tunnel of length ~ 500 m would reduce the statistics to 65%.

7.4.4 Electron Neutrino Background

Another important element that enters into the beam design is the ν_e contamination of the beam. It is the main systematic error setting the sensitivity limits in the mixing angle. One sees in table 7.7 that the ratio of ν_e to ν_μ is of the order of 1%, going to 1.5% at 450 GeV. Fig. 7.10 shows the energy distribution and the z point of decay of the parent particle along the beam for ν_μ and ν_e that are within the NESTOR acceptance.

The parent particle of the ν_e events is also indicated. One notices that the decays of the μ are a large fraction of the ν_e background, and further they are concentrated at the low energy region. They are mainly produced at large z lengths of the decay tunnel, since they are products of secondary decays. One also notices that the ν_e coming from kaon decay are produced early in the decay tunnel, as expected from the lower kaon lifetime. Similar remarks hold for the Gran Sasso background.

7.5 Quadrupole Focusing

Table 7.8 shows the results obtained using quadrupole focusing. One observes that when one adds the ν_μ and $\overline{\nu}_\mu$ fluxes one obtains equivalent yields with the horn without reflector configurations, but with higher average energies, and larger ν_e backgrounds. The capability to control the beam polarity is also lost. Moreover, in order to obtain good acceptance, the quadrupoles have to be very close to the target, creating problems with radiation.

Geometry	ν fluxes	Events	$\langle E_\nu^{-2}\rangle^{-1/2}$ (GeV)	ν_e/ν_μ (%)
Q20 NESTOR	6.6	55(21)	13.9	2.01
Q40 NESTOR	8.3	83(27)	19.3	1.33

Table 7.8: NESTOR rates with 2 different quadrupole geometries, using a 450 GeV proton beam. The numbers of events in parentheses give the $\overline{\nu}_\mu$ rates. Units are the same as in table 7.6.

In connection with quadrupole focusing, we also examined the possibility to have a tunnel structure shaped like a **Y**, as shown in fig. 7.11. The beam configuration consists of a quadrupole triplet as the above, 100 meters of decay tunnel, where all the $K^\pm$ decays, and the K^0 decays, source of ν_e background occur, and a dipole magnet which sweeps the positive pions to one direction e.g. NESTOR and the negative to Gran Sasso into a second decay tunnel. This configuration has the originality to produce two beams of ν_μ and $\overline{\nu}_\mu$ concurrently, while it has reduced a large fraction of the ν_e background. As expected the dipole magnet introduces large dispersions, and one remains with only 5% of the flux after the dipole operation. So this idea is unrealistic, unless a clever non-dispersive focusing system (e.g. dipoles + quadrupole, or dipole + 2 new horns at each channel) is designed.

7.6 NESTOR Sensitivity

The event energy distribution for realistic focusing is shown in fig. 7.12. One sees that the focusing system effectively selects a central beam energy of 15 GeV with a small dispersion of the order of 5 GeV. The ratios of ν_e and $\overline{\nu}_\mu$ are 1.5% and 8% respectively for an energy of 450 GeV.

From table 7.6 one sees that one can realistically hope to obtain of the order of 100 events per kiloton per 10^{19} protons of 450 GeV at NESTOR.

We have studied what the present configuration for a single NESTOR tower will give in terms of sensitivity to mass and mixing oscillation parameters.

We may detect the oscillation as a change of the ratio of neutral current (NC) to charged current (CC) interactions, since all charged-current ν_e events will appear as NC, or "muonless" events. In the case of oscillation to ν_τ, all CC events will appear muonless, except the fraction where the τ decays to a μ ($B_\mu = 17\%$). There will also be a kinematical suppression η ($\sim 25\%$) due to the high mass of the τ. Therefore the sensitivity to ν_τ oscillations will be less than the one to ν_e. If P is the oscillation probability shown in (5.1), the change of the ratio for the ν_μ to ν_τ oscillation is shown below. The case of ν_μ to ν_e is obtained by setting $\eta = 1$ and $B_\mu = 0$.

$$R_\nu^{\rm obs} = \left(\frac{\rm NC}{\rm CC}\right)_{\rm obs} = \frac{R_\nu^{\rm th} + \eta P - \eta B_\mu P}{1 - P + \eta B_\mu P}, \tag{7.3}$$

where $R_\nu^{\rm obs}$ and $R_\nu^{\rm th}$ are the ratios of NC to CC observed and predicted by the Standard Model. The separation of μ from e and hadrons in the detector is under study. Preliminary MC results indicate that we should be able to distinguish between "muonless" (NC) and "muonlike" (CC) events, by using the time distribution of the events (Čerenkov light from muons comes earlier than the one from the hadronic or electromagnetic showers) and/or the shower development of the event (the muons distribute their Čerenkov light evenly along the track, while electrons emit their light according to the development of the electromagnetic shower). First results of Monte Carlo studies indicate that we will be able to tag an event as muon or electron with an efficiency of about 50% and a contamination less than 5%, in the case of equal electron and muon samples. The systematic effect due to this statistical separation is estimated to be less than 10%. This systematic error sets the lower limits of the one tower, low PMT density sensitivity on the mixing angle.

Our average efficiency to reconstruct a muon, depends on the incidence angle (see chapter 5 for more details). For this study we assumed an average efficiency of 20%, with a threshold ~ 5 GeV of neutrino energy. This is certainly a lower limit of what we can achieve, once we know the beam direction.

The present design of one NESTOR tower has a fiducial volume of the order of 200 ktons. Applying thus efficiency and tagging criteria we obtain 4000 events per year. The analysis of these events in terms of $\nu_\mu \to \nu_e$ oscillations, when one includes the effects of detection efficiency and tagging is shown in fig. 7.13.

The $\nu_\mu \to \nu_\tau$ analysis has of course a reduced sensitivity, but still covering the largest part of the KAMIOKA signal. In the case of ν_μ to ν_e, matter effects enhance the oscillation but 1676 km is not enough distance to have significant profit from these effects.

It is encouraging that without any rearrangement of the detector one obtains limits covering the area of the KAMIOKA possible oscillation results.

These limits should be considered though as lower limits, in what concerns the performance of the detector, since in the efficiency and tagging studies, no use was made of the known direction of the beam, and no optimization of the design with respect to the long baseline option was made.

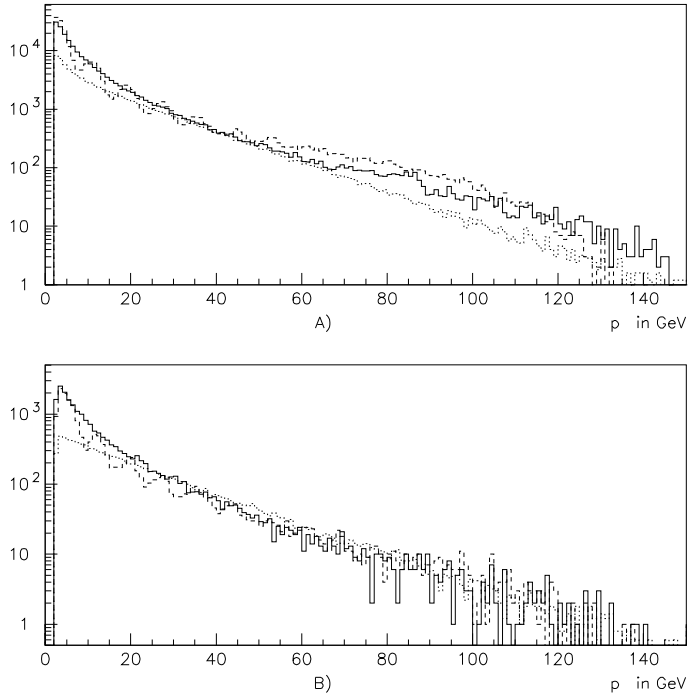

Figure 7.1: Momentum spectra of secondary pions (A) and kaons (B) for a 450 GeV incident proton beam given by FLUKA (solid) GHEISHA (dashed) and Atherton/Barton (dotted) with P.F.

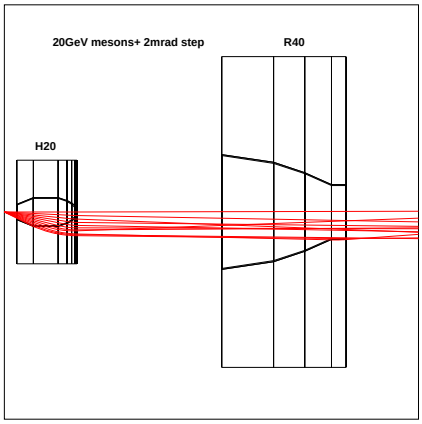

Figure 7.2: Rays of 20 and 40 GeV, with a ϑ step of 2 mrad, passing through the horn+reflector focusing system.

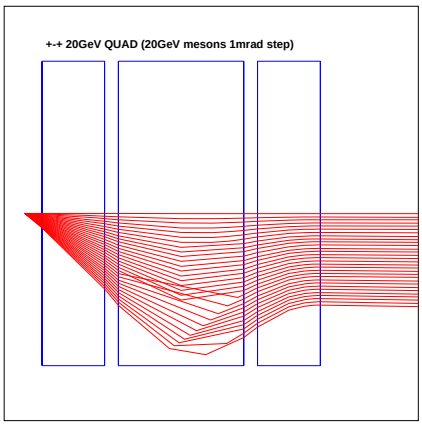

Figure 7.3: Rays of pions, with a ϑ step of 2 mrad, passing through the 20 GeV quadrupole focusing system.

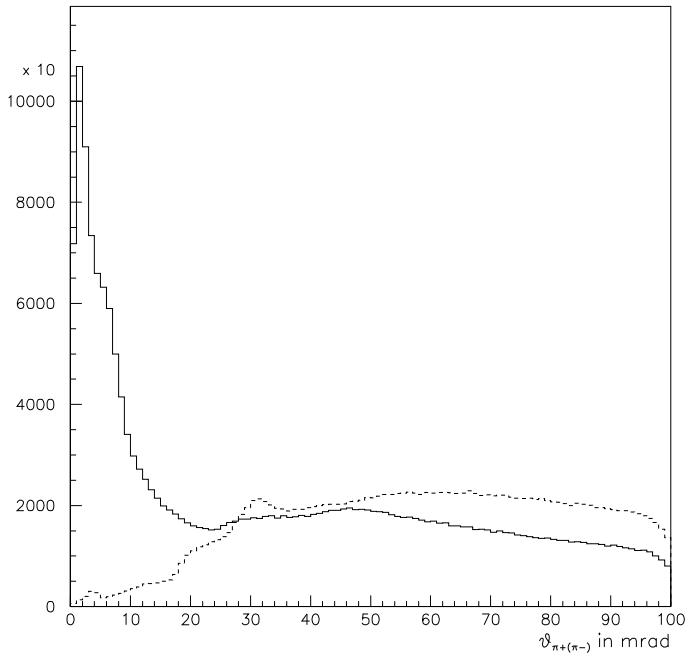

Figure 7.4: ϑ distributions (in mrad) of π^+ (solid) and of π^- (dashed) tracks, produced by a 450 GeV proton beam, at the entry of the decay tunnel after the H20R40 focusing system.

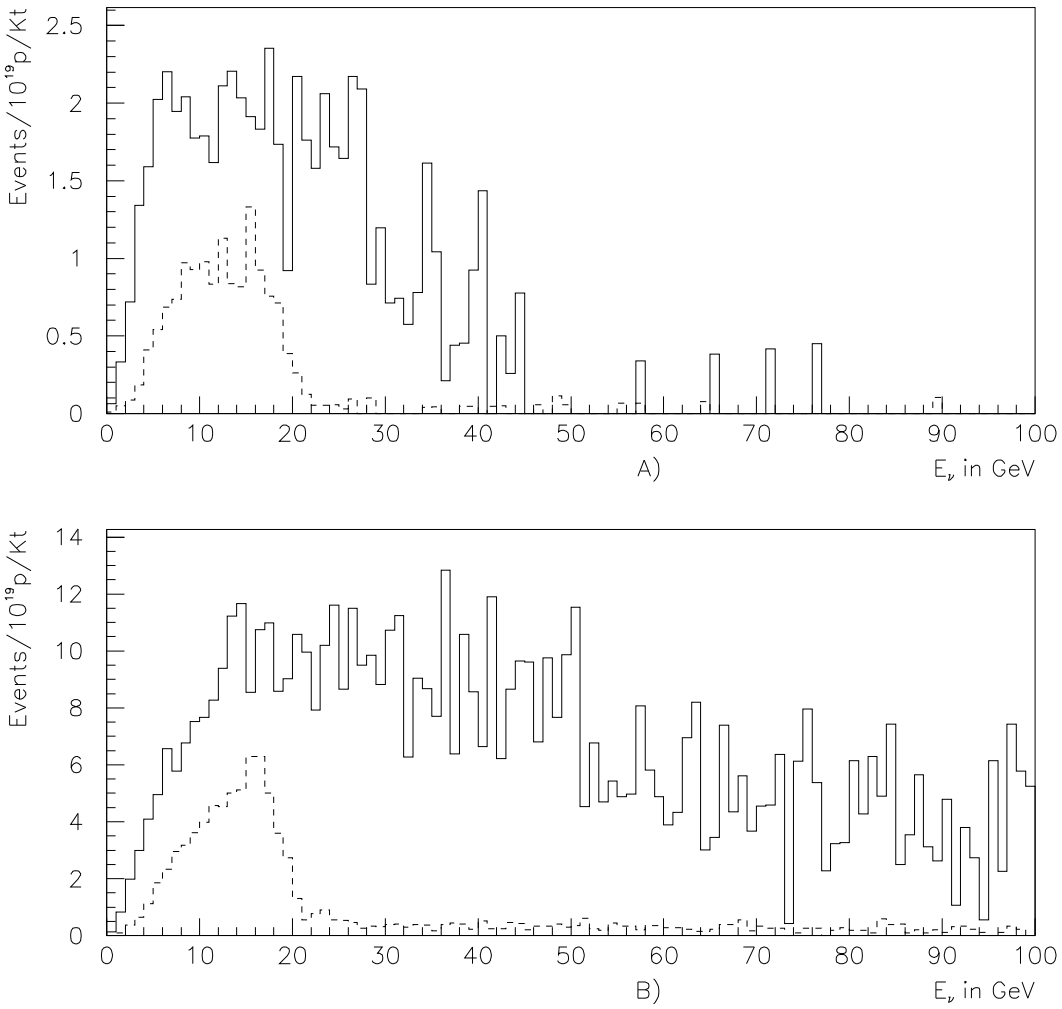

Figure 7.5: Comparison of the event energy distributions at NESTOR for P.F. (solid) and realistic horn (dashed) for 120 GeV (A) and 450 GeV (B) proton beams.

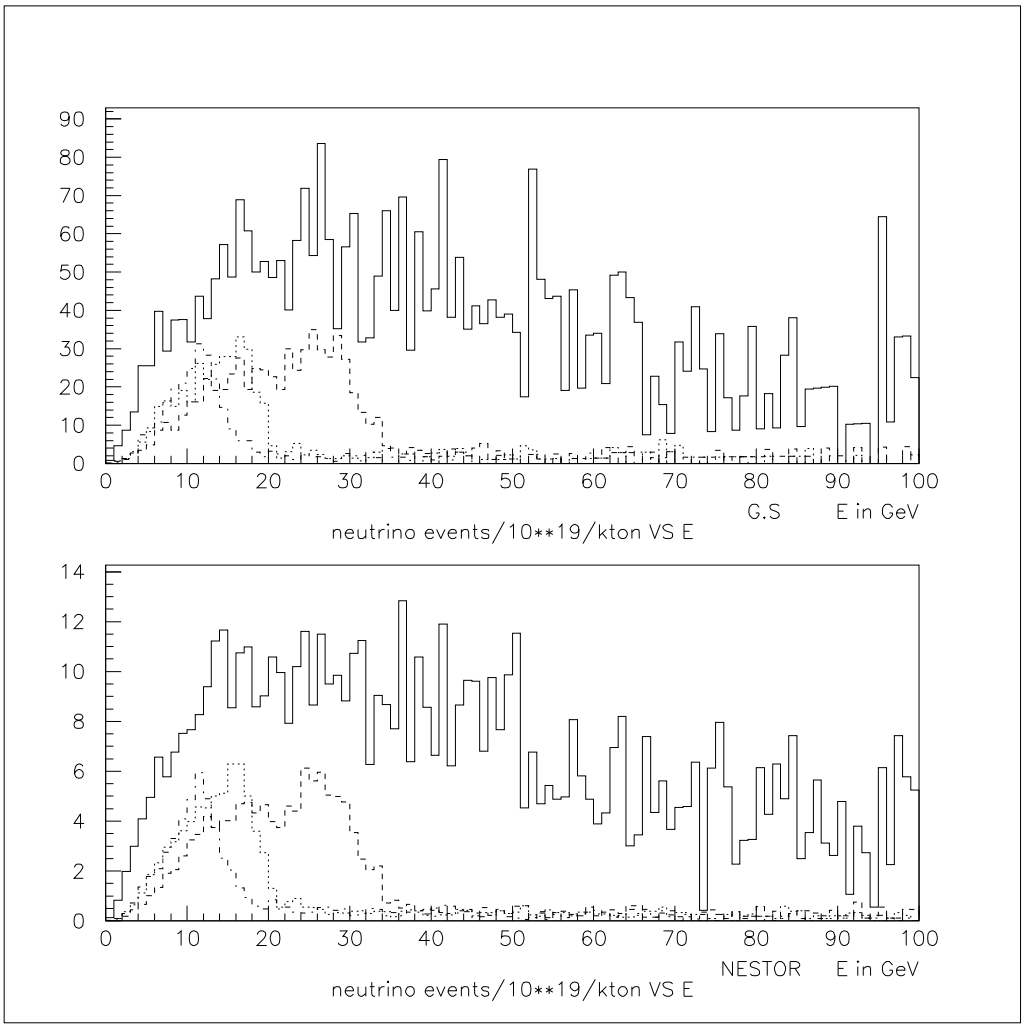

Figure 7.6: Comparison of the event energy distribution at Gran Sasso and NESTOR for P.F. (solid) and H15R15, H20R20, H40R70 horn/reflectors (dashed) for a 450 GeV proton beam.

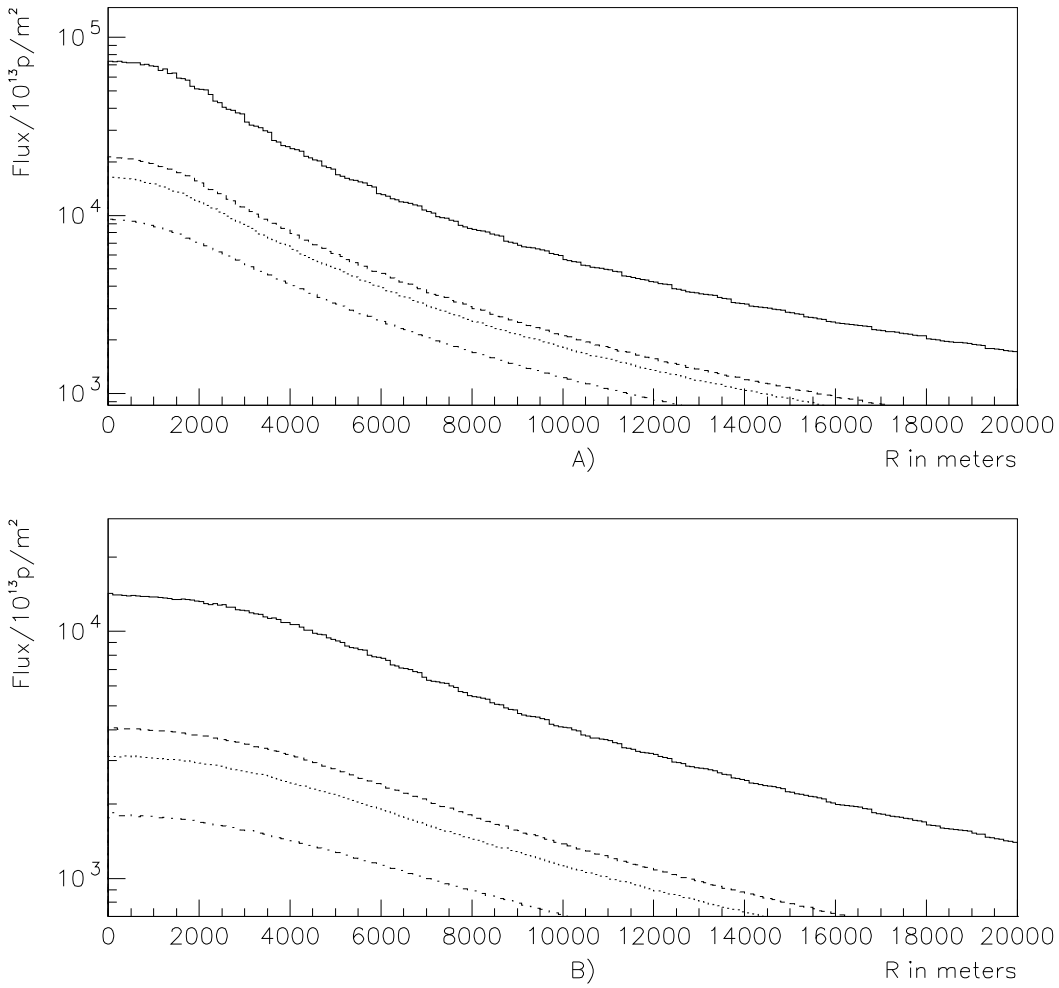

Figure 7.7: Flux radial distributions for 80, 120, 160, and 450 GeV beams (in ascending order) with realistic focusing for Gran Sasso (A) and NESTOR (B).

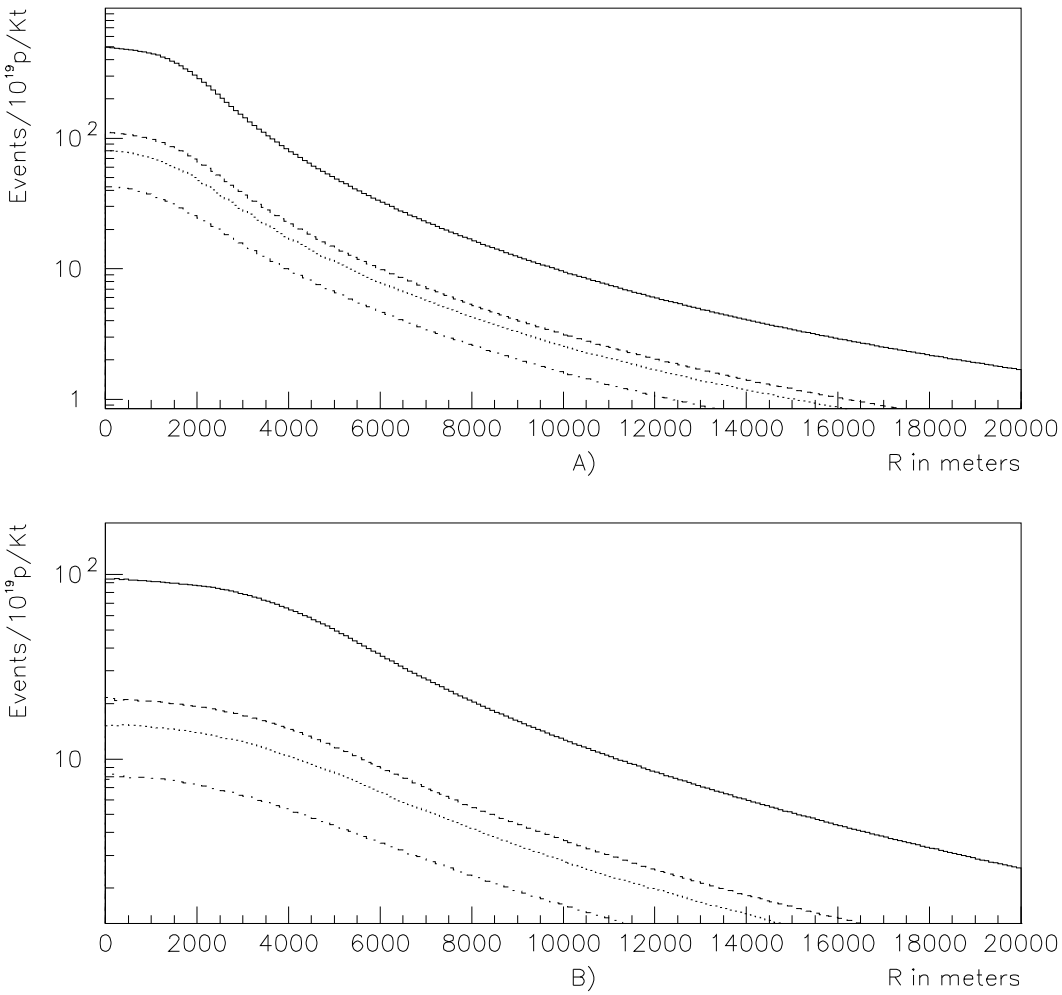

Figure 7.8: Event radial distributions for 80, 120, 160, and 450 GeV beams (in ascending order) with realistic focusing for Gran Sasso (A) and NESTOR (B).

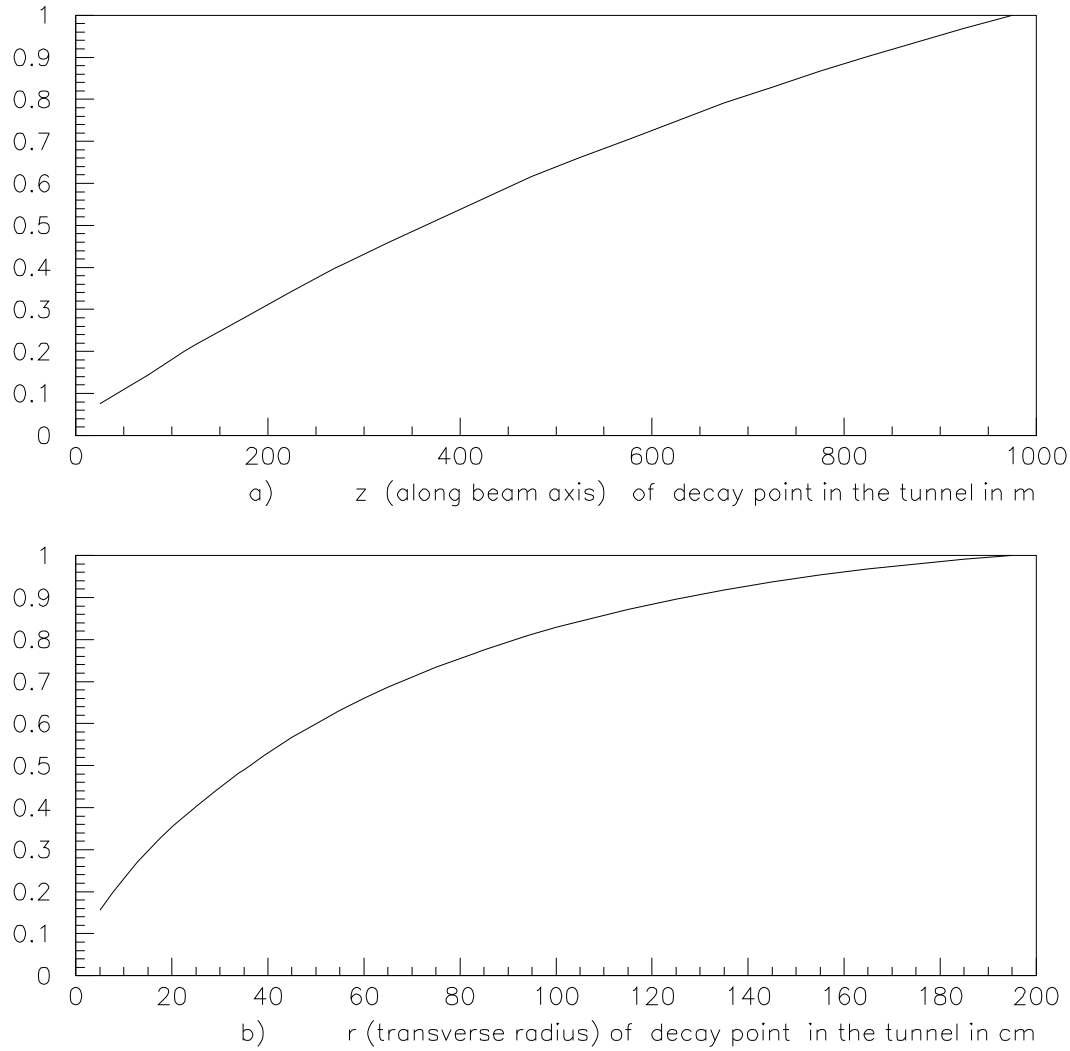

Figure 7.9: Cumulative z distribution (a) and r distribution (b) for events inside the fiducial area of NESTOR (a 450 GeV proton beam).

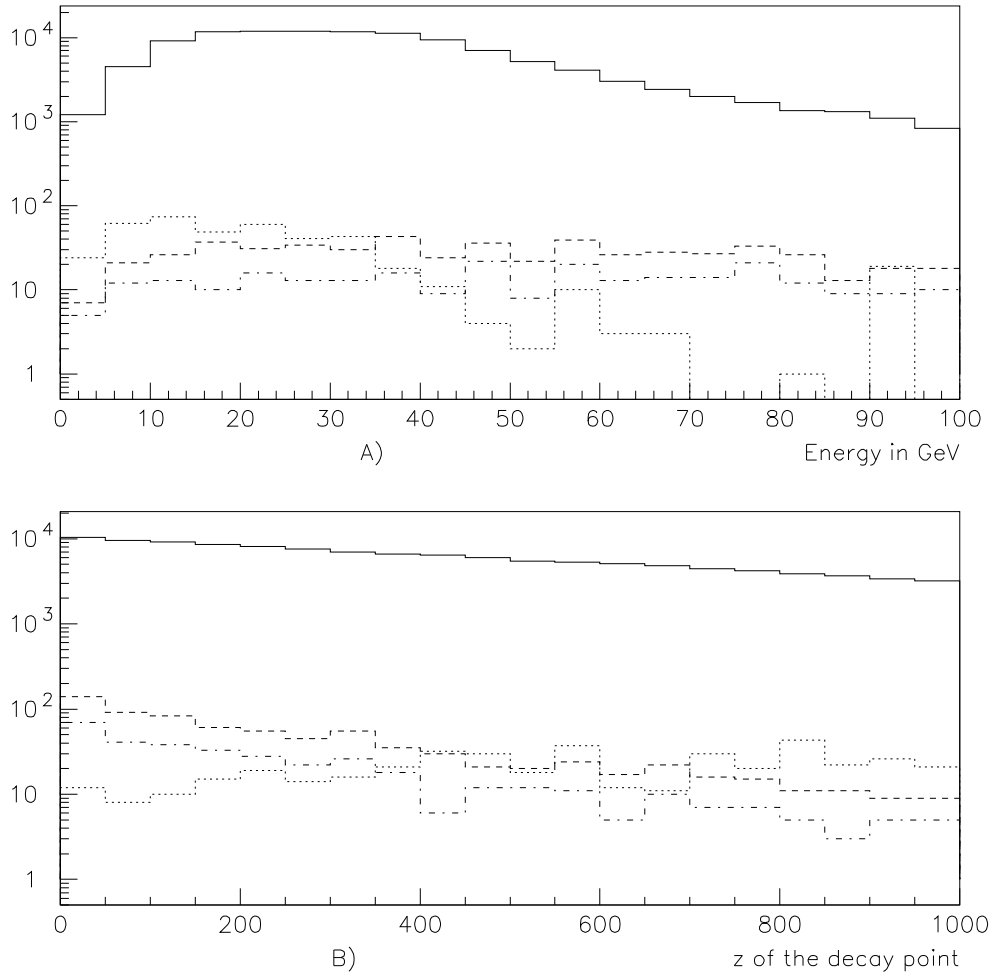

Figure 7.10: Energy distribution (A) and z distribution along the decay tunnel (B) for events within the NESTOR acceptance produced by a 450 GeV proton beam. The solid line denotes the ν_μ and dotted lines the ν_e originating from μ decays. The dashed and dash-dotted lines show the $K^\pm$ and K^0 decays to ν_e, respectively.

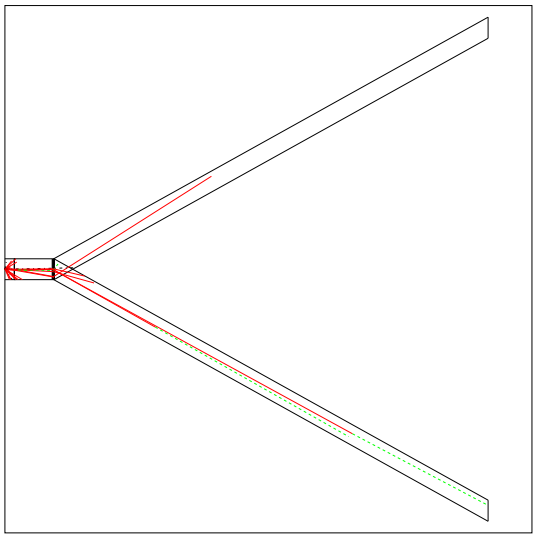

Figure 7.11: A quadrupole-dipole system with 3 decay tunnels, serving 2 locations with ν_μ and $\overline{\nu}_\mu$ beams synchronously.

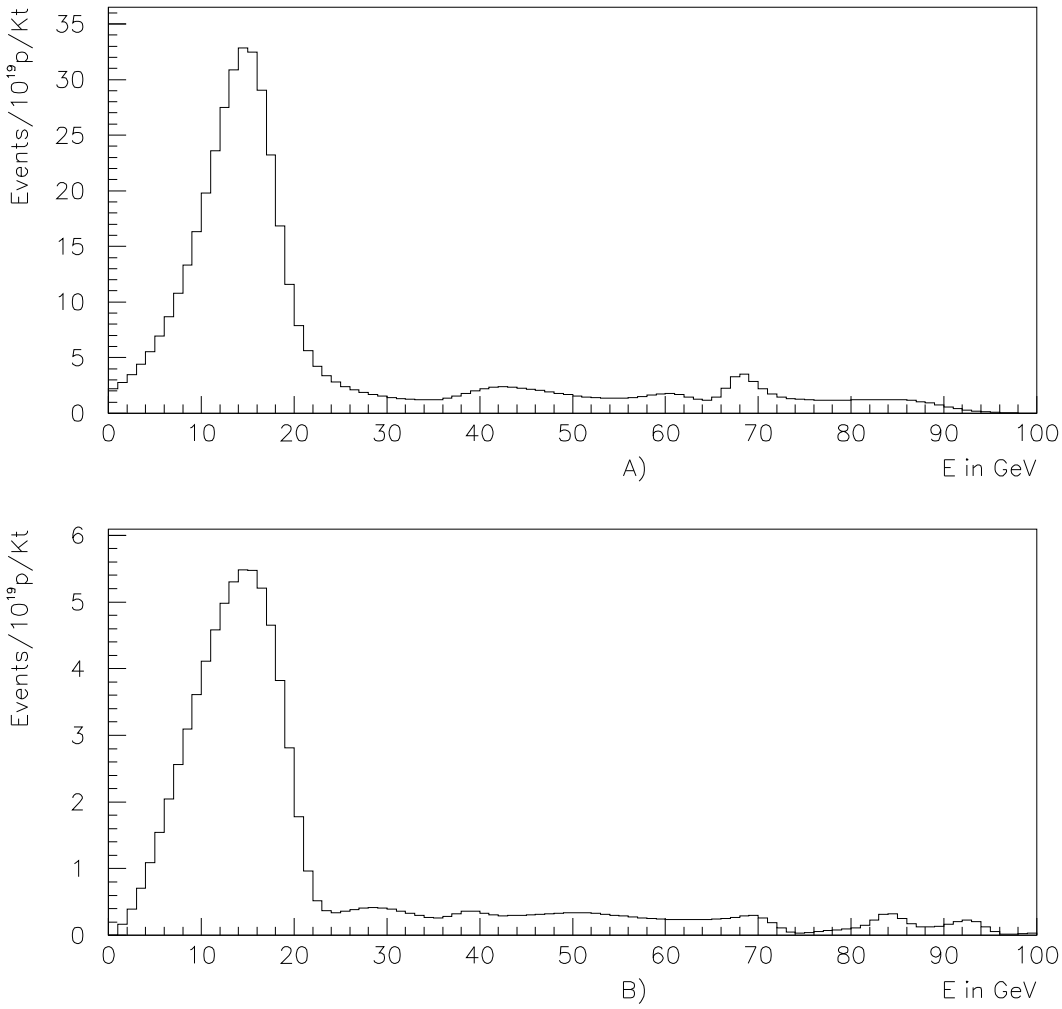

Figure 7.12: Event distributions for Gran Sasso (A) and NESTOR (B) for a 450 GeV proton beam and realistic focusing.

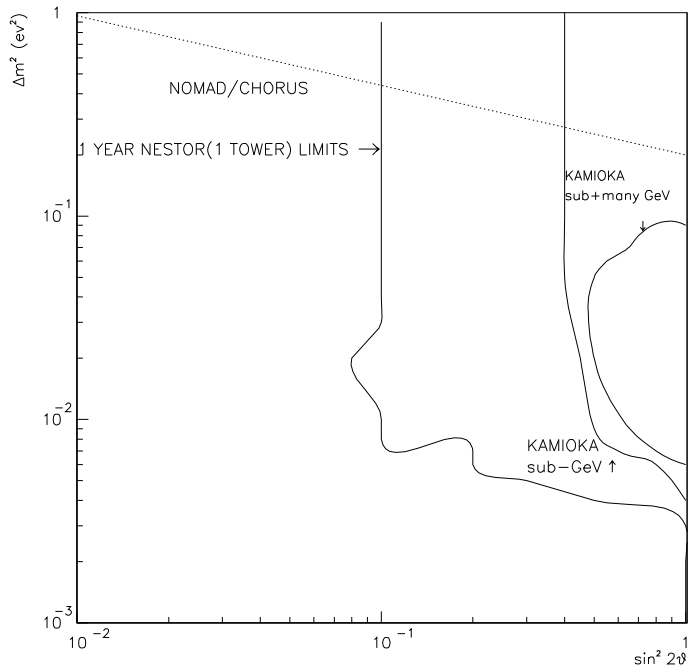

Figure 7.13: Sensitivity limits with one NESTOR tower and one year of running for $\nu_\mu \to \nu_e$ oscillations. The KAMIOKA signal and CHORUS/NOMAD sensitivity are also shown.

Chapter 8

U.H.E. ν Interactions and New Particle Physics

It is a well known fact that, although the Standard Model is at present extremely successful, since its predictions keep being experimentally verified with ever increasing accuracy, it has nevertheless some flaws that make it unsuited as a final theory of all interactions: it contains too many parameters, it does not really explain the symmetry breaking mechanism and it is not a unified model of the electroweak and strong interactions.

There is a need for new physics, physics which will hopefully appear at an energy not much greater than the scale of symmetry breaking ($\sim$ 250 GeV). Until the LHC is built neutrino telescopes will be the only tool to reach such an energy scale.

Two examples of possible new high energy physics have been discussed in detail in the 2^{nd} and 3^{rd} NESTOR Workshops:

- a search for a possible substructure of the elementary particles [10];
- a search for a possible non perturbative multiple production of intermediate vector bosons [8, 9].

In both cases the signature for the process is a narrow muon bundle with muon energies of the order of tens of TeV in the first case, and hundreds of TeV in the second case. The estimates on the expected number of events are affected by an error of several orders of magnitude, due to the lack of knowledge of the basic cross sections and to the lack of knowledge of the incoming neutrino flux. For an incoming neutrino energy of 10 PeV it is not unreasonable to expect, in the full NESTOR array, from a few to a few dozens of events a year in the zenith angle interval between 80° and 90°. The lower limit on the angular range is dictated by the requirement that the signal be clearly separated from the atmospheric muon bundles, while the upper limit is due to the absorption of the incoming neutrinos by the earth, for incidences lower than the horizontal, given the comparatively large cross sections ($\sim 10^{-32} - 10^{-29}$) cm^2 of the interesting processes.

In order to detect hints of physics beyond the Standard Model it is essential to be able to record and analyze multiple muon events and give at least an order of magnitude estimate of the muon energy. The detector we propose for NESTOR and the associated data aquisition system meet these requirements.

Part II

Technical Description

Chapter 9

The Site

At the S. W. of Peloponnisos (figure 9.1), in the depths of the Ionian Sea, lies a deep underwater plateau.

It is 7.5 nautical miles away from the island of Sapienza and 11 nautical miles from the small town of Methoni. The depth is 3800 m. This plateau fulfills the specific environmental requirements, which are desirable for the operation of a deep underwater detector as NESTOR [14]. NESTOR, the Mediterranean deep underwater neutrino detector will detect Čerenkov radiation produced by muons in a large volume of transparent matter, water. The muons are produced by neutrinos or by atmospheric interactions of cosmic rays. Hence, the most important requirements for the detector are: clear water (i.e. water with small light attenuation coefficient), deep site (to filter out the atmospheric muons), proximity to the shore (to use a short electro-optical cable to power the NESTOR detector and transfer the data to the shore with low light attenuation), low velocity of underwater currents (for minimal mechanical strain on the detector), flat and wide sea-bottom (to permit future expansion) and stable geological and other environmental characteristics (for long life time of the detector).

Those requirements are fulfilled by the selected site. We have designated as the NESTOR site, a location with co-ordinates 36° 37.5' N, 21° 34.6' E (figure 9.1), in the middle of the deep underwater plateau (figure 9.2) which has a gentle slope. The depth of the sea at this location is about 3800 m.

During the 1989–1994, four major cruises – three with Russian Oceanographic vessels, "Mendeleev" ('89), "Vityaz" ('91), and "Keldish" ('92), and one with the Greek Oceanographic vessel "Aegaeo" ('94) – were made. From those cruises we have a good environmental description of the NESTOR site, which is described in the following. Moreover, hydrographic survey and sub-bottom profiling of the NESTOR site and of the proposed route of the deep underwater cable have been made.

9.1 Water Transmissivity

As mentioned above, NESTOR detects Cerenkov photons. We shall use photomultipliers, 38 cm diameter, with a photosensitive area of 0.114 m^2, to detect the produced photons. These photomultipliers have the maximum light sensitivity in the blue-green wavelength region. Moreover, water is most transparent in the same wavelength region. The effective

Figure 9.1: S. W. tip of Peloponnisos with NESTOR site

Figure 9.2: Sea bottom relief map of the NESTOR site area and the access to the shore (Sapienza island) [ref.8]

area of our detector is proportional to the transmission length of those wavelengths into the water. Hence, it is quite important to know the water transmissivity of the blue-green light at the vicinity of the NESTOR site.

The water transmissivity usually is studied in the laboratory using water samples and a monochromator with well-collimated light beams. In those tight geometrical acceptance experiments, with well- collimated beams, most of the scattered light in the water path is lost. For clear water, monochromators with a light path about 1 m long are used. This path is marginal to measure accurately light transmissivity of very clear waters, as the ones that we can find in eastern Mediterranean.

NESTOR is a large acceptance experiment, i.e. it gets most of the scattered light. Hence, using a large acceptance device to measure water transmissivity **in situ**, we should get results representative of our detector measurement of water transmissivity.

We have performed mainly three sets of sea water transmissivity measurements on board the Russian Oceanographic Vessel "Academic Mstislav Keldish" in November 1992; a) Long base line with a monochromator (tight acceptance instrument), b) Tight geometry photometer **in situ** [155] and c) Long base line **in situ**, (large acceptance instrument) [156].

For the first set of measurements, we took water samples from various depths and locations in the general NESTOR area, using the ROZETTE, (the automatic pressure, temperature, salinity and water sample device) that was on board "Keldish". We got a total 47 water samples. The light attenuation of those samples was measured in the laboratory of the vessel, using a monochromator (tight acceptance experiment) with 1.1 m long cell and well-collimated light beam. In figure 9.3 a typical graph of the attenuation coefficient versus the wavelength for several depths is shown.

It should be noted that for depths greater than 2000 m, those graphs have the typical shape of very clean sea water. The attenuation coefficient was found equal to 0.025 m^{-1} to 0.040 m^{-1} (at the 470–490 nm region) and almost constant for depths more than 1000 m (figure 9.4).

From those values and the assumption that the ratio $\Lambda = \sigma/\epsilon$, for very clean water is about 20 % to 50 % (oceanographers differ in this correction), where σ is the scattering coefficient and ϵ the attenuation coefficient, it was calculated that the absorption length at 470 nm wavelength and depths more than 2000 m is

$$L = 42 \quad \text{to} \quad 67 \text{ m} \tag{9.1}$$

The second set of measurements was performed using **in situ** an autonomous photometer and light source that was attached on the ROZETTE. With the autonomous module we measured the light attenuation versus depth continuously (figure 9.5).

The third set of measurements was performed the same period in the same general area, **in situ**, using a long base line detector system (large acceptance experiment) developed by Bradner and Blackinton [157]. The detector was a two part instrument connected with a steel wire-rope, and lowered into the sea, at several depths, with a hydrographic cable (figure 9.6).

The lower part of the detector was a light source (strobe) with a diffuser, looking up towards the second part, the photo-detector with a photo diode. A 480 nm filter was used before the photo diode. The light transmitted through the water path (as long as the

Figure 9.3: A typical attenuation coefficient graph versus wavelength, for various depths. Measured in the laboratory using a monochromator with a path light 1.1 m long and water samples (tight acceptance instrument), [ref.2]

Figure 9.4: The attenuation coefficient versus depth (measured with the tight acceptance instrument on board) [ref.2]

Figure 9.5: The attenuation coefficient versus depth in arbitrary units (measured with tight acceptance instrument **in situ**) [ref.2]

Figure 9.6: Schematic diagram of the detector used **in situ** to measure the $1/e$ transmission distance (large acceptance instrument) [ref.3]

steel wire-rope between the two parts of the detector) was collected by the photo-detector and converted to signal. The signal was transferred to the Oceanographic vessel with the hydrographic cable.

Three different lengths of wire-ropes were used to separate the source and the detector; at each location a pair of wires was used, the long one "L" and the short one "S". The light intensities recorded was accordingly named I_L and I_S.

Then, the $1/e$ transmission distance, β, was calculated

$$\beta = (L - S)/[\ln(I_S/I_L) - 2\ln(L/S)] \tag{9.2}$$

We have taken measurements at three locations and at depth down to 3800 m. In figure 9.7, the calculated $1/e$ transmission distance versus the depth is plotted (with error bars).

From those values we calculated the mean $1/e$ transmission distance equal to:

$$\beta = 55 \pm 10 \tag{9.3}$$

All those measurements have consistent results and we conclude that the NESTOR site has very clear waters suitable for our detector.

9.2 Deep Underwater Current Velocities

The underwater current velocity's measurements at the general area of NESTOR were started in October 1989, on board "Mendeleev", at the general area of the future NESTOR site. Autonomous current meters were used at depths down to 4500 m [158]. The current meters were deployed at several depths and locations and for several days. In figure 9.8

Figure 9.7: The $1/e$ transmission distance versus depth (measured with the large acceptance instrument) [ref.3]

a typical plot of current velocities versus time is shown for a deployment at location: $36^\circ\,31.9\,\mathrm{N}$, $21^\circ\,27.2\,\mathrm{E}$.

The duration of this deployment was three days and the depth was 2.5 m above the bottom of the sea (4500 m). Generally the measured underwater current velocities were less than 8 cm/sec.

More measurements were taken in July 1991, on board the "Vityaz". We measured the current velocities with current meters attached on buoys [159]. The instruments were deployed twice at the NESTOR general area for seven days each time and at several depths, down to 100 m above the bottom of the sea. The depth of the sea bottom was 3900 m. It is expected that the current velocities measured with moored current meters, are influenced by the surface current and weather, giving slightly higher values and shifted directions. Nevertheless, we measured deep underwater current velocities (at less than 500 m above the bottom of the sea) smaller than 10 cm/sec going to various directions (Typical graph in figure 9.9).

Additional measurements were taken in November 1992, with the Oceanographic vessel "Keldish". We deployed twice autonomous current meters, at the general area of NESTOR site and at depths of 70, 170 and 440 m above the bottom of the sea, which was at a depth of more than 3800 m [160]. Each deployment lasted three days. The detected underwater current velocities were less than 4.5 cm/sec, North direction (at less than 400 m from the bottom of the sea, typical graph figure 9.10).

We got more underwater current measurements in July 1993, with the tug-boat NESTOR, deploying one autonomous current meter at a depth of 3800 m and 130 m above the bottom of the sea. The recorded period was 7 days. The underwater velocities

Figure 9.8: Typical underwater current velocities versus time as measured in 1989 on board “Mendeleev” [ref.5]

Figure 9.9: Typical underwater current velocities versus time as measured in 1991 on board “Vityaz” [ref.6]

Figure 9.10: Typical underwater current velocities versus time as measured in 1992 on board "Keldish" [ref.7]

that we measured were less than 10 cm/sec, with a north direction (figure 9.11, figure 9.12, figure 9.13).

Generally the NESTOR site has deep underwater current with low velocities that will impose minimal mechanical stresses on the detector.

9.3 Sea Bottom Morphology

The sea bottom morphology is an important aspect on the construction and future expansion of our underwater detector. Thus a more or less flat bottom is required, without high rises or ravines and the silt, found on the surface of most of underwater plains, should be stabilized and compact. Moreover the access to the shore should be well known, since we plan to have lying on the bottom of the sea an underwater electro-optical cable from the detector to the shore.

In November 1992, on board the Oceanographic vessel "Keldish" a study of the sea-bottom was performed by the Trimonis team [161]. The area around NESTOR site and the access to the shore was sounded with an ELAC echo-sounder and mapped using the GPS system (figure 9.2). Moreover samples of the surface of the underwater plain were retrieved with grabs (3 samples), as well with several gravity cores up to 2 m long (6 samples).

We conclude that NESTOR area, at a depth of more than 3800 m, is relatively uniform with a smooth bottom surface, aspect ratio about 1% and a size of about 5 square nautical

Figure 9.11: Typical Underwater current velocities versus time as measured in 1993. The dashed triangles indicate days of deployment

Figure 9.12: Direction of the underwater currents recorded in 1993. (The fig. was prepared by the "National Centre for Marine Research")

Figure 9.13: Progressive vector diagram ("Walking" diagram) of the underwater current recorded in 1993. (The fig. was prepared by the "National Centre for Marine Research")

miles. The deposited material has a mean surface density of 1.6 g/cm^3 and indicates a low rate of accumulation (7 to 18 cm in 3000 years).

Since the access to the shore is quite steep with ravines and high rises, we have performed additional hydrographic survey studies using a FURUNO echo-sounder (Model FE-824ET, 20kHz-200kHz), an Ocean Research Equipment high resolution 3.5 kHz deep Underwater Profiler with 16 transducer array (4×4) and a Bolt INC "Air-gun" profiler (Model: High rate 40, running at 2000 psi) on board the Greek Oceanographic vessel "Aegaeo". The absolute ship position was determined to $\pm$ 1 m using the Differential Global Positioning System (DGPS).

The informations on the sub-bottom structure of the sea-bottom at the NESTOR Site and at the two proposed routes of the electro-optical cable as well as the sea-bottom contour profile are under evaluation (see "Electro-optical cable").

9.4 Temperature

The temperature of water in the general area of NESTOR site, for depth greater than 1000 m, was measured in 1989 by the "Mendeleev" (figure 9.14a) [162] and in July 1991, by "Vityaz", we measured the water temperature at NESTOR site, using thermometers attached to the current meters that were deployed for measuring the underwater current velocities (figure 9.14b [159]). Similar measurements in the general area of NESTOR site were performed in November 1992, with the Oceanographic vessel "Keldish", using a temperature sensor on the "Rozette" (figure 9.14c) and temperature sensors attached on the current meters that we had deployed [163].

The conclusion is that the water temperature at NESTOR site, below the depth of 2500 m, varies slightly with depth and is found to be 14.0 degrees Celsius. This value is quite constant in time, changing less than 0.5 degrees within a year.

Figure 9.14: Temperature (in degrees Celsius), salinity, density and sound velocity (in m/sec) versus depth in the NESTOR area as measured during the cruise of: a) "Mendeleev" in 1989, b) "Vityaz" in 1991 and c) "Keldish" in 1992

9.5 Background from ^{40}K

The fundamental optical background in the deep sea is due to ^{40}K decays. The ^{40}K is a primordial natural radio nuclide with a half- life of 1.27x10^{9} years and its abundance is 0.0118% of K. The ^{40}K decays mainly to ^{40}Ca emitting electrons (branching ratio 89.5%) [164], [165].

The salinity in the vicinity of NESTOR site is about 38.70 parts per thousand and is variable with depth less than 0.05 parts per thousand (figures figure 9.14 . Sea-water with salinity 38.70 has 4.4x10^{-1}gr/lt(sea-water) of K (table 2), hence the radioactive ^{40}K should be 5.2x10^{-5}gr/lt(sea-water). The radioactive 40K disintegrates producing electrons that produce Cerenkov light. The calculated background on our detector due to ^{40}K is roughly 13 disintegrations/lt/sec, which is a typical value for underwater light collecting experiments.

9.6 Deep Water Cosmic Ray Measurements in the NESTOR Site

During July 1991, a collaboration of the Institute for Nuclear Research and the Institute of Oceanology of the Russian Academy of Sciences and the University of Athens carried out a successful cruise using the R/V VITYAZ, off the coast of Pylos. We deployed [14] from the Oceanographic ship "Vityaz" a Russian built hexagonal structure (figure 9.15) (7 m radius) built out of titanium alloy using 10 phototubes (15 inch photocathodes, earlier versions of the Hamamatsu PMT used in NESTOR) facing upwards, down to

a depth of 4100 m. Six of the phototubes were located at the corners of the hexagon and four 3.5 meters below the center. The sensitive area of this experiment was 373±75 m^2. We successfully measured the vertical muon intensity and the angular distribution of downcoming muons. As one can see from figure 9.16, figure 9.17, and figure 9.18, our results at 3300 m, 3700 m, and 4100 m agree very well with DUMAND I, the deep mine measurements, and Miyake's formula. In November 1992 we deployed [**?**] a linear string of five 15 inch phototubes (again the photocathodes were facing upwards). This time the deployment was made from the Russian research vessel "Ac. Mstislav Keldish". The string was deployed in depths from 3700 m to 3900 m, the vertical intensity of cosmic ray muons and their dependence of the muon flux as a function of the zenith angle was obtained. The results are in good agreement with the previous measurements and calculations. To summarize, at depths between 3700 m and 3900 m the vertical flux $(9.8 \pm 4.0) \times 10^{-9}$ $cm^{-2}s^{-1}sr^{-1}$. The background due to radioactive ^{40}K and bioluminescence in the water is 597±150 photons/(cm^2s). We note that this is an upper limit because since the phototubes were suspended from the ship the vertical motion excites the various organisms giving very high values for the bioluminescence compared to anchored phototubes

Figure 9.15: The test experiment

Figure 9.16: Muon zenith angular distribution

Figure 9.17: Depth intensity relation

Figure 9.18: Comparison with previous results

Chapter 10

Mechanical Design

10.1 System Configuration

The detector configuration is the result of a study to determine the optimum way to reach the goals defined in the first part of this Proposal, i.e. undersea neutrino physics and astronomy.

A simulation of signals and backgrounds has been made running two Monte Carlo programs: a) a modified version of the DUMAND Monte Carlo adapted to NESTOR, b) a GEANT-CERENKOV generation code.

Among the detector's specifications, some of them, like the effective area to be covered, the angular resolution for the single muon produced in the water, the granularity (i.e. the spacing of the PMT's related to the sensitivity of the light detectors) and the water transmissivity length, play a very important role to define the Physics Potential of the apparatus. A certain flexibility to change the detector geometry and to upgrade it, is also important. Finally the overall costs, including the costs of the materials, the deployment and the servicing also must be taken into account in order to be kept as low as possible.

The NESTOR's physics goals range from atmospheric neutrino oscillations (of a few GeV) to Very High Energy neutrinos from Extragalactic sources (at least 1 TeV).

We will start with a detector of a sensitive area of 20.000 m^2, expanding it in a modular fashion to 100.000 m^2 and hopefully later to the 1 km^3 detector which is probably required to detect point-like sources, given the expected neutrino fluxes. The Monte Carlo calculations indicate that the best geometrical symmetry to cover 100.000 m^2 (which is probably the minimum area required to start point source astronomy) is a cylinder of an enclosed mass greater than 20 Mtons and overall angular resolution better than 1 degree.

To construct a detector having such dimensions, one option is to use strings of PMT's located at the vertices of an octahedron or heptahedron inscribed in an ideal cylinder, anchored to the bottom of the sea. The strings should be connected to a common distribution box placed also at the bottom through an electro-optical cable which takes the power from the shore and sends the signals to the shore. In this case the use of a bathyscaphe is required to make the connections in a very sophisticated deployment operation. This approach has been chosen by DUMAND. Since the availability of bathyscaphes is rather limited (sometimes, a few years long waiting lists) and the daily charges are very high, almost 100.000$/day (including the necessary days of mother ship transit time to the de-

ployment location), we have conceived a detector which does not require any connection operations inside the water. The basic unit of our configuration is a hexagonal floor 16 m in radius. Twelve of those floors stacked one on top of the other with 20 m separation make up one tower. Six towers deployed in a hexagonal fashion radius 100-150 m around a central one make a reasonable approximation to a spherically symmetric detector with a sensitive area larger than 100.000 m^2.

10.1.1 The Basic Detector Element: the Omni Directional Module Pair

Instead of using one 15 inch phototube facing down (like DUMAND), we will use two 15 inch phototubes (each in its own protective glass 17 inch Benthosphere), one looking up and the other looking down. This way we get a detector with an isotropic (4π) response.

10.1.2 The Two Dimensional Array element: a 16 m Hexagon

Six pairs of PMT's will be placed at the corners of a horizontal hexagon and a seventh one in its center. The radius of the hexagon is planned for 16 m, and the arms made out of titanium piping. The electronics (data digitization/transmission to shore) and all the controls of the hexagon will be housed inside the titanium sphere located at the geometrical center of the hexagon.

10.1.3 The Three Dimensional Array Element: a 220 m Tower

By stacking hexagons we can build "towers". The vertical distance between these hexagonal floors will be around 20 m, this spacing matching well the light transmission length of 55 ± 10 m (at 460 nm) that we have measured (see previous chapter). With a 20 m vertical spacing between floors, each with 7 phototubes looking up and 7 phototubes looking down, the active volume between hexagonal floors will be monitored efficiently. A total of 12 such hexagonal floors is planned for one tower. This number of floors (with the dimensions chosen) provides the effective area required for the first physics and also, requiring 12 optical fibers for the data transmission to the shore, allows us to use currently commercially available electro-optical cables .

Each floor will be electrically and electronically independent from the other floors and will have its own optical fiber for data transmission. It will be possible to retrieve the tower for "servicing" by activating anchoring releases and thereby forcing the tower to float.

10.2 Material Investigation

Each single hexagonal plane of a tower is made up with a frame whose material should be a good solution to all the problems deriving from the long term operation in a marine environment at large depths. The material should be resistant to the corrosion due to the chloride ions contained in the salt and to the demetallification occurring between metals

within an alloy. It also should be resistant to the deformation due to the high pressure (620 kg/cm^2) and should have light weight. So, pure titanium and titanium alloys are an excellent choice (see also stress calculations below).

10.3 Shipboard Tests

During three oceanographic cruises made by the Russian vessels D. Mendeleev, Vityaz and Akademik Keldish from 89 to 92, three prototypes of possible detectors having different geometrical configurations have been tested. Drawings of how they were made are shown in figure 10.1.

Figure 10.1: Prototypes of the test modules

Two of them were made out of a titanium rigid frame and one with a kevlar rope string. The geometry we have chosen is similar to the detector tested on board of the Vityaz in 1991. It was constructed as an hexagonal frame of thin wall 30 mm diameter titanium tube. In the water, under the buoyancy of the optical module placed at the end of the arm, the lattice opened taking a hexagonal shape with a radius of 7 m. In the center a titanium sphere 55 cm in diameter housed the electronics. The detector has been deployed many times at a depth of around 4000 m. figure 10.2 and figure 10.3 show the apparatus being deployed with the arms folded and fully open.

Several new tests, of two floors at the beginning, in shallow water and in the deep sea, are foreseen. These tests, as well as the results of the first tower, will allow us to choose the final design for the construction of the following towers .

Figure 10.2: Photograph of the deployment in 1991

10.4 Design Options

We have considered two designs :

I) One design is a straightforward extension of the hexagonal autonomous module with rigid arms made up of an assembly of thin Ti tubes, that we used during the tests off Pylos in the summer of 91. The increase of the hexagon radius from 7 m to 16 m can be easily achieved (figure 10.4).

A first production of two prototype floors is under way in Russia. It is planned that the production drawings will be cross-checked by Saclay and by IFREMER (Institut Français de Recherche pour l'Exploitation de la MER) for reliability and successful deployment.

II) Another design uses telescopic arms for easy handling and deployment; we present this telescopic design in more detail below.

10.5 The Telescopic Arms Option

10.5.1 Conceptual Design

The central skeleton of a floor, shown in figure 10.5, is made up of titanium arms which are telescopic, with a total length of 16 m. They are build of 4 m long pieces of titanium rectangular beam, 2 mm thick, which can expand telescopically via a manual lever; figure 10.6 shows some details.

Figure 10.3: Photograph of the deployment in 1991

The optical module pairs are placed at the end of the arm with the help of titanium tubes, while at the center of the floor a titanium sphere of about 1 m diameter is placed, to house all the electronics. At the very bottom of the tower a weight platform of 2000–3000 kg made out of iron beams (e.g. old railroad rails) is attached to the first floor from the bottom via a complex of locks and cables. The tower is held vertically by 7 buoys, with a net buoyancy of 1000–2000 kg. The apices of the floors are connected together by kevlar ropes.

A stress calculation based on this design and on titanium alloy (Ti-6A114Va) has been made, taking into account the hydrodynamic forces during the deployment, the water resistance during sinking and due to the deep undersea currents, the system's buoyancy and the ship's motion. The hydrodynamic forces are given by:

$$F = s \times C \times \rho \times V^2/2 \tag{10.1}$$

for a Reynold number in the interval 80-60000, where C is the hydrodynamic resistance coefficient evaluated via a 1:3 scaled model, ρ is the water density, V is the water flow velocity and s is the middle surface-cross sectional area.

The buoyancy B is a function of the density ρ, g and the volume of the displaced water. The density ρ depends on the salinity, pressure and temperature. The maximum acceleration of the ship due to a possible rolling motion with respect to the water is 0.55 m/sec^2, assuming the oscillation ship's period about 5-7 sec and an amplitude of 1 m. The corresponding maximum speed is 0.5 m/sec.

Figure 10.4: Thin tube design of one floor

10.5.2 Structural Analysis of Stress in the Supporting Arm

A calculation of the maximum stress on the arm structure has been carried out with the commercial Finite Elements ANSYS version 5.0, using 250 3-D elastic elements. Different materials like titanium, titanium alloy (Ti-6A114Va) and two types of fiber reinforced resin, one with glass fiber (GFRP) and one with carbon fiber (CFRP), see figure 10.7, have been examined.

The properties of the above mentioned materials were provided by the manufacturers. The gravitational and water resistance forces have been applied uniformly on the surface. The elements used for the structure assume the materials to be homogenous and isotropic. Such an assumption even if not valid for the reinforced fiber, provides a good approximation. The analysis has been made for a total arm length of 16 m. The forces due to the buoyancy have been applied to the whole structure at 2.07 m from the end of the arm because of the supporting ropes, (position point 10 in Table 10.1) and to the inside end, where the arm is joined to the central structure (pivot point, called position 1 in Table I and figure 10.8) because of the force of reaction. In addition the water resistance during the sinking, the ship motion and the deep sea current forces have been

Figure 10.5: Telescopic design

applied over the whole area. As the four telescopic sections of the arms are expected to be joined via rubber "O"rings of Young's modulus nearly 3 orders of magnitude smaller than that of the arm material, the stresses across the joint interface have been assumed to be spread out over the whole area of contact. Due to symmetry and the nature of the detector structure, no rotation or twisting was allowed and the central joining nodes were constrained about the z-axis. Analyses were carried out for the materials under three loading cases (see Table 10.1).

Position 1 is at the pivot point of the arm and position 10 is at the point where the rope is connected to the arm. The considered cases are :

Case I The arm is fully extended in the sea without moving (only gravity and buoyancy acting).

Case II Arm sinking to the bottom at speeds of 0.5,1.0 and 1.5 m/s (gravity, buoyancy and water resistance).

Case III Arm on sea floor acted upon by transverse sea currents of speed of 0.5-1.5 m/s. These are extreme cases, highly unlikely to occur (e.g. the underwater currents are under 10 cm/s).

In each case we show the results for the point of maximum stress, i.e. for case I position 10 and for case II,III position 1.

The conclusions are that:

1. Pure titanium (yield strength about 170 MPa) * would not be able to withstand any sinking speed > 1.0 m/s or any deep sea current speed > 0.5 m/s with an acceptable factor of safety.

*Reminder: 1 atmosphere $\equiv$ 101325 Pascal

Figure 10.6: Details of Telescopic Module

2. titanium alloy Ti-6A114Va (yield strength of about 800 MPa) would be able to withstand all sinking speed with acceptable safety factors but would fail when the deep sea current would reach a velocity > 1.0 m/s. For this reason we intend to reinforce the weakest link, i.e. make a thicker tube for the outermost piece of the telescopic arm. This is easily and cheaply feasible.

3. GFRP displays low safety factors for all, except the static and low speed sinking cases; although its tensile strength is very high, about 1000 MPa, failures would occur by compression or delamination and the strength in such modes can be up to 5 times lower (200 MPa) depending on material.

4. CFRP (tensile strength given as 1800 MPa, failure stress in compression or delamination as low as 360 MPa) displays low safety factors for the high deep sea current cases.

In conclusion the structural analysis studies indicate that Ti alloy appears to be the best candidate for the construction.

10.6 Specifications for the Mechanical Structure of a Tower

On the basis of the studies mentioned above, we adopted the following specifications :

- The detector's minimum life time should be 10 years.

Material		CASE I	CASE II			CASE III		
			0.5m/s	1.0m/s	1.5m/s	0.5m/s	1.0m/s	1.5m/s
Titanium	Stress	76	4	49	130	130	370	820
	Safety Factor	2.2	43	3.5	1.3	1.3	0.5	0.2
	position	10	1	1	1	1	1	1
Ti-6A14V	Stress	76	4	49	130	130	370	820
	Safety Factor	11	200	16	6.2	6.2	2.2	1
	position	10	1	1	1	1	1	1
GFRP*	Stress	79	6	57	165	135	405	850
	Safety Factor	2.5	33	3.5	1.2	1.5	0.5	0.2
	position	10	1	1	1	1	1	1
CFRP*	Stress	85	6	59	165	155	460	940
	Safety Factor	4.2	60	6	2.2	2.3	0.8	0.4
	position	10	1	1	1	1	1	1

Table 10.1: Results of Finite Elements analysis of stresses in structure
* indicates very approximate values as GFRP and CFRP are not isotropic materials

- A single tower with 12 hexagonal floors should have each of them mechanically and electrically independent.
- Each floor should hold 14 PMT's and have an arm length of 16 m.
- The distance between the floors should range between 20 and 30 m.
- The height of the first floor should be about 100 m above the sea bottom.
- The opacity (i.e. the ratio between the surface of the mechanical structure of a floor and the surface of the hexagon defined by a floor) should be less than 10%.
- The anchoring platform must allow to connect other satellite detectors like seismographs or dark matter detectors.
- Between two floors on the central axis, LED's for the PMT's calibration should be mounted.
- The PMT's locations will be measured continuously with chirped sonars. One transducer for every floor will be mounted. The operation for the deployment of each tower should not exceed 24 hours in time.
- Finally, for the recovery of the telescope the structure will be self buoyant and such that during the recovery the floors are kept at safety distance from each other. In order to be able to retrieve the tower, the tower will be connected to the anchoring mechanism via a system of deep sea heavy duty releases which when activated will severe the connections between the tower and the anchoring. The activation will be done with coded acoustical signals or with the slow controls.

Figure 10.7: Details of the version in Composite Material

10.7 Mechanical Properties of the Transmission Cable

Signals and power are transmitted by an electro-optical cable (see chapter 4). Its mechanical properties are summarized here:

Twelve or eighteen optical fibers are located inside a plastic core and they are surrounded with a copper conductor, which delivers the required power for the operation of the NESTOR tower (as power "return" the sea water path will be used). This conductor will be insulated from the outer steel armour with an insulating sheath. The cable will have a length of about 22km, with three different kinds of armour. The lightest armour (typical diameter 25mm) will be used on the gentle slop of NESTOR site, from the detector location up to the beginning of the steep slope on the shore side. On the steep slope a medium armoured cable (typical diameter 40mm) will be used to withstand the abrasion of the rocks expected to be found there. The heavy armoured cable (typical diameter

Figure 10.8: Graphic mesh of the telescopic arm

60mm) will be used for depths less than 200m. This part will have to withstand abrasion on rocks and water movements expected on shallow waters and its last part where wave action is expected will be located inside a cement pipe conduit up to the surf-free zone. We do not expect that the cable will be subject of man-made dangers, since the area, being very rocky and very steep, is not used by deep sea trawlers. In 10.9 a typical heavy armoured cable is shown.

Typical characteristics of the armoured cable are:

Figure 10.9: Typical armoured electro-optical cable

Diameter of a medium armoured cable	40 mm
Weight in water	2.9 kg/m
Weight in air	3.5 kg/m
Breaking load	500 kN
Permanent allowable load	220 kN
Operating allowable load	350 kN
Torque	1.9 N× m/kN
Hydrodynamic constant	70deg/knots

The cable will be attached to the tower and all electrical and optical connections will be made in air before tower deployment.

Chapter 11

The Optical Modules

The NESTOR Optical Module (figure 11.1) consists of a photomultiplier tube (PMT) inside a high pressure glass housing sphere. The PMT is glued to one hemisphere using an optically transparent silicone gel which provides good optical coupling. To minimize the geomagnetic field inside the tube, the PMT is surrounded by a mu-metal mesh. The sphere contains also the PMT high voltage supply.

No other electronics are contained in the Optical Module.

11.1 The Choice of the NESTOR Photomultiplier

The lifetime and success of a deep underwater detector like NESTOR depend strongly on the quality and proper operation of the photomultipliers it uses.

11.1.1 Requirements

For such a detector the PMTs employed must meet the following requirements :

- High quantum efficiency of the photocathode.

  Quantum efficiency is the parameter which determines the number of emitted photoelectrons. It is crucial in assessing the spatial resolution and the time resolution. Hence the higher the quantum efficiency, of the PMTs used, the better the overall experimental features of the detector.

- Large angular coverage.

  The current design of NESTOR assumes the use of omni-directional units consisting of two back to back optical modules each containing one PMT. Each optical module should cover efficiently the space around it. It is therefore crucial to use a PMT with a large photocathode area and a uniform response over a large range of angles of incident light.

- Good timing response, which will allow a precise determination of the emitted Cherenkov light,

Figure 11.1: The optical module

- Good pulse height resolution for events which deposit light at the single photoelectron level.
- Small dark count rate.
- Large stability in its characteristics, thus ensuring a long, reliable operating life.

11.1.2 The 15 inch Hamamatsu R2018-03

The 15 inch Hamamatsu R2018-03 phototube was selected because of its main characteristics, namely: large (382 mm) diameter, hemispherical bialkali (Sb-K-Cs) photocathode, with high spectral sensitivity for blue light, spectral responseextending from 300 to 650 nm, low thermionic emission, and operating voltage lower than 2500 V giving a gain of 5×10^7.

The 15 inch Hamamatsu is based on the 20 inch Hamamatsu R1449 initially designed for the Kamiokande experiment. It is at present in the third phase of its evolution (R2018-03). Its characteristics have been significantly improved over the 2nd stage.

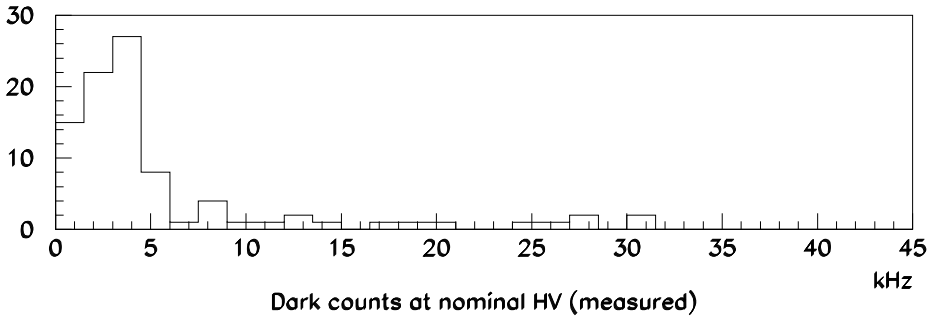

Figure 11.2: The measured dark count rate for all PMTs measured so far.

This PMT employs a venetian blind (13 stage) dynode structure. The parameters have been optimized in order to overcome the inherently low collection efficiency for electrons which characterize this type of dynode structure and to produce satisfactory time response and energy resolution. As a result, the typical value of the transit time spread (TTS) which is the FWHM of the electron transit time distribution, is 5.5ns and the typical value for the peak to valley ratio of the single photoelectron pulse height distribution is 1.4. The typical dark count rate of the PMT for pulses larger than 1/4 of the one photoelectron average pulseheight amplitude is less than 10kHz at a temperature of 25C (Figure 11.2). It is expected, from tests performed using the 20 inch PMT that the dark counts will drop by at least a factor of 2 when operated at 14C, the ambient sea temperature, instead of 30C, the ambient temperature during testing [166].

11.2 Tests Performed on NESTOR PMTs

In order to ensure that all the PMTs which will be employed for NESTOR meet the requirements set, operate properly and reliably and, at the same time, to create a database of all important parameters of each PMT, a series of tests are performed on each PMT following its delivery.

It is not possible to test all the properties of the PMT in the Lab. Quantum efficiency, cathode, cathode blue and anode luminous sensitivities are measured and guaranteed for each PMT by the manufacturer. Further tests performed on each PMT at the Lab include:

- Measurement of the single photoelectron pulse height distribution (peak to valley ratio, gain of the PMT).
- Measurement of the TTS for single photo electron pulses.
- Study of the photocathode and anode uniformity. The response of the PMT is measured as a function of the position of incident light on the photocathode.
- Study of the variation of the PMT gain as a function of the supplied voltage.
- Study of the TTS variation as a function of the amplitude of the incident light pulse.
- Determination and long term monitoring of the PMT dark count rate.
- Determination of rates for pre pulses (pulses arriving between 100 ns and 15 ns before the main pulse), late pulses (pulses arriving between 15 ns and 100 ns after the main pulse) and after pulses (pulses between 100 ns and 30 ns after the main pulse).

Results from some of these tests are discussed below.

11.2.1 Test Procedure

Following the PMT arrival, and after checking that the parameters tested by the manufacturer are within the specification limits, each PMT is set to a moderate voltage (1700V) and the output is examined to ensure that the PMT appears healthy. The PMT is then 'baked' at a higher voltage(2000V) for at least 24 hours, during which time its dark noise is continuously monitored. The 'baking' takes place in a dark room capable of baking up to 60 PMTs simultaneously. Each PMT is then taken from the 'baking' room and placed inside a light tight black box, situated in another black room, where the set of tests is completed. The PMT is then assigned an EMI PS2000 (Modified) power supply and is returned for further, long term, 'baking'. The long term monitoring of the PMTs after initial testing yields information on the stability of the PMT under operation conditions and allows identification of any aging effects that could create problems in their use as part of the detector.

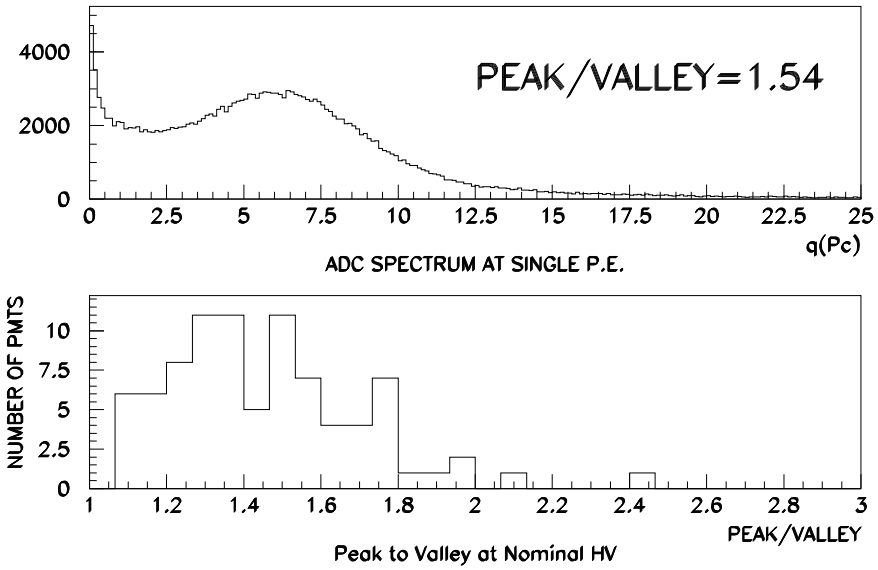

Figure 11.5: ADC spectrum under single photo electron conditions. The top plot shows a typical ADC spectrum obtained at single p.e. conditions, with a 1.5 peak/valley ratio. The lower plot shows the histogram of the peak/valley ratio for all PMTs measured so far.

11.2.2 Test Setup

The tests, as well as the dark noise monitoring, are performed using a software specially developed for this purpose. The test setup (Figure 11.3) consists of a light tight dark box containing a stand which holds the PMT within a grounded mu-metal mesh which is more than 93% transparent. Outside the mu-metal mesh, a selection of LED's is mounted on a movable arm, at a distance of approximately 2cm from the surface of the PMT. The position of the LEDs are controlled by stepping motors.

Full control of the light seen by the PMT is achieved, under computer control, by using the step motors to position the LED's, then sending pulses of known amplitude and duration to the chosen LED. Two different pulse generators are used for this. A CAEN pulser is used to drive an LED at a variable pulse amplitude and duration for the many photo-electron tests, while a 'Picosecond' pulser giving pulse amplitudes over 30V and a rise time of 0.5 ns is used to drive a reverse biased LED in order to achieve single photo-electron conditions with accurate timing. Full control of the system, including the supply and monitoring of HV to the PMT are achieved in a CAMAC system controlled by a PC. Data are recorded using a TDC, an ADC, a multi-hit TDC and a 12 channel scalar. A schematic of the setup is shown in figure 11.4.

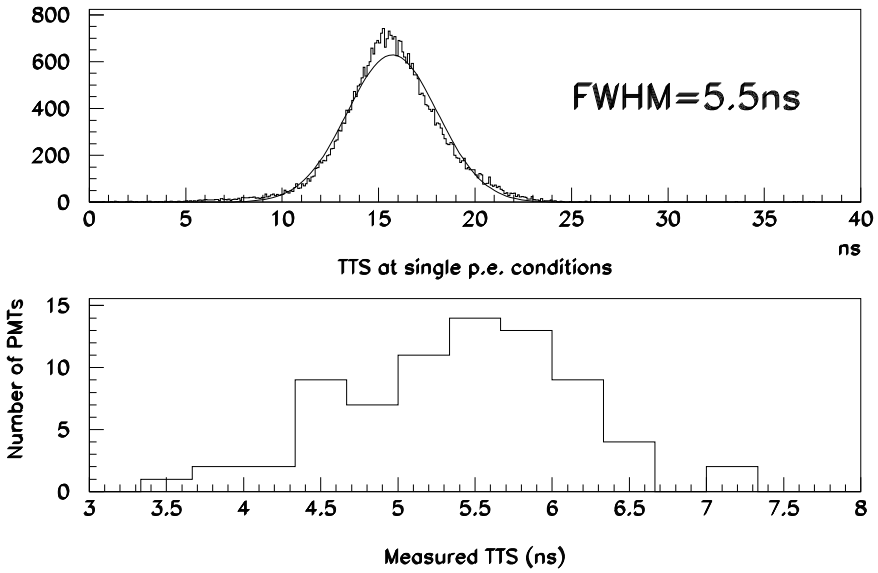

Figure 11.6: TDC spectrum under single photo electron conditions. The top plot shows a typical transit time distribution obtained under single p.e. conditions. The lower plot shows the histogram of the TTS for all PMTs so far measured.

11.2.3 Results of the Systematic Tests

Figure 11.5 shows a typical ADC spectrum taken under single photo electron conditions and a histogram of the values of peak-to-valley ratio obtained for the PMTs received so far. The peak obtained from the single photo electron is clearly visible separated from the dark noise. The peak-to-valley ratio is 1.5. Typically the peak to valley ratio is better than stated in the specifications.

Figure 11.6 shows the TTS (transit time spread) obtained at the single photo electron level for a typical tube, and a histogram of the values of the TTS for all tubes so far tested. The typical measured value is 5.5ns, which compares well with that stated in the specifications.

The variation of PMT response with the position of the incident light with respect to the photocathode is shown in Figure 11.7. It can be seen that the PMT has a nearly uniform response inside the region of the photocathode ($|\theta| < 63$degrees). Typically, the measured dark counts are below 10 kHz, and always below the 40 kHz stated as a maximum in the manufacturer specifications. The measured prepulses are less than 2.0%, while late and after pulses are below 3%.

Experience from over 10 years of use of Hamamatsu PMTs by Kamiokande[**?**] show that the gain stay constant to within 6% over many years of operation. Experience from IMB corroborates this[**?**]. For this reason it is not intended *not* to control the HV of the PMT during the experiment. Instead, each tube will be set to an operating HV determined in the Lab based on the tests performed.

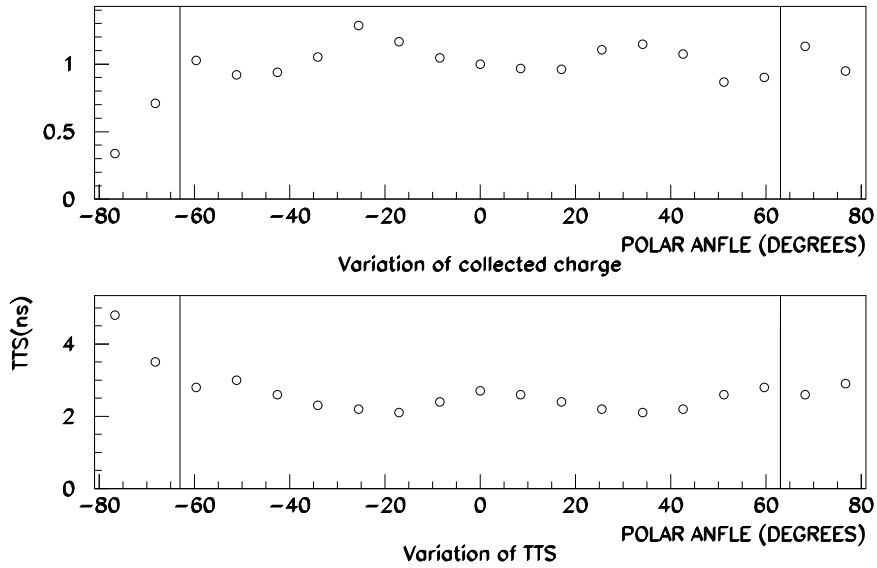

Figure 11.7: Variation of collected charge and TTS with polar angle θ at the many photo-electron level. The top plot shows the variation of the amount of charge collected (normalized to the zenith position). The lower plot shows the variation in the value of the TTS. The solid lines at 63 degrees indicate the limits of the photocathode.

11.2.4 Study of the Linearity of the PMT Response

Tests have been performed in Athens and in Saclay to determine the linearity range of the NESTOR phototube.

The Athens tests used a LED driven by a fast pulse generator. In Figure 11.8 the PMT signal pulse height is plotted as a function of the amplitude of the LED driving pulse. The PMT signal displays a good linearity for pulses up to 6V corresponding approximately to 100 photoelectrons.

In the Saclay tests, with the PMT operated at a HV of 2000 V, a typical pulse of 50 mV amplitude, 8 ns risetime and 12 ns falltime was observed for a single photo-electron (PE) signal. The peak/valley ratio was 1.2 and the noise rate above 1/4 p.e. was 5 kHz.

The test bench (Figure 11.9) consisted of:

- a fast pulse generator used to drive the light source
- two different light sources : a LED and a laser diode both emitting red light ; the source illuminated 2 optical fibers, one going to the R2018, the other one going to a Philips XP2020 PMT (operated at low voltage to ensure its linearity) used to monitor the light flux
- the R2018 PMT enclosed in a light tight box ; the optical fiber was connected to a feedthrough on the wall of the box 15 cm away from the PMT photocathode. The light spot on the photocathode was approximately 15 cm diameter.

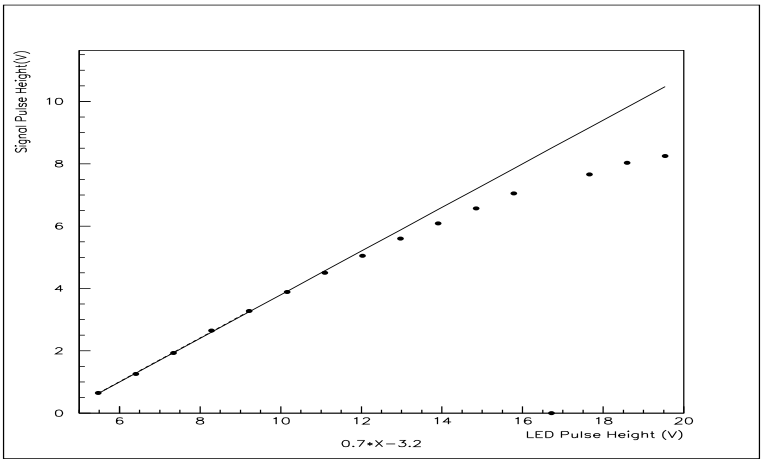

Figure 11.8: The PMT signal pulse height as a function of the LED amplitude

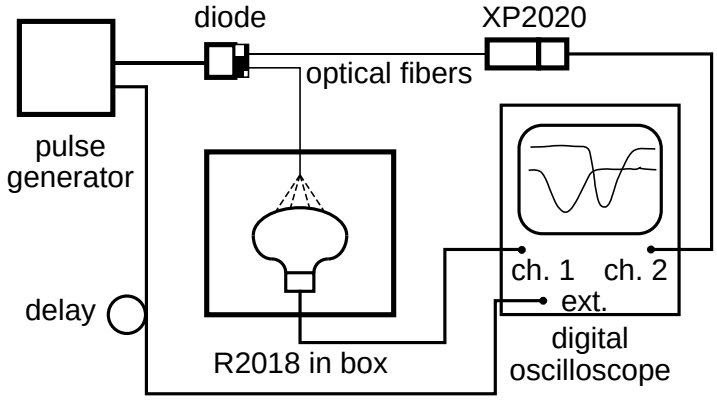

Figure 11.9: The testbench in Saclay

- a digital oscilloscope triggered by the pulse generator which measured the R2018 and XP2020 signals. Signals were characterised by their area and their pulse height .

The two PMTs signals were recorded for different settings of the light sources. The variation of the R2018 signal area as a function of the number of PE shows a behaviour consistent with that in the Athens tests.

More detailed studies are under way. The use of a more intense light source should allow to determine the overall PMT signal dynamic range. This is a basic parameter to which the transmission link dynamic range has to be matched. The physics requirements should dictate the type of compression, if any, to be be implemented prior to the transfer of the signal.

11.3 PMT Power Supply

The high voltage power supply we have chosen is the modified PS2000 power supply by THORN EMI Electron Tubes. This power supply has the following specifications:

Input voltage	+24V ±10% dc
Input current	350 mA at 24V dc
Fully adjustable output voltage	50 to 2500 V
Output current	0 to 1 mA

The output voltage is controlled by an externally adjusted control voltage from 0 to 10 V. The output voltage can be monitored using the ÷1000 test point of the unit. The output ripple is 20 mV p-p from 1 Hz to 100 KHz, while the operating range of temperature is 0 to +50°C. The MTBF (Mean Time Before Failure) is 50000 hours at +25°C. The unit is enclosed in a metallic box (100mm × 50mm × 30mm).

11.3.1 Evaluation Tests of the PS2000 (Modified)

We have tested thoroughly this supply unit using the setup described in the diagram (11.10).

Several series of measurements were performed in order to evaluate and accept each of the 200 power supplies that we have purchased.

First we checked each power supply in order to verify the general condition of each unit. We have tested all input and output voltages and currents of each unit i.e. control voltage, monitor voltage, input current, output voltage and output current.

Then we evaluated the performance of a random sample of 10 power supplies in order to check the high voltage output as a function of the control voltage with the nominal supply voltage of 24 V :

1. Measurements of the monitor voltage (i.e. High voltage divided by 1000) for every control voltage setting were taken for 10 minutes with a rate of 1 sample per second. The time, high voltage output and control voltage were measured. The mean values of high voltage and control voltage were calculated and plotted. Typical results are shown in figure 11.11 (the error bars are too small to be shown).

Figure 11.10: Diagram of the power supply measuring setup.

2. Measurements of the high voltage output as a function of supply voltage were taken, keeping the control voltage constant. Seven values of the supply voltage were used from 20 to 26 V with a step of 1 V i.e. from 4 V below the nominal value to 2 V above. Measurements of the monitor voltage, at a rate of 1 sample per second, were taken for about 12 hours per input voltage setting. Mean values of high voltage and control voltage were calculated and typical results are shown in 11.12.

3. A third series of measurements were performed in order to check the stability of the high voltage output. Stability was defined as the worse case peak to peak over the HV. The value of the short term (i.e. in any 10 minutes period) stability was found to be better than 0.2%.

11.3.2 Presetting the High Voltage

Since the Hamamatsu photomultiplier's gain does not change in time over many years of operation [**?**, **?**] we can preset each power supply to the appropriate HV so the corresponding photomultiplier will have the required gain. This is achieved easily with an adjustable resistor chain, powered by the input voltage of 24 V(figure 11.13). The output of the resistor chain sets the control voltage of the PS2000(modified) unit. The power supply will be installed into the BENTHOS high pressure housing with the photomultiplier.

11.4 Connectors/Penetrators

Electrical connectors are needed on the Benthos glass spheres and on the titanium spheres for the signal and the low voltage for the power supply.

We can use 4-conductor connectors ("2-pin"), or, if we transmit low voltage and signal on the same cable (see next section) we can use 2-conductor penetrators ("1-pin").

Figure 11.11: High voltage vs. control voltage.

Optical connectors/penetrators are needed on the titanium spheres to let through the optical fibers.

Electrical connectors are also needed on the LED calibration Benthos spheres (see chapter 6).

For our tests we have been using various types of connectors, research to chose the most appropriate ones is under way, in collaboration with marine research institutions.

11.5 Electrical Connections Between Benthos and Titanium Spheres

In order to reduce the risks we decided to drill only one hole on the glass (Benthos) spheres. We are going to use a single electrical connector on each side of the cable. The connector has one prong and two conductors. The cable is RG-58 (50 Ohm coaxial) appropriate for deep sea.

The pulse of the PMT is a fast pulse and it is easily coupled with capacitors to the cable. We maintain a continuous path for the low voltage (24 volts) which is required to feed the HV supply. We use a big capacitance in series to the signal and we introduce a big inductance in series to the dc line so that the overall impedance does not deviate significantly from 50 Ohm. The connector and its leads is not matched to 50 Ohm and we have to keep the leads as short as possible in order to minimize reflections and deterioration of the signal.

We performed a test using the parts as in Figures 11.14 to measure the effect of the connections on the signal. Using a narrow pulse with 4 ns rise time we found that the reflected signal is less than 3% and the deterioration of the rise time less than 1 ns. During this test we found that the HV supply is feeding back some noise through the low voltage line. For this reason we introduced a simple filter in front of the supply. The noise remaining after the filter is about 1.5 mV rms.

Figure 11.12: High voltage vs supply voltage.

11.6 The Optical Module

The NESTOR Optical Module consists of a hemispherical 381 mm (15") diameter photomultiplier tube (PMT), type R2018-03 made by Hamamatsu Photonics Inc. glued inside a high pressure glass housing sphere (fig. 11.1). The PMT base is soldered to the dynodes by Hamamatsu and is covered by them in a shower proof potting compound, using the same techniques as for the PMTs of SUPERKAMIOKA.

The phototube is protected from the hydrostatic pressure by the high pressure protecting glass housing (Benthos 2040-17H model) which is composed of a pair of precision matched glass hemispheres with finely ground flat edges. It has been the standard oceanographic instrument for about 50 years. The Benthos sphere has an outer diameter of 432 mm (17") and wall thickness of about 14 mm. Before delivery each Benthos sphere has been tested at the factory (two times) in their pressure tank at a pressure of 670 atm for one minute each time.One hole is drilled in one of the hemispheres at about 25^0 from the pole of the hemisphere for the combined signal and power connector (one pin, two conductors).

The PMT is fixed to the other hemisphere, which does not have any holes, using an optically transparent silicone gel (SEMICOSIL 912) with a refraction index of 1.403. In this way good optical coupling between Benthos sphere glass and PMT glass is achieved. Moreover the PMT is protected from possible damage because of the compression of the Benthos sphere in deep sea (It is calculated that the Benthos sphere shrinks approximately 2 mm in diameter at a depth of 4000 m).

To minimize the geomagnetic field inside the tube, the PMT is surrounded by a mu-metal mesh made out of 0.8 mm diameter wire, 93% transparent. The PMT high voltage supply is a modified EMI PS2000 power supply, which takes 24 V DC input and gives out up to 2500 V is mounted on a round circuit board, which is positioned around the neck of

Figure 11.13: Preset configuration for the PMT voltage.

the PMT. The value of the operating H.V. of each PMT has been decided after detailed gain measurements made on every one of the PMTs in the Lab and the EMI PS2000 output is set to this operating value with no further control possible. A cross-sectional view of the NESTOR Optical Module is presented in figure 7.9.

11.7 Tests on the Optical Modules

Detailed measurements have been carried out in the laboratory using a monochromator in order to determine the wavelength dependence of light transmission in the NESTOR Optical Module materials (figure11.15).

Clearly the probability for failure of a Benthos sphere is proportional to the number of the holes drilled in it, for this reason we drill only one hole in each Benthos sphere (while DUMAND drills three holes per Benthos sphere).

Each connector is pressure tested by the manufacturer and then by us in the Small Pressure Tank (usable volume : diameter 200 mm, length 1000 mm, figure 11.16b) up to 600 atm. In the same tank we test all small experimental components. After the installation of the connector we retest the empty Benthos glass housing at 600 atm for 20 minutes in our Large Pressure Tank (useable volume : diameter 500 mm, length 500 mm, figure 11.16a). To minimize the failure under pressure of an Optical Module after deployment, we test again the now assembled Optical Module in our Large Pressure Tank at a pressure of 600 atm for 20 minutes.

Every time that 14 Optical Modules (i.e. enough for one floor) are assembled they will be cabled up with their corresponding fast and slow electronics, they will be throughly burnt in and tested in the Laboratory. After passing the successful Laboratory tests the 14 Optical Modules, mounted on a hexagonal frame (fig. 11.17) with their corresponding Titanium sphere filled with all the fast/slow electronics will be immersed at a depth of 50 meters in the Bay of Navarino. They will be hooked up to a 1200 m long electrooptical cable (already in Pylos, fig. 11.18) whose other end will be at the Pylos Laboratory. The

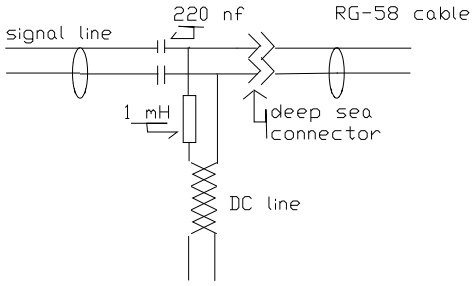

Fig 1.The signal connection on the titanium sphere

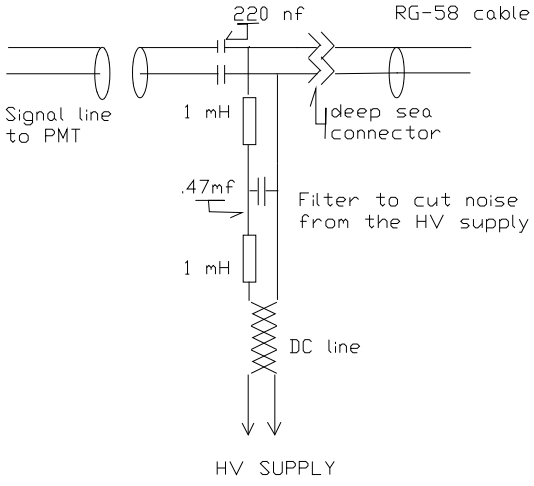

Fig 2. Signal connection in the Benthos Sphere

Figure 11.14: Connections on the Titanium and Benthos Spheres

Figure 11.15: Wavelength dependence of light transmission

Figure 11.16: a) Photograph of the Large high pressure tank, b) of the Small high pressure tank (upper half is shown)

PMT's will be covered in black opaque plastic and will be protected by hard hats. This way the full system will be exercised on electronic noise for a whole week. After the successful completion of this test the 14 Optical Modules and the corresponding titanium sphere will be stored waiting final deployment. The reason for this bay test is that oceanographers tell us that most accidents with water ingress happen during the first 10-20 meters of depth, after that the hydrostatic pressure helps to seal better. We feel that this final predeployment test is important.

11.8 A Water Tank to Study the Response of the Optical Modules

The detailed knowledge of the optical module response is essential for understanding the detector performances as well as for use as an input in the simulation of physics events. The goal of our test set-up is to get closer to real experimental conditions by measuring the signal from the PMT in its Benthos sphere for Cerenkov light emitted in water. We intend to study the signal as a function of the relative angle of the PMT axis with respect

Figure 11.17: Optical Modules on the hexagonal frame

Figure 11.18: The power and optical cable for the Navarino bay tests

to the muon direction, and in a limited range as a function of the distance of the muon trajectory to the optical module. The set-up consists of a water tank in which a NESTOR optical module is immersed, and of a detector which defines the trajectory of muons with respect to the optical module. Cosmic ray muons and a muon beam will be used.

The 1.35 m diameter 1.50 m high cylindrical stainless steel tank (fig. 11.19) is filled with purified water. A small pump circulates the water through filters and resin exchanger units. Purity of the water is permanently monitored by measuring its resistivity. The transmission length will thus be comparable to that in deep water. This is, however, not a crucial point, since relative measurements as a function of the incident angle do not depend on it.

The inner walls of the tank are lined with black paint in order to minimize reflection and scattering of the emitted Cerenkov light. The monitoring of the constancy of the conditions for light transmission in the water and scattering on the tank walls is performed using a blue LED emitting through a glass window a collimated vertical light beam from the top of the tank and detecting the reflected/diffused light with a phototube viewing the tank through another window also located on top of the tank. For a more precise monitoring we may use a direct view detection.

The optical module consists of the R2018 PMT housed in its Benthos sphere with a

Figure 11.19: The test tank

μ-metal shield [**?**], which can be rotated around a horizontal (x) axis. The center of the Benthos sphere is located approximately 0.35 m off the tank axis and 1 m from the top. The polar angle (with respect to the horizontal z direction) of the PMT axis (symmetry axis of the PMT) can be varied from 0^o to 180^o (fig. 11.19). Thus the average zenith (θ) incidence angle will be varied. The ϕ angle will vary for different tracks, (see definitions in 11.3) but we can also rotate the PMT and place it in different positions. The response of the optical module is calibrated against the reference signal from a Philips XP2020 phototube using a pulsed blue LED which illuminates the R2018 through a third window on top of the tank and the XP2020 through an optical fiber.

Muons are selected using two groups of two scintillator hodoscope planes measuring orthogonal coordinates. Each plane consists of six 0.80 $\times$ 0.125 $\times$ 0.005 m elements. When using cosmic rays the two groups are respectively installed at the top and at the bottom of the water tank. A 0.20 m lead absorber set immediately above the lower group allows triggering only on muons with energy larger than 800 MeV which thus saturate Cerenkov light emission in the water. For measurements planned at CERN in the halo of the 190 GeV M2 muon beam the detectors will be set in vertical planes upstream and downstream of the tank. Plastic scintillators are read at one end by XP2072 tubes and define the trigger. In order to reject cosmic ray showers as well as to allow unambiguous track definition, only triggers with a single hit in each hodoscope plane will be considered.

The set-up is presently under construction. It is expected to be completed by July 1995 and we have been accepted for parasitic run in the M2 muon beam at CERN.

11.9 Power Supply and Seawater Return

The power supply for the experiment is one important though not very sophisticated component of the shore station, beside the other main parts of the shore station, the central control system and the data acquisition and storage system. The design and lay-out of the power supply unit has to meet the demand of the NESTOR - experiment with all of its components. Therefore the power demand depends on the power requirements of the optical modules, the floor control units and the various environmental components as well as of the in-situ electronics for data digitizing and data transfer.

A complete tower consists of 12 floors with 7x2 optical modules - OM - (on each site of the hexagonal floor 1 up and 1 down looking) on each floor. So a total of 168 OMs has to be operated and supplied from the shore station. With an upper power limit of 25 - 30 W per module (including in this estimate all the other, partly not yet defined power consumers) the DC power supply has to be made out for a total 5 - 6 kW. In order to follow varying demand situations resulting from possible shut-downs or failures in the DC/DC-converters separately supplying the 12 floors the power supply has to be controlled by the central control computer and in case of emergency be switched off automatically. The general power requirements and the design of the power supply unit therefore are very similar to the already operational DUMAND equipment [**?**] and it can be considered as state of the art.

According to the present planning the data transfer and the power supply between the shore station and the NESTOR-site about 25 km off the shore of Methoni at a water depth

of 3800 m is performed via an optical fiber cable consisting of 12 (or more) monomode optical fibers with a concentric mantle of copper around the fibers and a cover/armor of fiber enforced plastic. Whereas for the bi-directional communication requirements between the land station and the deep sea experimental installation with 12 floors the number of available optical fibers with one fiber per floor is sufficient, the power transfer can only make use of the copper mantle in the cable as one metallic conductor. In order to have a complete electric circuit either a second concentric copper mantle has to be manufactured within the cable which would increase the diameter of the cable, its weight and of course its costs, or the seawater has to be included in the DC-power transfer which usually is referred to as "seawater return".

That seawater is a conductor for electric currents is a well known fact. In metallic conductors the electric charge is carried by the electrons available within the metal in the conducting state whereas in an electrolytic solution like seawater the charge carrying entities are the ions into which the salt molecules disintegrate while dissolving in the water. As the result of this process ions with opposing charge, cations and anions, are present in solution among the water molecules. These ions depending on their individual charge and size are surrounded by a shell of water dipoles because of the electrostatic ion/dipole interaction. An electric current through a so-called "second order conductor" like seawater therefore, because of the applied electric field, consists of the movement of such more or less hydrated ions through the matrix of water molecules similar to the flow of spheres through a viscous medium.

According to these differences in the elementary conductive process between metallic and electrolytic conductors it is understandable that the specific resistance of metals is considerably lower than of salt solutions in water in general or seawater in particular. So at 20°C the specific resistance of copper is 1.78×10^{-8} ohm meter, the respective value for seawater amounts to about 0.23 ohm meter which is higher by more than 7 orders of magnitude. The resistance of a conductor R with length l and cross-sectional area A can be calculated according to $R = \rho \times l/A$ with ρ as specific resistance of the conducting material. For a copper conductor as component of the fiber-optic cable with a length of 25 km (as for NESTOR) and an annular cross-section of about $21mm^2$ (di = 3 mm, da = 6 mm) the total resistance can be calculated to be $R_{Cu} = 21.3\Omega$. The same calculation for a seawater conductor of identical dimensions would result in a total conductor resistance of $R_{Sea} = 274 \times 106\Omega$ which seems to indicates that such a "seawater return" is unreasonable, inappropriate and cannot be used for power transmission at all. This situation is completely different though when instead of a well defined and limited cross-sectional area A so-called "open cell configurations" or "open electrodes" are used as in the case of the planned seawater return for NESTOR with two electrodes, one completely immersed in the surrounding seawater at some near-shore position and connected by cable to the shore station and the power supply , the other connected to a "fan-out unit" in the depth close to the bottom of the sea in the vicinity of the experiment. In this case the cross-section A of the electrode set-up approaches infinity with the result that the electric resistance of such a seawater return is in the order of 1 Ω or less depending on the area of the electrodes. It has been shown in several test runs in the past - for the planned NESTOR design as well as for the DUMAND experiment - that currents up to 20 A with such a seawater return can be operated stable to the milliohm level over many

hours which is an indication of the appropriate behaviour of the electrodes. In summer 1993 for a time period of about 7 weeks, from June to August, a test set-up consisting of 2 electrodes about 200 m apart at a depth of approximately 10 m has been operated in the Bay of Navarino at Pylos. A current of about 18 A was transmitted between the electrodes with an applied voltage of 22 V resulting in an overall resistance for the seawater return of 1.22 ohms.

In August 1991 a similar preliminary test of the seawater return has been performed during one week at the DUMAND site off the coast of the big island of Hawaii from the NSF ship ALPHA HELIX. The electrodes tested were made from Graphite (23 cm x 24 cm), from platinized Titanium (Platinum 20 cm x 20 cm), and from Iron (St 37 20 cm x 20 cm). The basic concept for the experimental arrangement consisted of one electrode suspended from the ship near the surface at a fixed depth of about 10 m (usually the anode), whereas the other was attached to a 3 conductor cable of about 5000 m length on a winch and was lowered to variable depths. The actual depth was controlled by an acoustic pinger which was attached to the cable just above the electrode. It was shown during these tests in the Pacific Ocean that even with the relatively small electrodes used a current of 4 A (upper limit of the available power supply unit) could be provided for the full water depth of 4300 m with voltages between 3.3 V (iron) to 6.0 V (graphite). The choice of the electrode materials depends on the electrode processes and therefore on their polarity. At the cathode (negative polarity) hydrogen is developed from H+ ions of the water whereas the anodic (positive polarity) reactions result in the development of oxygen from OH- ions and chlorine from Cl- ions in the sea water. Because of the hydrogen development the cathode material is not critical and can be iron, titanium or platinum, the anode material in contrary should be stable against developing chlorine and therefore platinum or platinized titanium is the best choice for long time operation.

Chapter 12

Data Transmission

12.1 Introduction

Each floor will have its own electronics, monitoring and controls housed in the titanium sphere at the center of the hexagon.

The signals for all fired PMTs will be transmitted over a distance of 25 km. We want to be able to transmit to the shore laboratory, in real time, the complete pulse of each PMT signal, keeping the time coherence between PMTs. This feature of the data transmission, that distinguishes NESTOR from the other neutrino telescopes, has many advantages:
1) real time control of the behaviour of the single PMT during data acquisition
2) trigger logic decided on shore (maximum flexibility)
3) the knowledge of the pulse shape.
The last point could be very helpful to distinguish different physics events. The pulse shape is expected to be muon energy dependent for energies greater than about 100 Gev, but in first order and within the limits imposed from statistics, independent from light absorption in the sea water. For instance, muons of different momenta and at different radial distance from a PMT could give the same number of photoelectrons (p.e.), but a different pulse shape: in the two cases the ratio between the number of p.e on the tail of the pulse with respect to the number in the peak is expected to be different. The same could happen for events with more than one muon, for which the pulse shape will play a crucial role in their identification. MonteCarlo calculations of these effects are at present in progress.

The transmission method of the PMT pulse shape on the optical fibre is strictly related to the characteristics of submarine multifibre optical cables that are commercially available. If a 200 fibres submarine cable were affordable the signal transmission could be achieved with one fibre per phototube. In this case a simple solution, in order to have a high (>10 years) mean time between failure (MTBF), would be to provide each PMT with one laser and to modulate the light power of the laser with the anode current. An interesting possibility for data transmission, related to the availability of such multifibre cable, is to send from the shore a laser signal to each PMT and to use the PMT pulse to drive the reflectivity of a Multiple Quantum Well modulator, close to the PMT and coupled to the fibre (See Section 4.5.2). This technique has been developed by the RD23

Collaboration [171] and it is still under study.

The collaboration has investigated a possible transmission method based on 12 or 18 fibres submarine optical cables at present available (ALCATEL, AT&T, PIRELLI etc). With such a cable the use of one fibre per (at least) one floor is mandatory: signals from the 14 PMTs of each floor are first multiplexed and then transmitted on one single fibre. The data of the whole tower are transmitted on 12 fibres.

Different methods have been examined:

1. digitization and time multiplexing
2. amplitude modulation and frequency multiplexing
3. frequency modulation and frequency multiplexing
4. wavelength division multiplexing

The last three methods are discussed in Section 4.5.

The first one has been retained by the INFN-Rome group and is in the most advanced state. The collaboration will probably choose this one as the main option, described in detail in Sections 4.3 and 4.4. In this scheme the signal of a PMT is sent to the Titanium sphere at the center of the floor, which contains the electronics for the 14 PMTs. The signal is first sampled with a Flash A/D, then multiplexed together with the signals of all the PMTs of the same and of the adjacent floor. The multiplexed signal modulates a laser and the light output is sent via an optical fiber to the fan-out sphere where 12 fibers enter the electro-optical cable. One laser per floor transmits to shore the data and the informations of the 28 PMTs of every two adjacent floors. The PMT pulse data are transmitted only when the result of the digitization is over a certain threshold. The transmission contains the A/D samples together with the time when the PMT pulse amplitude crosses the threshold (threshold time, further on also referred to as "event time") and pulse information. The synchronization between signals of different PMTs is assured from the transmission of a unique Master Clock signal from the shore to the 12 floors and from a synchronous answer sent from each floor to the shore. This allows also a correlation of the PMT event time with the on shore time.

On shore the data of each PMT collected in a time window of 6144 μs, periodically cleared, are memorized in a RAM (data RAM). Moreover the event time and the charge are extracted from these data and used from a dedicated processor ($DECPeRLe_1$) to build a first level trigger.

Once the trigger condition is met, the full PMT data collected in the data RAM are read using the event number as memory address.

12.2 Optical Link

The transmission of the signal over 25 km forces the choice of a single mode (or monomode) optical fibre and of a laser as light source. Power transfer to the NESTOR tower and data retrieval to the shore will be performed with an electro-optical cable. For the data transfer

and the telemetry support we will use the standard deep sea electro-optical telecommunication cable. It is composed of (at least) 12 monomode optical fibers, one for each floor. Typical characteristic of the fibers are:

Core diameter		10 μm
Average attenuation	At 1300 nm	0.36 dB/km
	At 1550 nm	0.20 dB/km
Dispersion	between 1280 and 1330 nm	$\leq$ 3.5 ps/(nm·km)
	between 1525 and 1575 nm	$\leq$ 18 ps/(nm·km)

We see that the loss of optical power at $\lambda = 1550$ nm is 0.2 dB/km. The optical receivers working at some Gbit/s show an error probability of the order of 10^{-9} for incident optical power of about -20 dBm (0.01 mW). Since present lasers are able to send on fibre more than 0 dBm (1 mW) the light attenuation ($<$ 6 dB at $\lambda = 1550$ nm over 25 km distance) is not a problem.
The chromatic dispersion for a normal (not dispersion shifted) optical fibre can rise to 18 ps/(nm·km); the Distributed Feedback lasers (DFB) have a spectral width close to 10 MHz at $\lambda = 1550$ nm. The resulting bandwidth of the optical link (fibre and laser) is then much larger than the data bandwidth transmission.

The mechanical structure and properties of the cable were described in chapter 2.

12.3 Off Shore Electronics

12.3.1 Front End

The main purpose of the electronics for the data transmission is the detailed description of the amplitude and time characteristics of the PMT signals. In each floor the signal of each PMT is sampled and digitized.

A maximum bandwidth of 100 MHz has been observed in pulsing a HAMAMATSU PMT used in the NESTOR experiment with a very short light pulse from an LED, so that the Nyquist limit of the sample frequency is 200 Msample/s. A good compromise among sampling frequency and input signal dynamics has led to choose an 8 bit A/D converter (256/1 of dynamics) at 300 Msample/s, saturating at 2 Volt input signal. The gain of each PMT is chosen in order to have 30 mV for a 1/4 of the average amplitude of a single photoelectron (p.e.) on the 50 Ω anode resistive load. At this gain the PMT, if pulsed with an LED light, shows a linear pulse height up to an output of $\sim$ 6 V, while at $\sim$ 8 Volt the deviation from linearity becomes $>$ 20% (see chapter 3).

The high voltage setting for the PMT ensures a good efficiency for the single p.e. detection and high fidelity in the reconstruction of its pulse shape. In order to get information even for pulses with an amplitude which saturates the A/D converter, the total charge of each pulse (Q_{tot}) will be measured independently from the amplitude sampling, using the same A/D converter, so that the total charge will be measured and the information about the "tail to peak" ratio (see the introduction) is kept, even for a pulse saturating some samples of the A/D.

12.3.2 Transmission and Synchronization

Redundancy and independence among floors are the fundamental requirements for the data transmission to get high MTBF. Each floor of one tower is provided with one laser working at 1550 nm and a receiver, working at 1300 nm, coupled to one optical fiber. The data transmission is organized grouping the 12 floors of one tower in 6 pairs. The data of one pair of floors are transmitted, at the same time, from each one of the two laser of the pair, gaining then a factor of two in the redundancy of the transmitted data (figure 12.1).

The transmission is performed via a bidirectional optical link (Hot Rod, [172]) synchronized at 20 MHz (Master Clock). The Master Clock provides the synchronization of the data from the 12 floors. This clock, sent from shore via a 1300 nm laser, is synchronized with an external reference time (e.g. Cesium atomic clock). This general synchronization structure will be maintained also for the measurement of the times in different towers. For each FADC a 300 MHz frequency is obtained with a Phase Locked Loop (PLL 15x in figure 12.2) multiplying 15 times the Master Clock frequency. In this way, apart from constant relative delays that must be measured, the time of the signals of each PMT is known with respect to the Master Clock time.

The figure 12.2 shows the off shore electronics, the organization of the signals of 14 PMT of a same floor and their transmission together with those of the 14 PMT of the adjacent floor.

A 15 bit Time Register (TR) is common to the read out electronics of the PMT of the same floor. This counter is continuously incremented by the 300 MHz clock. Every 27000 counts (corresponding to 90 μs) a Terminal Count signal (T_c) is generated and the TR is reset. In this way a PMT event time t is defined, with respect to an initial time, from the number M_{TC} of T_c signals and the number N_{TR} of TR counts at that time

$$t = M_{TC} \cdot 90\mu s + N_{TR}/(300MHz) \tag{12.1}$$

The coded time of the T_c pulse is transmitted to shore in synchronism with the transmitting data cycle, so that the number M_{TC} is counted on shore. For each PMT the Time Register count N_{TR} is read (in 4 nibbles *) at the event time, written in a FIFO memory buffer together with the A/D data and then synchronously transmitted.

Each A/D generates continuously a flux of data at 300 Mbyte/s. In order to reduce the data transmission rate of two adjacent floors to that of the Hot Rod serial link (800 Mbit/s), a zero skipping is operated. At the time (event time) when an A/D sampled voltage value is found greater than a threshold value, adjustable from shore, a PMT "Read Cycle" starts and a PMT event is written in a FIFO memory buffer. The Read Cycle time consists of at least five subsequent time slots. During each time slot five bytes of data and informations are written in five FIFO. The data content depends from the position of the time slot inside the Read Cycle: in the first four time slots four consecutive A/D pulse samples are made for each time slot, for a time of

$$4 \cdot 3.\overline{3}ns = 13.\overline{3}ns$$

In this case the information byte contains one nibble of four flags (INFO:Over Threshold, Over Flow, FIFO Full and Terminal Count flags) and one nibble of the TR count relative

*1 nibble $\equiv$ 4 bits

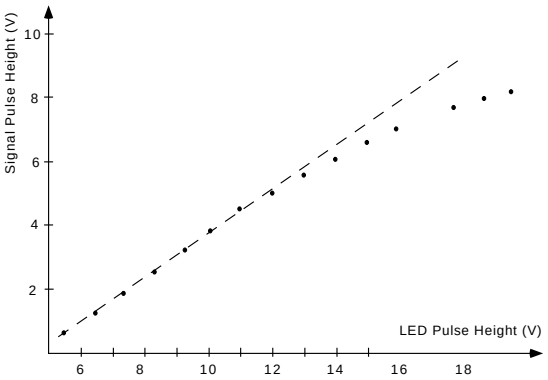

Figure 12.1: General transmission layout

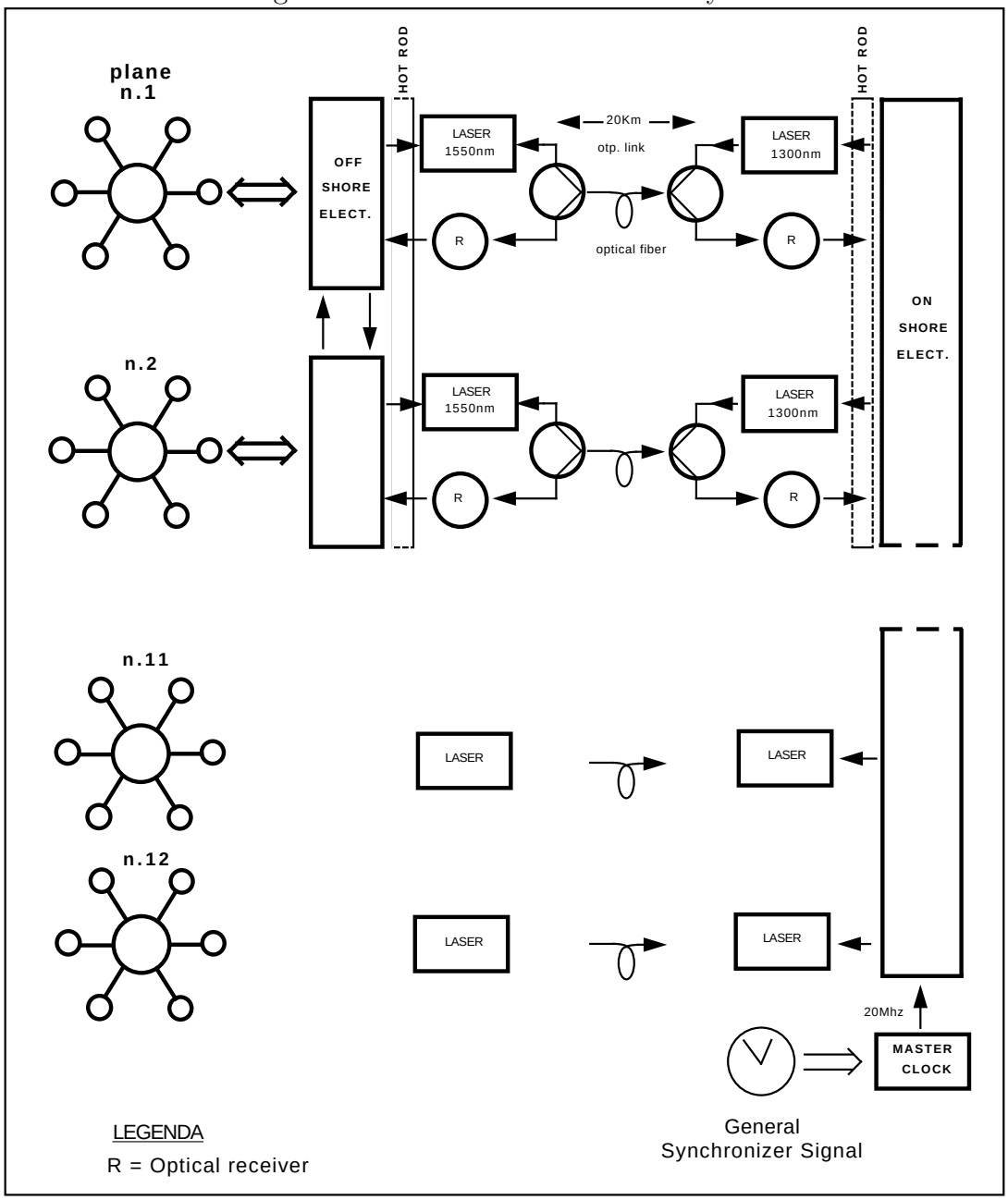

Fig. 2

Figure 12.2: Off shore electronics

to the event time. Further series of four time slots (four A/D sample bytes and one information byte each) are opened and added to the Read Cycle until the PMT amplitude is under threshold for an entire time slot. In this case a last time slot is written and the Read Cycle is closed.

The structure of the last time slot is different from the others: it contains three A/D sample bytes, one information byte and one byte for the A/D conversion of the pulse charge Q_{tot} integrated over all the time slots of the Read Cycle.

In a five time slots Read Cycle 19 A/D pulse samples for a total sample time of

$$19 \cdot 3.\overline{3}ns = 63.\overline{3}ns$$

are made. During this time the pulse is expected to be over threshold for a maximum of $53.\overline{3}$ ns.

The transmitted data and information volume of this Read Cycle amounts to

$$\frac{5byte}{timeslot} \cdot 5timeslots = 25bytes$$

The *threshold time* corresponds to the time of the last A/D sample of the first time slot. In this way the data related to the 10 ns preceding the threshold time are also kept.

The synchronization between the PMT event time and the Master Clock on shore is an important and delicate task. This synchronization is kept by transmitting the reset time of the Time Register, i.e. the T_c pulse time. If at the T_c pulse time a Read Cycle is running, a bit (TC) is set true into the information byte (INFO word, see figure 12.3 for the description of its content) of the time slot coincident with the T_c time. Otherwise one, and only one, time slot is transmitted with the proper INFO byte (TC=1, OT=0) and the four bytes corresponding to A/D samples will contain useful informations for a periodic evaluation of pedestals.

A complementary synchronization method is also foreseen and it will be described afterwards.

A high speed (300 ps propagation time) Laser Programmable Gate Array (LPGA) builds the time slot five byte word from the A/D samples, the event time and pulse informations and writes this 40 bit word in five parallel 8 bit FIFO. Thanks to a double buffer structure implemented in the LPGA, the writing rate into each FIFO is reduced from the 300 Mbyte/s of the A/D to

$$300/4Mbyte/s = 75Mbyte/s$$

At the FIFO output this word is read on the 40 parallel bit bus of the Hot Rod and strobed in the transmitter device at the continuous rate of 20 Mword/s. The Hot Rod transmission system acquires the data at the rate of 800 Mbit/s and transmits them serially, together with its own protocol, at 1 Gbit/s, across either coaxial or optical fiber link.

In figure 12.4 the synchronism scheme for reading the FIFO on the Hot Rod bus is shown. From the 20 MHz clock a train of 15 read signals (RD), 50 ns each, are created, for a time of 750 ns, to read a FRAME of single floor data. One pulse of the train reads the 5 byte word of the floor synchronism (SYN register) and the following 14 pulses read

as many groups of five FIFO, each group corresponding to one time slot PMT data and information (figure 12.3). Moreover at the end of this time another train of 15 pulses reads a data FRAME of the adjacent floor, so that a SUPER FRAME of data, made of two FRAMEs of single floor data, is transmitted in 1500 ns. Because every 50 ns five bytes are transferred to the HOT ROD bus, the total transmission rate results:

$$5 \cdot 8\ bit/50\ ns = 800\ Mbit/s$$

fitting the HOT ROD transmission capability.
Every

$$T_h = 2 \cdot 15 \cdot 50\ ns = 1500\ ns$$

one byte of each FIFO is read. One PMT event is read on the Hot Rod bus in at least

$$T_{evt} = 5 \cdot T_h = 7500\ ns \tag{12.2}$$

A T_c pulse is sent every 90μs. This time interval is an integer multiple (60) of the SUPER FRAME transmission period and implies a modulo 27000 Time Register (TR) counter.
The secondary synchronization method, mentioned above, is realized using the information carried by the SYN Register (figure 12.3). Two registers of five bytes each (see also figure 12.2), one for each of the two floors, are directly and alternatively read, on the Hot Rod bus, every 750 ns. The first byte contains a synchronism word (SYN), in the second byte 6 bits distinguish the local from the adjacent floor data and 2 bits are coded at the time of the Tc pulse. Three bytes are free for spare data. This transmission uses only 16 bits every 750 ns (corresponding to a rate of $\sim$ 21.3 Mbit/s) leaving $\sim$ 32 Mbit/s available for transmission of other data (e.g. slow control data).

Each FIFO is written in asynchronous way each time that a PMT signal is greater than a threshold, at the average rate of

$$f_w = 5 \cdot < R > \text{ byte/s}$$

where $< R >$ is the average PMT event rate. The same FIFO is read in synchronous way at the rate of (figure 12.4)

$$f_r = 1/T_h = 1\ byte/1500\ ns = 0.\overline{6}\ Mbyte/s$$

so that the number of bytes accumulated in a FIFO in a time t results

$$N_b = (f_w \cdot T_h - 1) \cdot t/T_h \tag{12.3}$$

The accumulation starts if

$$f_w = 5 \cdot < R > \ \geq 1/T_h$$

i.e.

$$< R > \ \geq R_o = 133.\overline{3} Kevts/s \tag{12.4}$$

R_o is much greater than the expected single PMT event rate in the NESTOR location. This limiting rate decreases in proportion to the rate of those pulses (if any) whose

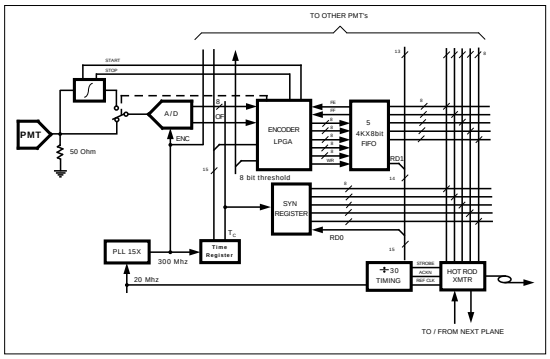

Fig.3

Figure 12.3: Single Floor Data Frame Structure

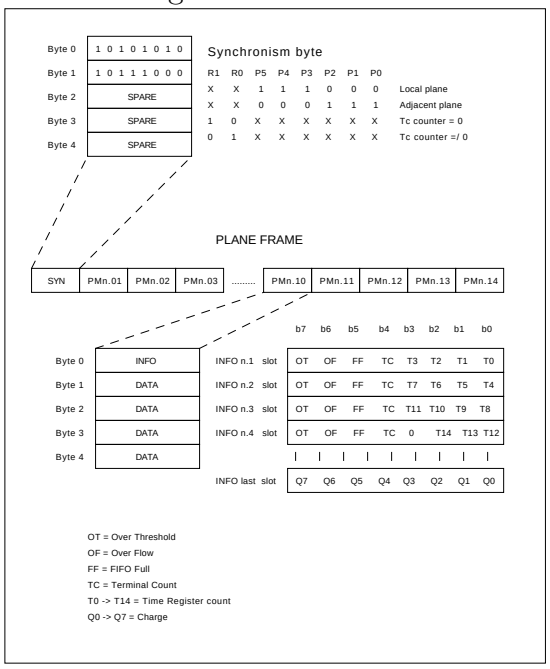

Fig. 4

Figure 12.4: Data Transmission Synchronism

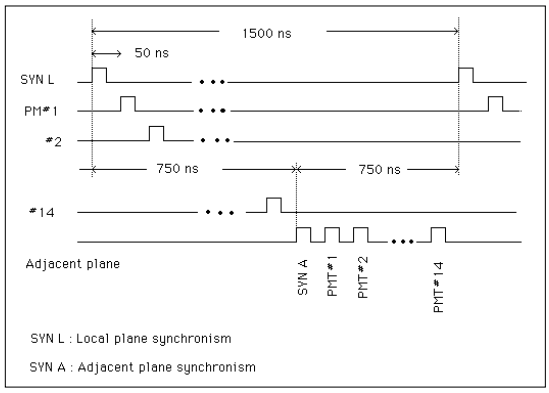

Figure 12.5: On Shore Electronics

amplitude is over threshold for a time greater than the $53.\overline{3}$ ns allocated in a normal Read Cycle (five time slots).

12.4 On Shore Electronics

The on shore electronics for the data from one floor is shown in figure 12.5.

For each optical link a Hot Rod receiver decodes the 800 Mbit/s of the serial data in a 40 parallel bit word at 20 Mword/s. The Hot Rod transmission protocol makes possible the reconstruction on shore of a bus of data having the same order as the transmitting data bus of the off shore electronics.

A Synchronism Extractor apparatus reads from the appropriate bytes of the bus and extracts the synchronism signal and the information of which floor out of the two is sending data.

Every time that a floor synchronism signal is found, the successive 14 pulses of the 20 MHz Master Clock are used to read, in a precise sequence, the information of a Frame of floor data. In five Frames one Read Cycle of a PMT (25 bytes) is read.

Moreover every time that the SYN and INFO words show a Time Register reset (TC=1), the number M_{TC} of counts is increased, so that the PMT *event time* can be obtained from equation (12.1).

All the data contained in the off shore FIFO are transferred in a RAM memory (on shore data RAM). For each PMT this memory is organized in words of 32 bytes (event words), one per PMT Read Cycle (at least 25 bytes). This memory is addressed using as pointer the PMT event number,which is extracted from a Volume Table of Contents (VTOC) at the event time address.

A data RAM volume of 1024 event words contains all the data of one PMT off shore FIFO since the maximum number of PMT events present at the same time in the off shore FIFO memories of one PMT is

$$\frac{5\ FIFO}{PMT} \cdot \frac{4096\ bytes/FIFO}{25 bytes/PMT event} = 819.2 \frac{events}{PMT}$$

The PMT data RAM contain all the events that occurred in a time equal to the reading time of a full off shore FIFO, i.e.

$$4096byte/f_r = 4096byte \cdot 1.5\mu s/byte = 6144\mu s \tag{12.5}$$

corresponding to

$$M_{TC} = 6144\mu s/90\mu s = 68.2\overline{6}$$

cycles of the Time Register.

$$819.2\ evt/6144\ \mu s = 1/(7.5\ \mu s/evt) = 133.\overline{3}Kevt/s$$

that is the rate of reading events from the FIFO, as expected.

The data RAM buffers contain the memory of the Over Threshold data of all the PMT events which happened in a time window of 6144 μs. Two buffers are required: while the first is ready to be read and analysed (read memory buffer), the second is filled in 6144 μs (write memory buffer). Therefore the time window of the read memory appears to be moving forward in steps of 6144 μs. If all the off shore FIFO are found empty, at that time the on shore write memories can be read.
The window width of 6144 μs has to be compared with the time required by a relativistic muon to cross the apparatus, i.e. few microseconds. Events which last more than 6144 μs, if any, could be detected adding as many on shore data RAM as required to cover the time length of the event.
For triggering purpose the count N_{TR} of the Time Register at the PMT event time (i.e. when a transition to the active state of the Over Threshold flag (OT) is found) and the charge of the event are extracted from the PMT data and stored in a Reduced data RAM (see figure 12.5).

As for the data RAM a double buffer structure is required for the Reduced data RAM.

A dedicated processor ($DECPeRLe_1$) reads the 168 Reduced data RAM of all the NESTOR PMT in words of four bytes: two bytes for the PMT event time, one byte for the charge and one byte for the PMT number. From the correlation of the times and from the charge of PMT events a first level trigger is built before the time window information is cleared (6144 μs). Once the first level trigger is set, the full data RAM are available for a second-level decision.

A different arrangement of extracted PMT data can be envisaged in order to correlate event times of different PMT in a first level trigger, arranging the data of different PMT in the memories assuming the *event time*, i.e. the N_{TR} and M_{TC} counts, as order parameter. In this case the *event time* extracted from each time slot is used, as memory address, to write the Over Threshold flag, i.e only one bit of information, in the Time Realign Memory (TRM).

The number of bit of the TRM memory amounts to

$$27000\ bit/(TR\ cycle) \cdot 68.2\overline{6}\ cycles = 1843200\ bits$$

Since one active bit corresponds to one count of the Time Register, the maximum difference in the time registered in the TRM results

$$1843200\ bit/(300\ Mbit/s) = 6144\ \mu s$$

equal to the width of the time window.
The maximum number of PMT events, i.e. active bits corresponding to *event time*, which can be found memorized at the same time in a TRM memory of one PMT, is found taking into account the time needed to write one PMT event in the Hot Rod bus, i.e. from (2) and (5)

$$6144\ \mu s/(7.5\ \mu s/evt) = 819.2\ events \tag{12.6}$$

Nine RAM memories per PMT, each 8 bit wide and 32 Kwords deep , can be used as TMR memory of a PMT.

The 168 TRM memories of all the NESTOR PMT form a unique memory composed of 168 rows, one for each PMT and 1843200 columns, one for each value of the event time. In this memory the event time of all the 168 NESTOR PMT are realigned in a single word (168 bits), whose address is the same *event time*. The trigger processor, therefore, can assume the event time (12.1) as unique pointer to read the data of all the 168 NESTOR PMT. The active bits of one word correspond to those PMT having Over Threshold signals in coincidence within a $3.\overline{3}$ ns resolution at the time pointed out from the word address.
A first level trigger can be constructed reading in the TMR memories the *event times* and analysing the data before the time window informations are cleared, i.e. in a time less than 6144 μs. In order to reduce the trigger decision time at this level, the TMR event times is rearranged in as many Trigger Memories as foreseen classes of trigger (like upward and downward muon trigger, or subclasses of these). Several columns of the TRM can be grouped, according to the time resolution, and a new memory (trigger Memory, TR), reduced in size, can be written to replace the TRM. Each fired PMT is represented in this memory by only one active bit occurring at the *event time*. The first level trigger can then be built using this reduced memory. Once the first level trigger condition is set, the data RAM can be read using the event number as memory address.

12.5 The Analog Signal Transmission Scheme

The transmission by optical link of the analog signals of the PMTs has the powerful advantage of leaving a complete flexibility for the subsequent processing of these signals on shore.

The use of single frequency laser diodes, usually distributed feedback (DFB) laser diodes, is required in order to transmit through a 25 km optical fiber the R2018 PMT signal which has a 8 ns rise time.

We have considered direct or external modulation of the laser diode.

12.5.1 Direct Modulation

In order to comply with the available optical cables and to minimize the number of the DFB laser diodes one has to rely on multiplexing, i.e. transmitting into one fiber several

Figure 12.6: 4×4 multiplexing scheme by MARCONI

signals by modulating a common optical device. Frequency (RF) Division Multiplexing (FDM) or Wavelength Division Multiplexing (WDM) are possible.

The RF modulation can be either amplitude modulation which minimizes the required laser frequency bandwidth at the expense of a reduced dynamic range, or frequency modulation with the complementary drawback and advantage.

Several studies are under way.

The first studies were done by the Athens group with FOXCOM and then with MARCONI. MARCONI proposed a combination of a 4-channel FDM and a 4-channel WDM (fig.12.6)

The INFN group also considered the possibility to multiplex 14 channels of 150 MHz each. For AM the signal of each PMT modulates the amplitude of its own carrier. The double side band modulation choice imposes that the frequency of the 14 carriers are relatively shifted more than the double of the PMT signal bandwidth (assumed 150 MHz). Then the range of microwaves (5÷10 GHz) is reached and refined electronics technologies are required. The study of the problem has been entrusted to an industry leader in this field (ELETTRONICA s.p.a.): the technical feasibility of the whole project has been

demonstrated, but the cost as evaluated is far beyond any realistic possibility. For FM the required transmission bandwidth is more than a factor five bigger than that required for the amplitude modulation method. For this reason the solution has been rejected and the INFN group did not pursue the analog transmission scheme.

The Saclay group is studying the possibilities of analog transmission schemes with lower bandwidths. A reasonable design which would also match the number of fibers in commercially available optical cables would multiplex by FDM the 14 channels of a floor to modulate each DFB laser diode. Each PMT signal modulates an oscillator output and the 14 resulting signals are combined to modulate the laser.

Oscillators have to be in the immersed detector since any solution with oscillators on shore will require additional lasers and photodiodes as well as multiplexing systems. The carrier frequencies should be such that the first harmonics are outside of the useful frequency range.

Direct modulation of laser diodes is a solution which is currently used for cable TV applications. We performed in June 1994 a short test of transmission of a fast PMT signal using a system loaned to us by the ORTEL company. The system (ORTEL 5510B) operating at 1310 nm included as a transmitter a DFB laser, and as a receiver a 6 GHz photodiode. The shape of the 2 ns risetime signal was transmitted without alteration through a 25 km monomode fiber. However the attenuation of the signal required using a fast amplifier with gain 200 at the output of the photodiode. The transit time dispersion FWHM of the link was measured to be 0.8 ns.

Building of a 3 channel prototype for a frequency modulation multiplexing system is presently considered for evaluating the feasibility of a system associated with a 10 GHz DFB laser. A schematics of the prototype is shown on figure 12.7.

The 3 modulation bands will be 100 MHz wide, centered on 1.05 GHz, 1.35 GHz and 1.65 GHz typically. These central frequencies will be moved in order to study intermodulation (cross-talk), dynamic range and distortions of the signals.

12.5.2 External Modulation

External modulation has in principle the advantage of allowing the laser to be on shore. However Mach-Zehnder modulators utilize incident polarized laser light. In the option of on-shore laser sources, in order to maintain polarization along the 25 km fiber requires either using special elliptical fibers not integrated in submarine cables or having a device to correct for shifts of the state of polarization. Since, in addition, Mach-Zender modulators which are expensive systems require separate fibers for the input and the output light this solution has not been pursued.

External modulation using asymmetric Fabry-Perot (multi-quantum well - MQW) modulators on the other hand has none of these drawbacks , although modules are not yet commercially available. It is one of the most interesting systems to get the NESTOR photomultiplier analog signal to the shore. It is based on a infrared link under development by the CERN DRDC Project RD23 and MARCONI. With this system, an infrared laser beam is generated on the shore and is guided with a single mode fiber to a reflective modulator. The analogue signal of each photomultiplier modulates the reflected light intensity and an infrared detector on the shore reproduces the analogue signal.

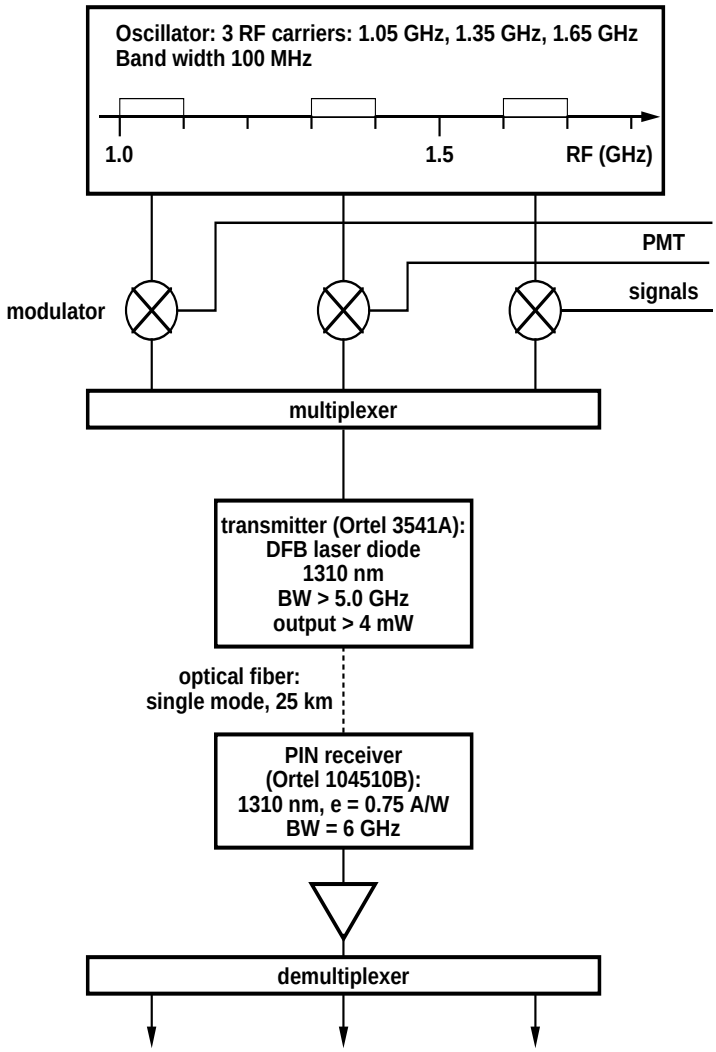

Figure 12.7: Schematic view of a 3 channels frequency modulation multiplexing system

Figure 12.8: Block diagram of the RD23 test set up

The reflective modulator is a monolithic Asymmetric Fabry Perot Modulator, built by MARCONI. The front mirror has a reflectance of 15% and the back mirror 95 %. If a bias voltage of -5.5 V is applied between the two mirrors then negative pulses up to -2.5 V will change linearly the reflectance of the AFPM from about 52 % down to 42 %. The bandwidth of the AFPM is about 1 GHz. The evaluation of the link is being done at CERN by the RD23 group.

Advantages:

The photomultiplier analog signal is transmitted to the shore.

Minimum and passive electronics in the sea, with low power consumption.

Only two 8 channel modulator packages per floor and the bias power supply, derated for reliability.

No military specifications components should be used on the shore, the system is easily serviceable.

Disadvantages:

For the time being multiplexing does not seem feasible, but it has still to be studied. Without multiplexing one fiber per photomultiplier is needed (a cable with 168 fibers per tower)

At least, one infrared laser and splitter 1-to-16 per floor.

168 1-to-2 splitters and photodetectors+amplifiers per tower.

The signal to noise ratio has still to be improved: for the moment the signal to noise ratio is about 10 and is attributed mainly to the amplifier of the receiver. This ratio is calculated by applying a sinusoidal signal on the AFP modulator (1 MHz, 1 Vpp). The signal on the receiver is amplified and the mean peak-to-peak voltage is taken. This is divided by the rms noise of the link without modulation on the AFPM.

The fiber length is usually of the order of twenty meters. Using the same technique a measurement with a 20 km single mode fiber was performed at CERN (the fiber length

was chosen to be approximately equal to the future NESTOR fibers). The system worked easily, the signal attenuation in the fiber was low, as expected.

Additional measurements were done, with a Demonstration Box from Marconi, using photomultiplier negative pulses. In fig. 12.8 the set up of the measurement is shown. The single mode fiber had a length of about 10m and the wavelength was 1538 nm. Two sets of measurements were performed:

a) Using a pulser, a negative pulse similar in shape to a photomultiplier pulse was generated. The repetition rate was 1MHz and the pulse had 5nsec rise time, 30nsec fall time and 15nsec FWHM. Using this pulse shape on the modulator for several negative pulse heights and with a bias voltage of -6.25V, we checked the linearity of the modulator on simulated photomultiplier signals. The output signal was the average of 50 modulated samples. In figures 12.9 typical input (a) and output (b) signals are shown. We should note that the time characteristics of the pulse are not maintained, i.e. while the rise time of the input pulse is less than 8 nsec the output pulse has a rise time of about 15 nsec. This is attributed to the photodetector amplifier bandwidth.

b) Using photomultiplier-scintillator pulses. The results were compatible with the previous ones.

From the above it is clear that, as expected, the signal to noise ratio should be improved. For the moment we could not apply discrimination thresholds on the receiver signal to trigger the digital processing of pulses.

Figure 12.9: a) Typical input voltage to the modulator. (Bias voltage -6.25V) and b) typical output voltage from the amplifier of the photodetector. The dark line is the average of 50 samples. The dots correspond to one sample.

Chapter 13

Trigger and Data Acquisition

NESTOR will be sensitive to neutrinos that range from the TeV scale, e.g neutrinos coming from Active Galactic Nuclei (1 per day), to atmospheric neutrinos (GeV scale) or neutrinos coming from neutralino annihilation (a few per day), and should be able to record hit multiplicity fluctuations in order to detect a signal of Supernovae explosions, or very slow heavily ionizing particles (monopoles). Further it should record the downcoming cosmic ray muon background (∼1 Hz) which will serve as calibration of the detector. Table 13.1 shows the expected number of physical events that will occur in the detector per day.

Process	1 tower	7 towers
AGN ($\geq$ 1 TeV)	0.5-1	1-2
Atmospheric throughg.. ($\geq$ 1 TeV)	4-5	10-12
Atmospheric contained	2	14
Atmospheric upcoming μ	1.5	10
χ upcoming μ (earth) m_χ=56 GeV	5	35
χ upcoming μ (earth) m_χ=100 GeV	1	7
χ upcoming μ (sun) m_χ=100 GeV	1	7
Cosmic ray downcoming μ	86500	600000

Table 13.1: Expected events per day from main physical processes

The natural background to the photomultiplier tubes (PMT): bio-luminescence and natural sea radioactivity, ^{40}K, gives a initial high counting rate ($\sim$ 50 kHz/PMT, maximum 100 kHz/PMT) that has to be reduced down to the few Hz level through a series of trigger decisions of increasing complexity.

Table 13.2 shows the expected number of double triple etc. coincidences due to the above accidental background expected in one tower. For the higher level coincidences the time-coincidence window depends on the actual distance of the PMT's hit, and some causality criteria have been applied. This is the ideal situation, assuming large computing times, any realistically fast scheme will tend to give larger rates, as can be seen in the next section where a specific hardware oriented algorithm has been applied. In table 13.3 one also sees the data load in MB/s that will be transmitted to the next level of triggering if one accepts a 1-2 μs window for each event, under the same optimistic conditions.

Noise Frequency	50 kHz	100 kHz
singles	8400	16800
doubles	537	1500
triples	18	78
quadruples	.5	4

Table 13.2: Random coincidence rates in kHz

Noise Frequency	50 kHz	100 kHz
singles	320	640
doubles	160	640
triples	6	50
quadruples	.15	3

Table 13.3: Dataload in Mbytes/s, assuming that after a trigger the next microsecond of data are passed to the second level

One obviously needs to go above the four-fold coincidence level to transmit realistic dataloads of a few MB/s, to the next level of triggering.

The field programmable gate array technique is a very good candidate for a first level trigger due to its low latency * and essentially through its flexibility to be rapidly and simply reconfigured, since the trigger will have to adapt to changing environmental conditions, and physics interests. From then on the computing power of processors with high-level languages (e.g alpha) or farms of processors will be adequate to treat the data.

From the trigger point of view, NESTOR presents as can be seen from the above tables, similarities with LHC experiments, and it will be probably one of the first experiments where the feasibility of the new-generation data-acquisition systems (transmission of signals through long optical fibers, optoelectronics, programmable gate-arrays, fast point to point links (e.g SCI) or ATM switches and fast processors (e.g alpha) will be tested thoroughly.

13.1 Data Rates

The raw data rate in NESTOR is dominated entirely by the background pulses. The time and charge profile (sampled with a 300 MHz FADC on the PMT analog output) will be transported with optical fibers to shore, every time a PMT gives an output larger than a threshold (e.g .25 of single photoelectron) (see chapter 5). The time stamp and the integrated charge will be separated from the digitally sampled analog signal and fed into the 1^{st} level trigger processor. The rest of the event will remain in large FIFO's awaiting the first level trigger decision, to be transmitted to the 2^{nd} level. The trigger info will be 4 bytes per hit where the first 2 bytes will be used for the time information (100 μs

*time needed to make a decision in a pipeline environment

depth, 3.3 ns/channel), 1 byte will be used for the integrated charge information and the last byte will label the PMT that fired. The signals from the whole detector will be thus fed in the 1^{st} level trigger processor with a frequency of 20-25 MHz. The goal is that the 1^{st} level trigger processor will reduce the rate below the kHz level, and thus it will reduce the data rate from an average 320 MB/s (maximum 640 MB/s) down to a few MB/s. The event building, will be done by the 2^{nd} level processor collecting 1-2 μs worth of information from the 12 floors. At the 2^{nd} level a single processor (e.g the alpha) or a farm of processors connected with point-to-point links (e.g SCI) or ATM switches can perform high level fits to reduce the event rate down to a few Hz.

13.1.1 DECPeRLe$_1$NESTOR's First Level Processor

DECPeRLe$_1$is a PAM [173, 174], a novel form of universal hardware co-processor based on *Field-Programmable Gate Array* (FPGA) technology and controlled by a general purpose computer system. PAM technology permits the construction of high performance synchronous digital circuits containing application tailored datapaths that can handle data rates of hundreds of megabytes per second. PAMs can be quickly reprogrammed by software permitting rapid prototyping and the exploration of alternative architectures without incurring the cost of conventional hardware development. These features make them well suited for NESTOR.

The computational challenge of NESTOR's first level trigger is to detect correlated pulses from several PMTs due to Cherenkov photons emitted by tracks traversing the array against a background of random uncorrelated PMT firings.

Among the major architectural choices to be made is how to order and buffer this data prior to feeding it to DECPeRLe$_1$. This choice in turn leads to different architectures for the pulse correlation detector that is the basis of the NESTOR trigger. Since data from each floor arrive using a different fiber (12 in all) and remain in a FIFO, a ring counter can clock them into the DECPeRLe$_1$at a constant rate e.g 25 MHz. Another possibility is to use a HiPPi switch developed at CERN to multiplex blocks of data from the 12 floors into a single input FIFO.

DECPeRLe$_1$is a single board system housed in a desktop workstation enclosure. The computational core of DECPeRLe$_1$is a 4 by 4 matrix of Xilinx XC3090 FPGAs [176] connected in a regular mesh. Local storage is supplied by 4 independently addressable one megabyte RAM banks, each bank being organized as 2^{18} 32 bit words. Five auxiliary XC3090s provide efficient switching of data to and from the periphery of the matrix, the RAMs and the host interface and a further two XC3090s generate the RAM addresses and control. The DECPeRLe$_1$system is connected to a host computer system through a TURBOchannel [175] option interface. This 32 bit wide interface provides low latency host CPU access and direct memory transfer (DMA) rates approaching 100 MB/s. Direct connection to external devices is provided by four 64 bit wide bidirectional interfaces on each of the four sides of the computational matrix. These link to connectors on the DECPeRLe$_1$mother board. The physical packaging of the DECPeRLe$_1$system allows three of these interfaces to double as TURBOchannel slots permitting the direct connection of standard option cards to the matrix. An efficient global clock distribution scheme coupled with the DECPeRLe$_1$programming methodology permits the implementation of

synchronous digital circuits at clock rates of 25-40 MHz.

13.2 1st Level Trigger Architecture

NESTOR is a volume array of PMTs organized as one or more towers of 12 vertically stacked *floors*. Each floor consists of 14 optical modules. A muon in sea water emits a cone of Cherenkov photons at a characteristic angle of 43°. Such a muon in or near the NESTOR tower will produce a correlated set of PMT pulses. The distance between PMTs places a strict upper bound on the time difference between pulses that may be correlated. For neighbouring PMTs in NESTOR this is $\sim 100ns$. These events need to be distinguished from randomly correlated pulses among groups of PMTs, due to background fluctuations.

We need to detect from double to multiple coincidences and then apply a weighed sum to all coincidences found in a given time window. When correlation scores exceed a given threshold associated data will be passed to the reconstruction process.

Incoming data is saved in a DECPeRLe$_1$RAM bank before it enters a processing pipeline that computes the correlation score. If the trigger threshold is exceeded, associated data in a time window enclosing the interesting period is extracted from the FIFO's further upstream and passed to the host processor.

Note that one DECPeRLe$_1$RAM bank can accommodate the 10 ms (1MB RAM at 100 MB/s) of NESTOR data–this is far in excess of the time required by the correlation pipeline.

We decompose the currently favoured algorithm to be implemented in DECPeRLe$_1$[**?**] in four major units:

Store. The *Store* buffers all inputs for a few milliseconds. It passes what the trigger deems relevant to the next level of processing.

Hit Generator. The function of this unit is simply to present PMT hits to the array of processors resident in the DECPeRLe$_1$.

A set of Tower Processors (estimated 20). Their function is to analyse hits presented by the Hit Generator. A tower processor may be either empty, and in this case according to a specified logic grabs a newly presented hit, pending validation, or filled already with a previous hit, or sets of hits. In the second case based on the closeness of times ($\sim$ 100 ns) and locations of PMT's, it may decide to *merge* them into a single longer hit, with charge the sum of the merged PMT charges. When the time information of incoming hits indicates that it is impossible to form further coincidences, e.g time-differences longer than 1-2 μs, the corresponding tower processor sends its content to the master processor and declares itself empty. Each tower processor is data driven, the hits are broadcasted, and the only communication with the rest of the processors is the validation bit a tower processor resets whenever it has formed a coincidence. This action prevents a hit to be stored to an available free processor once it has been "grabbed" by an active processor and has formed a coincidence, avoiding the unnecessary multiplication of active processors.

Master Processor. Its function is to decide, based on hits received from the Tower Processors,which time interval is relevant, and should be passed as such to the next level of processing for a detailed analysis. It can also record the frequency of singles, and double or higher multiplicity coincidences.

This algorithm has been tested with signal events (1 to 50 GeV contained muons, pointing at random directions) and noise. The efficiency of the algorithm [†] as a function of the number of photoelectrons (p.e) required and the rate as a function of the same number are shown in table 13.4:

Trigger	Noise rate kHz	Muon Efficiency
3 p.e	40kHz(100)	-
4 p.e	8(30)	-
5 p.e	2(10)	100%
6 p.e	0.3(5)	98%
7 p.e	$\leq$0.1(1)	96%
8 p.e	$\leq$0.1(0.3)	94%
9 p.e	$\leq$0.1(0.2)	92%

Table 13.4: Noise rates for the whole detector in kHz under the assumption of 50(100) kHz singles rate/PMT and efficiency for contained muon events from 1 to 50 GeV, normalized to the requirement of at least 5 p.e

Two other approaches are also currently investigated:

- The first is to process the 168 PMT streams in parallel under a strictly increasing model of time. The 256 DECPeRLe$_1$mother board connectors can sink 6.4 Gbit/s when operated at 25 MHz. These rates however exceed the bandwidth of the DECPeRLe$_1$RAM so some buffering and reliance on statistically average rates is required. See chapter 5 for a possible implementation of this model.
- The second consists of a neural network implementation of the trigger. This way one could even incorporate some of the more "sophisticated" requirements on the triggering pattern, obtaining a larger reduction factor on the data rate.

Both the above approaches warrant further evaluation and it is very likely that the flexibility and versatility of DECPeRLe$_1$will suggest yet other architectures before a final method is chosen.

The scalability of the system permits the extension of the filtering to the 7 tower scheme without major difficulties.

13.3 2nd Level Trigger and DAQ

One should expect of the order of 1-5 MB/s of data with a frequency between 2 and 10 kHz, to be transmitted to the data acquisition workstation. A relatively simple and fast

[†]normalized to the events that had a total of more than 4 detected photoelectrons

algorithm written in a high language could reduce further the event rate by using part of the "pre-fit" (see section 8 for more details) to less than a hundred of Hz. We estimate that one alpha workstation of the high end should be able to cope with the rate. In the case that more computing power is needed, e.g in the case of unexpectedly high noise, the system is easily upgradable to a small farm of alpha workstations. This scheme concerns ofcourse only one tower. In the case of more towers one should go to a multiprocessor environment with fast point to point links of the type SCI, or ATM switches. The trends in technology are such that it would be premature to fix the 7-tower $2^n d$ level scheme now. The events are not extremely big, one conservatively expects to write into tape less than 50 KB/s. With this rate one should write one 10 GB tape every 2 days. A special robot should be used for the tape handling.

Chapter 14

Monitoring and Controls

In this chapter, the solutions foreseen so far by the collaboration for the controls, calibration and monitoring are presented. Other systems are also under study and we have contacted several firms specialized in oceanological and monitoring equipments.

14.1 The Slow Control System

The Slow Controls System is a collection of subsystems responsible for the following functions:

- The communications between the shore station and the undersea NESTOR detector.
- The control of the main power distribution to the twelve Ti spheres (one per floor) and of the high voltage of the photomultipliers (PMT).
- The readout of the internal and environmental monitors.
- The control of the calibration system.
- The communication between NESTOR and the associated experiments (Geology, Oceanology, Marine Biology ...).

The Slow Controls System is also capable of setting any desired threshold to the undersea electronics and of controlling and reading out the positioning system hydrophones by adding more DACs, ADCs or other VME modules.

Central to the Slow Controls philosophy is the general NESTOR philosophy that if a floor fails the rest of the system is not disturbed and continues its normal operation. This design is based on an undersea optical cable with a minimum number of 12 fibers.

The Slow Controls System consists of the Shore Master Control, the Fan-Out Sphere under the NESTOR tower and the Undersea Monitoring and Control located in each one of the twelve Ti spheres (see photographs of Ti spheres). We will describe each one of these components and their functions in the following sections.

Figure 14.1: Shore station and Undersea Monitoring and Control

14.1.1 The Shore Master Control

The Shore Master Control station includes (see figure 14.1):

- The control computer with a serial interface.
- An encoder/decoder for reliable digital transmissions.
- The laser transmitter (at 1310 nm) for slow control commands and a receiver for the modulated laser light carrying the slow controls monitoring information. The 1310 nm light is mixed (separated) into (out of) one fiber using a Wavelength Division Multiplexer (Demultiplexer) along with the laser light at 1550 nm transmitting the PMT data information. One of the following schemes may be used:
  - The incoming slow controls information is included in the stream of PMT data. This information is transmitted via the 1550 nm laser light along with the data and filtered out at the receiving end on the shore station for further processing.
  - A different wavelength laser light (in the vicinity of the 1310 nm) is used for the incoming slow controls information. The three wavelengths are mixed or separated into the same fiber per floor using wavelength division multiplexors.

14.1.2 The Fan-Out Sphere

The Fan-Out sphere, located below the NESTOR tower, is responsible for the power and fiber distribution to the titanium spheres at the centers of the NESTOR floors. This is a titanium sphere which contains:

- The optical fiber splice which will separate the twelve fiber bunch to twelve individual fibers (one for each floor).
- A power distribution panel with one output for each of the twelve NESTOR floors and for the associated experiments (LAERTIS etc...). Each output is supplied with a slow blow fuse and is controllable via a relay switch by the Slow Controls.

The power will be transmitted via the underwater optical fiber cable to the Fan-Out sphere which will distribute the power to the twelve Ti spheres via the controllable relays. This sphere is filled with oil to counteract the possibility of shorts and ensure continuous supply of electrical power to the floors in the unlikely case of a sea water leak. If there is a problem in one of the Ti spheres, its power can be switched off via the controllable relay in the Fan-Out sphere. We are also investigating the possibility to have an additional control of the power to the spheres by using a slow modem system on the cable carrying the power . This will allow us to switch the power from the Fan-Out sphere to the individual Ti spheres on and off independently of the status of the Slow Controls system. This way the supply of power to the floors will be very robust.

14.1.3 The Titanium Spheres

The twelve Titanium spheres (one per floor) contain the bulk of the slow control electronics. Their basic functions are to collect all the monitoring information and transmit it to shore and receive all the control information and execute the commands. Each sphere contains the Undersea Monitoring and Control which consists of (see figure 14.1):

- A VME crate that will hose an on-board computer with communication interfaces, VME ADC modules for the recording of the monitoring information and DAC modules for the control as well as a VME relay board for the control of the power distribution. The CPUs used will include a software controllable watchdog circuit which will reboot the computer when it is stuck.

- Receiver and laser transmitter and digital signal decoder and encoder. In the case of using the main data transmission system for the sea-to-shore communication the slow controls data is merged with the PMT data and a common laser at 1550 nm is used.

- A power regulator that will power the local electronics and provide the 24 V supply voltages for the PMT high voltage DC to DC power converters housed in the Benthos spheres where a voltage divider will set the appropriate voltage for each photomultiplier. In each floor, if a PMT is malfunctioning, its power can be turned off.

14.1.4 Reliability Issues

This system has to operate for at least a period of ten years as it is not easily serviceable. To obtain this the components will be chosen to have the appropriate reliability and also minimization of the number of components will be required. In addition the system will be enriched with bypass mechanisms to allow the rest of the system to operate if a part fails.

In the Fan-Out sphere, the cable gets split into twelve conductors going through controllable fuses to the Ti spheres. These fuses will allow us to switch off any Titanium sphere in case it is flooded, so that the rest of the system will continue to operate. The receiving and transmitting system, the main VME crate and the on-board computer follow industrial (and MIL spec) standards.

In general all the components will be tested exhaustively prior to deployment to ensure their ruggedness. This scheme will prevent any partial failure that may occur to become a full failure. It most likely will affect only a few channels.

14.1.5 Implementation

Most of the important components are chosen for the sake of cost estimation and reliability questions. We describe below the components needed for the system using the main data transmission in the sea-to-shore direction. The shore station computer will have communication interfaces and OS2 real time software (application and development). The transmission system will be based on the optical fiber link QLINK by Lasertron. We need

Figure 14.2: The LED module.

They are electrically connected in a mixed series and parallel way in order to match the 20 Ohm output impedance of the LED pulser. This way the maximum light output can be obtained. Each LED ball is installed in the center of a Benthos glass sphere which is located in the middle of the distance of any two consecutive NESTOR floors and additionally one at the bottom looking up and one at the top looking down (see figure 14.3).

Figure 14.3: The setup for the calibration system for a NESTOR floor dou

The LED clusters are powered by Picosecond Pulse Labs pulsars delivering 1 ns square pulses of adjustable amplitude up to 45 V at up to 1 MHz repetition rate. The pulsars are located inside the LED Benthos spheres and controlled by the Slow Control system. The pulser is triggered by the Slow Control system at specific time intervals. The photomultiplier signals are consequently processed by the main data acquisition system and transferred to shore. The calibration data are recognized as such from the information the Slow Control system enters in the data stream just before the pulsing of the LEDs starts. The pulsing of the floors occurs serially for cross floor calibration reasons.

14.2.2 Laboratory Tests

We have performed a series of laboratory measurements to check the feasibility of the method. Blue and green LEDs of various manufactors were tested for light output and timing properties. We will select LEDs which response time jitter will be negligible with respect to the transit time spread (TTS) of the NESTOR phototubes. Tests have shown that this can be achieved to better than 1 ns. We have used several setups to study the method. Initially a dark box was used which was able to accommodate one Hamamatsu 15 inch photomultiplier and a LED stand, up to a distance of about one meter. Later a large dark room was used to make sure there is enough light reaching the PMT at distances more than 15 m.

Time distributions were obtained using a blue LED (CREE 102CR-ND) pulsed by 5 ns square pulses and at various light levels. The start of the time was determined by the LED pulse and the stop by the PMT signal. For light levels of the order of one photoelectron, with the LED about 1 m away from the photomultiplier, the Full Width at Half Maximum of the time distribution was about 7 ns and the accuracy of the timing done by the location of the peak was less than 1 ns. The charge calibration was also done by the constant LED light pulse. The stability of the time and charge calibration is less than 3%, as determined by repeating the measurements in the same setup. The time calibration also depends on the amount of light each photomultiplier sees. The time measured must be corrected for this effect which is known as slewing correction. The slewing corrections are measured and recorded by the PMT testing system for each one of the Hamamatsu photomultipliers.

We have also verified the possibility of cross floor calibration. The number of photoelectrons expected per LED is 0.9 photoelectrons per nanosecond (of LED pulse) per PMT for the adjacent floors and 0.1 photoelectrons per nanosecond (of LED pulse) per PMT for the next ones.

14.2.3 Implementation

The laboratory tests have proved the feasibility of the calibration method chosen. The implementation requires further tests in the sea. A setup has been constructed and awaits the proper time for deployment to check the calibration system at the NESTOR site. It includes two NESTOR optical modules (PMT's housed in Benthos glass spheres) and an LED module (an LED ball housed inside a Benthos glass sphere). This system is powered by batteries and a CAMAC system is employed for the data acquisition and control. It

is an autonomous system and as such will also measure the background light in the sea water.

The existence of lasers emitting in the blue allows us to also design another system for backup purposes. Various schemes are under investigation. Last, one should not forget that straight through down-going muons will also provide the final timing calibration information.

14.3 Environmental Monitoring

The environmental monitoring is not only essential for the interpretation of the NESTOR results but it will also provide valuable data for a plethora of earth scientists as oceanologists, geologists, climatologists and marine biologists. The monitoring will be internal as well as external to the Ti spheres. The internal monitoring will provide information on the conditions inside the titanium spheres. The continuous monitoring of the temperature, pressure and salinity of the sea water will monitor the speed of sound at the NESTOR site which is needed for the accurate determination of the locations of the Optical Modules with the acoustical positioning system.

14.3.1 Description of the Monitors

- Internal Monitoring:
  - Temperature transducers. There will be two temperature sensors per Ti sphere in order to monitor the temperature variations inside the sphere due to the electronics heat load.
  - Humidity and water level sensors. Two sensors per Ti sphere will be installed. The detection of high humidity will allow us to turn off the power in case of water leakage.
  - Tilt meters. Two tilt meters per Ti sphere (per floor) will be included to measure the tilt of every NESTOR floor. This is a backup of the positioning information from the acoustic transponders.
  - Flux gate compasses. Two flux gate compasses per Ti sphere will provide the orientation of every NESTOR floor. This too is a backup of the positioning system.
- External Monitoring:
  - Temperature transducers. The water temperature along the NESTOR tower will be read by twelve temperature sensors (one per floor).
  - Pressure gauges. Twelve pressure gauges (one per floor) will monitor the pressure variations along the NESTOR tower.
  - Current meters. Three current meters will measure the velocity of the undersea currents at different places along the tower (bottom, middle and top).

- Additional Monitors: More monitors for environmental observations will be added.
  - Video Cameras and lighting system for visual inspection of the NESTOR tower.
  - Salinity meter. The variation of the salinity will be also useful for oceanographic studies.
  - Release control. We will also include a release for the anchoring system of the whole tower, which will be controlled by the Slow Controls system. This will be a backup of the acoustic releases.

14.3.2 Implementation

The monitors internal and external to the Ti spheres are essential to the monitoring of the operation of NESTOR. The additional monitors will add to the scientific value of NESTOR by providing more information of the NESTOR site not otherwise available in a continuous base.

All the monitors will be powered and read out by the Slow Controls System. The operator at shore will determine the frequency of reading them out and record the information.

Chapter 15

Deployment of the Tower

15.1 Deployment

The advantage of working in the Mediterranean Sea a few miles away from a natural harbour is that one can essentially "choose" the weather conditions and deploy the tower when the sea is absolutely flat calm. The NESTOR tower will be deployed in the selected site following a very simple and well rehearsed procedure. Central to the NESTOR philosophy for deployment is to avoid the use of bathyscaphes for connections in the sea (e.g. DUMAND) and oceanographic vessels in order to minimize the costs and the complexity of the operation. A flat deck barge will be used which will carry the NESTOR floors in their folded position (see figure 15.1). There are three cranes in Pylos each of which can reach a distance of 45 meters and can be used for the deployment in existing barges. The barge will hold station during the deployment with the help of one or two tug boats (they both exist in Pylos).

First, the weight platform with the anchor release goes into the water and held by a winch. Each floor will then be picked up with the crane. The first active item to be submerged in the water will be the Fan-Out titanium sphere which will have the main connection of the undersea power and optical cable and the power and optical connections for each floor. Before each floor is immersed into the sea, the electrical and optical connections (only two connections per floor) will be made.

No connection will be made in the water. Each floor is joined to the one above and the one below with kevlar ropes (six on the appeces and two in the center). The kevlar ropes will be attached in the sea by divers. The floors will be held in the sea under the barge with the help of the winch and a steel wire cable until all floors are immersed in the sea and the whole NESTOR tower is formed. Then the tower will be lowered to the bottom of the sea with the help of the weight of the anchoring platform and 4 km long steel wire cable. The lowering of the cable will be controlled by the winch and will be done with a speed a 20-30 cm/sec to avoid excessive drag loads on the mechanical structure.

The first tower will be positioned very roughly at the center of the NESTOR basin. The next six towers will have to be positioned around the first one at a radius of 150 ± 10 meters. This can be easily accomplished with the use of the existing technology (oil rig technology). The six towers will be positioned assymetrically around the first in order to break the symmetry and avoid the effect of ghost events in the reconstruction. We plan

to hold a series of workshops of specialists for the deployment. We have started contacts with specialized firms for consulting e.g. IFREMER, TECNOMARE, GKSS,...

In our meetings with IFREMER in France (Brest and GENAVIR near Toulon), NESTOR was discussed and it was confirmed that they can provide us with expertise on the mechanical structure, materials to use, connectors, buoys, deployment, positioning (sonars and GPS), bathymetry, sedimentology, video monitoring etc.

Figure 15.1: The deployment of the NESTOR tower, a schematic. (Distances are not to scale)

15.2 Positioning

The expected deviation from the vertical of the NESTOR tower depends on the undersea water currents which have been measured to be under 10 cm/sec. Depending on the strength of the currents the axis of symmetry of the tower will not necessarily be a straight line parallel to the vertical but occasionally it may be parabolic, catenary. The exact location of the NESTOR Optical modules has to be known to a meter in order to reconstruct the muon track direction accurately (to within 1 degree). The continuous recording and monitoring of these positions will be accomplished by the use of a chirped sonar system which is controlled by the Slow Controls System. This acoustic system consisting of a

set of transducers (responders) will be located at positions a few hundred meters around the NESTOR tower and will emit, when commanded from a central control, frequency modulated acoustical signals (chirps). The chirps will be detected by hydrophones located at each NESTOR floor. The distance of the optical modules from the hydrophones is known because the hexagon arms are rigid. Their coordinates will then be determined via triangulation. Parameters like pressure, temperature and salinity of the environment which influence the speed of sound in the water will be recorded by the Slow Controls System.

Each responder unit is a combination of a pinger and a hydrophone and it is acoustically interfaced to the Slow Controls System. We will use commercial responders and hydrophones. The responder units are battery powered and will be dropped at distances of about 200-300 m around the NESTOR tower at deployment time. They typically have a battery life (lithium batteries) of several years and will respond for 10^5 pulses after which we can recycle them. They will respond to acoustic commands sent by one of three transponders located close to the bottom of the NESTOR tower and controlled by the Slow Controls system. The response will be the emission of acoustic chirps which will be detected by the NESTOR hydrophones. The differential time between floors will give the curvature of the NESTOR tower and the timing with respect to the transponders will give the relative position of the tower. The use of a surface ship with differential GPS (precise satellite navigation) will yield the absolute location at the responders to $\pm$ 1m. The relative PMT positions will be determined to within 10 cm.

In addition to the acoustical data there will be information from the compasses and the tilt meters (discussed in the Environmental Monitors part). This information will be correlated with the acoustical information and provide a redundancy in the determination of the physical shape of the NESTOR tower.

15.3 Retrieval and Servicing

After several years of operation NESTOR might need maintenance. It has then to be recovered, serviced and redeployed. The NESTOR tower is designed in a way to provide for easy deployment and recovery. Each NESTOR floor has close to neutral buoyancy so the whole tower does not need a lot of buoys to acquire a positive (upwards) net force in order to be able to resurface. Also care must be taken so the floors do not crash with the upper floors while they are moving up. This is accomplished by the weight of the electrooptical cable which also provides the proper riting. Further each floor has enough ballast to be a little heavier than the floor immediately above it. The crucial component for the recovery of the tower is the anchor release mechanism which could be triggered either by the Slow Controls system or by acoustic signaling. As a final backup it will be possible to literally grab the tower with a grapnel (hook) and winch it up to the surface. The buoy system on top is equipped with light and radio beacons which energize when the pressure becomes low and stand upwards when the tower has surfaced.

The recovery starts when the anchor release is triggered. The anchor platform stays at the sea floor and the whole tower moves upwards. The weight of the electrooptical cable keeps the tower upright. When the tower surfaces the light and radio beacons stick up

and the nearby barge receives their signals and approaches for the final stages of recovery and service. The crane hooks to the top of the buoy system and with the crane-winch cooperation the tower is either examined and serviced on the spot or is lifted into the barge for longer service operations, to be redeployed later.

15.4 Cable Route Investigation

As stated previously the route from the deep plateau to the shallow waters near the shore is very steep and rocky (15.2).

Figure 15.2: 3-D relief graph of the NESTOR area and the route to Methoni

The sea bottom contour and sub-bottom profile of the selected cable route have been investigated and charted. This route should be as short as possible to minimize cost of the cable. It should also impose minimal strain and minimize environmental effects on the cable, as it will lie on the bottom of the sea.

Two possible routes have been investigated. The first route is towards the small town of Methoni, at a distance of 13 nautical miles, where power and service for the Shore Control Station is readily available. The second route is towards the island of Sapienza at a distance of 7.5 nautical miles. This route is shorter but power and service must be provided, since the island is uninhabited. We have already run "sea bottom contour investigation" (i.e. depth versus position) on the route "NESTOR site-Sapienza island" and on the route "NESTOR site-Methoni" (15.3). The route "NESTOR site-Methoni" is finally chosen as the most appropriate one.

Moreover, a sub-bottom profile investigation has been performed for both routes with the Greek Oceanographic vessel "AEGAEO", using a high resolution 3.5kHz sub- bottom profiler, an "air-gun" profiler and Differential Global Positioning System for absolute positioning ($\pm$1m). The results indicate a difficult but stable area (See also chapter 1).

15.5 Deployment of the Electro-optical Cable

The telecommunications industry has many years of experience in deploying deep sea electro-optical cables. The easiest and least costly way for deploying the cable is to deploy it earlier and independently of the NESTOR tower, then its deep sea end will be attached on a buoy for later connection to the tower. In this way we can use either "THALES", the local cable laying ship of the National Telecommunications Organism of Greece, or a cable laying ship of opportunity on its way to/from cable laying operations in the Eastern Mediterranean which is a hub of cable laying activity connecting the Middle East and North Africa to Europe (as discussed, e.g. with the French Télécom). This is the cheapest way because we will not have to pay the transit time of the ship. According to the experts, the cable laying should be done comfortably in less than 24 hours.

The detector will be connected to the electro-optical cable on board of the deploying ship, before deployment. Then as each floor will be deployed, the end of the electro-optical cable will be payed out along with the tower deploying cable.

Deep underwater transponders, deployed prior to the detector deployment, will be used to navigate the tower to the required position. During the cable deployment towards to shore, we shall follow the charted and predetermine cable route on the sea bottom, using the Differential Global Positioning System.

Figure 15.3: Sea contour at the NESTOR area as obtained by the survey with theGreek Oceanographic vessel “AEGAEO”

Chapter 16

The Pylos Laboratory and The Shore Station

The PYLOS laboratory is an old school building (presently under restoration, figure 16.1), that the City of Pylos has generously provided for NESTOR. This is a two storey building with more than adequate floor space (about 500 m^2 each floor, figure 16.2). The building is situated on the shore of the bay of Navarino, at a short walking distance from the main square of Pylos. Navarino bay is a 4 by 2.5 km wide bay with depths down to 60 m (figure 16.3).

Figure 16.1: The Pylos Laboratory (before the restoration)

It is separated from the Ionian sea by the island of Sfaktiria, leaving only a 1 km wide

Figure 16.2: The Pylos Laboratory; architect drawing of the front side

navigable opening. Pylos is a well-equipped small rural town with good accommodation potential for the personnel of the laboratory. The Kalamata international airport is 35km from Pylos and Athens is a 3.5 hour drive away (2/3 on National freeway). Supplies that are unusual on the scale of a small rural town will have to be brought in from the industrial city of Kalamata, 45 km away. The harbour of Pylos is well equipped to provide berth to medium size ships and to provide services to large ships at anchor in Navarino Bay and unload or load cargo from them. The NESTOR deployment operations will be scheduled out of Pylos.

The PYLOS laboratory will serve several functions in the preparation and testing of the detector and in the running of the experiment:

- Providing general laboratory and test facilities for the preparation of the NESTOR Optical Module and of other components of the detector.
- Providing general machine shop facilities and drilling installation for the connector holes on the glass high pressure housing.
- High pressure testing of the glass housing and NESTOR optical module, in the Large high Pressure Tank (internal volume: diameter 500 mm, depth 500 mm) at pressures up to 600 atm (figure 11.16 a). In the small high pressure tank (internal volume: diameter 200 mm, depth 1000 mm) connectors, cables and others small sea-going equipment can be also pressed up to 600 atm (figure 11.16 b).
- Assembling the Nestor optical module and testing it.
- Monitoring and testing the photomultipliers before the installation into the NESTOR optical module as needed.

Figure 16.3: Chart of Navarino Bay

- Assembling each tower floor and deploying it into the Bay of Navarino for water, electric and electronic long time tests. For those tests, each NESTOR optical module will be covered in order to be shielded from the ambient light and algae's. For those test we already have the needed power cable and optical cable with monomode fibers, 1200 m long (figure 11.18).
- Providing computer facilities for event selection, track reconstruction and physics analysis. Moreover it will be connected with the international computer network for data, information and communication transfer.
- Distributing the data to collaborators for further analysis.
- Providing general support services for repairs (as those found in a well instrumented University Laboratory).
- Connecting the laboratory to the Shore Control Station.

The shore control station will be located on the shore where the electro-optical cable will emerge out of the sea in the town of Methoni, 13 nautical miles from the site. The shore control station will be situated in the Methoni Meteorological Station (figure 16.4), where power for the shore control station is readily available and it is only 10km drive away from the PYLOS laboratory at Pylos. We have been allowed to use the observation room of the Meteorological Station where there is a lot of free space and, according to the agreement that has been signed, it is at the disposal of NESTOR as of the end of March 95.

Figure 16.4: Photograph of the Methoni Meteorological Station

The shore control station will support several functions:

- Terminating the electro-optical cable on the shore.
- Generating the regulated high-voltage DC power for the NESTOR tower.
- Receiving the data from the tower and pre-process them.
- Providing the necessary computer power to process the received data at the first level with the neural network.
- Providing the slow control of the tower and process the position and environmental data.
- Providing the control to the calibration system of the tower.
- Transferring the information to the PYLOS laboratory at Pylos through a radio link or a link with high speed computer networking methods.

At the beginning of the operation we expect that the shore control station has to be staffed continuously, but we expect that eventually it will run remotely from Pylos, through the data link, requiring only occasionally service.

Chapter 17

Study of the Detector Response

17.1 Signal Simulation

The NESTOR apparatus is dedicated to the detection of Čerenkov light emitted by charged particles which cross its effective area.

The expected signals arise from a large variety of events : single and multiple muons coming from any direction with energy ranging between few GeV and PeV or more; neutrinos with the same energy range which can produce μ, electromagnetic and hadronic showers at any point of the detector. Moreover μ bremsstrahlung, direct pair production and photonuclear cross sections increase with energy together with the production of energetic δ rays and each charged particle created along the μ path contributes to Čerenkov light. As a consequence the light emitted by a very high energy μ behaves very differently from the simple light cone emitted by a single charged particle.

The only way to perform a detailed simulation of the photons detection in each phenomenon, taking into account all sources of fluctuations, is to follow each secondary particle produced inside every shower and assign to it the production of Čerenkov photons according to the well known formulas.

The simulation of detector response at NESTOR is performed by two different software packages which respond to a different philosophy and different requests of performance. The first code (MCN) has been derived from the DUMAND Monte Carlo and is based on an approximate but fast algorithm. The program makes a large use of parametrization formulas and associates to a muon of a given energy a light wave front of the corresponding intensity. MCN does not allow either the simulation of electromagnetic and hadronic showers or the temporal shape of the signal at one PMT, but due to its low CPU time consumption, it is essential for high statistic simulation of μ events with $E_\mu > 10 - 100$ TeV.

Recently a new simulation code has been developed by the NESTOR collaboration in order to accomplish the task of a full and accurate Monte Carlo despite the time consumption. The program (MC_NESTOR) is based on the GEANT software package [177] which performs the generation and the tracking of primary and secondary particles through the detector volumes and materials. Every particle is tracked by GEANT with a propagation "step by step". For every step relative to every generated charged particle the emission of Čerenkov photons is taken into account and every generated photon is then tracked until

its absorbtion. For every photon the following processes are simulated :

1. Absorption and light scattering inside transparent media (sea water, glass, gell) and inside opaque media (opaque zones inside the Benthos Spheres, opaque materials in the mechanical structure.)

2. Reflection and refraction at the surface separating materials with different refraction indices.

3. Detection at photocathode with emission of photoelectrons.

These processes and the generation of photons are simulated taking into account, in the probability distributions, the functional dependence on wavelength of Čerenkov emission, transparency, index of refraction and quantum efficiency.

Due to the large CPU time consumption, the Čerenkov simulation package of the GEANT software library is not usable for a big detector like NESTOR.

For this reason we have developed a package devoted to Čerenkov light emission which replaces the GEANT default subroutines. The new code performs a more efficient and 'intelligent' generation of Čerenkov photons making also use of tree structures in the geometrical routines. The result is a factor of 50 gain in CPU time consumption without any loss in the simulation power.

Nevertheless for very high energy muons (E_μ >10-100TeV) the amount of CPU time needed to simulate a single event with the GEANT tracking of secondary particles (mainly electrons and gammas) leads to a quite slow program which does not allow high statistic simulations.

An interface to a neutrino interaction package which makes use of recent determinations of structure functions [178] can be used to perform a detailed simulation of detector response to contained neutrino interactions with $E_\nu > 1$GeV, using MC_NESTOR.

Several geometrical parameters which define the NESTOR dimensions like the separation between floors and the dimensions of the arms which connect the Benthos spheres are left as variable parameters. This characteristic, together with the possibility to simulate alternative NESTOR tower structures besides the nominal one, can be used to study the optimization of the detector geometry.

17.1.1 Photoelectrons production

Due to the light attenuation and to the reduction of the solid angle the mean number of photoelectrons produced by a muon at one PMT decreases with the distance from the track. Fig.17.1 shows the mean number of detected photoelectrons (P.E.) as a function of the radial distance (i.e. the distance of closest approach) between the track and the PMT (for the NESTOR site the water transparency is equal to 55 meters). The emission of Čerenkov light from secondaries is not considered here.

Figure 17.2 shows the increase in the mean number of P.E. as a function of the muon energy, for a track at a radial distance of 18 m from the PMT.

As the muon energy increases, the fluctuations of the number of photoelectrons around the mean value increase drastically as a result of the large fluctuations which characterize

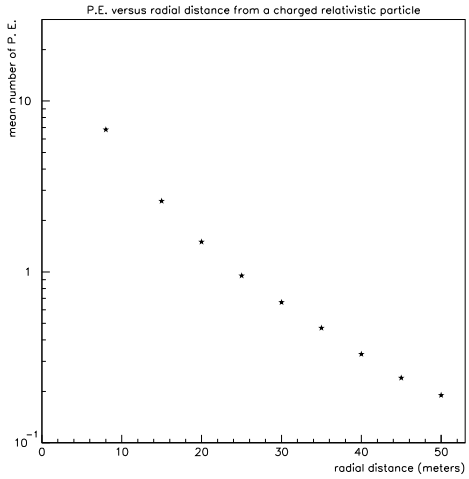

Figure 17.1: Mean number of P.E. versus the radial distance

the generation of secondaries by the muon. The increase of the tail in the distributions is the major factor in the increase of mean P.E. number with energy. Fig.17.3 shows the probability distribution of the number of photoelectrons, detected by one PMT, produced by the photons emitted from a muon track at two different energies at a radial distance of 18 m from the PMT. The area under each curve is normalized to 1.

The photons coming directly from the muon arrive within a time interval of about $2ns$ but a small amount of photons coming from electromagnetic showers around the μ arrive later because they are emitted , respect to the muon direction , at an angle different from the Čerenkov angle Θ_C. The amount of such delayed photons increases with the energy of the muon due to the increase in the number of electromagnetic showers around it. Fig.17.4 shows the probability distribution for the P.E. arrival time. The arrival times are smeared with a Gaussian spread ($\sigma = 2.5$ ns. The signal comes from a muon track at a radial distance of 18 m from the PMT.

Fig. 17.5 shows that the time spread of the signal is an important factor in the identification of single from double or multiple muons. The capability of discriminating multiple muons, which can be considered either signal or background, is of great importance for many physics questions that can be addressed by NESTOR. The figure shows the P.E. arrival time at one PMT for one typical double muon event (separation=5 meters). A Gaussian spread with variance 2.5 ns has been added to the arrival time of the photons in order to simulate the PMT time response. The double pulse resolution of our PMTs can handle this time difference very comfortably.

17.2 Track Reconstruction

Once the signal and the detector's response have been simulated, the track reconstruction algorithm reads in the event and tries to reconstruct the track parameters, using the

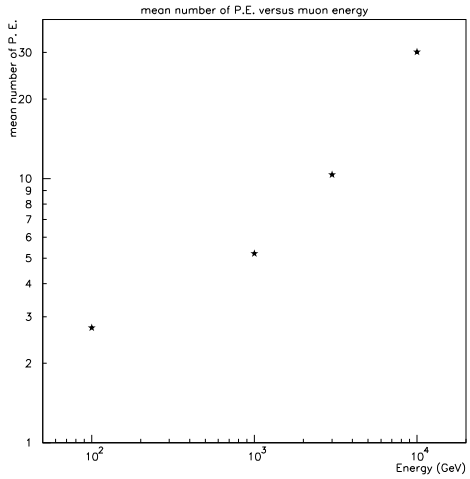

Figure 17.2: Mean number of P.E. versus the muon energy for 18 m radial distance

available information: time and charge of all the optical modules hit in the particular event. This algorithm consists of 3 successive steps of increasing sophistication, accuracy and cpu time consumption.

17.2.1 Hit definition, trigger hit, filter

For a photomultiplier in an event to be considered hit, it must have registered charge above a certain threshold, presently at the level of 0.5 Photoelectrons(P.E.). We need at least 6 pmt hits in the event to proceed with the reconstruction. We search through the hits in the event, to find the trigger hit, that is a hit that most likely is not a background hit (i.e. radioactive ^{40}K or bioluminescence). We find the tightest double coincidence in the event, and between the 2 hits of the coincidence, we define as the trigger hit the one with the higher charge. Once the trigger hit has been found we proceed with the Filter algorithm. We compare all the hits in the event to the trigger hit. If the time difference between the time of the trigger hit and the time of the hit we are testing, is greater than the time it would take for the light to go from the first photomultiplier to the other, the hit is rejected. To avoid loosing any real hits, the maximum allowed time difference is increased by 3σ of the time resolution plus the expected least count of our time measuring device. This algorithm is designed to reject random background hits. In our final design it will be incorporated into the triggering scheme.

17.2.2 Preliminary fit

After the first pass on the data has been performed using the Filter, we proceed to find preliminary track parameters, using a fast but not very accurate analytic algorithm, called

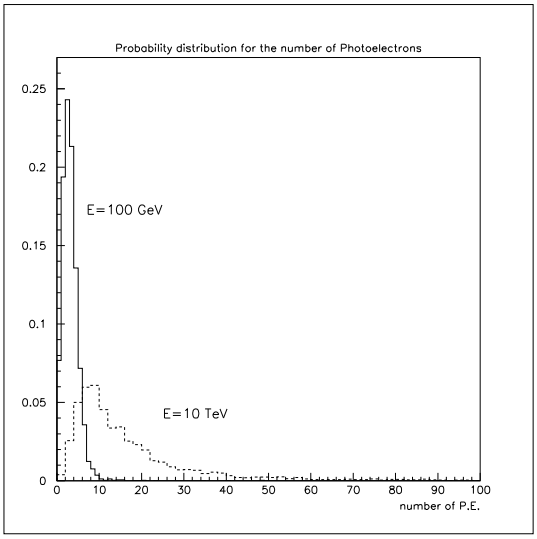

Figure 17.3: Distribution of the number of photoelectrons detected by the phototubes for muons with 100 GeV and 10 TeV energy.

Prefit. The position vector of a muon at time t is,

$$r = r^o + vt \tag{17.1}$$

where r^o is the initial position, and v the muon speed in the water. Let consider the muon speed as an unknown, express r,r^o and v as x^j,x_o^j and v^j j=1,3 and define the quantity,

$$\chi^2 = \sum_{j}^{1,3} \sum_{i}^{1,N} q_i (x_i^j - x_o^j - v^j t) \tag{17.2}$$

where, N=Number of hits and q_i the registered charge of hit i.

Taking the derivatives of the above quantity with respect to x_o^j and v^j and setting the results equal to 0, we end up with 6 equations for x and v. Solving these equations we find initial values for the track parameters x,y,z,$cos\theta$, and ϕ and calculate the speed of light. If the value found is different by more than 30%, from the known value, we reject the hits that contribute most to this difference and repeat the procedure. This algorithm, by performing an early reconstruction and comparing its results with a well known quantity, rejects random background hits that happen to be within our time window and also photon hits coming from processes other than Cerenkov.

17.2.3 Final fit

Using the results of the preliminary fit as input values to the final fit, we perform a χ^2 minimization, in order to find the muon vertex or earliest recorded position and the track parameters. In our detector, the nearest approximation to the interaction vertex is to reconstruct the coordinates of the emission point of the earliest detected photon. We

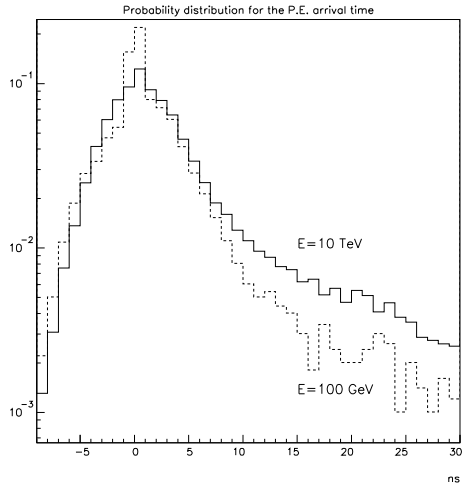

Figure 17.4: Distribution for the P.E. arrival time

call this point a pseudovertex. In order to reconstruct the pseudovertex and the track direction we perform a χ^2 minimization between the time registered by our TDC's and the expected time of arrival for the hit detector modules.

$$\chi^2 = \sum_i \frac{\left(T^i_{exp} - T^i_{data}\right)^2}{\sigma^2} \tag{17.3}$$

where σ is our expected time resolution.

The expected time for Cerenkov photons coming from a muon moving in the water is :

$$T^{muon}_{exp} = \frac{D_\mu}{c} + \frac{D_\gamma}{c/n} \tag{17.4}$$

where D_μ is the distance travelled by the muon to the emission point, D_γ is the distance travelled by the photon from the emission point to the detector module, and n is the index of refraction.

If the minimum χ^2 is less than a certain value, we reject the worst hits and repeat the procedure.

There are currently two versions of the final fit, their merits still being investigated. One is a 5 parameter fit for all parameters x,y,z,$cos\theta$,and ϕ and the other is to project at the z=0 point, solve for $x_{z=0}$,$y_{z=0}$,$cos\theta$,ϕ and then find analytically x,y,z,$cos\theta$ and ϕ. The 4 parameter fit seems to work better for vertical tracks since we have fewer unknowns and minimum projection error, but it works worse than the 5 parameter one for tracks around the horizontal where the projection error at z=0 is maximum.

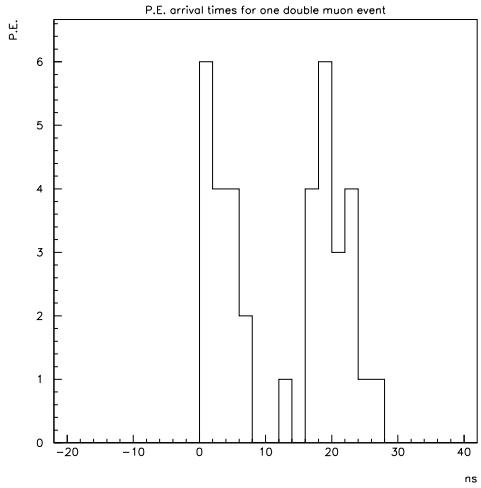

Figure 17.5: P.E. Arrival time at one PMT for one typical double muon event (the time "spread" properties of the PMT have been included, see text)

17.2.4 Low energy muon and electron reconstruction,

New versions of the code are being developed to reconstruct low energy electrons and muons generated within the geometrical volume of our detector and to try to discriminate between the two types of events. The electron reconstruction algorithm is based on the fact that the electron will shower within a few radiation lengths from its generation ($X_0 = 36$ cm). We assume that all the electron photons are coming from the same point like a spherical wave. The expected time for photons produced by electrons will then be

$$T_{exp}^{electron} = \frac{D_\gamma}{c/n}. \tag{17.5}$$

In order to distinguish between muons and electrons in an event we perform a "muon hypothesis" and an "electron hypothesis" fit. We apply cuts on the χ^2 of the two fits. We then apply cuts that take advantage of the differences between the two processes: for an electron we require that most of the charge be localized within a couple of detector floors, whereas for the muon that it be more or less evenly distributed along its path. We cut also on the maximum angle α_{max} formed between the lines joining a pair of hit pmts and the reconstructed pseudovertex. This cut is applied because the vast majority of the muon photons come from Cerenkov emission and the angle α cannot be more than $2 * \Theta_C$, whereas for the electrons α_{max} is much wider. Performing the two types of fits and applying the series of cuts mentioned, we get for 12 Gev electrons and muons roughly 60% reconstruction efficiency and 5% misidentification.

17.2.5 Low Energy ν_μ Interaction

The reconstruction of the interaction of a low energy neutrino that interacts within the geometrical volume of our detector is a complex problem. Two dedicated codes to handle these events are at the development stage. Based on studies done with the Pythia and Geant simulation programs, the photons that come from non muons (pions, kaons, nucleons) are emitted within a few meters from the interaction. Therefore a charged current ν_μ event looks like an overlap of a spherical wave, almost like an electron event, and a muon track.

The first code tries to distinguish the two types of hits in the same event, using the non muon hits to reconstruct the pseudovertex and the muon hits to reconstruct its direction. We weigh the early hits (most of them come from non muons) to reconstruct the pseudovertex and the distant hits to reconstruct the direction.

The second code does the track parameter fitting in 4 steps:

1) Spherical-type fit: under the assumption that all hits come from shower development and not from Cerenkov radiation from the muon, we use all possible 4-PMT (above 1 P.E.) combinations in the event to define the centre of the sphere that could have produced them. Most of the reconstructed centres converge to a single space point, which we consider to be a preliminary vertex position for the interaction . In real fact, this point is the position of the shower maximum.

2) hit-discrimination: having determined the preliminary vertex point r_v, we can determine a t_0 for the event. We then calculate for each hit the time difference

$$\delta t \;=\; t_{hit} - \frac{|r_v - r_{hit}|}{c} \tag{17.6}$$

where

- t_{hit} is the time of the hit w.r.t. t_0
- r_v is the preliminary vertex position determined before
- r_{hit} is the position of the PMT

δt is then a measure of the compatibility of the observed hit with the assumption that the hit has originated from a spherical wave with the origin at r_v. We find that Cerenkov photons from the muon contribute significantly to $\delta t < 0$. By a suitable cut on δt we can select hits coming directly from the muon.

3) muon-fit: the hits selected by the above procedure, are then fitted with a procedure similar to the one described in eq. 9.3, 9.4 to find the direction of the incoming track.

4)global fit: the preliminary vertex position r_v and track direction are then refitted using all the hits in the event under the assumption that a fraction of them come from the development of a spherical wave (late hits) and the prompt ones (early hits) directly from the muon.

These algorithms are by no means frozen and there are no quantitative results available yet.

17.3 High Energy Muon Reconstruction and Effective Area

In order to calculate our reconstruction efficiency, accuracy and effective area for high energy muons we have generated muons evenly distributed on the surface of a disk of radius,

$$R = \frac{DIAG}{2} + 3\Lambda \tag{17.7}$$

where $DIAG$ is the diagonal of our detector and Λ is the water Transmission Length at the detector site. The disk is situated at a distance from the detector center equal to its radius and the muons are generated perpendicular to the surface of the disk. By rotating the disk, the muons are generated flat in $\cos\theta$ and ϕ. The effective area then is:

$$A_{eff} = \frac{N_{reconstructed}}{N_{generated}} AREA \tag{17.8}$$

where $N_{generated}$ is the number of generated and $N_{reconstructed}$ the number of reconstructed muons and $AREA$ is the area of the flux disk. We show in figure 17.6 the effective area for 1 TeV muons and 10° reconstruction accuracy as function of $\cos\theta$ (zenith angle) and in figure 17.7 the effective area averaged over all angles as function of the muon energy, for muon energies from 0.1 TeV to 1000 TeV.

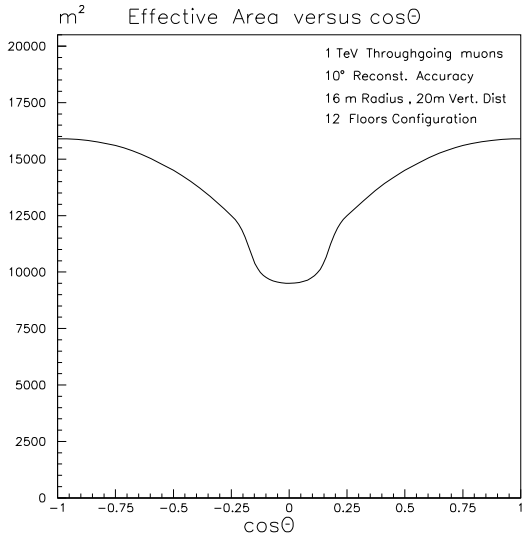

Figure 17.6: Effective area of 1 Tower for 1 Tev muons and 10° reconstruction accuracy vs the zenith angle ($\cos\theta = 0$ is the horizontal, $cos\theta = 1$ means downgoing)

In order to study our efficiency for vertical throughgoing muons we have generated muons up to 100 m from the detector center. The efficiency for 5^o reconstruction accuracy and three different energies is shown in figure 17.8.

The θ resolution of our detector for 1 TeV muons and all incidence angles is shown in figure 17.9.

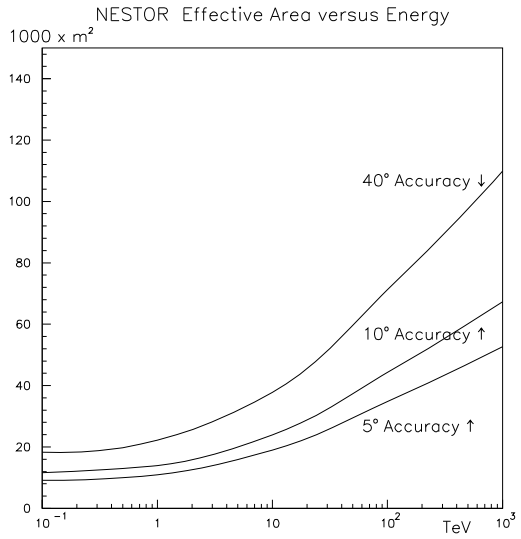

Figure 17.7: Effective area of one Tower averaged over all angles

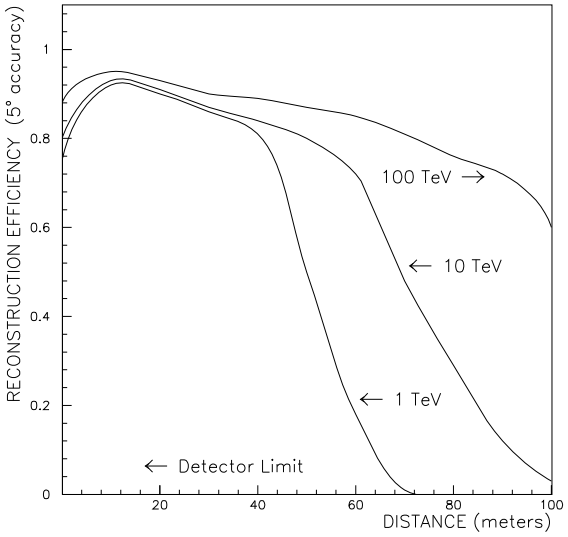

Figure 17.8: Efficiency for 5^o reconstruction accuracy and three different energies

Figure 17.9: Detector resolution for 1 TeV Muons

Chapter 18

Long Term Projects

18.1 The km^3 Detector

As already mentioned in Volume I, the main aims of a neutrino telescope are:

1. Observation and study of possible neutrino sources: Sun, Supernovæ, atmosphere, Galactic or extra-Galactic sources (e.g. X-ray binaries, Active Galactic Nuclei etc.)

2. Study of intrinsic properties of neutrinos: mass, mixing, lifetime;

3. Search for non-baryonic dark matter by searching for neutrinos produced in the annihilations of neutralinos in the Earth core or in the Sun.

Moreover, a neutrino detector may be also sensitive to nucleon decay and neutron-antineutron oscillations.

As described throughout this document, a single NESTOR tower will allow us to detect ν_μ and $\overline{\nu}_\mu$ with energies above a few GeV. This would allow the study of neutrino oscillations using neutrinos produced in the atmosphere or using a neutrino beam from CERN and this study should at least give significant constraints on the mixing angle between the ν_μ and the other two species of neutrinos and on the mass differences.

The study of an unexplored domain of the phase space of the parameters describing the theoretical models which predict the presence of neutralinos as cold dark matter in the halo of the Galaxy may be performed by searching for an excess of neutrinos of several tens of GeV arising from the Earth core.

Several galactic sources could be detected as neutrino emitters.

The Active Galactic Nuclei could contribute to a very high energy diffuse flux which may be detected as an excess of events in the horizontal plane.

In order to study the other items listed above and to obtain a better sensitivity on the physics subjects that we will hane started studying with one tower, a bigger detector and/or a detector with a lower energy threshold is needed.

The definition of the detector parameters in order to study each physics subject may be done using the neutrino fluxes predicted by the theoretical models. In the absence of any model one can try to define a detector with a sensitivity significantly greater than already existing detectors.

Financial and technological considerations would be severe constraints. In a first approach, one should push these constraints as far away as possible.

The best design of the next generation detector could be made by assembling several detectors, as they are actually projected, spaced by 100-200 m. This would be, for instance, a network of NESTOR towers and strings, as described in chapter 1 of volume 1, reaching a surface of $1\,km^2$. With a detector of this size the search for the non-baryonic dark matter would be performed using not only the Earth core as a neutrino source but also the Sun. This would enlarge considerably the domain of the phase space of the parameters to be explored. The search of galactic sources would gain in sensitivity and it would be possible to detect the Active Galactic Nuclei as individual sources of neutrinos (see also [**?**, **?**]).

Inside such a detector a second one with a volume of a few $10^5\,m^3$ and with an energy threshold of a few hundreds of MeV could allow us to reach a sensitivity an order of magnitude greater than that of SuperKamiokande. The total mass of such a detector will contain a few 10^{35} nucleons and, then, the sensitivity needed to detect the nucleon decay as predicted by the super-symmetrical models could be reached in a few years.

The detection of neutrinos from extra-galactic Supernovæ(as Andromeda for instance) needs a detector of at least $10^5\,m^3$ equipped with 10^4 optical modules.

In conclusion, the next generation detector should occupy a volume of $1\,km^3$ and should be equipped with at least 10^5 optical modules. Its structure must be multi-modular with a core with a higher density of optical modules and with external regions with lower density of light detectors.

This will constitute a formidable challenge from a financial and technological point of view. For this reason it cannot be materialized without the collaboration of the institutes which are now participating to the realization of the various actual projects, which may be considered as prototypes of the future detector.

In 1994 an initiative has been undertaken to create the kernel of such a cooperation. In February 1994 at the Sixth International Workshop in Venice (Italy) about thirty physicists, among which several members of the various actual projects, have decided to meet regularly to exchange informations and experience obtained during the preparation, construction and running of their experiments.

In 1994 the OCDE Megascience Forum discussed such projects [**?**].

In June 94 an international meeting was organized in Saclay (France). During this meeting a letter addressed to the Chairman of the OECD Megascience Forum of Particle Physics by L. Sulak (DAPNIA/SPP, CE-Saclay, France and Boston University, Boston, MA, USA) and M. Spiro (DAPNIA/SPP, CE-Saclay, France) has been written to report on the consensus of the participants to begin to work together. This letter was endorsed by 36 physicists of France, Germany, Greece, Italy, Netherlands, Russia, Spain, Sweden, Switzerland, UK and USA including the representatives of AMANDA, Lake Baikal, DUMAND and NESTOR. In July 94 special sessions of the workshop on the "Physics of the Next Millennium" in Snowmass (CO, USA) were devoted to this effort of collaboration. The members of BAND (for Baikal, AMANDA, NESTOR, DUMAND) have decided to create some working groups on various scientific and technical subjects. In December 94 a meeting was organized in Berkeley (CA, USA) by the Jet Propulsion Lab on software and physics. It was decided by the members of BAND present at this meeting to join

their effort in software development. It was also decided to organize a technical workshop in 95 followed, in 96, by a large scientific workshop, to be held in Europe, devoted to the realization of a cubic kilometer project.

The goal of these discussions is the realization of a scientific, technical and administrative structure which could allow to coordinate these efforts.

18.2 R&D for Other Techniques

New techniques are also being considered for later stages of NESTOR.

18.2.1 Acoustic Detection: Status and Prospects

The acoustic detection of elementary particles was suggested by G. A. Askaryan in the '50s [179] . A possibility of deployment of the deep ocean acoustic detector to search for ultrahigh energy (UHE) neutrinos (with energies above 10 PeV) has been discussed almost 20 years ago by G. A. Askaryan and B. A. Dolgoshein [180] , T. Bowen [181] and J. G. Learned [182] . The prediction of considerable UHE neutrino fluxes from active galactic nuclei (AGN) by Stecker et al. [183] supported much the idea of deployment of the large-scale cosmic neutrino detectors and in particular, the acoustic neutrino telescope [184] .

The deep underwater acoustic neutrino telescope SADCO (Sea Acoustic Detector of Cosmic Objects) with a threshold energy above 5 PeV was suggested to be deployed at a depth of 3.5 – 4 km in the Ionian Sea near Pylos just at the site of the optical neutrino telescope NESTOR [185, 186, 187] .

The search for UHE neutrinos via detection of an acoustic bipolar pulse caused by the expansion of the water due to the highly localized heating caused by the energy deposit in electron-hadron cascades initiated by interactions of these neutrinos of all flavors with nucleons in matter and particularly by the resonance interactions of electron-antineutrino with electrons is the main goal of the SADCO project. The tremendous advantage is that, in the frequency of 10–20 kHz, the attenuation length is of the order of a few kilometers. The fiducial volume of the SADCO neutrino telescope should be the order of $10^8 - 10^9 m^3$ if dozens of events per year caused by neutrinos with the resonance energy are to be measured. The sound pressure level and the duration of the bipolar pulse produced by the electron- hadron cascades as well as acoustic noise conditions at the SADCO site are important.

The results of the preliminary measurements of the acoustic background in the Ionian Sea at depth of 4 km near the coast of Pylos, (the NESTOR site) and calculations of the characteristics of the acoustic pulses produced by the electron- hadron cascade with an energy of 10 PeV as well as future plans are presented in the next sections.

18.2.2 Tests of a Prototype of the SADCO Module

A SADCO prototype module was tested during cruises of the research vehicles "Vityaz" (in 1991) and "Academic Mstislav Keldysh" (in 1992) in the Ionian Sea near the South-West coast of Greece. The calm sea, large depths (up to 4 km) and the relatively high

temperature of water (about $14°C$ at the depth range of 200–4000 m) make the NESTOR area very attractive for a long term acoustic neutrino detection.

The prototype module consists of a spherical ball made of titanium and an acoustic antenna above it . All electronics, some apparatus and a power supply were contained inside a titanium ball with a diameter of 1 m. The acoustical antenna was designed as a series of hydrophones attached to a string which was vertically positioned with the help of a floatation package on its top. A special heavy load (sinker) was attached to the titanium ball to compensate for the positive buoyancy of the module. The module was descended to a depth of about 4 km and stayed at a distance of 20 m from the bottom. The retrieval of the module was possible by commands either from the vehicle using an acoustical channel of communication or from a timer turning on the automatic switch to release the sinker. The module was equipped with light and radio beacons to recovery in the open sea.

The acoustical background measurements were carried out with the help of the 8-element (hydrophones) equidistant antenna which was 25 m long and the 12-element nonequidistant antenna with 1.5 m length. The threshold sensitivity of these antennas were 5 and 3 $\mu Pa/Hz^{0.5}$ * respectively at the frequency of 20 kHz [185, 186, 187] . The acoustical signals at the frequency band of 3 – 50 kHz were stored both in the analog and digital forms. The data were sampled in blocks of 512 counts for treatment. The stationarity and homogeneity hypotheses were tested by the criteria of series and the Kolmogorov-Smirnov test [188] . It was found out that the measured noise was stationary during at least 5 minutes. The hypothesis of the Gaussian approximation of distributions involved was tested by the Kolmogorov criterion, chi-square and the skewness and excess (kurtosis) methods [188] . The deviations from the Gaussian distribution were found out at a level above 5–6 sigma. The minimal level of the acoustical noise detected was $12\mu Pa/Hz^{0.5}$ at the frequency band of 15–30 kHz.

18.2.3 Acoustical Pulse Generated by a 10 PeV Cascade

The bipolar acoustical signal was calculated [191] taking into account the energy deposits by the electron-hadron cascade estimated in terms of the quark-gluon string model [187] . Fig. 18.1 shows the bipolar acoustical pulses caused by a cascade with an energy of 10 PeV at a distance of 400 m from the cascade core allowing for the sound absorption in

*Reminder: 1 atmosphere ≡ 101325 Pascal

the sea water.

Figure 18.1: The acoustical pulse in sea water at a distance of 400 m from a cascade with energy of 10 PeV. (1)- Learned ; (2)- Askaryan ; (3)- Dedenko

Curve 1 was taken from [182] and curve 2 from [189] while curve 3 displays our calculations. All signals were recalculated for the parameters of the NESTOR polygon (4 km depth and $14°C$ temperature of water). It should be noted that in reference [190] the new estimate of the acoustical pressure of $250\mu Pa$ at a distance of 40 m from the cascade core was given. This value corresponds to the pressure of $80\mu Pa$ at a distance of 400 m but not allowing for the absorption of the sound. Fig. 18.1 shows that the amplitude of our signal (3) is approximately twice as much as the pulse (2). This can be accounted for the more narrow radial distribution of electrons in the cascade [187] in comparison with an approximation used in [189] . Thus according to different estimates the amplitude of the acoustical pulse caused by the electron-hadron cascade with an energy of 10 PeV in sea water can vary from 25 to $60\mu Pa$ at the distance of 400 m from the cascade core allowing for the sound absorption. The main fraction of the acoustical signal energy is distributed inside the frequency band of 2–30 kHz in [189] and inside the band of 4–50 kHz in case of our pulse (3). Fig. 18.2 illustrates the dependence of the maximal acoustical pressure Pmax on the distance from the cascade with energy of 10 PeV.

Curve 1 is calculated disregarding absorption of sound in water and the curve 2 takes into account this absorption. Fig. 18.3 shows the dependence of acoustical pulse on displacement along the cascade axis for distances 100 m (1), 400 m (2) and 1000 m (3).

Figure 18.2: The dependence of an acoustical signal amplitude on a distance from the cascade shower: (1)- without absorption, (2)- with absorption taken into account.

18.2.4 The New Prototype of the SADCO Module

Our tests showed how the construction of the acoustic module should be modified. We are building now a module with the antenna in form of a grid which consists of 48 hydrophones. The data acquisition system will be designed on the base of the IBM- compatible controller. The autonomy of a module should be increased to 100 days to measure the long-term variations of acoustical noise parameters. The hydroacoustical communication apparatus and the system of searching for a module on the surface of the open sea will also be improved.

The daily and seasonal variations of acoustical noise parameters, the random large impulses and the spatial distributions of the noise level will be measured. Searching for the sources of the bipolar pulses which look like those caused by the high energy cascades and their localization is important.

18.2.5 Conclusion

The results of our measurements carried out in the Ionian sea near Pylos (Greece) in 1991 and 1992 displayed the relatively low level of acoustic noises of $12\mu Pa/Hz^{0.5}$ in the frequency band of 15–30 kHz and rather high temperature of water of about $14^{\circ}C$ at depths of 0.2–4 km, that make this polygon near Pylos very attractive for a deployment of the acoustic neutrino telescope SADCO.

Our calculations of the acoustic signal yield the amplitude of pulse of $60\mu Pa$ for the electron-hadron cascade with the energy of 10 PeV at the distance of 400 m from the

Figure 18.3: The dependence of an acoustical signal amplitude on a displacement Z along the cascade axis.(1) R=100 m; (2) R=400 m; (3) R= 1000 m.

cascade core allowing for the sound absorption in the sea water. This amplitude is a few times bigger than earlier estimates [189, 190] .

The calculated frequency spectrum of the acoustical pulse is localized inside the range of 4-50 kHz which is rather attractive from the point of view both of a detection and the minimal noise level in the sea.

Thus the results of both our measurements and our calculations of the acoustical signal are of interest for investigations of UHE neutrino fluxes from active galactic nuclei by the acoustic method. In particular the search for resonant interactions of cosmic electron antineutrino with electrons in water at the energy of 6.4 PeV is of importance. The detailed measurements of spatial noise distributions should give some additional arguments for the realization of detection of this resonant reaction (acoustic noises at large depths are minimal in horizontal directions and thus the signal/noise ratio is maximal). In any case the search for cosmic neutrinos with energies above 10 PeV could be carried out.

We propose to develop and to construct a prototype of deep underwater SADCO module consisting of 48 (64) hydrophones, to investigate longtime variations of deep underwater acoustic noises and their spatial distribution in the 1-50 kHz range. A search for acoustic signals induced by superhigh energy cascades will be realized.

These investigations will allow to elaborate the SADCO design, to estimate the number of hydrophones and effective detection volumes for detection of superhigh energy cosmic neutrinos.

Appendix 1

Tables of Atmospheric Neutrino Spectra

V (1980)	cos ϑ						
	1.0	0.6	0.4	0.3	0.2	0.1	0.0
E_ν (GeV)	$\nu_\mu + \overline{\nu}_\mu$ flux [(cm^2 s sr GeV)$^{-1}$]						
10^0	5.06×10^{-2}	5.80×10^{-2}	6.30×10^{-2}	6.56×10^{-2}	6.87×10^{-2}	7.09×10^{-2}	7.23×10^{-2}
3×10^0	1.74×10^{-3}	2.02×10^{-3}	2.25×10^{-3}	2.41×10^{-3}	2.63×10^{-3}	2.85×10^{-3}	2.96×10^{-3}
10^1	4.38×10^{-5}	5.19×10^{-5}	5.91×10^{-5}	6.50×10^{-5}	7.33×10^{-5}	8.28×10^{-5}	8.86×10^{-5}
3×10^1	1.53×10^{-6}	1.86×10^{-6}	2.17×10^{-6}	2.42×10^{-6}	2.79×10^{-6}	3.25×10^{-6}	3.57×10^{-6}
10^2	3.91×10^{-8}	4.95×10^{-8}	5.89×10^{-8}	6.62×10^{-8}	7.70×10^{-8}	9.19×10^{-8}	1.05×10^{-7}
3×10^2	1.22×10^{-9}	1.60×10^{-9}	1.95×10^{-9}	2.22×10^{-9}	2.63×10^{-9}	3.20×10^{-9}	3.69×10^{-9}
10^3	2.48×10^{-11}	3.43×10^{-11}	4.27×10^{-11}	4.94×10^{-11}	5.99×10^{-11}	7.42×10^{-11}	8.59×10^{-11}
3×10^3	5.62×10^{-13}	8.30×10^{-13}	1.08×10^{-12}	1.30×10^{-12}	1.65×10^{-12}	2.14×10^{-12}	2.54×10^{-12}
10^4	7.25×10^{-15}	1.17×10^{-14}	1.64×10^{-14}	2.08×10^{-14}	2.84×10^{-14}	3.95×10^{-14}	4.86×10^{-14}
3×10^4	1.32×10^{-16}	2.20×10^{-16}	3.18×10^{-16}	4.14×10^{-16}	5.84×10^{-16}	8.52×10^{-16}	1.08×10^{-15}
10^5	1.51×10^{-18}	2.52×10^{-18}	3.67×10^{-18}	4.84×10^{-18}	6.98×10^{-18}	1.06×10^{-17}	1.41×10^{-17}
3×10^5	2.66×10^{-20}	4.45×10^{-20}	6.58×10^{-20}	8.66×10^{-20}	1.27×10^{-20}	1.96×10^{-19}	2.62×10^{-19}
10^6	2.53×10^{-22}	4.21×10^{-22}	6.31×10^{-22}	8.20×10^{-22}	1.20×10^{-21}	1.85×10^{-21}	2.47×10^{-21}
3×10^6	3.00×10^{-24}	5.01×10^{-24}	7.51×10^{-24}	9.77×10^{-24}	1.43×10^{-23}	2.21×10^{-23}	2.95×10^{-23}
10^7	2.32×10^{-26}	3.88×10^{-26}	5.74×10^{-26}	7.55×10^{-26}	1.10×10^{-25}	1.70×10^{-25}	2.26×10^{-25}
E_ν (GeV)	$\nu_e + \overline{\nu}_e$ flux [(cm^2 s sr GeV)$^{-1}$]						
10^0	2.20×10^{-2}	2.92×10^{-2}	3.41×10^{-2}	3.66×10^{-2}	3.95×10^{-2}	4.17×10^{-2}	4.30×10^{-2}
3×10^0	4.65×10^{-4}	7.26×10^{-4}	9.64×10^{-4}	1.13×10^{-3}	1.36×10^{-3}	1.58×10^{-3}	1.68×10^{-3}
10^1	6.81×10^{-6}	1.17×10^{-5}	1.69×10^{-5}	2.13×10^{-5}	2.83×10^{-5}	3.66×10^{-5}	4.18×10^{-5}
3×10^1	1.45×10^{-7}	2.49×10^{-7}	3.74×10^{-7}	4.90×10^{-7}	7.00×10^{-7}	1.01×10^{-7}	1.27×10^{-6}
10^2	2.15×10^{-9}	3.40×10^{-9}	5.00×10^{-9}	6.70×10^{-9}	1.01×10^{-8}	1.65×10^{-8}	2.42×10^{-8}
3×10^2	5.08×10^{-11}	7.82×10^{-11}	1.11×10^{-10}	1.46×10^{-10}	2.15×10^{-10}	3.47×10^{-10}	5.09×10^{-10}
10^3	9.01×10^{-13}	1.36×10^{-12}	1.83×10^{-12}	2.26×10^{-12}	3.01×10^{-12}	4.34×10^{-12}	5.93×10^{-12}
3×10^3	1.82×10^{-14}	2.83×10^{-14}	3.83×10^{-14}	4.77×10^{-14}	5.39×10^{-14}	9.13×10^{-14}	1.21×10^{-13}
10^4	2.21×10^{-16}	3.64×10^{-16}	5.20×10^{-16}	6.76×10^{-16}	9.51×10^{-16}	1.40×10^{-15}	1.81×10^{-15}
3×10^4	3.91×10^{-18}	6.54×10^{-18}	9.48×10^{-18}	1.25×10^{-17}	1.79×10^{-17}	2.68×10^{-17}	3.47×10^{-17}
10^5	4.46×10^{-20}	7.47×10^{-20}	1.09×10^{-19}	1.44×10^{-19}	2.08×10^{-19}	3.20×10^{-19}	4.25×10^{-19}
3×10^5	7.72×10^{-22}	1.30×10^{-21}	1.89×10^{-21}	2.51×10^{-21}	3.64×10^{-21}	5.66×10^{-21}	7.55×10^{-21}
10^6	6.39×10^{-24}	1.08×10^{-23}	1.56×10^{-23}	2.07×10^{-23}	3.00×10^{-23}	4.67×10^{-23}	6.24×10^{-23}
3×10^6	7.49×10^{-26}	1.25×10^{-25}	1.84×10^{-25}	2.44×10^{-25}	3.54×10^{-25}	5.49×10^{-25}	7.35×10^{-25}
10^7	5.72×10^{-28}	9.51×10^{-28}	1.41×10^{-27}	1.86×10^{-27}	2.71×10^{-27}	4.18×10^{-27}	5.60×10^{-27}

Table A.1: Differential energy spectra of $\nu_\mu + \overline{\nu}_\mu$ and $\nu_e + \overline{\nu}_e$ from (π, K) decays for different zenith angles as calculated in Ref. [104].

E_ν	$\nu_\mu/\overline{\nu}_\mu$		$\nu_e/\overline{\nu}_e$	
(GeV)	$\vartheta = 0^\circ$	$\vartheta = 90^\circ$	$\vartheta = 0^\circ$	$\vartheta = 90^\circ$
10^1	1.30	1.30	1.30	1.30
10^2	1.70	1.50	1.30	1.45
10^3	2.10	2.10	1.40	1.45

Table A.2: Estimates of the ratio $\nu_l/\overline{\nu}_l$ in fluxes of the (π, K) neutrinos from Ref. [104].

BDZ (1989)	$\cos\vartheta$						
	1.0	0.6	0.4	0.3	0.2	0.1	0.0
E_ν (GeV)	$\nu_\mu + \overline{\nu}_\mu$ flux [in $(\mathrm{cm}^2\ \mathrm{s\ sr\ GeV})^{-1}$]						
10^0	4.22×10^{-2} (1.22)	4.29×10^{-2} (1.13)	5.39×10^{-2} (1.08)	5.60×10^{-2} (1.06)	5.87×10^{-2} (1.06)	6.05×10^{-2} (1.06)	6.17×10^{-2} (1.03)
3×10^0	1.86×10^{-3} (1.35)	2.16×10^{-3} (1.23)	2.41×10^{-3} (1.15)	2.57×10^{-3} (1.12)	2.80×10^{-3} (1.08)	3.04×10^{-3} (1.06)	3.16×10^{-3} (1.03)
10^1	5.52×10^{-5} (1.47)	6.42×10^{-5} (1.36)	7.26×10^{-5} (1.26)	7.89×10^{-5} (1.20)	8.78×10^{-5} (1.13)	9.87×10^{-5} (1.07)	1.07×10^{-4} (1.04)
3×10^1	1.99×10^{-6} (1.57)	2.37×10^{-6} (1.48)	2.72×10^{-6} (1.40)	2.99×10^{-6} (1.34)	3.38×10^{-6} (1.25)	3.94×10^{-6} (1.15)	4.56×10^{-6} (1.07)
10^2	4.50×10^{-8} (1.67)	5.59×10^{-8} (1.61)	6.63×10^{-8} (1.56)	7.42×10^{-8} (1.51)	8.58×10^{-8} (1.44)	1.12×10^{-7} (1.33)	1.23×10^{-7} (1.16)
3×10^2	1.30×10^{-9} (1.76)	1.66×10^{-9} (1.71)	2.01×10^{-9} (1.66)	2.29×10^{-9} (1.63)	2.70×10^{-9} (1.58)	3.29×10^{-9} (1.50)	4.02×10^{-9} (1.38)
10^3	2.32×10^{-11} (1.82)	3.18×10^{-11} (1.78)	4.02×10^{-11} (1.75)	4.66×10^{-11} (1.73)	5.62×10^{-11} (1.69)	6.97×10^{-11} (1.64)	8.43×10^{-11} (1.56)
3×10^3	4.87×10^{-13} (1.84)	7.23×10^{-13} (1.82)	9.72×10^{-13} (1.80)	1.18×10^{-12} (1.79)	1.49×10^{-12} (1.76)	1.93×10^{-12} (1.73)	2.37×10^{-12} (1.68)
10^4	6.14×10^{-15} (1.83)	9.56×10^{-15} (1.83)	1.35×10^{-14} (1.82)	1.71×10^{-14} (1.81)	2.29×10^{-14} (1.80)	3.19×10^{-14} (1.78)	4.13×10^{-14} (1.76)
3×10^4	1.08×10^{-16} (1.80)	1.71×10^{-16} (1.80)	2.46×10^{-16} (1.80)	3.16×10^{-16} (1.80)	4.36×10^{-16} (1.80)	6.35×10^{-16} (1.79)	8.60×10^{-16} (1.78)
10^5	1.26×10^{-18} (1.77)	2.01×10^{-18} (1.77)	2.92×10^{-18} (1.77)	$3,78 \times 10^{-18}$ (1.77)	5.28×10^{-18} (1.77)	7.85×10^{-18} (1.76)	1.09×10^{-17} (1.76)
3×10^5	2.18×10^{-20} (1.73)	3.49×10^{-20} (1.73)	5.10×10^{-20} (1.73)	6.60×10^{-20} (1.73)	9.26×10^{-20} (1.73)	1.39×10^{-19} (1.73)	1.93×10^{-19} (1.72)
10^6	2.56×10^{-22} (1.69)	4.09×10^{-22} (1.69)	5.98×10^{-22} (1.69)	7.75×10^{-22} (1.69)	1.09×10^{-21} (1.69)	1.63×10^{-21} (1.69)	2.28×10^{-21} (1.69)
E_ν (GeV)	$\nu_e + \overline{\nu}_e$ flux [in $(\mathrm{cm}^2\ \mathrm{s\ sr\ GeV})^{-1}$]						
10^0	1.72×10^{-2} (1.31)	2.33×10^{-2} (1.28)	2.77×10^{-2} (1.25)	2.97×10^{-2} (1.24)	3.21×10^{-2} (1.23)	3.38×10^{-2} (1.22)	3.49×10^{-2} (1.22)
3×10^0	5.15×10^{-4} (1.31)	7.69×10^{-4} (1.28)	9.95×10^{-4} (1.25)	1.15×10^{-3} (1.24)	1.38×10^{-3} (1.23)	1.61×10^{-3} (1.22)	1.71×10^{-3} (1.21)
10^1	8.52×10^{-6} (1.32)	1.42×10^{-5} (1.28)	2.04×10^{-5} (1.25)	2.57×10^{-5} (1.24)	3.34×10^{-5} (1.23)	4.36×10^{-5} (1.22)	5.18×10^{-5} (1.21)
3×10^1	1.72×10^{-7} (1.33)	2.93×10^{-7} (1.30)	4.50×10^{-7} (1.26)	6.01×10^{-7} (1.25)	8.66×10^{-7} (1.23)	1.31×10^{-6} (1.22)	1.85×10^{-6} (1.21)
10^2	2.43×10^{-9} (1.37)	3.82×10^{-9} (1.33)	5.74×10^{-9} (1.30)	7.75×10^{-9} (1.26)	1.17×10^{-8} (1.24)	1.98×10^{-8} (1.23)	3.45×10^{-8} (1.21)
3×10^2	5.25×10^{-11} (1.48)	7.80×10^{-11} (1.42)	1.10×10^{-10} (1.37)	1.42×10^{-10} (1.31)	2.06×10^{-10} (1.26)	3.46×10^{-10} (1.24)	6.69×10^{-10} (1.22)
10^3	7.50×10^{-13} (1.58)	1.12×10^{-12} (1.54)	1.55×10^{-12} (1.49)	1.94×10^{-12} (1.46)	2.65×10^{-12} (1.39)	4.04×10^{-12} (1.30)	7.15×10^{-12} (1.25)
3×10^3	1.41×10^{-14} (1.63)	2.18×10^{-14} (1.62)	3.07×10^{-14} (1.59)	3.88×10^{-14} (1.57)	5.25×10^{-14} (1.52)	7.65×10^{-14} (1.47)	1.17×10^{-13} (1.36)
10^4	1.68×10^{-16} (1.64)	2.66×10^{-16} (1.64)	3.84×10^{-16} (1.63)	4.92×10^{-16} (1.62)	6.79×10^{-16} (1.61)	9.96×10^{-16} (1.58)	1.41×10^{-15} (1.52)
3×10^4	2.90×10^{-18} (1.63)	4.63×10^{-18} (1.63)	6.73×10^{-18} (1.63)	8.69×10^{-18} (1.63)	1.21×10^{-17} (1.62)	1.80×10^{-17} (1.61)	2.52×10^{-17} (1.59)
10^5	3.39×10^{-20} (1.62)	5.42×10^{-20} (1.62)	7.91×10^{-20} (1.62)	1.03×10^{-19} (1.62)	1.44×10^{-19} (1.61)	2.15×10^{-19} (1.61)	3.01×10^{-19} (1.60)
3×10^5	5.88×10^{-22} (1.60)	9.40×10^{-22} (1.60)	1.37×10^{-21} (1.60)	1.78×10^{-21} (1.60)	2.50×10^{-21} (1.60)	3.75×10^{-21} (1.59)	5.24×10^{-21} (1.59)
10^6	6.88×10^{-24} (1.57)	1.10×10^{-23} (1.57)	1.61×10^{-23} (1.57)	2.09×10^{-23} (1.57)	2.93×10^{-23} (1.57)	4.40×10^{-23} (1.57)	6.16×10^{-23} (1.57)

Table A.3: Differential energy spectra of $\nu_\mu + \overline{\nu}_\mu$ and $\nu_e + \overline{\nu}_e$ from (π, K) decays for different zenith angles as calculated in Ref. [68]; the numbers in parenthesis are the ratios $\nu_l/\overline{\nu}_l$.

L (1993)	$\cos\vartheta$						
	1.0	0.6	0.4	0.3	0.2	0.1	0.0
E_ν (GeV)	$\nu_\mu + \overline{\nu}_\mu$ flux [in (cm^2 s sr GeV)$^{-1}$]						
10^0	3.64×10^{-2} (1.18)	4.11×10^{-2} (1.13)	4.43×10^{-2} (1.10)	4.63×10^{-2} (1.08)	4.85×10^{-2} (1.07)	5.12×10^{-2} (1.05)	5.30×10^{-2} (1.04)
3.16×10^0	1.31×10^{-3} (1.29)	1.52×10^{-3} (1.21)	1.70×10^{-3} (1.16)	1.82×10^{-3} (1.13)	1.96×10^{-3} (1.10)	2.11×10^{-3} (1.07)	2.19×10^{-3} (1.06)
10^1	4.46×10^{-5} (1.44)	5.20×10^{-5} (1.35)	5.90×10^{-5} (1.28)	6.43×10^{-5} (1.23)	7.18×10^{-5} (1.18)	8.22×10^{-5} (1.12)	8.98×10^{-5} (1.09)
3.16×10^1	1.42×10^{-6} (1.63)	1.69×10^{-6} (1.53)	1.92×10^{-6} (1.45)	2.10×10^{-6} (1.40)	2.37×10^{-6} (1.33)	2.81×10^{-6} (1.23)	3.30×10^{-6} (1.16)
10^2	4.08×10^{-8} (1.90)	5.00×10^{-8} (1.76)	5.84×10^{-8} (1.67)	6.47×10^{-8} (1.60)	7.38×10^{-8} (1.52)	8.79×10^{-8} (1.42)	1.01×10^{-7} (1.29)
3.16×10^2	1.09×10^{-9} (2.20)	1.37×10^{-9} (2.07)	1.63×10^{-9} (1.96)	1.83×10^{-9} (1.89)	2.12×10^{-9} (1.79)	2.56×10^{-9} (1.66)	3.07×10^{-9} (1.52)
10^3	2.59×10^{-11} (2.38)	3.48×10^{-11} (2.32)	4.27×10^{-11} (2.26)	4.87×10^{-11} (2.20)	5.72×10^{-11} (2.11)	6.98×10^{-11} (1.98)	8.17×10^{-11} (1.85)
3.16×10^3	4.93×10^{-13} (2.42)	7.28×10^{-13} (2.41)	9.63×10^{-13} (2.40)	1.15×10^{-12} (2.38)	1.42×10^{-12} (2.34)	1.81×10^{-12} (2.27)	2.12×10^{-12} (2.19)
10^4	7.90×10^{-15} (2.43)	1.24×10^{-14} (2.43)	1.74×10^{-14} (2.42)	2.18×10^{-14} (2.42)	2.87×10^{-14} (2.42)	3.98×10^{-14} (2.40)	4.91×10^{-14} (2.38)
3.16×10^4	1.17×10^{-16} (2.42)	1.88×10^{-16} (2.43)	2.72×10^{-16} (2.43)	3.49×10^{-16} (2.43)	4.79×10^{-16} (2.43)	7.07×10^{-16} (2.42)	9.18×10^{-16} (2.42)
10^5	1.67×10^{-18} (2.42)	2.72×10^{-18} (2.42)	3.97×10^{-18} (2.42)	5.15×10^{-18} (2.42)	7.18×10^{-18} (2.43)	1.09×10^{-17} (2.43)	1.46×10^{-17} (2.43)
3.16×10^5	2.37×10^{-20}	3.87×10^{-20}	5.67×10^{-20}	7.38×10^{-20}	1.03×10^{-20}	1.59×10^{-19}	2.14×10^{-19}
E_ν (GeV)	$\nu_e + \overline{\nu}_e$ flux [in (cm^2 s sr GeV)$^{-1}$]						
10^0	1.46×10^{-2} (1.32)	1.90×10^{-2} (1.32)	2.22×10^{-2} (1.32)	2.41×10^{-2} (1.31)	2.63×10^{-2} (1.31)	2.89×10^{-2} (1.31)	3.05×10^{-2} (1.31)
3.16×10^0	3.76×10^{-4} (1.32)	5.64×10^{-4} (1.32)	7.28×10^{-4} (1.32)	8.41×10^{-4} (1.32)	9.77×10^{-3} (1.31)	1.13×10^{-3} (1.31)	1.20×10^{-3} (1.31)
10^1	7.42×10^{-6} (1.32)	1.24×10^{-5} (1.32)	1.78×10^{-5} (1.32)	2.23×10^{-5} (1.32)	2.91×10^{-5} (1.32)	3.87×10^{-5} (1.32)	4.62×10^{-5} (1.31)
3.16×10^1	1.34×10^{-7} (1.32)	2.21×10^{-7} (1.32)	3.32×10^{-7} (1.32)	4.39×10^{-7} (1.32)	6.25×10^{-7} (1.32)	9.80×10^{-7} (1.32)	1.43×10^{-6} (1.32)
10^2	2.71×10^{-9} (1.35)	4.00×10^{-9} (1.33)	5.69×10^{-9} (1.33)	7.40×10^{-9} (1.32)	1.07×10^{-8} (1.32)	1.81×10^{-8} (1.32)	3.26×10^{-8} (1.32)
3.16×10^2	5.77×10^{-11} (1.44)	8.16×10^{-11} (1.40)	1.08×10^{-10} (1.37)	1.33×10^{-10} (1.36)	1.80×10^{-10} (1.34)	2.89×10^{-10} (1.33)	5.49×10^{-10} (1.33)
10^3	1.10×10^{-12} (1.54)	1.62×10^{-12} (1.51)	2.17×10^{-12} (1.47)	2.65×10^{-12} (1.45)	3.43×10^{-12} (1.42)	4.96×10^{-12} (1.38)	8.09×10^{-12} (1.37)
3.16×10^3	1.80×10^{-14} (1.60)	2.81×10^{-14} (1.58)	3.93×10^{-14} (1.56)	4.91×10^{-14} (1.54)	6.50×10^{-14} (1.52)	9.26×10^{-14} (1.48)	1.30×10^{-13} (1.45)
10^4	2.70×10^{-16} (1.62)	4.34×10^{-16} (1.61)	6.25×10^{-16} (1.61)	7.99×10^{-16} (1.60)	1.09×10^{-15} (1.59)	1.61×10^{-15} (1.57)	2.17×10^{-15} (1.55)
3.16×10^4	3.90×10^{-18} (1.63)	6.32×10^{-18} (1.62)	9.23×10^{-18} (1.62)	1.19×10^{-17} (1.62)	1.66×10^{-17} (1.61)	2.52×10^{-17} (1.61)	3.39×10^{-17} (1.60)
10^5	5.54×10^{-20} (1.63)	9.02×10^{-20} (1.63)	1.32×10^{-19} (1.63)	1.72×10^{-19} (1.63)	2.41×10^{-19} (1.62)	3.70×10^{-19} (1.62)	5.00×10^{-19} (1.62)
3.16×10^5	7.85×10^{-22}	1.28×10^{-21}	1.88×10^{-21}	2.45×10^{-21}	3.44×10^{-21}	5.30×10^{-21}	7.17×10^{-21}

Table A.4: Differential energy spectra of $\nu_\mu + \overline{\nu}_\mu$ and $\nu_e + \overline{\nu}_e$ from (π, K) decays for different zenith angles as calculated in Ref. [100]; the numbers in parenthesis are the ratios $\nu_l/\overline{\nu}_l$.

Bibliography

[1] F. Stecker et al., *Astrophys. J.* **390** (1992) L49.

[2] O. C. De Jager et al., *Letters to Nature* **369** (1994) 294.

[3] R. J. Gould and G. P. Schréder, *Phys. Rev.* **155** (1967) 1408;
G. Yodh, in: *Proceedings of the 1994 Heidelberg Workshop on Gamma Rays*, to be published by Kluwer.

[4] V. S. Berezinskiĭ, S. V. Bulanov, V. A. Dogiel, V. L. Ginzburg, and V. S. Ptuskin, *"Astrophysics of Cosmic Rays"*, edited by V. L. Ginzburg (North-Holland, Elsevier Science Publishers B. V., 1990).

[5] J. G. Learned, in: *Proceedings of the 13th European Cosmic Ray Symposium, "Cosmic Rays'92"*, Geneva, Switzerland, 27–31 July, 1992 [*Nucl. Phys. B (Proc. Suppl.)* **A 33** (1993) 8.

[6] J. G. Learned, *Phil. Trans. R. Soc. London* **A 346** (1994) 99.

[7] V. J. Stenger, *Astrophys. J.* **284** (1984) 810; in: *Proceedings of the 2nd NESTOR International Workshop*, Fortress of Niokastro, Pylos, Greece, 19–21 October, 1992, edited by L. K. Resvanis (Physics Laboratory, University of Athens, Athens, 1993), p. 79.

[8] L. Dell'Agnello, B. Monteleoni, V. A. Naumov, and Tang Hong, in: *Proceedings of the 2nd NESTOR International Workshop*, Fortress of Niokastro, Pylos, Greece, 19–21 October, 1992, edited by L. K. Resvanis (Physics Laboratory, University of Athens, Athens, 1993), p. 75.

[9] D. A. Morris and A. Ringwald, in: *Proceedings of the 3rd NESTOR International Workshop*, Fortress of Niokastro, Pylos, Greece, 19–21 October, 1993, edited by L. K. Resvanis (Physics Laboratory of the Athens University, Athens, 1994), p. 101; *Astroparticle Phys.* **2** (1994) 43.

[10] G. Domokos and S. Kovesi-Domokos, in: *Proceedings of the 2nd NESTOR International Workshop*, Fortress of Niokastro, Pylos, Greece, 19–21 October, 1992, edited by L. K. Resvanis (Physics Laboratory, University of Athens, Athens, 1993), p. 41.

[11] G. Domokos and S. Kovesi-Domokos, *Phys. Lett.* **B 343** (1995) 269.

[12] A. Suzuki, in: *Proceedings of the 13th International Conference on Neutrino Physics and Astrophysics "Neutrino'88"*, Boston, USA, June 1988, edited by J. Schneps, T. Kafka, W. A. Mann, and P. Nath (World Scientific, Singapore, 1988); KEK preprint 88-38.

[13] A. Suzuki, in: *Proceedings of the 3rd NESTOR International Workshop*, Fortress of Niokastro, Pylos, Greece, 19–21 October, 1993, edited by L. K. Resvanis (Physics Laboratory of the Athens University, Athens, 1994), p. 361.

[14] L. K. Resvanis (for the NESTOR Collaboration), in: *Proceedings of the Workshop on High Energy Neutrino Astrophysics*, Honolulu, Hawaii, 23–26 March, 1992, edited by V. J. Stenger, J. G. Learned, S. Pakvasa, and X. Tata (World Scientific, Singapore, Utopia Press, 1992), p. 325; L. K. Resvanis (for the NESTOR Collaboration), in: *Proceedings of the 2nd NESTOR International Workshop*, Fortress of Niokastro, Pylos, Greece, 19–21 October, 1992, edited by L. K. Resvanis (Physics Laboratory, University of Athens, Athens, 1993), p. 1; in: *Proceedings of the 5th International Workshop on Neutrino Telescopes*, Venice, Italy, 2–4 March, 1993, edited by M. Baldo Ceolin (Tipografia CLEUP di Padova, 1993), p. 321; in: *Proceedings of the 3rd NESTOR International Workshop*, Fortress of Niokastro, Pylos, Greece, 19–21 October, 1993, edited by L. K. Resvanis (Physics Laboratory of the Athens University, Athens, 1994), p. 1.

[15] C. Kourkoumelis (for the NESTOR Collaboration), in: *Proceedings of the 3rd NESTOR International Workshop*, Fortress of Niokastro, Pylos, Greece, 19–21 October, 1993, edited by L. K. Resvanis (Physics Laboratory of the Athens University, Athens, 1994), p. 491.

[16] S. Katsanevas (for the NESTOR Collaboration), in: *Proceedings of the 2nd NESTOR International Workshop*, Fortress of Niokastro, Pylos, Greece, 19–21 October, 1992, edited by L. K. Resvanis (Physics Laboratory of the Athens University, Athens, 1993), p. 171.

[17] S. Katsanevas (for the NESTOR Collaboration), in: *Proceedings of the 3rd NESTOR International Workshop*, Fortress of Niokastro, Pylos, Greece, 19–21 October, 1993, edited by L. K. Resvanis (Physics Laboratory of the Athens University, Athens, 1994), p. 504.

[18] T. K. Gaisser, F. W. Stecker, A. Harding, and J. Barnard, *Astrophys. J.* **309** (1986) 674.

[19] K. S. Thorne and A. N. Zytkow, *Astrophys. J.* **832** (1977) 212;
G. T. Biehle, *ibid* **380** (1991) 167.

[20] See *Proceedings of the Workshop on High Energy Neutrino Astrophysics*, Honolulu, Hawaii, 23–26 March, 1992, edited by V. J. Stenger, J. G. Learned, S. Pakvasa, and X. Tata (World Scientific, Singapore, Utopia Press, 1992).

[21] A. Roberts, *Rev. Mod. Phys.* **64** (1992) 259.

[22] J. G. Learned and V. J. Stenger, in: *Proceedings of the Workshop on High Energy Neutrino Astrophysics*, Honolulu, Hawaii, 23–26 March, 1992, edited by V. J. Stenger, J. G. Learned, S. Pakvasa, and X. Tata (World Scientific, Singapore, Utopia Press, 1992), p. 288;
see also Ref. [5].

[23] T. Stanev, in: *Proceedings of the 4th International Workshop on Neutrino Telescopes*, Venice, Italy, 10–13 March, 1992, edited by M. Baldo Ceolin (Tipografia CLEUP di Padova, 1992), p. 385.

[24] G. Giacomelli, in: *Proceedings of the 13th European Cosmic Ray Symposium "Cosmic Rays 92"*, July 1992, [*Nucl. Phys. B* (Proc. Suppl.) **A 33** (1993) 8].

[25] A. Di Credico (for the MACRO Collaboration), in: *Proceedings of the 23rd International Cosmic Ray Conference*, Calgary, Canada, 19–30 July, 1993, edited by D. A. Leahy (The University of Calgary, Calgary, 1993), Vol. **4**, p. 450.

[26] G. Vacanti et al. (WHIPPLE Collaboration), *Astrophys. J.* **377** (1991) 467;
M. Punch et al., (WHIPPLE Collaboration), *Nature (London)* **358** (1992) 477.

[27] A. Butkevich et al., in: *Proceedings of the 2nd NESTOR International Workshop*, Fortress of Niokastro, Pylos, Greece, 19–21 October, 1992, edited by L. K. Resvanis (Physics Laboratory of the Athens University, Athens, 1993), p. 347;
A. Trenikhin, *ibid*, p. 354.

[28] S. Barwick et al. (AMANDA Collaboration), in: *Proceedings of the Workshop on High Energy Neutrino Astrophysics*, Honolulu, Hawaii, 23–26 March, 1992, edited by V. J. Stenger, J. G. Learned, S. Pakvasa, and X. Tata (World Scientific, Singapore, Utopia Press, 1992), p. 291;
R. Morse, in: *Proceedings of the 5th International Workshop on Neutrino Telescopes*, Venice, Italy, 2–4 March, 1993, edited by M. Baldo Ceolin (Tipografia CLEUP di Padova, 1993), p. 309;
A. Bouchta (for the AMANDA Collaboration), in: *Proceedings of the 6th International Workshop on Neutrino Telescopes*, Venice, Italy, 22–24 February, 1994, edited by M. Baldo Ceolin (Tipografia CLEUP di Padova, 1994), p. 561;
P. Askebjer et al. (AMANDA Collaboration), in: *Proceedings of the 16th International Conference on Neutrino Physics and Astrophysics "Neutrino'94"*, Eilat, Israel, 29 May–3 June, 1994, edited by A. Dar, G. Eilam, and M. Gronau [*Nucl. Phys. B (Proc. Suppl.)* **38** (1995) 287].

[29] R. Morse, 1994, private communication.

[30] F. Halzen, 1994, private communication.

[31] S. Tilav et al. (AMANDA Collaboration), in: *Proceedings of the 24th International Cosmic Ray Conference*, Rome, Italy, 28 August – 8 September, 1995, Vol. **1**, p. 1013.

[32] F. Halzen, in: *Proceedings of the 17th Johns Hopkins Workshop "Particles and the Universe"*, Budapest, 1993 (World Scientific, 1993), p. 206.

[33] B. Erlandsson et al. (AMANDA Collaboration), in: *Proceedings of the 24th International Cosmic Ray Conference*, Rome, Italy, 28 August – 8 September, 1995, Vol. **1**, p. 1039.

[34] P. C. Mock et al. (AMANDA Collaboration), in: *Proceedings of the 24th International Cosmic Ray Conference*, Rome, Italy, 28 August – 8 September, 1995, Vol. **1**, p. 758.

[35] R. Wischnewski (for the Baikal Collaboration), in: *Proceedings of the 5th International Workshop on Neutrino Telescopes*, Venice, Italy, 2–4 March, 1993, edited by M. Baldo Ceolin (Tipografia CLEUP di Padova, 1993), p. 299; in: *Proceedings of the 3rd NESTOR International Workshop*, Fortress of Niokastro, Pylos, Greece, 19–21 October, 1993, edited by L. K. Resvanis (Physics Laboratory of the Athens University, Athens, 1994), p. 213;
G. V. Domogatzky (for the Baikal Collaboration), in: *Proceedings of the 6th International Workshop on Neutrino Telescopes*, Venice, Italy, 22–24 February, 1994, edited by M. Baldo Ceolin (Tipografia CLEUP di Padova, 1994), p. 541.

[36] C. Spiering, 1994, private communication.

[37] R. Wischnewski, 1994, private communication.

[38] I. A. Belolaptikov et al. (Baikal Collaboration), in: *Proceedings of the 24th International Cosmic Ray Conference*, Rome, Italy, 28 August – 8 September, 1995, Vol. **1**, p. 841.

[39] I. A. Belolaptikov et al. (Baikal Collaboration), in: *Proceedings of the Workshop on Trends in Astroparticle Physics*, Stockholm, Sweden 22–25 September, 1994, edited by L. Bergström et al. [*Nucl. Phys. B (Proc. Suppl.)* **43** (1995) 241].

[40] I. A. Belolaptikov et al. (Baikal Collaboration), in: *Proceedings of the 24th International Cosmic Ray Conference*, Rome, Italy, 28 August – 8 September, 1995, Vol. **1**, p. 742.

[41] P. K. F. Grieder (for the DUMAND Collaboration), in: *Proceedings of the 3rd NESTOR International Workshop*, Fortress of Niokastro, Pylos, Greece, 19–21 October, 1993, edited by L. K. Resvanis (Physics Laboratory of the Athens University, Athens, 1994), p. 168; in: *Proceedings of the Workshop on Trends in Astroparticle Physics*, Stockholm, Sweden 22–25 September, 1994, edited by L. Bergström et al. [*Nucl. Phys. B (Proc. Suppl.)* **43** (1995) 146].

[42] S. A. Khanaev and A. F. Kuleshov, in: *Proceedings of the 2nd NESTOR International Workshop*, Fortress of Niokastro, Pylos, Greece, 19–21 October, 1992, edited by L. K. Resvanis (Physics Laboratory, University of Athens, Athens, 1993), p. 253.

[43] E. Anassontzis, *Nucl. Instruments and Methods* **A 349** (1994) 242.

[44] T. A. Demidova and I. A. Repin, in: *Proceedings of the 2nd NESTOR International Workshop*, Fortress of Niokastro, Pylos, Greece, 19–21 October, 1992, edited by L. K. Resvanis (Physics Laboratory, University of Athens, Athens, 1993), p. 284.

[45] E. Trimonis and M. Rudenko, in: *Proceedings of the 2nd NESTOR International Workshop*, Fortress of Niokastro, Pylos, Greece, 19–21 October, 1992, edited by L. K. Resvanis (Physics Laboratory, University of Athens, Athens, 1993), p. 321.

[46] K. S. Hirata et al. (Kamiokande Collaboration), *Phys. Lett.* **B 205** (1988) 416; *ibid* **B 280** (1992) 146;
A. Suzuki, in: *Proceedings of the 5th International Workshop on Neutrino Telescopes*, Venice, Italy, 2–4 March, 1993, edited by M. Baldo Ceolin (Tipografia CLEUP di Padova, 1993), p. 221;
see also E. W. Beier et al., *ibid* **B 283** (1992) 446 for a survey of atmospheric neutrino data.

[47] Y. Fukuda et al. (Kamiokande Collaboration), *Phys. Lett.* **B 335** (1994) 237.

[48] D. Casper et al. (IMB Collaboration), *Phys. Rev. Lett.* **66** (1991) 2561;
R. Becker-Szendy et al. (IMB Collaboration), *ibid* **69** (1992) 1010; *Phys. Rev.* **D 46** (1992) 3720; D. Kiełczewska (for the IMB Collaboration), in: *Proceedings of the 6th International Workshop on Neutrino Telescopes*, Venice, Italy, 22–24 February, 1994, edited by M. Baldo Ceolin (Tipografia CLEUP di Padova, 1994), p. 507;
R. Becker-Szendy et al. (IMB Collaboration), in: *Proceedings of the 16th International Conference on Neutrino Physics and Astrophysics "Neutrino'94"*, Eilat, Israel, 29 May – 3 June, 1994, edited by A. Dar, G. Eilam, and M. Gronau [*Nucl. Phys. B (Proc. Suppl.)* **38** (1995) 331].

[49] P. Litchfield (for the SOUDAN 2 Collaboration), in: *Proceedings of the 5th International Workshop on Neutrino Telescopes*, Venice, Italy, 2–4 March, 1993, edited by M. Baldo Ceolin (Tipografia CLEUP di Padova, 1993), p. 235; in: *Proceedings of the International Workshop on ν_μ/ν_e Problem in Atmospheric Neutrinos*, Gran Sasso, Italy, 5–6 March, 1993, edited by V. Berezinsky and G. Fiorentini (LNGS, L'Aquila, 1993), p. 114;
W. W. Allison et al. (SOUDAN 2 Collaboration), in: *Proceedings of the 23rd International Cosmic Ray Conference*, Calgary, Canada, 19–30 July, 1993, edited by D. A. Leahy (The University of Calgary, Calgary, 1993), Vol. **4**, p. 446;
M. C. Goodman (for the SOUDAN 2 Collaboration), in: *Proceedings of the 16th International Conference on Neutrino Physics and Astrophysics "Neutrino'94"*, Eilat, Israel, 29 May–3 June, 1994, edited by A. Dar, G. Eilam, and M. Gronau [*Nucl. Phys. B (Proc. Suppl.)* **38** (1995) 337].

[50] M. Aglietta et al. (NUSEX Collaboration), *Europhys. Lett.* **8** (1989) 611.

[51] Ch. Berger et al. (Fréjus Collaboration), *Phys. Lett.* **B 245** (1990) 305.

[52] K. Daum et al. (Fréjus Collaboration), *Z. Phys.* **C 66** (1995) 417;
W. Rhode et al. (Fréjus Collaboration), in: *Proceedings of the 24th International Cosmic Ray Conference*, Rome, Italy, 28 August – 8 September, 1995, Vol. **1**, p. 726.

[53] A. E. Ball, S. Katsanevas, and N. Vassilopoulos, *"Design Study for a Long Baseline Neutrino Beam*, CERN/ECP Note 95-13 (1995).

[54] P. V. Ramana Murthy and A. W. Wolfendale (editors), *"Gamma-Ray Astronomy"* (Cambridge University Press, Cambridge, 1986).

[55] T. C. Weeks, *Physics Reports* **160** (1988) 1.

[56] W. T. Vestrand and D. Eichler, *Astrophys. J.* **261** (1982) 251.

[57] D. Kazanas and P. M. Giovanoni, in: *Proceedings of the Workshop on High Energy Neutrino Astrophysics*, Honolulu, Hawaii, 23–26 March, 1992, edited by V. J. Stenger, J. G. Learned, S. Pakvasa, and X. Tata (World Scientific, Singapore, Utopia Press, 1992), p. 94.

[58] M. Sikora and M. C. Begelman, in: *Proceedings of the Workshop on High Energy Neutrino Astrophysics*, Honolulu, Hawaii, 23–26 March, 1992, edited by V. J. Stenger, J. G. Learned, S. Pakvasa, and X. Tata (World Scientific, Singapore, Utopia Press, 1992), p. 114.

[59] G. R. Fontaine, in: *Proceedings of the International Workshop "Towards a Major Atmospheric Čerenkov Detector – II for TeV Astro/Particle Physics"*, Calgary, Canada, 17–18 July, 1993, edited by R. C. Lamb (Iowa State University, Ames, 1993), p. 12

[60] R. C. Lamb, in: *Proceedings of the International Workshop "Towards a Major Atmospheric Čerenkov Detector for TeV Astro/Particle Physics"*, Palaiseau, France, June 1992, edited by P. Fleury and G. Vacanti (Editions Frontières, Gif-sur-Yvette, 1993).

[61] P. T. Reynolds et al., *Astrophys. J.* **404** (1993) 206.

[62] M. Punch et al., *Nature (London)* **358** (1992) 477.

[63] C. E. Fichtel et al., *"H.E. Gamma Ray Emission from AGN Observed by the EGRET"*, EGRET contribution to *Proceedings of the Compton Gamma Ray Observation Symposium* (Washington University, 1993).

[64] L. K. Resvanis et al., *Astrophys. J.* **L 328** (1988) 9.

[65] F. W. Stecker, C. Done, M. H. Salamon, and P. Sommers, in: *Proceedings of the Workshop on High Energy Neutrino Astrophysics*, Honolulu, Hawaii, 23–26 March, 1992, edited by V. J. Stenger, J. G. Learned, S. Pakvasa, and X. Tata (World Scientific, Singapore, Utopia Press, 1992), p. 1.

[66] A. P. Szabo and R. J. Protheroe, *Astroparticle Phys.* **2** (1994) 374.

[67] P. L. Biermann, in: *Proceedings of the Workshop on High Energy Neutrino Astrophysics*, Honolulu, Hawaii, 23–26 March, 1992, edited by V. J. Stenger, J. G. Learned, S. Pakvasa, and X. Tata (World Scientific, Singapore, Utopia Press, 1992), p. 86.

[68] A. V. Butkevich, L. G. Dedenko, and I. M. Zheleznykh, *Yad. Fiz.* **50** (1989) 142 [*Sov. J. Nucl. Phys.* **50** (1989) 90].

[69] M. Diemoz et al., *Z. Phys.* **C 39** (1988) 21.

[70] E. Akhmedov, P. Lipari, and M. Lusignoli, *Phys. Lett.* **B 300** (1993) 128.

[71] V. Trimble, *Rev. Mod. Phys.* **55** (1983) 511.

[72] A. D. Kerrick et al., *"Outburst of TeV Photons from Mrk 421"*, submitted to *Astrophysical Journal Letters* (1995).

[73] D. Kazanas, in: *Proceedings of the 2nd NESTOR International Workshop*, Fortress of Niokastro, Pylos, Greece, 19–21 October, 1992, edited by L. K. Resvanis (Physics Laboratory, University of Athens, Athens, 1993), p. 20.

[74] T. K. Gaisser, F. Halzen, and T. Stanev, preprint University of Wisconsin–Madison MAD/PH/847 (August 1994).

[75] P. Hantzios (for the NESTOR Collaboration), in: *Proceedings of the 3rd NESTOR International Workshop*, Fortress of Niokastro, Pylos, Greece, 19–21 October, 1993, edited by L. K. Resvanis (Physics Laboratory of the Athens University, Athens, 1994), p. 523.

[76] A. Schwartz, D. Joutras, and D. Cline, *Phys. Rev.* **D 37** (1988) 1758;
P. Fayet, *Phys. Lett.* **B 219** (1989) 521;
V. A. Naumov and E. S. Zaslavskaya, *Nucl. Phys.* **B 361** (1991) 675.

[77] See, for example, G. M. Frichter, D. W. McKay, and J. P. Ralston, *Phys. Rev. Lett.* **74** (1995) 1508, and references therein.

[78] K. O. Mikaelian and I. M. Zheleznykh, *Phys. Rev.* **D 22** (1980) 2122;
M. Bander and H. R. Rubinstein, *Phys. Rev.* **D 51** (1995) 1410.

[79] A. V. Butkevich et al., *Z. Phys.* **C 39** (1988) 241.

[80] W. Frati, T. K. Gaisser, A. K. Mann, and T. Stanev, *Phys. Rev.* **D 48** (1993) 1140.

[81] D. H. Perkins, *Nucl. Phys.* **B 399** (1993) 3.

[82] T. Stanev, in: *Proceedings of the 5th International Workshop on Neutrino Telescopes*, Venice, Italy, 2–4 March, 1993, edited by M. Baldo Ceolin (Tipografia CLEUP di Padova, 1993), p. 247; in: *Proceedings of the International Workshop on ν_μ/ν_e Problem in Atmospheric Neutrinos*, Gran Sasso, Italy, 5–6 March, 1993, edited by V. Berezinsky and G. Fiorentini (LNGS, L'Aquila, 1993), p. 4.

[83] V. A. Naumov, in: *Proceedings of the International Workshop on ν_μ/ν_e Problem in Atmospheric Neutrinos*, Gran Sasso, Italy, 5–6 March, 1993, edited by V. Berezinsky and G. Fiorentini (LNGS, L'Aquila, 1993), p. 25.

[84] T. K. Gaisser, in: *Proceedings of the 3rd International Workshop on Theoretical and Phenomenological Aspects of Underground Physics "TAUP'93"*, Gran Sasso, Italy, 19–23 September, 1993, edited by C. Arpesella, E. Bellotti, and A. Bottino [*Nucl. Phys. B (Proc. Suppl.)* **35** (1994) 209].

[85] T. K. Gaisser et al., in: *Proceedings of the 24th International Cosmic Ray Conference*, Rome, Italy, 28 August – 8 September, 1995, Vol. **1**, p. 702.

[86] P. F. Harrison, D. H. Perkins, and W. G. Scott, *Phys. Lett.* **B 349** (1995) 137. An important point is that the threefold maximal mixing hypothesis explains not only the results of underground experiments, related to fully contained ν events, but also the data from solar neutrino experiments as well as the combined available data from accelerators and reactors.

[87] W. A. Mann, T. Kafka, and W. Leeson, *Phys. Lett.* **B 291** (1992) 200. The interpretation of the R anomaly in terms of the decay $p \to e^+\nu\nu$ is appropriate *solely* for the KAMIOKANDE result in the sub-GeV energy range [46] and with the AN flux from Ref. [90]. It fails, or seems to be very ill-founded, for the IMB [48] and SOUDAN 2 [49] results, independently of the AN flux model.

[88] O. G. Ryazhskaya, *Nuovo Cimento* **18 C** (1995) 77;
Pis'ma Zh. Éksp. Teor. Fiz. **61** (1995) 229 [*JETP Lett.* **61** (1995) 237].

[89] G. Barr, T. K. Gaisser, and T. Stanev, *Phys. Rev.* **D 39** (1989) 3532.

[90] É. V. Bugaev and V. A. Naumov, *Phys. Lett.* **B 232** (1989) 391; *Yad. Fiz.* **51** (1990) 774 [*Sov. J. Nucl. Phys.* **51** (1990) 77].

[91] M. Honda, K. Kasahara, K. Hidaka, and S. Midorikawa, *Phys. Lett.* **B 248** (1990) 193.

[92] H. Lee and Y. S. Koh, *Nuovo Cimento* **105 B** (1990) 883.

[93] D. H. Perkins, *"A New Calculation of Atmospheric Neutrino Flux"*, Oxford University Report OUNP-93-92 (1993); *Astroparticle Phys.* **2** (1994) 249.

[94] M. Honda, T. Kajita, K. Kasahara, and S. Midorikawa, *Calculation of the Flux of Atmospheric Neutrinos*, ICRR-Report-336-95-2 (February, 1995).

[95] T. K. Gaisser and T. Stanev in: *Proceedings of the 24th International Cosmic Ray Conference*, Rome, Italy, 28 August – 8 September, 1995, Vol. **1**, p. 694.

[96] É. V. Bugaev and V. A. Naumov, *Yad. Fiz.* **45** (1987) 1380 [*Sov. J. Nucl. Phys.* **45** (1987) 857].

[97] P. Lipari and T. Stanev in: *Proceedings of the 24th International Cosmic Ray Conference*, Rome, Italy, 28 August – 8 September, 1995, Vol. **1**,p. 516.

[98] É. V. Bugaev and V. A. Naumov, in: *Proceedings of the 21st International Cosmic Ray Conference*, Adelaide, Australia, 6–19 January, 1990, edited by R. Protheroe (The University of Adelaide, Northfield, South Australia, 1990) Vol. **10**, p. 8;
T. Cheung and E. C. M. Young, *ibid*, p. 16;
D. P. Bhattacharyya and P. Pal, *ibid*, p. 26;
M. Kawasaki and S. Mizuta, *Phys. Rev.* **D 43** (1991) 2900;
L. V. Volkova, *Phys. Lett.* **B 316** (1993) 178.

[99] M. Treichel, *Z. Phys.* **C 54** (1992) 469.

[100] P. Lipari, *Astroparticle Phys.* **1** (1993) 195.

[101] V. Agrawal, T. K. Gaisser, P. Lipari, and T. Stanev, in preparation (see also Refs. [80, 82]).

[102] M. Honda, T. Kajita, K. Kasahara, and S. Midorikawa, in: *Proceedings of the 24th International Cosmic Ray Conference*, Rome, Italy, 28 August – 8 September, 1995, Vol. **1**, p. 710.

[103] O. C. Allkofer, T. Kitamura, A. Okada, and W. Vernon, in: *Proceedings of the 16th International Cosmic Ray Conference*, Kyoto, Japan, 1979 (Institute for Cosmic Ray Research, University of Tokyo Press, Tokyo, 1979), Vol. **10**, p. 411.

[104] L. V. Volkova, *Yad. Fiz.* **31** (1980) 1510 [*Sov. J. Nucl. Phys.* **31** (1980) 784].

[105] K. Mitsui, Y. Minorikawa, and H. Komori, *Nuovo Cimento* **9 C** (1986) 995.

[106] Particle Data Group, L. Montanet et al., *Phys. Rev.* **D 50** (1994) 1173.

[107] L. V. Volkova and G. T. Zatsepin, *Yad. Fiz.* **37** (1983) 353 [*Sov. J. Nucl. Phys.* **37** (1983) 212];
H. Inazawa and K. Kobayakawa, *Prog. Theor. Phys.* **69** (1983) 1195;
A. V. Butkevich, L. G. Dedenko, and I. M. Zheleznykh, in: *Proceedings of the 1st All-Union Conference "Investigation of Muons and Neutrinos in Large Water Volumes"*, Alma-Ata, 1983, p. 180; in: *Proceedings of the 18th International Cosmic Ray Conference*, Bangalore, India, 1983, edited by N. Durgaprasad et al. (Tata Institute of Fundamental Research, Colaba, Bombay, 1983), Vol. **11**, p. 435;
L. V. Volkova and G. T. Zatsepin, *Izv. Akad. Nauk SSSR, Ser. Fiz.* **49** (1985) 1386;
É. V. Bugaev, E. S. Zaslavskaya, V. A. Naumov, and S. I. Sinegovsky, in: *Proceedings of the 20th International Cosmic Ray Conference*, Moscow, USSR, 2–15 August, 1987, edited by V. A. Kozyarivsky et al. ("Nauka", Moscow, 1987), Vol. **6**, p. 305.

[108] É. V. Bugaev, V. A. Naumov, S. I. Sinegovsky, and E. S. Zaslavskaya, *Nuovo Cimento* **12 C** (1989) 41.

[109] M. Thunman, G. Ingelman, and P. Gondolo, in: *Proceedings of the Workshop on Trends in Astroparticle Physics*, Stockholm, Sweden 22–25 September, 1994, edited by L. Bergström et al. [*Nucl. Phys. B (Proc. Suppl.)* **43** (1995) 274].

[110] R. Bellotti et al. (WIZARD/MASS Collaboration), *"A Measurement of the Negative Muon Spectrum between 0.3 and 40 GeV/c in the Atmosphere"*, preprint INFN, LNGS–95/02 (January, 1995), submitted to *Journal of Geophysical Researches*;
G. Basini et al. (WIZARD/MASS Collaboration), in: *Proceedings of the 24th International Cosmic Ray Conference*, Rome, Italy, 28 August – 8 September, 1995, p. 585.

[111] J. F. Krizmanic et al. (IMAX Collaboration), in: *Proceedings of the 24th International Cosmic Ray Conference*, Rome, Italy, 28 August – 8 September, 1995 p. 593.

[112] E. Schneider et al. (HEAT Collaboration), in: *Proceedings of the 24th International Cosmic Ray Conference*, Rome, Italy, 28 August – 8 September, 1995 p. 690.

[113] O. C. Allkofer and P. K. F. Grieder, *"Cosmic Rays on Earth"* (Fachsinformationszentrum, Karlsruhe, 1984), Number **25-1** of Physik Daten.

[114] É. V. Bugaev et al., in: *Proceedings of the 3rd NESTOR International Workshop*, Fortress of Niokastro, Pylos, Greece, 19–21 October, 1993, edited by L. K. Resvanis (Physics Laboratory of the Athens University, Athens, 1994), p. 268; in *Proceedings of the RIKEN International Workshop on Electromagnetic and Nuclear Cascade Phenomena in High and Extremely High Energies*, Tokyo, Japan, 22–24 December, 1993, edited by M. Ishihara and A. Misaki (RIKEN, Tokyo, 1994) pp. 264.

[115] U. Becker et al., *"L3, a New Tool for Cosmic Ray Muon Studies and the Search of High Energy Cosmic Ray Sources"*, L3 internal note 1676 (November 23, 1994), unpublished;
see also P. Le Coultre, in: *Proceedings of the 3rd NESTOR International Workshop*, Fortress of Niokastro, Pylos, Greece, 19–21 October, 1993, edited by L. K. Resvanis (Physics Laboratory of the Athens University, Athens, 1994), p. 253
L. W. Jones et al. in: *Proceedings of the 24th International Cosmic Ray Conference*, Rome, Italy, 28 August – 8 September, 1995, Vol. **1**, p. 609.

[116] S. Bussino (for the MACRO Collaboration), in: *Proceedings of the 24th International Cosmic Ray Conference*, Rome, Italy, 28 August – 8 September, 1995, Vol. **1**, p. 540;
M. Ambrosio et al. (MACRO Collaboration), *"Vertical Muon Intensity Measured with MACRO at Gran Sasso Laboratory"*, preprint INFN, LNGS-95/03 (February, 1995), to be published in *Phys. Rev.* **D 52** (1995).

[117] G. Sartorelli (for the LVD Collaboration), in: *Proceedings of the 24th International Cosmic Ray Conference*, Rome, Italy, 28 August – 8 September, 1995, Vol. **1**, p. 734;
M. Aglietta et al. (LVD Collaboration), *Astroparticle Phys.* **3** (1995) 311.

[118] I. A. Belolaptikov et al. (Baikal Collaboration), in: *Proceedings of the 24th International Cosmic Ray Conference*, Rome, Italy, 28 August – 8 September, 1995, Vol. **1**, p. 636.

[119] P. Pramantiotis and C. Kourkoumelis, in: *Proceedings of the 2nd NESTOR International Workshop*, Fortress of Niokastro, Pylos, Greece, 19–21 October, 1992, edited by L. K. Resvanis (Physics Laboratory, University of Athens, Athens, 1993), p. 359.

[120] See, for example, E. D. Carlson, *Phys. Rev.* **D 34** (1986) 1454.

[121] G. L. Cassiday, J. W. Keuffel, and J. A. Thompson, *Phys. Rev.* **D 7** (1973) 2022.

[122] W. Lohmann, R. Kopp, and R. Voss, *"Energy Loss of Muon in the Energy Range 1–10000 GeV"*, CERN Yellow Report 85-03 (1985).

[123] J. F. Owens, *Phys. Lett.* **B 266** (1991) 126.

[124] A. D. Martin, R. G. Roberts, and W. J. Stirling, preprint RAL-94-055 (1994).

[125] M. Glück, E. Reya, and A. Vogt, preprint DO-TH 94/24 (1994).

[126] General review of dark matter are given in V. Trimble, *Ann. Rev. Astron. Astrophys.* **25** (1987) 425;
J. R. Primack, D. Seckel, and B. Sadoulet, *Ann. Rev. Nucl. Part. Sci.* **38** (1988) 751.

[127] J. Yang et al., *Astrophys. J.* **281** (1984) 493.

[128] A. Milsztajn (for the EROS Collaboration), in: *Proceedings of the 3rd International Workshop on Theoretical and Phenomenological Aspects of Underground Physics "TAUP'93"*, Gran Sasso, Italy, 19–23 September, 1993, edited by C. Arpesella, E. Bellotti, and A. Bottino [*Nucl. Phys. B (Proc. Suppl.)* **35** (1994) 137];
E. Aubourg et al. (EROS Collaboration), *Nature (London)* **365** (1993) 623;
F. Cavalier, Ph. D. Thesis, Orsay preprint LAL 94-18 (1994).

[129] C. Alcock et al. (MACHO Collaboration), *Nature (London)* **365** (1993) 621; *Phys. Rev. Lett.* **74** (1995) 2867
W. Sutherland et al. (MACHO Collaboration), in: *Proceedings of the 16th International Conference on Neutrino Physics and Astrophysics "Neutrino'94"*, Eilat, Israel, 29 May–3 June, 1994, edited by A. Dar, G. Eilam, and M. Gronau [*Nucl. Phys. B (Proc. Suppl.)* **38** (1995) 379];
see also B. Sadoulet, in: *Proceedings of the 3rd International Workshop on Theoretical and Phenomenological Aspects of Underground Physics "TAUP'93"*, Gran Sasso, Italy, 19–23 September, 1993, edited by C. Arpesella, E. Bellotti, and A. Bottino [*Nucl. Phys. B (Proc. Suppl.)* **35** (1994) 117] for a review.

[130] A. Udalski et al. (OGLE Collaboration), *Acta Astronomica* **43** (1993) 289; **44** (1994) 165; **44** (1994) 227; *Astrophys. J.* **L 69** (1994) 426;
M. Szymanski (for the OGLE Collaboration), *"Results from OGLE"*, talk given at the *14th Moriond Workshop*, Villars-Sur-Ollon, Switzerland, 22–29 January, 1994.

[131] L. Moscoso, in: *Proceedings of the 16th International Conference on Neutrino Physics and Astrophysics "Neutrino'94"*, Eilat, Israel, 29 May–3 June, 1994, edited by A. Dar, G. Eilam, and M. Gronau [*Nucl. Phys. B (Proc. Suppl.)* **38** (1995) 387].

[132] see also E. I. Gates, G. Gyuk, and M. S. Turner, *Phys. Rev. Lett.* **74** (1995) 3724, and references therein.

[133] G. F. Giudice and E. Roulet, *Nucl. Phys.* **B 316** (1989) 429;
G. B. Gelmini, P. Gondolo, and E. Roulet, *ibid* **B 351** (1991) 623;
A. Bottino, et al., *Phys. Lett.* **B 265** (1991) 57;
F. Halzen, M. Kamionkowski, and T. Steltzer, *Phys. Rev.* **D 45** (1992) 4439;
V. S. Berezinsky, in: *Proceedings of the 15th International Conference on Neutrino Physics and Astrophysics "Neutrino'92"*, Granada, Spain, 7–12 June, 1992, edited by A. Morales [*Nucl. Phys. B (Proc. Suppl.)* **31** (1993) 413)];
M. Drees et al., *Phys. Rev.* **D 49** (1994) 636;
R. Gandhi et al., *ibid* **D 49** (1994) 3691.

[134] K. Kamionkowski, *Phys. Rev.* **D 44** (1991) 3021.

[135] M. Mori et al., *Phys. Rev.* **D 48** (1993) 5505.

[136] A. Gould, *Astrophys. J.* **321** (1987) 571.

[137] A. Gould, *Astrophys. J.* **328** (1988) 919; **368** (1991) 610.

[138] See, for example, K. Griest and D. Seckel, *Nucl. Phys.* **B 283** (1987) 681.

[139] A. Bottino, N. Fornengo, G. Mignola, and L. Moscoso, *Astroparticle Phys.* **3** (1995) 65.

[140] J. M. LoSecco et al., *Phys. Lett.* **B 188** (1987) 388;
R. Svoboda et al., *Astrophys. J.* **315** (1987) 420;
D. Casper, in: *Proceedings of the 23rd Rencontres de Moriond*, Les Arcs, France, 1988, edited by J. Audouze and J. Trân Thanh Vân (Editions Frontières, Gif-Sur-Yvette, France, 1988).

[141] P. Abreu et al., *Phys. Lett.* **B 245** (1990) 276;
B. Adeva et al., *ibid* **B 251** (1990) 3111;
M. Z. Akrawy et al., *Z. Phys.* **C 49** (1991) 1.

[142] S. J. Parke, FERMILAB Conf-91/251-T (September 1991);
M. C. Goodman, summary talk given at the *Workshop on Long Baseline Neutrino Oscillations*, Fermilab, 17–20 November, 1991, ANL-HEP CP-92-17;
R. Bernstein, *"Ideas for a Long-Baseline Neutrino Detector"*, February 1992, FERMILAB-Conf-92/63.

[143] J. Brunner (for the CHORUS Collaboration), in:*Proceedings of the International Europhysical Conference on High Energy Physics*, Marseille, France, 1993, edited by J. Carr and M. Perrottet (Editions Frontières, Gif-Sur-Yvette, France, 1993), p. 555.

[144] L. DiLella (for the NOMAD Collaboration), in: *Proceedings of the 15th International Conference on Neutrino Physics and Astrophysics "Neutrino'92"*, Granada, Spain, 7–12 June, 1992, edited by A. Morales [*Nucl. Phys. B (Proc. Suppl.)* **31** (1993) 319)]; *CERN Annual Report*, Vol. **2** (1993) 14.

[145] L. Wolfenstein, *Phys. Rev.* **D 17** (1978) 2369; **D 20** (1979) 2634;
S. P. Mikheyev and A. Yu. Smirnov, *Yad. Fiz.* **42** (1985) 1441 [*Sov. J. Nucl. Phys.* **42**(1985) 913]; *Nuovo Cimento* **9 C** (1986) 17.

[146] A. E. Ball et al., *"CERN Beams for Long Baseline Neutrino Oscillation Experiments"*, CERN-SL Note 92-75 (BT) (1992).

[147] M. Mayoud, unpublished.

[148] B. C. Barish et al. & S. Wojcici et al., FNAL letters of intent.

[149] R. Brun et al., *"GEANT 3.21"*, CERN Data Handling Division DD/EE/84-1.

[150] Atherton et al., *"Precise Measurements of Particle Production from a 400 GeV Beam on Beryllium Targets"*, preprint CERN 80-07.

[151] Barton et al., Fermilab CONF 80-48 EXP.

[152] H. C. Fesefeldt, *"Simulation of Hadronic Showers, Physics and Applications"*, Physikalisches Institut der Techische Hochshule Aachen Technical Report PITHA 85/02 (1985).

[153] A. Fasso et al., *"FLUKA 92"*, in: *Proceedings of the Workshop on Simulating Accelerator Radiation Environments*, Santa Fe, USA, 11–15 January, 1993.

[154] A. Fasso et al., *Nucl. Instruments and Methods* **A 332** (1993) 459.

[155] S. A. Khanaev and A. F. Kuleshov, Measurements of water transparency South-West of Greece, Proceeding of the 2nd NESTOR International Workshop, editor L. K. Resvanis, (1993) 253

[156] E. G. Anassontzis, P. Ioannou, Chr. Kourkoumelis, L. K. Resvanis, and H. Bradner, Light transmissivity in the NESTOR site, NIM A349 (1994) 242.

[157] H. Bradner and G. Blackinton, Long base line measurements of light transmission in clear water, Applied Optics, vol 23, no7 (1984) 1009.

[158] T. A. Demidova and E. A. Kontar, On near-bottom currents in the Mediterranean Sea. Gen. ass. EGU., Vienna 1991.

[159] V. G. Krivosheya, The report of the R/V "Vityaz" 22 cruise, P. P. Shirshov Oceanology Inst., Moscow, 1991 (in Russian)

[160] T. A. Demidova and I. A. Repin, Investigation of near bottom currents in Inouse pit in the vicinity of NESTOR site, Proceeding of the 2nd NESTOR International Workshop, editor L.K.Resvanis, (1993) 284

[161] E. Trimonis and M. Rudenko, Geomorphology and bottom sediments of the Pilos area, Proceeding of the 2nd NESTOR International Workshop, editor L. K. Resvanis, (1993) 321.

[162] The report of the R/V "Mendeleev" 45 cruise (In russian) P. P. Shirshov Oceanology Inst., Moscow, 1989, TOM I, Fonde A.S. U.S.S.R.

[163] The report of the R/V "Keldish" 29 cruise (In russian) P. P. Shirshov Oceanology Inst., Moscow, 1993

[164] A. W. Klement, CRC Handbook of Enviromental Radiation, CRC Press, Inc. 1982.

[165] A. B. Brodsky, CRC Handbook of Radiation Measurement and Protection, CRC Press, Inc. Sec. A, Vol. I (1982) 277.

[166] Improvements of 20-inch diameter photomultiplier tubes, Asuzuki and Mori

[167] Physics and Astrophusics of Neutrinos, M. Fukugita, A. Suzuki

[168] Private communication, L. Sulak, Boston University

[169] M. Fukugita and A. Suzuki (Eds). Physics and Astrophysics of Neutrinos (page 267). Springer - Verlag.

[170] L. Sulak (1994), private communication on the IMB experience

[171] RD23 Collaboration, CERN/DRDC 93-95

[172] TriQuint Semiconductor: Hot Rod High-Speed Serial Link

[173] P. Bertin, D. Roncin, J. Vuillemin, *Introduction to Programamble Active Memories*, PRL Research Report 3, Digital Equipment Corp., Paris Research Laboratory, 85 Av. Victor Hugo. 92563 Rueil-Malmaison Cedex, France, 1989.

[174] P. Bertin, D. Roncin, J. Vuillemin, *Programmable Active Memories: a Performance Assessment*, PRL Research Report 24, Digital Equipment Corp., Paris Research Laboratory, 85 Av. Victor Hugo. 92563 Rueil-Malmaison Cedex, France, 1993.

[175] Digital Equpment Corporation *TURBOchannel Developer's Kit, Version 2* EK-TCDEV-DK-002, September 1990.

[176] Xilinx Inc., *The Programmable Logic Data Book*, Xilinx Inc., 2100 Logic Drive, San Jose, CA 95124 1993.

[177] R. Brun, M. Hansroul, and J. C. Lassalle, *GEANT User's Guide*, DD/EE/82, 1982.

[178] A. D. Martin, R. G. Roberts, and W. J. Stirling, RAL-93-077, 1993.

[179] G. A. Askaryan, *Atomnaya energiya*, No.**3** (1957) 152 (in Russian).

[180] G. A. Askaryan and B. A. Dolgoshein, Report on the 1976 DUMAND Summer Workshop Hawaii, September 1976; Preprint P. N. Lebedev Physical Institute No. 160 (in Russian); *Pis'ma Zh. Éksp. Teor. Fiz.* **25** (1977) 232 [*JETP Lett.* **25** (1977) ?].

[181] T. Bowen, Conference Papers (15th Intern. Cosmic Ray Conf., Plovdiv) 1977, V.6, p.277.

[182] J. Learned, *Phys. Rev.* **D 19** (1979) 3293.

[183] F. W. Stecker et al., Proc. 3d Int. Workshop on Neutrino Telescopes, Venezia, 1991, p. 487.

[184] J. Learned and T. Stanev, Proc. 3d Int. Workshop on Neutrino Telescopes , Venezia, 1991,p.473.

[185] Butkevich A. et al. Proc. 2nd Int. Conf. on Trends in Astroparticle Physics (1991), Aachen, Germany. Tubner-Texte Zur Physik, 1994, V.B28, p.128.

[186] Butkevich A. et al., Proc. 2nd NESTOR Int. Workshop, Pylos, Greece, 1992, p.345; Trenikhin A, ibid, p.354.

[187] Karaevsky S. et al. 23-rd Int. Cosmic Ray Conf., Calgary, 1993, p.550.

[188] Bendat J., Piersol A., Random data. Analysis and measurements procedures, 1986.

[189] Askarian G. A., Dolgoshein B. A., Kalinovsky A. N., Mokhov N. V. Acoustic Detection of High Energy Particle Showers in Water, NIM, 1979, V.164, N 2, p.267.

[190] Learned J., Wilkes R. J. 23-rd Int. Cosmic Ray Conf., Calgary, 1993, p.538.

[191] L. G. Dedenko et al. Izv. RAN, ser. fiz., 58, N.12, pp. 83-86 (1994).